Thèse n°9427

Lightning to tall structures: Characterization, Modeling and Protection

Présentée le 3 décembre 2021

Faculté des sciences et techniques de l'ingénieur
Groupe SCI STI FR
Programme doctoral en génie électrique

pour l'obtention du grade de Docteur ès Sciences

par

Antonio ŠUNJERGA

Acceptée sur proposition du jury

Dr S.-R. Cherkaoui, président du jury
Prof. F. Rachidi-Haeri, Prof. M. Rubinstein, directeurs de thèse
Prof. V. Rakov, rapporteur
Prof. C. A. Nucci, rapporteur
Prof. A. Skrivervik, rapporteuse

École
polytechnique
fédérale
de Lausanne

2021

To Antea

Résumé

La physique de la foudre est hautement multidisciplinaire, impliquant des domaines tels que la physique des plasmas, le génie électrique, la météorologie, la thermodynamique et la physique des particules. Un coup de foudre ascendant est une décharge développée à partir de structures hautes. Ce type de décharge a récemment suscité beaucoup d'intérêt en raison de la hauteur croissante des structures telles que les éoliennes. Comprendre les coups de foudre ascendants est d'abord important pour mieux comprendre la physique de l'initiation et du développement de la foudre, à la fois dans les éclairs ascendants et descendants car ils partagent des propriétés similaires, mais aussi pour les études de protection contre la foudre. L'objectif de cette thèse est d'apporter des réponses à certaines des questions ouvertes concernant à la fois les mécanismes impliqués dans le processus physique et la protection contre la foudre.

Dans le cadre de cette thèse, nous avons développé et modernisé le site d'observation de la foudre à la tour Säntis. Cette tour est instrumentée pour les mesures de la foudre depuis 2010. Nous avons installé des capteurs spécifiques dans différentes bandes de fréquences à différents endroits autour du site pour obtenir des mesures à large bande qui peuvent nous donner plus d'informations sur les mécanismes impliqués dans le déclenchement des éclairs ascendants depuis la tour. Les nouvelles installations comprennent des capteurs de champ électrique, des capteurs de rayons X, des caméras haute vitesse et des caméras haute résolution. Au cours des saisons estivales 2019 et 2021, un système interférométrique appartenant à New Mexico Tech (New Mexico Institute of Mining and Technology) a été installé à proximité de la tour. Ce système est capable de reconstituer le trajet de la déchargedre avec une résolution spatiale de l'ordre du mètre et une résolution temporelle inférieure à la microseconde.

Des données d'observation simultanées ont été utilisées pour caractériser les décharges ascendantes. Sur la base des observations d'un système LMA (Lightning Mapping Array), nous avons étudié différents mécanismes de déclenchement des décharges ascendantes. Des scénarios typiques conduisant à l'initiation d'une décharge ascendante suite à des décharges à proximité sont présentés et analysés. De plus, nous avons utilisé des observations de caméras à haute vitesse pour étudier le rôle des "recoil leaders" (traceurs qui utilisent le chemin créé par les leaders positifs mais évoluant dans le sens inverse) dans les impulsions rapides se produisant dans des décharges négatives ascendantes. Nous avons observé que tous les différents processus rapides se produisant dans les éclairs négatifs ascendants proviennent des traceurs à reculons.

Pour la première fois, nous avons expliqué théoriquement le mécanisme derrière l'initiation de la foudre ascendante déclenchée par une activité orageuse à proximité, comme observé à la tour du

Säntis et d'autres sites d'observation dans le monde. Le modèle théorique développé est basé sur une géométrie simplifiée, et des expressions analytiques ont été développées pour évaluer les critères de déclenchement d'un traceur ascendant en fonction des propriétés géométriques et électriques des décharges ayant lieu à proximité. Le modèle analytique proposé a ensuite été utilisé pour estimer l'incidence de la foudre ascendante. Nous avons montré que le nombre d'éclairs ascendants déclenchés par des activités orageuses à proximité peut être considérablement sous-estimé par l'utilisation de formules empiriques proposées dans les normes.

À l'aide d'une approche rigoureuse (full wave) et de simulations numériques, nous avons étudié l'influence des systèmes de mise à la terre des éoliennes interconnectés dans les parcs éoliens. La réponse aux excitations typiques de la foudre dans les zones entourant une éolienne a été analysée à la fois dans les domaines temporel et fréquentiel. Nous avons montré que l'impédance de mise à la terre en basse fréquence pouvait être réduite d'un facteur de deux ou plus en raison de l'interconnexion de deux systèmes de mise à la terre séparés par une distance de 100 m. De plus, pour la première fois dans la littérature, nous avons analysé l'influence d'un terrain non plat sur la résistance de mise à la terre des électrodes hémisphériques. Nous avons montré que la résistance de mise à la terre des électrodes dans les terrains surélevés pouvait être considérablement augmentée par rapport à la résistance de mise à la terre de la même électrode dans un sol plat.

Liste de mots-clés: Décharge ascendante, tour Säntis, éclairs ascendants déclenchés, éclairs ascendants auto-déclenchés, traceur à reculons, critères de déclenchement, incidence des décharges ascendantes, éolienne, système de mise à la terre, élévation du potentiel au sol, simulation numérique, solution analytique

Abstract

Lightning physics is highly multidisciplinary, involving areas such as plasma physics, electrical engineering, meteorology, thermodynamics and particle physics. Upward lightning is a special type of lightning initiated from tall structures that has attracted a great deal of interest recently due to growing heights of structures such as wind turbines. Understanding upward lightning is important first to better understand the physics of lightning initiation and development, both in upward and downward flashes as they share similar properties, but also for lightning protection studies. The aim of this thesis is to provide answers to some of the open questions both concerning the mechanisms involved in the lightning process and lightning protection.

In the scope of this thesis, we have expanded and upgraded the lightning observation facility at the Säntis Tower that has been instrumented for lightning measurements since 2010. We have installed specific sensors in different frequency bands at different locations to obtain broadband measurements that can give us more insights into the mechanisms involved in the initiation of upward lightning flashes from the tower. The new installations include electric field sensors, x-rays sensors, high-speed cameras, and high-resolution cameras. During the summer season of 2019 and 2021, an interferometer system belonging to New Mexico Tech (New Mexico Institute of Mining and Technology) was installed in proximity of the tower capable of reconstructing the lightning path with spatial resolution in the order of one meter and temporal resolution of less than a microsecond.

Simultaneous observational data were used to characterize upward lightning. Based on the lightning mapping array observations, we have studied different mechanisms of triggering upward lightning. Typical scenarios leading to the initiation of upward lightning by preceding nearby lightning events are presented and analyzed. Furthermore, we used high-speed camera observations to study the role of recoil leaders in fast subsequent events occurring in upward negative flashes. We observed that all different fast subsequent processes occurring in upward negative lightning are originated from recoil leaders.

For the first time, we have explained theoretically the mechanism behind the initiation of upward lightning triggered by nearby lightning activity as observed at the Säntis Tower and other upward lighting observational sites around the world. The developed theoretical model is based on a simplified geometry, and analytical expressions were derived to evaluate the upward leader initiation criteria as a function of geometrical and electrical properties of nearby lightning events. The proposed analytical model was further used to estimate the incidence of upward lightning. We showed that the number of upward flashes triggered by nearby lightning can be significantly underestimated by use of empirical formulas proposed in standards.

Using a full-wave approach and numerical simulations, we studied the influence of interconnecting wind turbine grounding systems in wind turbine parks. The response to typical lightning excitations in areas surrounding a wind turbine were analyzed both in the time and in the frequency domain. We showed that the low frequency grounding impedance could be reduced by a factor of two or more as a result of interconnecting two grounding systems separated by a 100-m distance. Further, for the first time in the literature, we analyzed the influence of a non-flat terrain on the grounding resistance of hemispheric electrodes. We showed that the grounding resistance of electrodes in elevated terrains could be significantly increased with respect to the grounding resistance of the same electrode in a flat ground.

Keywords: Upward Lightning, Säntis Tower, Other-triggered flashes, self-triggered flashes, Recoil Leader, Initiation Criteria, Upward Lightning Incidence, Wind Turbine, Grounding System, Ground Potential Rise, Numerical Simulation, Analytical Solution

Acknowledgements

I would like to express my deep gratitude to my first supervisor Prof. Farhad Rachidi. Great scientist, no doubt one of the best in the field but more importantly great person and one could always rely on him. Thank you for all your kindness, patience, guidance and constructive suggestions.

Special thanks to my co-supervisor Prof. Marcos Rubinstein for all the great discussions. Always offering advice and encouragement with a perfect blend of insight and humor. Thank you for always being there when needed. It was a great pleasure to work with you.

I would like to express my gratitude to all the people from EPFL EMC lab especially to Dr. Carlos Romero and Dr. Mohammad Azadifar for their Säntis instrumentation legacy. Thanks to Amirhossein Mostajabi, Zhaoyang Wang, Aleksandr Smorgonskii and Hamidreza Karami.

Special thanks to Dr. Gerhard Deindorfer and Prof. Vernon Cooray for their advice, support and scientific collaboration.

I would like to thank as well our colleagues from Swisscom, Swisscom Broadcast, Armasuisse, and Huber&Suhner, whom kindly supported us during this project. I would like also to acknowledge the Swiss National Science Foundation (Project 200020_175594) for funding this dissertation.

Special thanks to Prof. Dragan Poljak, his passion for science and research motivated me for scientific career. Thank you for all the great lectures.

I would like to express my deep gratitude to all good professors that were involved in my 21 years of education during the elementary school, high school, university and PhD. Your work could never be appreciated enough. Among the many, special thanks to Prof. Ivica Puljak, Prof. Franjo Sokolić, Prof. Karlo Lelas, Prof. Ante Bilušić and Prof. Nikola Godinović. I have enjoyed your lectures and all the discussions. Special thanks to Dragica Bibić for motivating me to get the most of myself.

Thanks to all the people from ELL building for great memories and making my life easier in Switzerland, especially Francesco Gerini, Li Quanxin, Johanna Becker and Alexandra Karpilow.

Thanks to EasyJet for providing cheap Geneva-Split flights otherwise I would not survive for long.

Thanks to my friends and family from Čista Velika, there is no better feeling than coming home.

Thanks to Hajduk Split for not winning any titles while I was away, I'm sure they have been waiting for me.

My sincere gratitude to my friends and family for all the great memories.

To my dear wife Antea Čačvić, thank you for all the love and support. My special gratitude to your family for all the support.

To my sister and brother and last but not least, my deepest and forever thanks to my beloved parents, to my mother Branka Storić and to my father Ante Šunjerga thank you for being there for me.

List of Papers

This thesis is based on the following papers, which are referred to in the text by their capital Roman numerals. The author of the thesis is the main author of these papers and has been the main contributor in conceptualization, data curation, formal analysis, methodology, experimental measurements and analyses, software development and writing the original draft.

I Sunjerga, A., Mostajabi A., Paolone M., Rachidi F., Azadifar M., Rubinstein A., Rubinstein M., Romero C., Pavanello D., Hettiarachchi P. , Cooray V. & Smith D. Säntis Lightning Research Facility Instrumentation, accepted for 2021 joint 34th International Conference on Lightning Protection (ICLP) and 2021 International Symposium on Lightning Protection (XVI SIPDA)

II Sunjerga, A., Rubinstein, M., Pineda, N., Mostajabi, A., Azadifar, M., Romero, D., Van der Velde, O., Montanya, J., Figueras i Ventura, J., Besic, N., Grazioli, J., Hering, A., Germann, U., Diendorfer, G., & Rachidi, F. (2020). LMA observations of upward lightning flashes at the Säntis Tower initiated by nearby lightning activity. Electric Power Systems Research, 181, 106067. https://doi.org/10.1016/j.epsr.2019.106067

III Sunjerga, A., Rubinstein, M., Azadifar, M., Mostajabi, A., & Rachidi, F. (2021). Bidirectional Recoil Leaders in Upward Lightning Flashes Observed at the Säntis Tower. Journal of Geophysical Research: Atmospheres, 126(18). https://doi.org/10.1029/2021jd035238

IV Sunjerga, A., Rubinstein, M., Rachidi, F., & Cooray, V. (2021). On the Initiation of Upward Negative Lightning by Nearby Lightning Activity: An Analytical Approach. Journal of Geophysical Research: Atmospheres, 126(5). https://doi.org/10.1029/2020jd034043

V Sunjerga, A., Rubinstein, M., Rachidi, F., & Cooray, V. (2021) Incidence of Upward Lightning Triggered by Nearby Lightning: A Monte Carlo Simulation accepted for 2021 joint 34th International Conference on Lightning Protection (ICLP) and 2021 International Symposium on Lightning Protection (XVI SIPDA)

VI Sunjerga, A., Li, Q., Poljak, D., Rubinstein, M., & Rachidi, F. (2019). Isolated vs. Interconnected Wind Turbine Grounding Systems: Effect on the Harmonic Grounding Impedance, Ground Potential Rise and Step Voltage. Electric Power Systems Research, 173, 230–239. https://doi.org/10.1016/j.epsr.2019.04.010

VII Sunjerga, A., Rachidi, F., Rubinstein, M., & Poljak, D. (2019). Calculation of the Grounding Resistance of Structures Located on Elevated Terrain. IEEE Transactions on Electromagnetic Compatibility, 61(6), 1891–1895. https://doi.org/10.1109/temc.2018.2877214

VIII Sunjerga, A., Rubinstein, M., Poljak, D., Karami, H., & Rachidi, F. (2020). Grounding Resistance of a Hemispheric Electrode Located on the Top of a Finite-Height, Cone-Shaped Mountain. IEEE Transactions on Electromagnetic Compatibility, 62(5), 1889–1892. https://doi.org/10.1109/temc.2020.2974579

Reprints were made with permission from the respective publishers.

Selected contributions during doctoral studies of the author, which are not the main focus of this thesis are given below.

Journal Articles:

i Wang, J., Li, Q., Cai, L., Zhou, M., Fan, Y., Xiao, J., & Sunjerga, A. (2019). Multiple-Station Measurements of a Return-Stroke Electric Field From Rocket-Triggered Lightning at Distances of 68–126 km. IEEE Transactions on Electromagnetic Compatibility, 61(2), 440–448. https://doi.org/10.1109/temc.2018.2821193

ii Sunjerga, A., Gazzana, D. S., Poljak, D., Karami, H., Sheshyekani, K., Rubinstein, M., & Rachidi, F. (2019). Tower and Path-Dependent Voltage Effects on the Measurement of Grounding Impedance for Lightning Studies. IEEE Transactions on Electromagnetic Compatibility, 61(2), 409–418. https://doi.org/10.1109/temc.2018.2819693

iii Gazzana, D. S., Smorgonskiy, A., Mora, N., Šunjerga, A., Rubinstein, M., & Rachidi, F. (2018). An experimental field study of the grounding system response of tall wind turbines to impulse surges. Electric Power Systems Research, 160, 219–225. https://doi.org/10.1016/j.epsr.2018.02.020

iv Li, Q., Wang, J., Rachidi, F., Rubinstein, M., Sunjerga, A., Cai, L., & Zhou, M. (2019). Importance of Taking Into Account the Soil Stratification in Reproducing the Late-Time Features of Distant Fields Radiated by Lightning. IEEE Transactions on Electromagnetic Compatibility, 61(3), 935–944. https://doi.org/10.1109/temc.2018.2840702

v Figueras i Ventura, J., Pineda, N., Besic, N., Grazioli, J., Hering, A., van der Velde, O. A., Romero, D., Sunjerga, A., Mostajabi, A., Azadifar, M., Rubinstein, M., Montanyà, J., Germann, U., & Rachidi, F. (2019). Polarimetric radar characteristics of lightning initiation and propagating channels. Atmospheric Measurement Techniques, 12(5), 2881–2911. https://doi.org/10.5194/amt-12-2881-2019 vi Pineda, N., Figueras i Ventura, J., Romero, D., Mostajabi, A., Azadifar, M., Sunjerga, A., Rachidi, F., Rubinstein, M., Montanyà, J., Velde, O., Altube, P., Besic, N., Grazioli, J., Germann, U., & Williams, E. R. (2019). Meteorological Aspects of Self-Initiated Upward Lightning at the Säntis Tower (Switzerland). Journal of Geophysical Research: Atmospheres, 124(24), 14162–14183. https://doi.org/10.1029/2019jd030834

vii Figueras i Ventura, J., Pineda, N., Besic, N., Grazioli, J., Hering, A., van der Velde, O. A., Romero, D., Sunjerga, A., Mostajabi, A., Azadifar, M., Rubinstein, M., Montanyà, J., Germann, U., & Rachidi, F. (2019). Analysis of the lightning production of convective cells. Atmospheric Measurement Techniques, 12(10), 5573–5591. https://doi.org/10.5194/amt-12-5573-2019

viii Šunjerga, A., Sokolić, F., Rubinstein, M., & Rachidi, F. (2018). Lorentz Force from a Current-Carrying Wire on a Charge in Motion under the Assumption of Neutrality in the Symmetrical Frame of Reference. Journal of Modern Physics, 09(14), 2473–2481. https://doi.org/10.4236/jmp.2018.914159

ix Produit, T., Walch, P., Herkommer, C., Mostajabi, A., Moret, M., Andral, U., Sunjerga, A., Azadifar, M., André, Y.-B., Mahieu, B., Haas, W., Esmiller, B., Fournier, G., Krötz, P., Metzger, T., Michel, K., Mysyrowicz, A., Rubinstein, M., Rachidi, F., … Houard, A. (2021). The laser lightning rod project. The European Physical Journal Applied Physics, 93(1), 10504. https://doi.org/10.1051/epjap/2020200243

Conference Proceedings:

i Sunjerga, A., Rachidi, F., & Poljak, D. (2017, September). On wind turbine impedance analysis via different approaches. 2017 25th International Conference on Software, Telecommunications and Computer Networks (SoftCOM). https://doi.org/10.23919/softcom.2017.8115546

ii Sunjerga, A., Li, Q., Poljak, D., Rubinstein, M., & Rachidi, F. (2018, September). Transient Impedance of Interconnected Wind Turbine Grounding Systems. 2018 26th International Conference on Software, Telecommunications and Computer Networks (SoftCOM). https://doi.org/10.23919/softcom.2018.8555790

iii Sunjerga, A., Rubinstein, M., Diendorfer, G., & Rachidi, F. (2018, September). An Analysis of the Distribution of Inter-Flash Time Intervals in the Area of the Säntis Tower. 2018 26th International Conference on Software, Telecommunications and Computer Networks (SoftCOM) https://doi.org/10.23919/softcom.2018.8555816

iv Sunjerga, A., Mostajabi, A., Rachidi, F., Pineda, N., Romero, D., Van der Velde, O. A., Montanya, J., Azadifar, M., Rubinstein, M., & Diendorfer, G. (2018, September). On the Classification of Self-Triggered versus OtherTriggered Lightning Flashes. 2018 34th International Conference on Lightning Protection (ICLP). https://doi.org/10.1109/iclp.2018.8503322 v Mostajabi, A., Sunjerga, A., Azadifar, M., Smorgonskiy, A., Rubinstein, M., Rachidi, F., & Diendorfer, G. (2018, September). On the Impact of Meteorological Conditions on the Initiation of Upward Lightning Flashes from Tall Structures. 2018 34th International Conference on Lightning Protection (ICLP). https://doi.org/10.1109/iclp.2018.8503310

vi Sunjerga, A., Rachidi, F., Rubinstein, M., & Poljak, D. (2019, June). On the Influence of an Elevated Terrain on the Grounding Resistance of a Vertical Rod. 2019 IEEE International Conference on Environment and Electrical Engineering and 2019 IEEE Industrial and Commercial Power Systems Europe (EEEIC / I&CPS Europe).
https://doi.org/10.1109/eeeic.2019.8783741

vii Sunjerga, A., Ventura, J. F. i, Besic, N., Grazioli, J., Hering, A., Germann, U., Rachidi, F., Rubinstein, M., Mostajabi, A., Azadifar, M., Pineda, N., Romero, D., Velde, O. V. der, Montanya, J., & Diendorfer, G. (2019, September). LMA Observation of Upward Bipolar Lightning Flash at the Säntis Tower. 2019 International Symposium on Lightning Protection (XV SIPDA). 2019
https://doi.org/10.1109/sipda47030.2019.8951538

viii Sunjerga, A., Rachidi, F., Rubinstein, M., & Poljak, D. (2019, September). Reduction of a Cone-Shaped Terrain Grounding Resistance by Remote Grounding. 2019 International Conference on Software, Telecommunications and Computer Networks (SoftCOM).
https://doi.org/10.23919/softcom.2019.8903728

ix Sunjerga, A., Hettiarachchi, P., Smith, D., Rubinstein, M., Cooray, V., Azadifar, M., Mostajabi, A., & Rachidi, F. (2021). X-rays observations at the Säntis Tower: Preliminary results. Copernicus GmbH. https://doi.org/10.5194/egusphere-egu21-9586

Contents

List of Figures

List of Tables

List of Equations

Chapter 1 Introduction

This thesis is written in the form of a collection of papers. The aim of this chapter is to contextualize the work presented in this thesis. We first present a short introduction about the origin of lightning. The main subject of the thesis, the upward lightning, is presented in more detail. Finally, we present the background, motivation and objectives of each of the papers presented in this thesis.

1.1 Lightning Phenomenology

Fossil evidence shows that lightning was already present more than 250 million years ago [1]. There are also theories that suggest that lightning may have been responsible for the start of life on Earth [2]. Many civilizations have been awed by lightning throughout the history of mankind [3] . The study of lightning is multidisciplinary, involving disciplines such as plasma physics, electrical engineering, meteorology, thermodynamics and particle physics. Due to the overall complexity of lightning, many of its processes are still not well understood [4].

To understand the phenomenon, one can first look at the big picture, as shown in Fig 1. The Earth is constantly being bombarded by energetic solar and cosmic rays that can even originate from distant galaxies. Some of them may have travelled for over 14 billion years from the Big Bang itself. These cosmic rays give rise to conductivity in the upper layers of the atmosphere by creating ions through collisions. However, up to about 3 km height, the dominant effect in ion creation is the Earth's natural radioactivity. The electric conductivity of air at sea level is about 10^{-14} S/m and it increases up to 10^{-11} S/m at 35 km and 10^{-3} S/m at 100 km [3]. The line integral of the fair-weather electric field gives a voltage difference of about 300 kV from mean sea level to the lower layer of the ionosphere, considered as an equipotential surface (at about 65 km). Fair weather field measurements (e.g., [5] and [6]) suggest that, due to the finite conductivity of the air, there is a leakage current with an average of about 2.7 μA/km^2, effectively transferring positive charge to earth. Integrating over the closed surface, the overall current is about 1500 A. This current would neutralize the charge on the Earth that is responsible for the above-mentioned potential difference in about 10 minutes. There must therefore exist a mechanism that maintains the potential difference. It was suggested by Wilson [6] that the negative charge on the Earth is maintained by the action of thunderstorms. This concept is commonly referred to as the global electric circuit [7]. At any time, there is an average of 1500 active storms across the world with an average current of 1 A per storm.

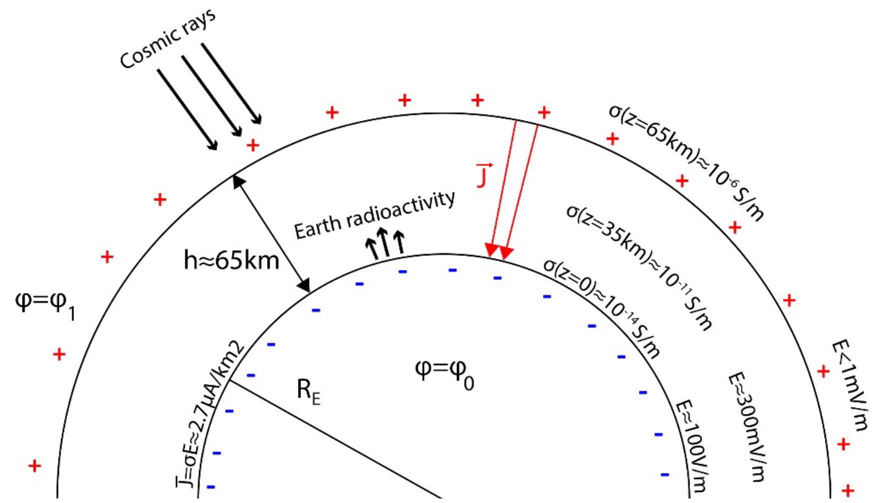

Figure 1.1 Earth atmospheric electricity under fair weather conditions.

Thunderclouds develop from small fair-weather clouds, named "cumulus" [8], which are themselves formed when parcels of warm, moist air rise and cool by adiabatic expansion. If the temperature decrease is larger than the moist-adiabatic lapse rate (0.6°C per 100 m), particles of warm, moist air will continue to rise. At a temperature of 0°C, some of the particles will start to freeze, and the liquid and solid phases will coexist. At about -40 °C, all the particles will be frozen. The vertical extent of the cloud is typically about 10 km and its horizontal dimension ranges from 3 km to over 50 km, where clouds can be composed of multiple cells. The mixture of liquid and solid phases between 0 °C and -40 °C is responsible for the cloud electrification. There are several mechanisms proposed in the literature (e.g., [9], [10] and [11]) that lead to the typical tripole structure shown in Fig 2. The currents caused by storms (shown in Fig 2) compensate the fair-weather current. The values in Fig. 2 are averaged over time and over the earth surface.

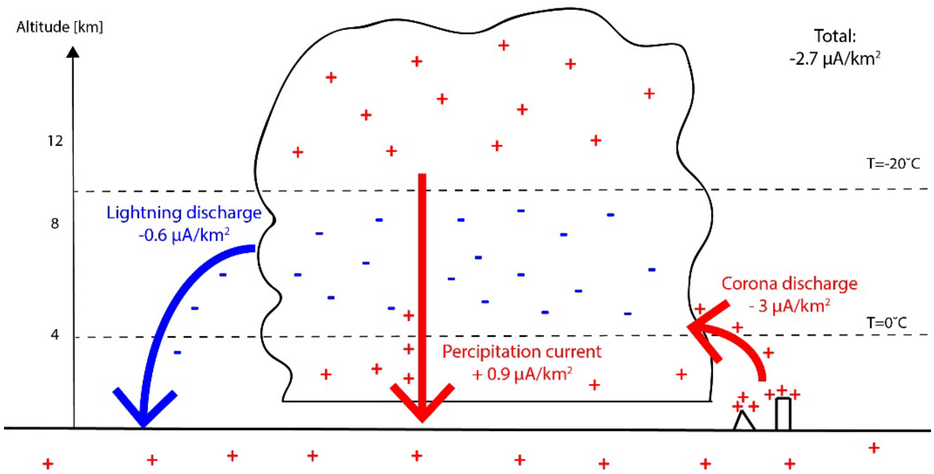

Figure 1.2 The total current averaged over time and over the earth surface caused by storms, re-charging the ionosphere.

A lightning discharge is a transient event in the atmosphere that transfers large amounts of charge and propagates by thermalizing air. A lightning discharge will be initiated at some point if the level of electric field is higher than the breakdown electric field ($3x10^6$ V/m at sea level for dry air). This will cause an electron avalanche and the number of electrons will increase exponentially in the opposite direction of the field. When the number of electrons reaches a critical value [12], the path from the origin to that point will become conducting, a process called avalanche-to-streamer transition. A high current will flow through the streamer and thermalize it (see Fig. 3). This is referred to as the streamer-to-leader transition. The leader can be either positive or negative and the physics of propagation of each is different [13].

Lightning discharges can be classified into the following categories [14]:

I. Intracloud flashes, which occur entirely inside a cloud (IC).

II. Cloud-to-cloud (or inter-cloud) flashes, which occur between two adjacent clouds (CC).

III. Cloud-to-ground flashes, which occur between a cloud and the ground (CG).

IV. Air discharge flashes, which occur between a cloud and the surrounding air.

V. Discharges in the upper and middle atmosphere.

Cloud-to-ground flashes are of highest interest since they directly affect life on earth. They can be classified into four types according to the direction of their initial leader propagation (either upward or downward) and the polarity of the effective charge transfer to the ground (either positive or negative) [15].

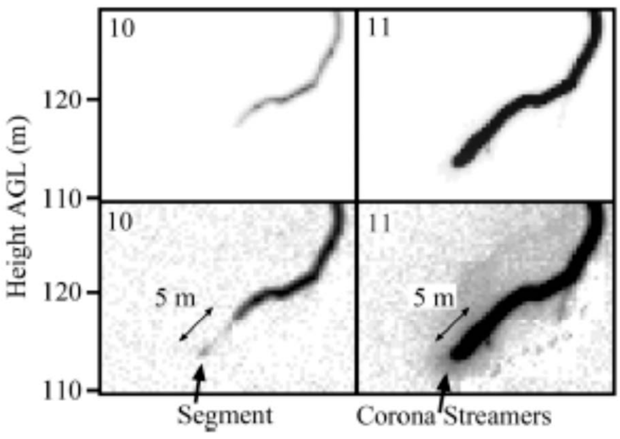

Figure 1.3 High speed camera record of leader propagation. Bottom left panel: ionization of path (streamer) through the process of electron avalanche, followed by (bottom right panel), thermalization (streamer to leader). The top panels show the same events but without contrast enhancement. Only the thermalized channel can be observed in air. Adapted from [16].

1.2 Upward Lightning

Upward flashes occur only from tall objects (>100 m or so) or from objects of moderate height located on mountain tops. Research shows that the presence of elevated objects can increase the lightning discharge incidence considerably [17], thereby increasing the risk of damages, especially for the case of poorly-conducting objects made of composite materials, such as wind turbines (WT) and airplanes. Damages to wind turbines caused by lightning account for approximately 80% of wind turbine insurance claims [18]. Wind turbines are indeed very vulnerable to lightning because of their height, sharp edges and the remote locations where they are often erected (e.g., [19] and [20]). The probability of lightning incidence is also increased by the rotation of the blades [21]. Somewhere between 4% and 8% of wind turbines in Europe suffer damages due to lightning strikes each year [20].

Several tall structures have been instrumented for lightning observations over the world (e.g., the Gaisberg, Peissenberg, Säntis, Skytree, Eagle Nest and CN towers). Most of the lightning strikes to these towers are of the upward type. Data from these instrumented towers have led to reports on lightning current measurements (e.g., [22], [23], [24], [25] and [26]), electric field measurements (e.g., [24], [27] and [28]), and high-speed camera (HSC) observations (e.g., [29] and [30]). These observations are of high importance for understanding both upward and downward lightning since downward lightning share similar properties with upward lightning [14]. Despite considerable attention focused recently on the physics of upward flashes in the literature, their initiation is still under debate and not well understood.

1.3 Scope of the Study

1.3.1 Broadband Measuring System at Säntis Tower

Lightning radiates electromagnetic fields over a very wide frequency spectrum. Each frequency range is important to understand different small-scale or large-scale phenomena. Simultaneous measurements in different frequency ranges and at different locations are of high importance to understand the underlying mechanisms of lightning initiation and development. From the electrical engineering point of view, the parameters of interest are the currents and fields, while for the complete physical description of the phenomenon, other parameters, such as, for example, the temperature and pressure inside the channel play an important role.

One of the main objectives of this study is the extension and upgrade of the Säntis Tower lightning observations site in Switzerland. For this reason, as shown in **Paper I** we have installed a series of sensors, namely a field mill, electric field antennas at multiple locations, x-rays sensors, a high-speed camera, and high resolution cameras.

1.3.2 Lightning Flashes Initiated by Nearby Lightning Activity

In [31], Wang et al. observed two different scenarios of upward lightning: self-triggered (ST) and other-triggered (OT), based on the absence or the presence of other lightning activity in the geographical and temporal vicinity of the tower-initiated flash. In case of absence of nearby lightning activity, it is believed that cloud charging is responsible for the increase of the field and the initiation of the flash. Further, it was hypothesized -even though never fully explained in theory- that the nearby lightning activity could also create electric field intensification at the tip of the tower. Later, Saba et al. [32] and Schumann et al. [33] reported one of the most extensive datasets of high-speed camera observations of other-triggered upward lightning flashes. The relative number of ST and OT flashes has been shown to vary depending on the geographical area (see e.g., [34]). The exact mechanism leading to the other-triggered scenario is not yet fully understood. Understanding of other-triggered scenarios and predicting lightning incidence due to this mechanism is of high interest for lightning risk estimation.

To shed some more light on the phenomenon of other-triggered flashes, in **Paper II** we used the data obtained at the Säntis Tower observation site together with simultaneously-measured data from a lightning mapping array that was installed in 2017 in the area of the tower. Further, in **Paper IV,** we developed a fully analytical model explaining theoretically, for the first time, observed scenarios (at the Säntis Tower and in other areas reported in the literature) of triggering upward negative lightning by nearby lightning discharges. In **Paper V,** we used this analytical model to estimate the upward lightning incidence to tall structures due to the nearby lightning mechanism by means of Monte Carlo simulations.

1.3.3 Role of Recoil Leaders in Upward Negative Lightning

Recoil leaders are self-propagating discharges, moving along a previously ionized channel [35] observed to occur in decayed positive leaders. It was suggested and observed ([35], [36] and [29]) that these recoil leaders occur in a bidirectional manner as predicted by Kasemir [37], with the negative end propagating downward and the positive end propagating upward in upward negative flashes. Mazur [35] argued that unidirectional propagation observed by lightning mapping systems is due to the fact that the negative leader radiates much more than the positive, and these systems are not able to measure both positive and negative leaders at the same time. In ([35], [36] and [29]), the origin of all fast processes that occur in negative cloud-to-ground lightning (such as dart leaders, M-components and attempted leaders) was ascribed to bidirectional recoil leaders .

To extend the understanding of the role of the recoil leader in upward negative lightning, we analyzed in detail high-speed camera data with other simultaneous measurements at the Säntis Tower in **Paper III** for the case of three tower events.

1.3.4 Special Concerns Designing Tall Structure Grounding Systems

Tall structures such as wind turbines and mobile phone base stations are often installed in remote and hilly locations. Those locations are very likely to be struck by lightning due to their geographical elevation (e.g., [38] and [39]) and to initiate upward flashes (e.g., [40] and [41]) from them. Remote locations make them less accessible, therefore complicating the tasks of maintenance and repair. Wind turbines are very vulnerable to lightning because of their height, sharp edges and remote and hilly locations where many of them are erected, often with low soil conductivity. Designing proper grounding systems that satisfy all required standards is of high importance.

For this reason, in **Paper VI,** we investigated the high frequency response of typical wind turbine grounding systems by way of full-wave numerical simulations. We investigated the influence of interconnecting grounding systems in wind turbine parks. Since many of the tall structures are located on non-flat terrain, in **Paper VII** and **Paper VIII,** we investigated for the first time the influence of non-flat terrain on the grounding resistance of simplified grounding systems by means of analytical solutions and steady-state numerical simulations.

Chapter 2 Measuring System

In this chapter, we briefly present the work done in Paper I related to the upgrade of the measuring system at the Säntis Tower. Some of the data collected by the upgraded system will be presented in this thesis while a large set of data of high interest remains for future analysis.

2.1 History of Measurements at the Säntis Tower

The Säntis Tower was instrumented in May 2010 to measure currents of lightning discharges striking the tower. The Säntis Tower is 124 m tall and it sits at the top of the 2502 m tall Säntis Mountain. The Säntis Mountain is located in the northeast of Switzerland, in the Appenzell region (47°14’57” N, 9°20’32” E). The tower is made of a conical metallic structure with an outer Plexiglas cover which protects the telecommunications infrastructure installed in the interior part. The lightning current waveform and its time derivative are measured at two different heights, 24 m and 82 m above ground level, using Rogowski coils and B-dot sensors (see [42] and [43] for more detailed information).

An EFM-100 field mill has been installed since July 15, 2016, to measure the electrostatic field in the immediate vicinity of the Säntis tower. Two fast antennas for the measurement of electric fields are also installed at two different locations. The first one is located 14.7 km away from the Säntis Tower, on the roof of a 25-m tall building in Herisau. The second station is located at Neudorf, Austria, about 380 km from the Säntis tower and it is operated by our partners from ALDIS (Austrian Lightning Detection and Information System). The Säntis area is also covered by the European lightning location system (EUCLID) and the Zurich weather radar.

2.2 Upgrade of the System (Paper I)

In order to upgrade the measuring system at the Säntis Tower, multiple other sensors were installed. These include another electric field sensor, an x-ray sensor, a high-speed camera and three high-resolution cameras. All these sensors are working with a pre-trigger window and receive a trigger over the Internet as shown in Figure 2.1. Each of these sites has a fixed IP address and they can be controlled remotely. Furthermore, to add another layer of stability, both modems and industrial computers can be restarted via SMS command. In addition to these sensors, another high-speed camera operated by the University of Geneva was installed in the summer of 2021, along with another x-ray sensor operated by the University of California Santa Cruz (UCSC). The data from the weather radar covering the Säntis Tower area are also made available by MeteoSwiss.

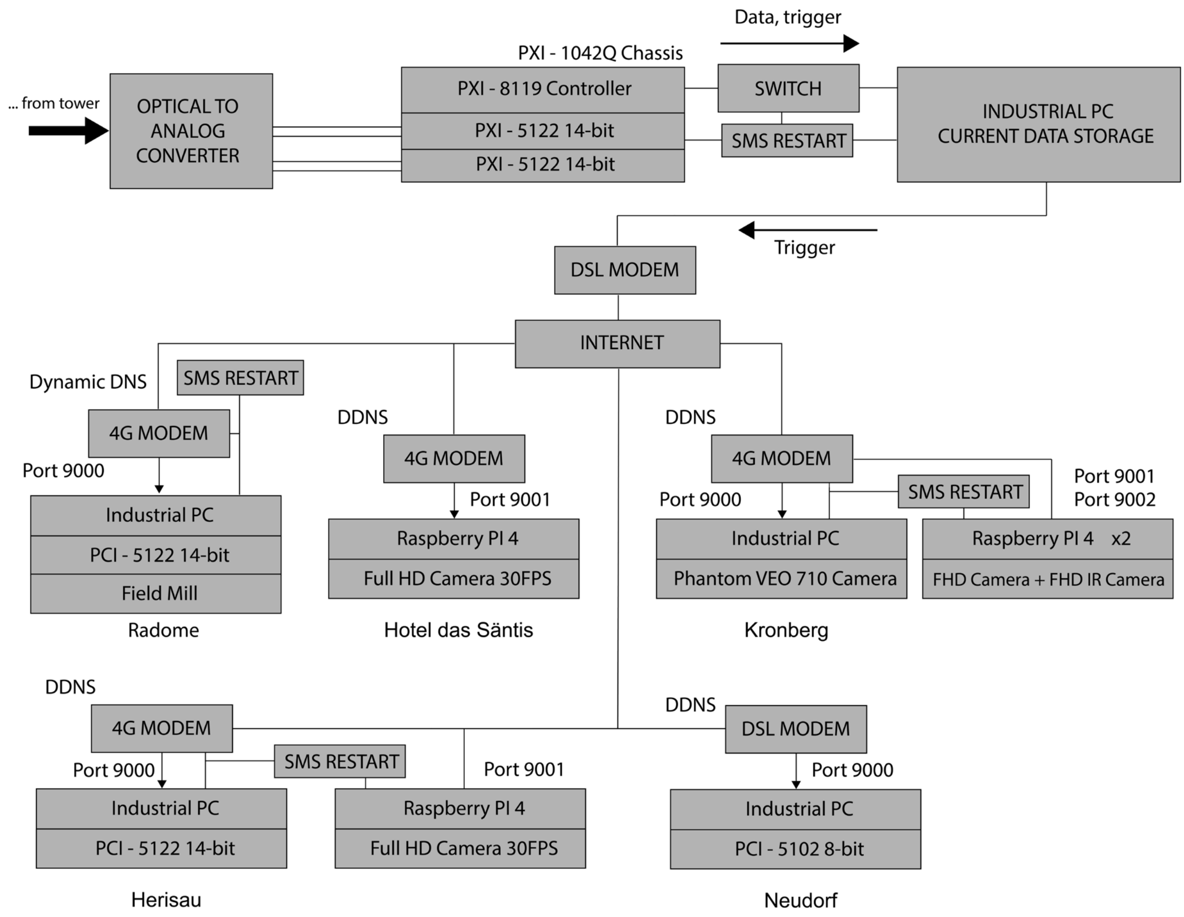

Figure 2.1 Simplified graph of the measuring system. The TCP trigger is sent from the tower to all other trigger-based sites. Figure taken from Paper I.

The locations of the different measuring sensors are shown in Figure 2.2. In total, there are seven different sites [Paper I]:

1. The Säntis Tower (2502 m ASL). Lightning current and its time derivative are measured at two different heights (24 m and 82 m above ground level), using at each location a Rogowski coil and a B-dot sensor. The measurement systems on the tower are thoroughly described in [42], [43] and [44].

2. Radome (2500 m ASL). The radome is located about 20 m away from the tower (see Fig. 4). At this location, we have installed a fast electric field antenna, an electrostatic field mill, and two x-ray sensors, one belonging to our partners from Uppsala University and operated by us and the second one operated by the University of California at Santa Cruz.

3. Säntis - Das Hotel (1400 m ASL). Located about 2 km away from the tower on the slope of Mount Säntis, this station is equipped with a high-speed camera operated by the University of Geneva.

4. Mount Kronberg (1663 m ASL) is about 5 km away from the tower. At this location, a high-speed video camera and two full HD (FHD) cameras are installed. One of the FHD cameras operates in the visible spectrum, while the other one works in the infra-red (IR) spectrum.

5. Herisau (800 m ASL). This site is located at a distance of 14.7 km from the tower. A fast E-field antenna is installed on the top of a building belonging to the Huber+Suhner company.

6. Neudorf (600 m ASL). This station, operated by ALDIS, is located in Neudorf, northern Austria, 380 km away from the tower. The station is equipped with a fast E-field antenna.

7. Albis radar located near the city of Zurich, 60 km east from the Säntis area (more details in [45] and [46]).

In addition to the permanent facility, during the 2017 summer season, a lightning mapping array (LMA) belonging to the Polytechnic University of Catalunya (UPC) was installed in the Säntis area (more details can be found in Paper II). Furthermore, during the summer seasons of 2019 and 2021, an interferometer belonging to New Mexico Tech (which is an upgraded version of the interferometer presented in [47]) was installed in the vicinity of “Säntis das Hotel” whose extensive dataset is yet to be processed.

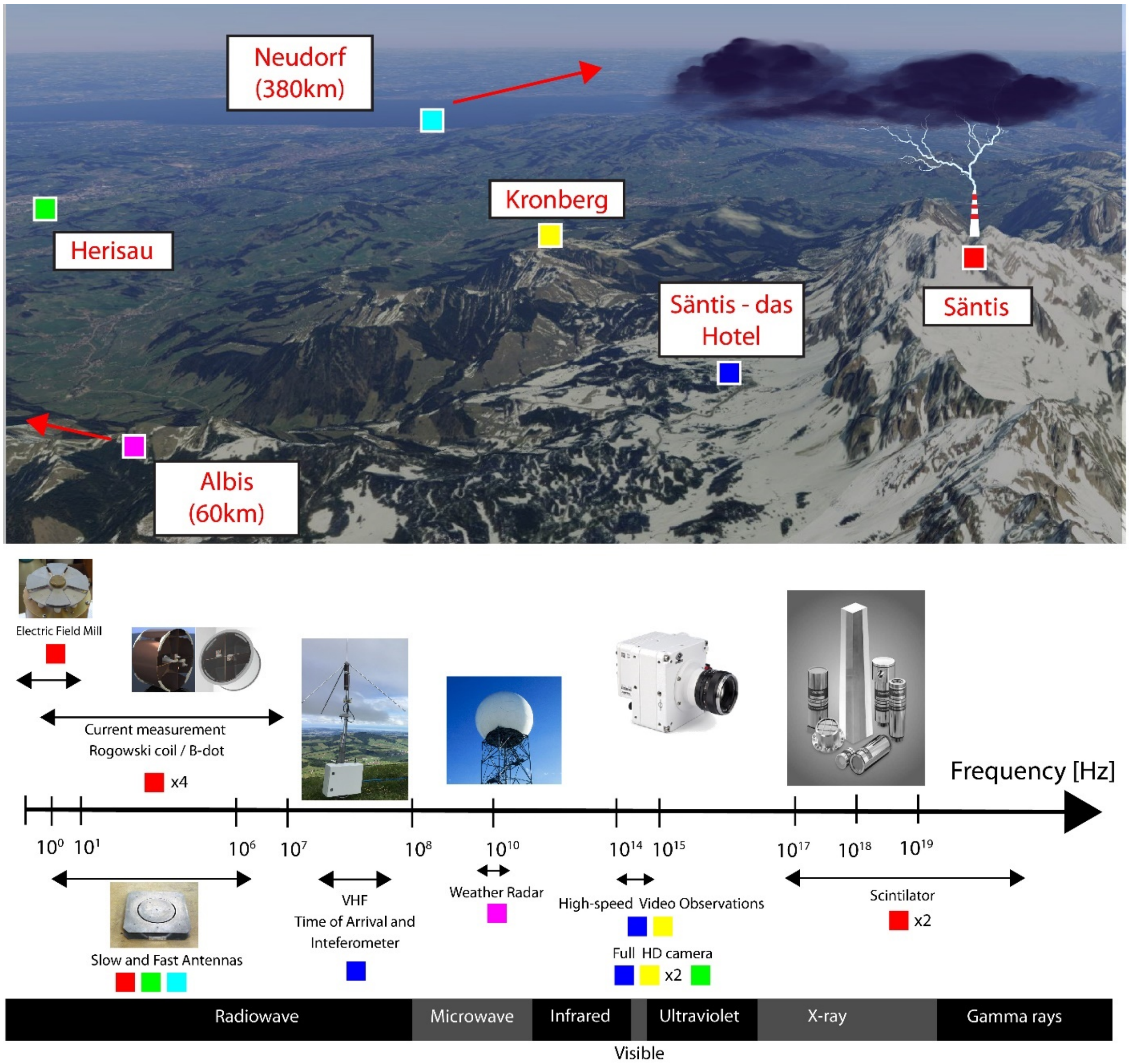

Figure 2.2 Locations of different measuring equipment. Not to scale.

Chapter 3 Characterization of Upward Flashes

In this chapter, we report observational results obtained at the Säntis Tower. Here, we report a summary of the methodology and the obtained results from Paper II and Paper III. The aim of Paper II is to analyze upward negative lightning triggered by nearby lightning using simultaneous observations of current, electric field, lightning mapping array (LMA) and radar measurements. The aim of Paper III is to investigate the role of recoil leaders in fast processes of negative upward lightning by means of high-speed camera, close electric field and current observations.

3.1 Lightning Mapping Array Observations of Upward Lightning initiated by nearby lightning activity (Paper II)

3.1.1 Methodology

A lightning mapping array (LMA) network was installed in the Säntis Tower region in June 2017. The system consists of six stations measuring VHF radiation in the 60-66 MHz band. The locations of the LMA stations were chosen considering several factors, namely:

1) The magnitude of the local noise within the frequency band,

2) the availability of reliable AC power and communication means,

3) the distance to the source (Säntis Tower), and,

4) a good combination of accessibility and security.

The selected locations correspond to mobile base stations belonging to Swisscom and Swisscom Broadcast and they are shown in Figure 3.1. The measurement stations were deployed in the vicinity of the Säntis Tower, at distances ranging from 100 m to 11 km. The area of interest around the Säntis Tower, which as mentioned before is located in the northeastern part of Switzerland, covers parts of the cantons of Appenzell Inner-Rhodes, Appenzell Outer-Rhodes, and St. Gallen. The LMA takes the maximum power of VHF radiation within a time window of 80 microseconds and measures the time of arrival with a 50 ns accuracy using a PC-based digitizer card coupled to a GPS receiver.

The LMA data were synchronized with the lightning current data using GPS time stamps. Results from the LMA network were transformed from global coordinates to the local coordinate system of the tower taking into account the curvature of the Earth. The coverage of the LMA system is about

30 km to the west of the tower, about 15 km to the east and 25 km to the south and north (for more details, see Fig. 1 in [48]).

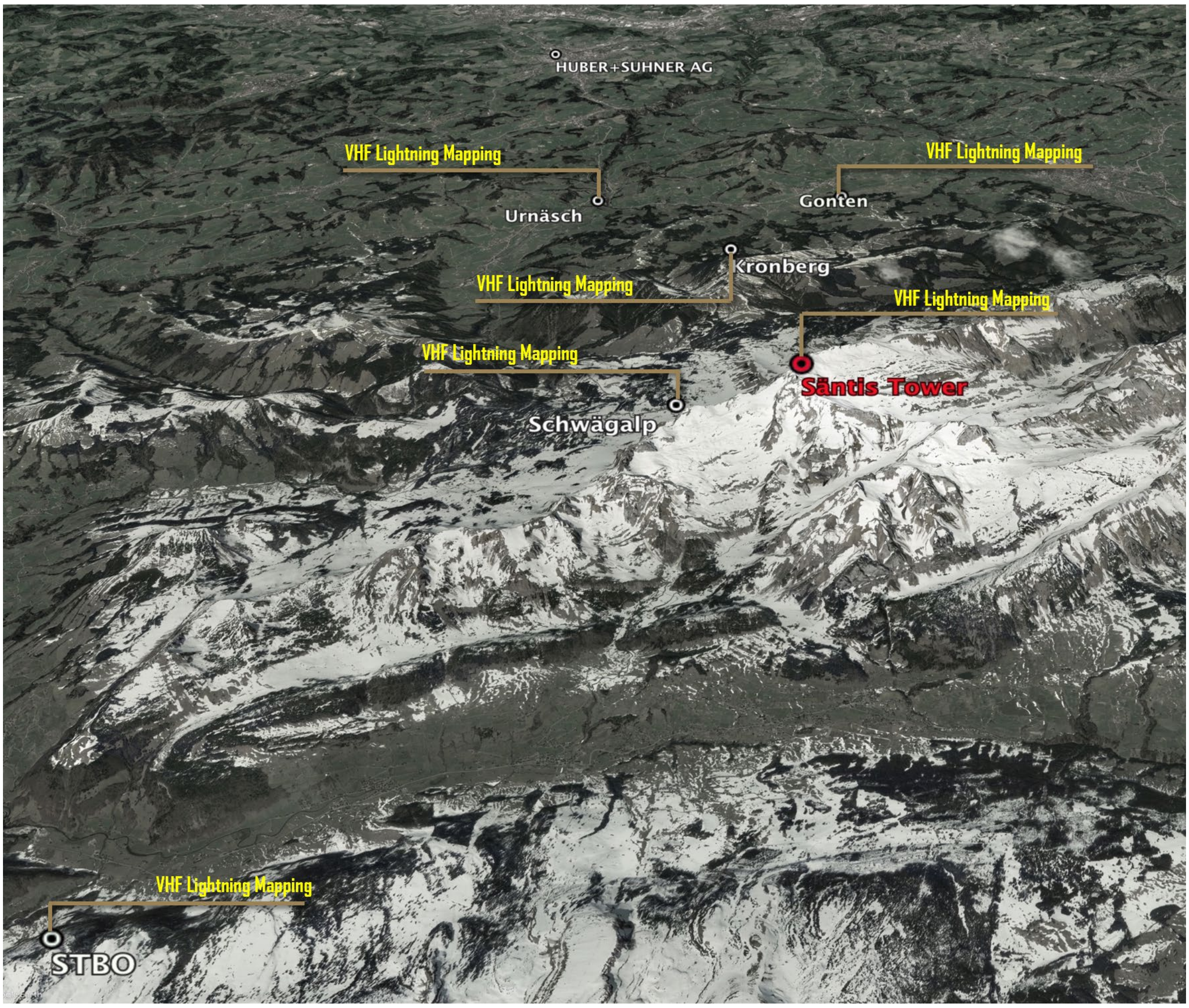

Figure 3.1 Lightning mapping array stations around the Säntis Tower. The measurement stations were deployed in the vicinity of the Säntis Tower, at distances ranging from 100 m to 11 km. (Figure taken from Paper II)

In addition to LMA data, current measurements at the tower, close electric field measurements and radar observations were used in this study (see Chapter 2 for more details about the measuring system).

Since the negative leaders propagate through positive charge regions and radiate more strongly (compared to positive leaders) in the VHF spectrum [49], the LMA observations over longer periods can be used to infer the charge structure of the cloud. The average horizontal speed can be used to estimate the polarity of the leader. Van der Velde and Montanyà [50] showed that negative leaders propagate with an average speed of 10^5 m/s (during positive cloud to ground flashes, the speed can sometimes go up to 10^6 m/s), while the average speed for positive leaders is around $2x10^4$ m/s. Knowing the polarity of the leaders can also be used to infer the charge structure, since negative leaders propagate through positive charge regions and positive leaders propagate through negative charge regions [49].

3.1.2 Results

In this paper, we analyzed three tower events that were preceded by nearby lightning activity, two of them being negative upward flashes and one a positive upward flash. The overall measuring systems and applied methods enabled us to infer the charge structure of clouds as well as the polarity of the leaders involved in each process. The illustrative summary of results for the three events is shown in Figures 3.2-3.4. We observed two negative upward flashes (Figure 3.2 and Figure 3.3) triggered by approaching negative leaders. In Figure 3.4, an approaching positive leader triggered an upward negative leader (positive flash) from the tower. More details can be found in Paper II.

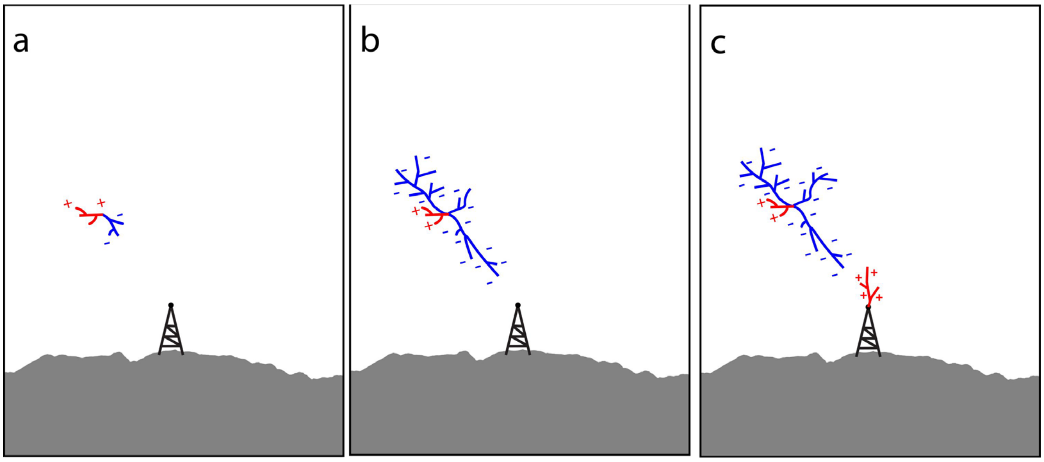

Figure 3.2 Sketch of the initial phase of the flash initiated from the Säntis Tower on 18.07.2017 at 16:28:01 UTC. View from the South. Not to scale. (Figure obtained from Paper II)

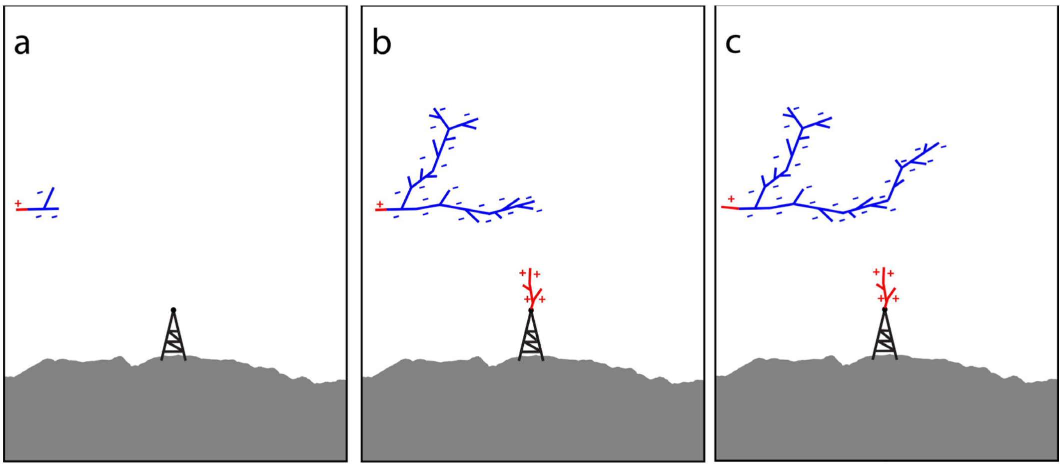

Figure 3.3 Sketch of the initial phase of the flash initiated from the Säntis Tower recorded on 18.07.2017 at 16:30:57 UTC. View from the East. Not to scale. (Figure obtained from Paper II)

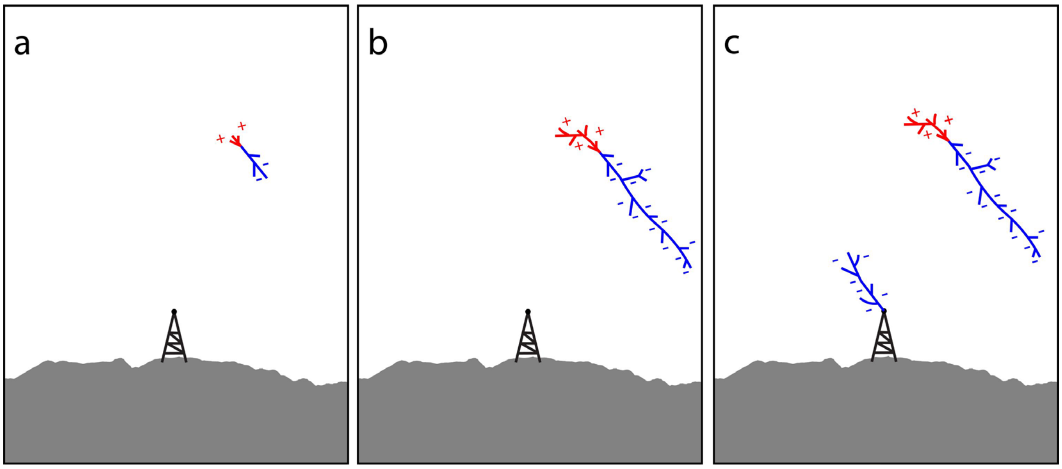

Figure 3.4 Sketch of the positive flash initiated from the Säntis Tower recorded on 29.06.2017 at 13:28:27 UTC. View from the East. Not to scale. (Figure is obtained from Paper II)

3.2 High-speed Camera Observations of Upward Negative Lightning (Paper III)

3.2.1 Methodology

In this paper, we report simultaneous measurements of current, close electric field and high-speed camera images for three upward negative flashes initiated from the Säntis tower in Switzerland. The close-range electric field was only measured in one of the flashes, which was analyzed in detail.

The Phantom VEO 710L high-speed video camera installed on the Kronberg mountain about 5 km away from the tower (see Section 2.2) can record up to 1,000,000 FPS at its lowest resolution of 8 x 8 pixels. To have a wider view of 512 x 512 pixels, the number of frames per second was reduced to 10,000. These pixels are distributed over a view of about 1700 m by 1700 m in the plane of the tower, perpendicular to the view with a resolution of about 3.4 m per pixel. The camera records during a 3-second time window with a pre-trigger delay of 1.5 s.

Using high-speed camera recordings, we observed parts of the upward positive leader (UPL) propagation during the initial continuous current (ICC) phase that reveal different processes that started as recoil leaders. As mentioned earlier, recoil leaders are self-propagating discharges, moving along a previously ionized channel [35] observed to occur in decayed positive leaders. They are thought [29] to be the cause of K-changes.

3.2.2 Results

Different terms have been used to identify different processes in the lightning discharge, which are briefly summarized in what follows. In upward negative and downward negative lightning, one can observe subsequent return strokes (RSs) preceded by dart leaders that propagate from the upper parts of the channel to the ground termination. If the dart leader stops before reaching the ground, the process is called an attempted dart leader (ADL). Although no current is observed at the bottom of the channel in attempted dart leaders, they do produce electric field changes that are known as K-changes or K-events [51]. Note that a K-event can occur both in cloud-to-ground and in cloud lightning. M-components occur when a floating leader connects to the upper part of the conducting channel created by the previous RS. Additionally, mixed mode (MM) pulses and M-component-type pulses occurring during the initial continuous current (the latter referred to as M-component-type ICC pulses) are only observed in upward lightning (e.g., [27] and [52]). These two types of pulses exhibit similarities, respectively, with the main pulse in the return stroke process and with the pulses that characterize the M-component process, the main difference being that MM and M-component-type ICC pulses occur during the ICC phase in upward negative lightning.

Our observations showed that different processes occurring in upward negative flashes, including the return stroke, mixed-mode pulses, M-components, M-component-type ICC events and attempted leaders all started as recoil leaders as shown in Figure 3.5. A dart leader is created when the recoil leader reaches either (i) the ground (or the tip of the tower), resulting in a subsequent stroke or a MM pulse, or (ii) a conducting channel, resulting in an M-component or an M-component-type ICC pulse. What follows will depend on the type of junction (to the structure or to a conducting channel) and the presence of another conducting branch. This confirms once again ([53] and [35]) that a recoil leader is the main cause for the sequence of different events observed in upward and downward negative lightning. Recoil leaders have also been observed, to a lesser degree, in decayed negative leaders [54]. Bidirectional propagation of recoil leaders was also observed in three recoil leaders of which two developed into return strokes and one ended up as an attempted leader. It is possible that all recoil leaders were bidirectional but this was not seen due to the frame rate limitation of the high-speed camera. Our observations suggest also that in later stages of the recoil leader development, the positive end ceases to propagate (consistent with other studies (e.g., [53], [35] and [29]). What makes our study different is that we report all the different fast processes involved in upward lightning at the same location, while many of the previous observations report single processes. One of the four fast processes involved in upward lightning, mixed-mode pulses, has not been observed in other studies with a high-speed camera.

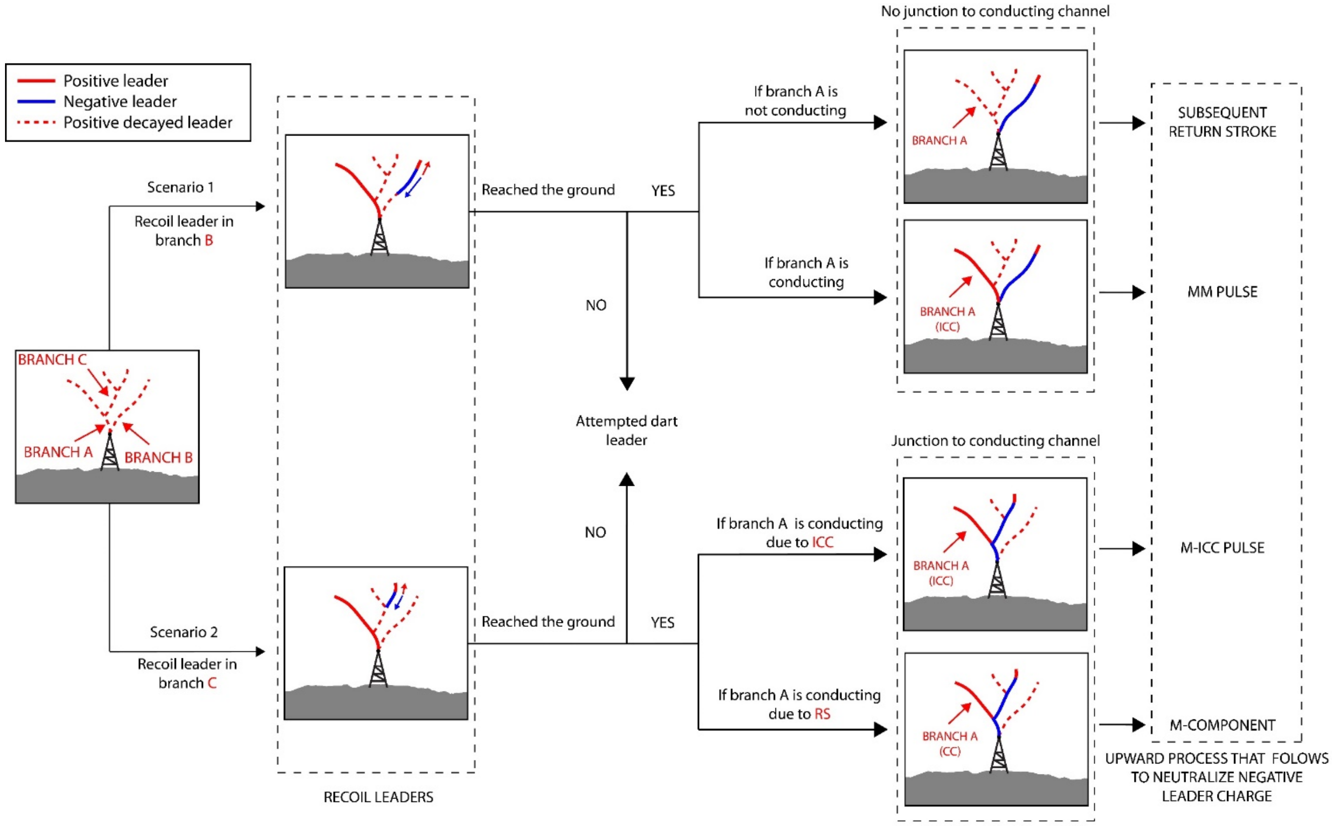

Figure 3.5 Sketch of mechanisms involved in the initiation of different charge transfer modes in upward negative flashes, all of them starting from recoil leaders, as observed at Säntis. Not to scale. (Figure obtained from Paper III)

Chapter 4 Modeling of Upward Negative Lightning Initiation Criteria

In this chapter, we first present the results of an analytical modelling of upward negative lightning initiation criteria from Paper IV. For the first time in the literature, we theoretically explain how nearby lightning events can trigger upward positive leaders from tall structures. In Paper V, we further use the developed model to estimate the incidence of upward negative lightning to structures of arbitrary height as a function of the lightning flash density in the area.

4.1 Analytical Modeling of Upward Negative Lightning Initiation Criteria (Paper IV)

4.1.1 Methodology

The aim of this paper is to estimate the salient parameters (such as peak value and risetime) of the electric field waveforms associated with the different nearby lightning triggering scenarios observed in [33] shown in Figure 4.1. Furthermore, we investigate to which extent the estimated electric fields can initiate a sustained upward leader. The analysis is performed for an upward negative lightning and a positive corona discharge. Within the framework of an electrostatic analysis, simplified closed-form formulas for the electric field at ground level as a function of time are derived that are applicable both, to the case of a horizontal and of a vertical leader. The ground is assumed to be a perfect electric conductor. These solutions can be used to obtain the electric field at any position on the ground for any of the scenarios shown in Figure 4.1. To evaluate the criterion for the upward leader initiation, the electric field at ground level is then used as an input to the simplified, analytical corona discharge model for tall structures that was proposed by Aleksandrov et al. in [55].

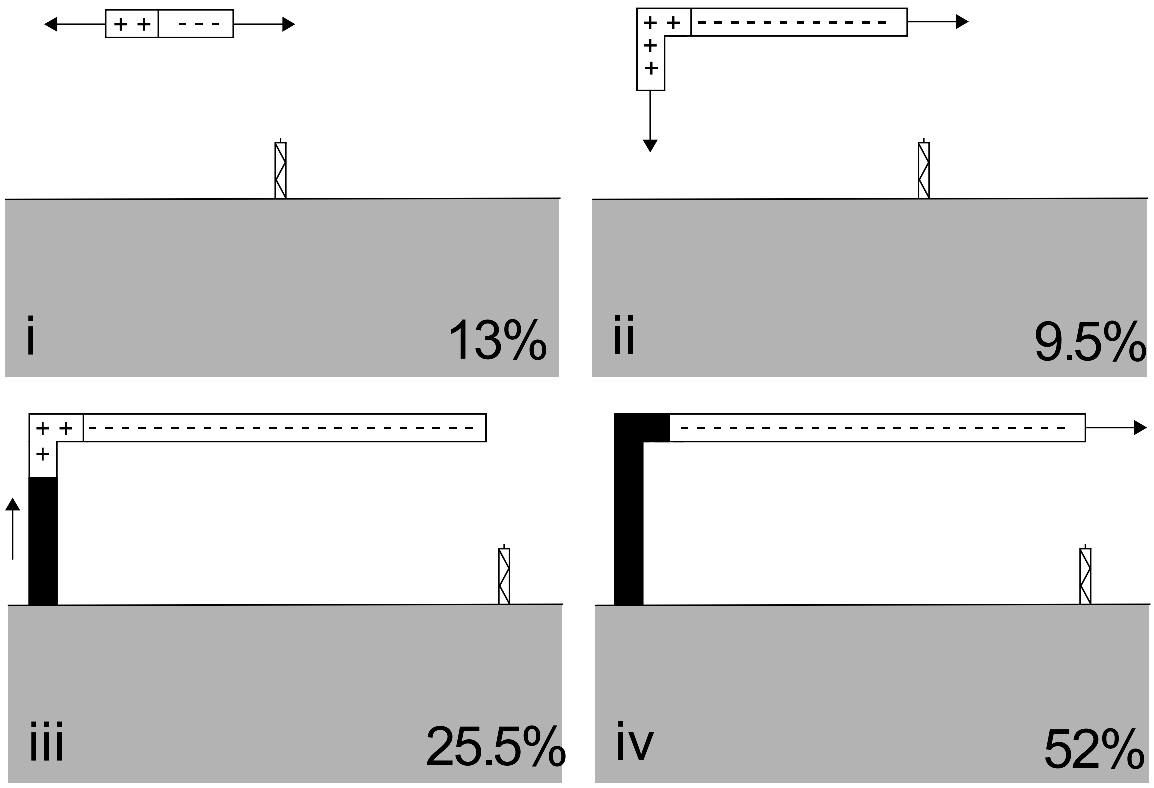

Figure 4.1 Typical scenarios leading to the triggering of a negative upward flash from a tower. (i) In-cloud leader above the tower, (ii) in-cloud leader prior to a positive RS, (iii) positive RS, (iv) Continuing Current (CC) extending the negative leader above the tower. Not to scale. The percentage of occurrence of these scenarios as observed in [33] is given in each panel. (Figure obtained from Paper IV)

4.1.2 Results

We estimated risetimes and peak electric field values for the classes of events observed in the literature to be potentially triggering upward negative flashes. Using the criteria from [55] for the initiation of a sustained leader and making certain assumptions on the waveform of the electric field (see Paper IV for more details), we can estimate whether a certain event will trigger or not an upward negative lightning. Two typical classes of events are observed as preceding events: leader processes and faster return stroke processes. Figure 4.2 presents critical values of electric field and risetime necessary for the upward lightning initiation for these two classes of events for three different object heights. We provided an open-source code and graphical user interface (https://itoni93.github.io/other_triggered_lightning_analytical/) with which users can simulate the triggering of upward negative flashes by nearby lightning events for arbitrary input parameters.

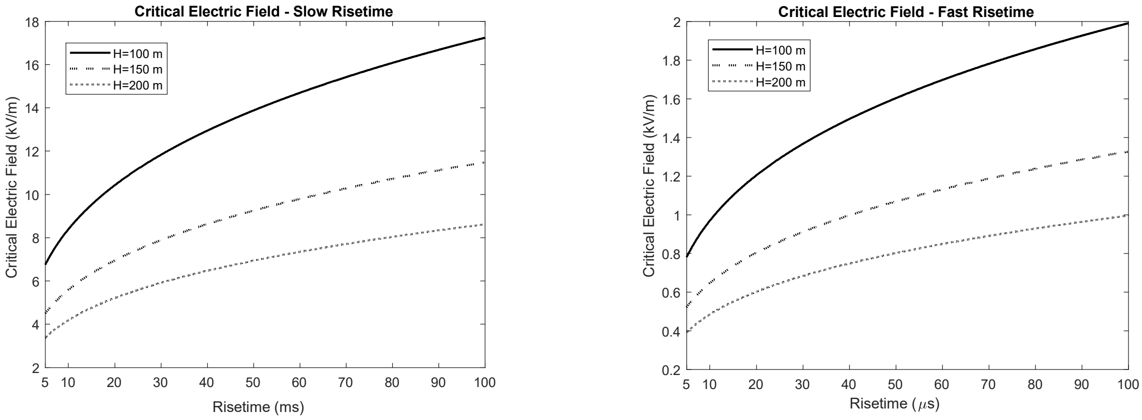

(a) (b)

Figure 4.2 Critical electric field change for the development of a sustained leader as a function of the risetime for different tall structure heights. (a) As a function of risetimes characteristic of leader processes. (b) As a function of risetimes characteristic of return stroke processes.

The obtained results suggest that the mechanism of triggering of an upward lightning from a tall structure by a preceding nearby lightning is plausible. Our analysis shows that it is possible for an upward negative lightning to be triggered by nearby lightning activity, either during the relatively slow leader propagation phase, or after the faster return stroke phase. In most of the analyzed cases, the field change due to nearby lightning activity was high enough to trigger an upward flash from a structure of moderate height, even without the background electric field. Nearby return strokes with relatively fast risetimes (some tens of microseconds) can trigger upward negative flashes even for field values about ten times lower than in the case of slower leader propagation processes (risetime of some tens of milliseconds).

We also provided an open-source code with a graphical interface as supplementary material [56] that Interested readers can use to run any specific case. Since the method is fully analytical, it can obtain the 2D distribution of the electric field for an arbitrary case, essentially instantaneously in terms of computational time.

4.2 Incidence of Upward Lightning Triggered by Nearby Lightning – Monte Carlo Approach (Paper V)

4.2.1 Methodology

In this paper, we present a method to estimate the number of upward flashes from a tower triggered by nearby lightning. Based on the analytical model presented in Paper IV, we employ Monte Carlo simulations considering a possible range of values for the electrical and geometrical parameters of positive cloud-to-ground (CG) lightning. We take into account both, the relatively slow processes due to the leader propagation and the faster return stroke processes. The adopted geometrical parameters are based on the scenarios observed in [33]. Similar to [57], one of the scenarios in which cloud discharges are the triggering mechanism was not considered because of the low efficiency of lightning location systems to detect these events and the lack of available statistical data. This omission would, however, not significantly impact the overall prediction since this scenario represents only 13% of the observed cases ([32] and [33]).

Table 4.1 Input parameters and considered ranges of variation.
(Table is obtained from Paper V)

	MIN	MAX
Φ [°]	0	360
altitude [km]	1.5	5
$v_{Positive}$ [10^4 m/s]	1	4
$v_{Negative}$ [10^5 m/s]	0.5	2
$v_{return\ stroke}$ [10^8 m/s]	0.7	1.2
Horizontal duration [ms]	30	200
CC duration [ms]	200	700
$\lambda_{negative}$ [C/km]	0.5	2

The input parameters of our model are the leader angle, the initiation altitude above the ground, the speed of the positive leader end, the speed of the negative leader end, the return stroke velocity, the duration of the horizontal propagation before the leader veers down to ground, the duration of the continuing current phase, and the line charge density of the negative leader end. Note that the line charge density of the positive end is obtained by assuming a zero-net charge along the leader (see Paper IV for more details). For the sake of simplicity and due to lack of experimental data, we use a uniform distribution for each random experiment. More advanced models can be built by using more representative distributions for each parameter. The exact values are chosen based on some typical values observed experimentally (see Paper V for more details) and they are shown in Table 4.1. The aim of each random experiment is to evaluate the upward leader criterion defined in Paper IV for each successive scenario related to the process of a positive lightning flash, as shown in Figure 4.3.

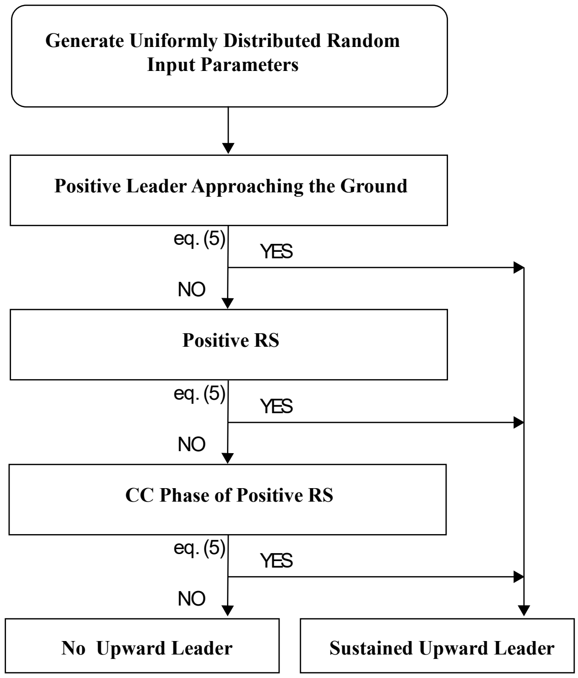

Figure 4.3 Flowchart for each random experiment. (Figure obtained from Paper V)

4.2.2 Results

Table 4.2 presents in the first row the total number of expected flashes to structures of different heights using Eriksson's empirical formula [58]. Furthermore, the percentage of expected upward flashes is shown in the second row based on the equation derived in [59]. The total estimated number of other-triggered (OT) flashes obtained by using the Monte Carlo model averaged over a period of one year is shown in the last row of the table. The percentage of the total estimated number of OT flashes for each scenario is shown in the three rows above the last one. We can observe that the number of estimated OT flashes is 3 to 10 times (depending on the structure height) higher than the total number of flashes predicted by Eriksson's formula. The observed number of upward flashes is about 4 to 80 times higher than the one predicted by Eriksson's empirical formula. In line with [57], we observe a significant underestimation of Eriksson's empirical formulas, just by considering upward flashes caused by nearby lightning without the contribution of downward lightning and self-initiated upward lightning.

Table 4.2 Statistics for a 60 x 60 km2 observation area, and comparison with equations (8) and (9) from Paper V. Ng= 2 flashes/km^2 per year. (Table obtained from Paper V)

Height of structure [m]	100	125	150	175	200	250
N_T	0.6	0.95	1.39	1.9	2.5	3.95
P_U [%]	13.2	25	34.6	42.7	49.8	61.5
Positive leader approaching the ground [%]	33	33	33	34	34	35
Positive RS [%]	43	42	40	39	36	35
CC phase of positive RS [%]	24	25	27	27	30	30
Total number OT flashes per year	6.2	6.66	7.75	8.33	9.46	11.42

Chapter 5 Grounding Systems of Tall Structures

In this chapter, we present an analysis of the grounding systems of tall structures subjected to lightning strikes. First, in Paper VI, by means of full-wave numerical simulations, we analyze a typical wind turbine grounding system and obtain both frequency-domain and time-domain responses to typical lightning excitations. We analyze the influence of interconnecting grounding systems of wind turbines in a wind turbine park. In Paper VII and Paper VIII, we estimate the influence of non-flat ground on the resistance of grounding systems based on an analytical approximation derived in our work.

5.1 Wind Turbines Grounding Systems (Paper VI)

5.1.1 Methodology

Typical grounding systems (see [60], [61] and [62]) consist of several rings connected with horizontal and vertical rods. The depth of the rings is usually a few meters and they are located within a foundation made of concrete [60]. Vertical or horizontal rods are often added to reduce the overall impedance. In this paper, we have used the geometry shown in Figure 5.1 with maximum depth of 3 m and a maximum radius of 9 m. We will consider the interconnection of two wind turbine grounding systems separated by 100 m (center to center) and connected with a 100-m long bare cable buried at a 1-m depth. Further, we consider different conductivities of soil taking into account the frequency dependence of the soil conductivity and permittivity. More details about the geometrical and soil properties can be found in Paper VI.

Full-wave calculations in the frequency domain (FD) are carried out using the NEC-4 code, which is based on the numerical solution of the Pocklington integro-differential equation (for the case of wire structures) by means of the Method of Moments (MoM) [63]. Based on the typical lightning excitation, we obtain the response in FD and by use of the inverse fast Fourier transform (IFFT), we obtain the time domain response.

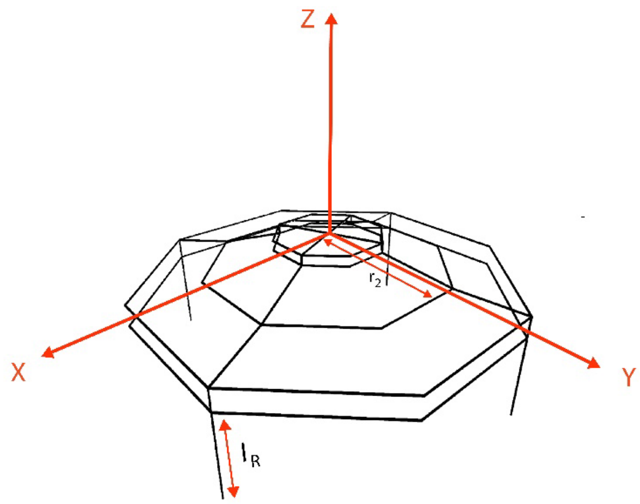

Figure 5.1 Geometry of the grounding system configuration used in the study. (Figure obtained from Paper VI)

5.1.2 Results

In Figure 5.2, we present the ground potential rise (GPR) and step voltage for one of the analyzed cases. The strongest voltage peak can be observed at the origin of the grounding system both in the case of the GPR and of the step voltage. The intensification of the GPR and step voltages can also be observed along the interconnecting cable. An animation of the GPR and step voltages as a function of time for each analyzed scenario in Paper VI can be found in the online version of the paper (Appendix A. Supplementary data of Paper VI, click DOI[1] for more).

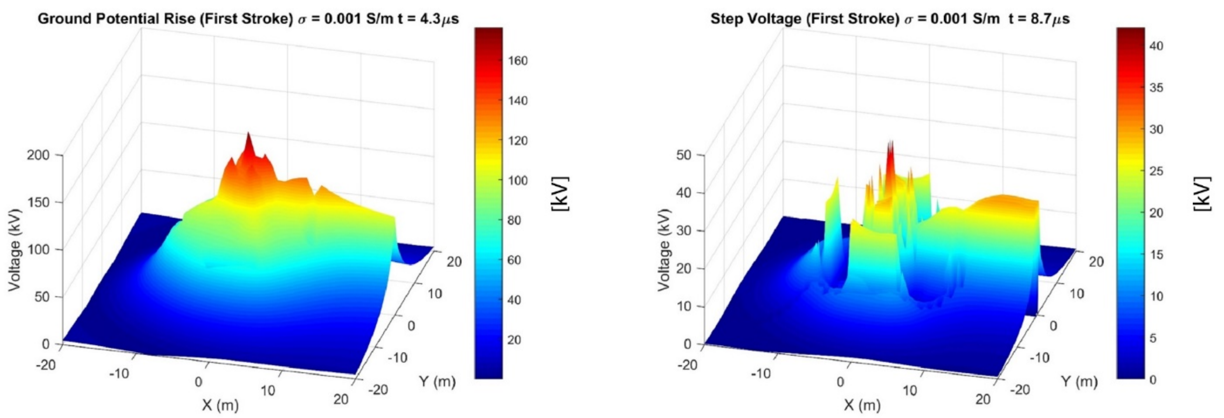

Figure 5.2 Ground potential rise and step voltage for the case of a lightning current typical of a first return stroke flowing into the wind turbine connected to an adjacent wind turbine 100 m away. The interconnecting bare cable is along the x axis. The conductivity of the soil is σ=0.001 S/m. (Figure obtained from Paper VI)

[1] https://doi.org/10.1016/j.epsr.2019.04.010

We analyzed the spatial distribution of the ground potential rise and the step voltage in response to typical first and subsequent lightning return stroke current waveforms. We showed that both, the ground potential rise and the step voltage could be significant along the wire, in particular for a low-conductivity soil. Furthermore, placing sensitive equipment near the interconnecting wire should be either avoided, or insulated wires should be used for the interconnection of the grounding systems.

It was shown that the low frequency grounding impedance could be reduced by a factor of two or more by interconnecting two grounding systems separated by a 100-m distance. However, the reduction is significantly lower at higher frequencies due to the influence of the interconnection wire's inductance.

5.2 Influence of Elevated Terrain on the Grounding Resistance – Analytical Model (Paper VII and Paper VIII)

5.2.1 Methodology

In this chapter we evaluate the influence of elevated terrain on the grounding resistance of structures. Tall structures such as telecommunication towers and wind turbines are often placed on top of hills in order to obtain better signal coverage for the case of telecommunication towers and better exposure to wind for the case of wind turbines. To our knowledge, no other study had considered the influence of non-flat terrain on the structure's grounding resistance.

We consider a simple geometry of a hemispheric grounding electrode. Note that even though this geometry is simple, it can represent a first approximation of a complex grounding system such as those of wind turbines. The geometry of the problem is shown in Figure 5.3. The solution for the grounding resistance of the structure shown in Figure 5.3-a is obtained in Paper VII. The solution was later extended in [64] for Figure 5.3-b and finally the analytical solution for a more general case shown in Figure 5.3-c with a finite height of the cone is derived in Paper VII. The validity of the derived analytical equations is tested by comparing their results with numerical solutions obtained via the commercial software COMSOL [65]. More details can be found in Paper VII, [64] and Paper VIII.

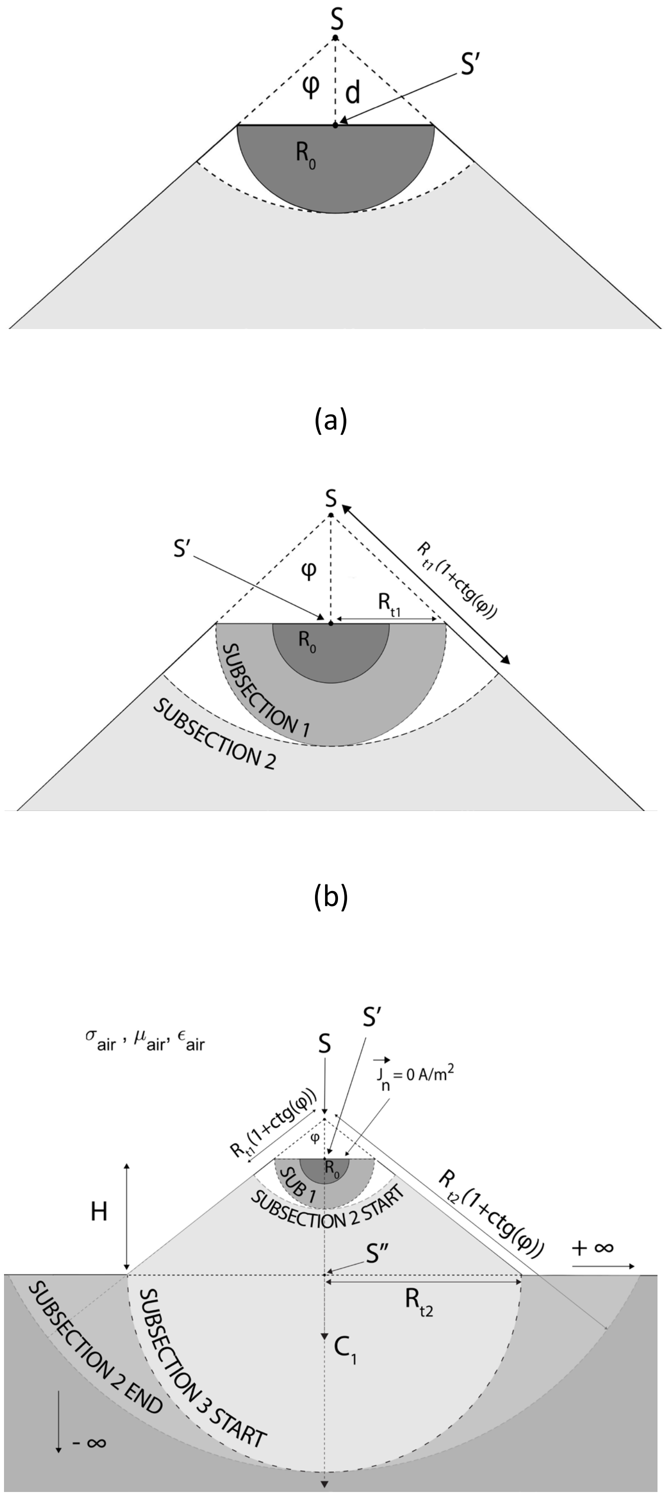

(c)

Figure 5.3 Hemispheric grounding electrode for three different geometries of the soil. (a) Electrode buried on the top of a truncated cone-shaped ground. The top radius of the cone is assumed to be equal to the radius of the electrode. (b) Same as in (a) but the top radius of the cone is bigger than the radius of the hemispheric electrode. (c) Same as in (b) but considering a cone-shaped mountain with a finite height. (Figure obtained from Paper VIII)

5.2.2 Results

The derived solution for the most general geometry shown in Figure 5.3-c is:

$$R_c = \left(\frac{1}{R_0} - \frac{1}{R_{t1}} + \frac{1}{R_{t1}(1-\cos(\varphi))\big(1+ctg(\varphi)\big)} - \frac{1}{R_{t2}(1-\cos(\varphi))\big(1+ctg(\varphi)\big)} + \frac{1}{R_{t2}}\right)\frac{1}{2\pi\sigma}$$

Equation 5.1 Resistance of hemispheric grounding system shown in Figure 5.3-c.

where σ is the ground conductivity, R_0 is the radius of the hemispheric grounding, φ is the apex angle, and the geometrical parameters R_{t1} and R_{t2} are shown in Figure 5.3-b and Figure 5.3-c. The analytical equation was checked for different scenarios against numerical simulations and it was found that in most of the cases, the difference is less than 10%.

Figure 5.4 presents the resulting plot from the analytical solution in Equation 5.1 of the increase of the grounding resistance as a function of the cone height and apex angle compared to the case of a flat ground. As the value of the apex angle increases, the results converge to those corresponding to the case of a flat ground. In a similar way, decreasing the height, the results converge to those of a flat ground or increasing it to infinity it converges to the solution for Figure 5.3-b. For example, for the case of an apex angle of 30° and a height of about 100 m, the increase of the grounding resistance is almost a factor of two.

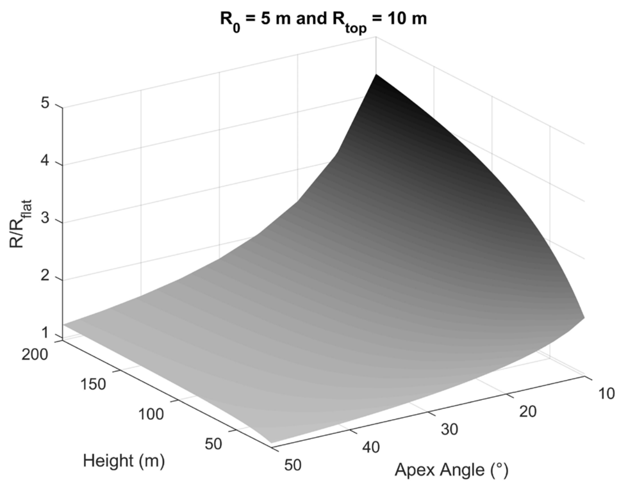

Figure 5.4 Increase of the grounding resistance predicted by the derived analytical formula as a function of the height of the truncated cone and its apex angle, for a 5-m radius hemispheric electrode. The top radius of the truncated cone is 10 m. (Figure obtained from Paper VIII)

Chapter 6 Conclusion

Paper I: We have upgraded the lightning observation site at the Säntis Tower with multiple sensors including electric field sensors at different locations, a high-speed camera, x-ray sensors, and high-resolution cameras. All the stations are GPS-time synchronized and triggered by the lightning current signal measured at the Säntis tower. Newly installed sensors during this thesis together with existing sensors and other meteorological sensors in the area covering the tower have helped and will continue to help in the future to better understand the processes involved in upward lightning.

Paper II: Based on the simultaneous measurements using different sensors, including lightning mapping array observations, we were able to infer the charge structure in the clouds as well as the polarity of leaders. In all the analyzed events, it was found that the leader channel approaching the tower triggered an upward leader of opposite polarity from the tower tip.

Paper III: Based on high-speed camera observations, the different fast processes occurring in upward negative lightning were found to originate from recoil leaders. Bidirectional propagation was observed in three recoil leaders leading to an attempted leader, and to two return strokes. It is possible that all recoil leaders were bidirectional, but this was not seen due to the frame rate limitation of the high-speed camera.

Paper IV: For the first time in the literature, we showed theoretically how both, relatively slow leader processes and faster return stroke nearby processes can trigger an upward lightning flash from the tip of a tall structure. The obtained results suggest that electric fields in the order of only 1 kV/m from nearby positive return strokes can potentially initiate an upward flash from a 100-m tall structure. Such field intensities are typical of return strokes at distances as large as a few kilometers.

Paper V: The number of upward flashes triggered by nearby lightning could be, depending on the height of the structure, as much as three to ten times as high as the total number of both upward and downward lightning flashes estimated using conventional empirical formulas.

Paper VI: For wind turbines, we obtained the transfer function of the grounding system and the time-domain response of the ground potential rise and step voltage as a function of a typical lightning excitation. It was shown that the low frequency grounding impedance could be reduced by a factor of two or more by interconnecting two individual wind turbine grounding systems separated by a 100-m distance. However, the reduction is significantly lower at higher frequencies due to the influence of the interconnection wire's inductance.

Paper VII and Paper VIII: The resistance of the grounding system of a structure located on a hilly terrain can be significantly increased with respect to the same structure located on flat ground. Analytical solutions for hemispherical grounding electrodes on the top of a conical hill were derived that can be used as a first approximation to estimate the influence of non-flat terrain.

Future development

Lightning observations at the Säntis Tower started in 2010. Some of the data in this thesis were obtained even before the start of the thesis itself (e.g., LMA data). Similarly, there is a large quantity of data collected with the upgraded system that need to be studied in the future. This mainly relates to two summer seasons during which simultaneous data of the interferometric system, new high-speed camera records and x-rays detections associated both with positive and negative flashes were obtained. Further upgrade of the system is possible, both increasing the reliability of the system and adding new sensors at different locations and at different frequencies.

Modeling of upward lightning still remains an interesting and open topic. The developed analytical model can be further enhanced and used to provide real-time (less than a millisecond) predictions that can be used in special applications to predict upward flashes from tall structures just before they occur. More advanced numerical models could be employed in order to relax some of the approximations adopted in the analytical model. Similar models could be developed for the case of upward positive lightning triggered by nearby events.

The design and analysis of the grounding system of tall structures is an important topic for industrial applications. Typical full-wave simulations are complex and time consuming. Simple approximations of wind turbine grounding systems with hemispherical grounding electrodes can be useful, bearing in mind the order of uncertainty imposed by the water content in the soil. For this reason, developing adequate high frequency models for hemispherical grounding systems is of high interest.

References

[1] L. H. W. B. Harland, «Fossil lightning strikes 250 million years ago,» *Adv. Sci., 1966. .*

[2] S. L. Miller, «Production of Amino Acids Under Possible Primitive Earth Conditions,» *Science 117, 1953..*

[3] D. R. Poelman, «On the Science of Lightning,» *Institut Royal Météorologique de Belgique,* vol. 564, 2010.

[4] J. R. D. a. M. A. Uman, «The physics of lightning,» *Physics Reports, vol. 534, no. 4, pp. 147–241, Jan. 2014..*

[5] G. J. Byrne, J. R. Benbrook, and E. A. Bering, «Balloon observations of stratospheric electricity above the South Pole: vertical electric field, conductivity, and conduction current.,» *Journal of Atmospheric and Terrestrial Physics, 53(9), 859–868 DOI: 10.1016/0021-9169(91)90099-s.*

[6] G. C. Reid, «Electrical structure of the middle atmosphere,» *In The Earth's Electrical Environment, DC: National Academy Press, 1986. .*

[7] C. T. R. Wilson, «Investigations on lightning discharges and on the electric field of thunderstorms,» *Phil. Trans. Roy. Soc. Lond. A 221, 73–115, 1920..*

[8] V. A. Rakov, Fundementals of Lightning, Cambridge University Press, 2016.

[9] C. T. R. Wilson, «Some thundercloud problems,» *J. Franklin Inst. 208, 1–12, 1929. .*

[10] D. R. MacGorman, The Electrical Nature of Storms, Oxford University Press , 1990.

[11] M. B. Baker and J. G. Dash, «Mechanism of charge transfer between colliding ice particles,» *JOURNAL OF GEOPHYSICAL RESEARCH, VOL. 99, 1994. .*

[12] J. Meek, «A Theory of Spark Discharge,» *Phys. Rev., 1940 DOI: 10.1103/PhysRev.57.722 .*

[13] D. Faircloth, «Technological Aspects: High Voltage,» *CERN Yellow Report CERN-2013-007, pp.381-419 DOI: 10.5170/CERN-2013-007.381.*

[14] V. A. Rakov and M.A. Uman , «Lightning: Physics and Effects,» *Cambridge University Pres, 2007..*

[15] M. A. Uman, The lightning discharge, Academic Press, 1987.

[16] J. D. Hill, M. A. Uman, and D. M. Jordan, «High-speed video observations of a lightning stepped leader,» *Journal of Geophysical Research, vol. 116, no. D16, Aug. 2011..*

[17] A. Smorgonskiy, F. Rachidi, M. Rubinstein, G. Diendorfer, and W. Schulz, «On the proportion of upward flashes to lightning research towers,» *Atmospheric Research, vol. 129–130, pp. 110–116, Jul. 2013. DOI: 10.1109/APL.2011.6110248.*

[18] D. I. B. Djalel, M. Mourad, and S. Ghoudelbourk, «Protection of wind turbine against the lightning damage,» *IREC2015 The Sixth International Renewable Energy Congress, 2015. DOI: 10.1109/IREC.2015.7110900.*

[19] D. Čavka and D. Poljak,, Properties and Characterization of Modern Materials, Chapter Electromagnetic Compatibility Aspects of Wind Turbine Analysis and Design, 2016.

[20] F. Rachidi et al.,, «A Review of Current Issues in Lightning Protection of New-Generation Wind-Turbine Blades,» *IEEE Trans. Ind. Electron., vol. 55, no. 6, pp. 2489–2496, Jun. 2008, DOI: 10.1109/TIE.2007.896443.*

[21] «Turbines shoot upside-down lightning,,» *Nature, vol. 506, no. 7488, pp. 268–268, Feb. 2014, DOI: 10.1038/506268a..*

[22] A. M. Hussein et al., «Simultaneous measurement of lightning parameters for strokes to the Toronto Canadian National Tower,» *J. Geophys. Res., vol. 100, no. D5, p. 8853, 1995, doi: 10.1029/95jd00543.*

[23] Diendorfer, G., H. Pichler, and M. Mair , «G. Diendorfer, H. Pichler, and M. Mair, "Some Parameters of Negative Upward-Initiated Lightning to the Gaisberg Tower (2000–2007),» *IEEE Trans. Electromagn. Compat., vol. 51, no. 3, pp. 443–452, Aug. 2009, DOI: 10.1109/temc.2009.2021616..*

[24] F. H. Heidler, M. Manhardt, and K. Stimper, «The Slow-Varying Electric Field of Negative Upward Lightning Initiated by the Peissenberg Tower, Germany,» *IEEE Trans. Electromagn. Compat., vol. 55, no. 2, pp. 353–361, Apr. 2013, DOI: 10.1109/temc.2012.2209121..*

[25] C. Romero, F. Rachidi, M. Paolone, and M. Rubinstein, «Statistical Distributions of Lightning Currents Associated With Upward Negative Flashes Based on the Data Collected at the Säntis (EMC) Tower in 2010 and 2011,» *IEEE Trans. Power Delivery, vol. 28, no. 3, pp. 1804–1812, Jul. 2013, DOI: 10.1109/tpwrd.2013.2254727..*

[26] T. Shindo et al., «Lightning observations at Tokyo Skytree,» *presented at the 2014 International Symposium on Electromagnetic Compatibility - EMC EUROPE, Sep. 2014. DOI: 10.1109/emceurope.2014.6930973..*

[27] H. Zhou, V. A. Rakov, G. Diendorfer, R. Thottappillil, H. Pichler, and M. Mair, «A study of different modes of charge transfer to ground in upward lightning,» *Journal of Atmospheric and Solar-Terrestrial Physics, vol. 125–126, pp. 38–49, Apr. 2015, DOI: 10.1016/j.jastp.2015.02.008..*

[28] M. Azadifar et al., «Fast initial continuous current pulses versus return stroke pulses in tower-initiated lightning,» *J. Geophys. Res. Atmos., vol. 121, no. 11, pp. 6425–6434, Jun. 2016, DOI: 10.1002/2016jd024900..*

[29] V. Mazur, L. H. Ruhnke, Tom. A. Warner, and R. E. Orville, «Recoil leader formation and development,» *Journal of Electrostatics, vol. 71, no. 4, pp. 763–768, Aug. 2013, DOI: 10.1016/j.elstat.2013.05.001..*

[30] X. Qie et al., «Bidirectional leader development in a preexisting channel as observed in rocket-triggered lightning flashes,» *J. Geophys. Res. Atmos., vol. 122, no. 2, pp. 586–599, Jan. 2017, DOI: 10.1002/2016jd025224..*

[31] D. Wang, N. Takagi, T. Watanabe, H. Sakurano, and M. Hashimoto, «Observed characteristics of upward leaders that are initiated from a windmill and its lightning protection tower,» *Geophys. Res. Lett., vol. 35, no. 2, Jan. 2008, DOI: 10.1029/2007gl032136..*

[32] M. M. F. Saba et al., «Upward lightning flashes characteristics from high-speed videos,» *J. Geophys. Res. Atmos., vol. 121, no. 14, pp. 8493–8505, Jul. 2016, DOI: 10.1002/2016jd025137..*

[33] C. Schumann et al., «On the Triggering Mechanisms of Upward Lightning,» *Sci Rep, vol. 9, no. 1, Jul. 2019, DOI: 10.1038/s41598-019-46122-x.*

[34] A. Smorgonskiy, F. Rachidi, M. Rubinstein, G. Diendorfer, and W. Schulz, «On the proportion of upward flashes to lightning research towers,» *presented at the 2011 7th Asia-Pacific International Conference on Lightning (APL), Nov. 2011. DOI: 10.1109/apl.20.*

[35] V. Mazur, «Physical processes during development of lightning flashes,» *Comptes Rendus Physique, vol. 3, no. 10, pp. 1393–1409, Dec. 2002, DOI: 10.1016/s1631-0705(02)01412-3..*

[36] V. Mazur and L. H. Ruhnke, «Physical processes during development of upward leaders from tall structures,» *Journal of Electrostatics, vol. 69, no. 2, pp. 97–110, Apr. 2011, DOI: 10.1016/j.elstat.2011.01.003..*

[37] H. W. Kasemir, «A contribution to the electrostatic theory of a lightning discharge,» *J. Geophys. Res., vol. 65, no. 7, pp. 1873–1878, Jul. 1960, DOI: 10.1029/jz065i007p01873..*

[38] R. M. Reap, «Evaluation of Cloud-to-Ground Lightning Data from the Western United States for the 1983–84 Summer Seasons,» *J. Climate Appl. Meteor., vol. 25, no. 6, pp. 785–799, Jun. 1986, doi: 10.1175/1520-0450(1986)025<0785:eoctgl>2.0.co;2..*

[39] A. Smorgonskiy, F. Rachidi, M. Rubinstein, and G. Diendorfer, «,On the relation between lightning flash density and terrain elevation,» *presented at the 2013 International Symposium on Lightning Protection (XII SIPDA), Oct. 2013. DOI: 10.1109/sipda.2013.67.*

[40] F. Rachidi, M. Rubinstein and A. Smorgonskiy, «Lightning Protection of Large Wind-Turbine Blades, in Wind Energy Conversion Systems,» *Springer, p. 227-242, 2012..*

[41] J. Montanyà, O. van der Velde, and E. R. Williams, «Lightning discharges produced by wind turbines,» *J. Geophys. Res. Atmos., vol. 119, no. 3, pp. 1455–1462, Feb. 2014, DOI: 10.1002/2013jd020225..*

[42] C. Romero et al., «Measurement of lightning currents using a combination of Rogowski coils and B-dot sensors,» *presented at the 2010 30th International Conference on Lightning Protection (ICLP), Sep. 2010. DOI: 10.1109/iclp.2010.7845959..*

[43] C. Romero et al., «A system for the measurements of lightning currents at the Säntis Tower,» *Electric Power Systems Research, vol. 82, no. 1, pp. 34–43, Jan. 2012, DOI: 10.1016/j.epsr.2011.08.011..*

[44] Azadifar .M, M. Paolone, D. Pavanello, F. Rachidi, C. Romero, and M. Rubinstein , «An Update on the Instrumentation of the Säntis Tower in Switzerland for Lightning Current Measurements and Obtained Results,» *in CIGRE 2014.*

[45] N. Pineda et al., «Meteorological Aspects of Self-Initiated Upward Lightning at the Säntis Tower (Switzerland),» *J. Geophys. Res. Atmos., vol. 124, no. 24, pp. 14162–14183, Dec. 2019, DOI: 10.1029/2019jd030834..*

[46] J. Figueras i Ventura et al., «Analysis of the lightning production of convective cells,» *Atmos. Meas. Tech., vol. 12, no. 10, pp. 5573–5591, Oct. 2019, DOI: 10.5194/amt-12-5573-2019..*

[47] M. G. Stock et al., «Continuous broadband digital interferometry of lightning using a generalized cross-correlation algorithm,» *J. Geophys. Res. Atmos., vol. 119, no. 6, pp. 3134–3165, Mar. 2014, DOI: 10.1002/2013jd020217..*

[48] J. Figueras i Ventura et al., «Polarimetric radar characteristics of lightning initiation and propagating channels,» *Atmos. Meas. Tech., vol. 12, no. 5, pp. 2881–2911, May 2019, DOI: 10.5194/amt-12-2881-2019..*

[49] al., J. T. Pilkey et, «,Rocket-triggered lightning propagation paths relative to preceding natural lightning activity and inferred cloud charge,» *J. Geophys. Res. Atmos., vol. 119, no. 23, p. 13,427-13,456, Dec. 2014, DOI: 10.1002/2014jd022139..*

[50] O. A. van der Velde and J. Montanyà, «Asymmetries in bidirectional leader development of lightning flashes,» *J. Geophys. Res. Atmos., vol. 118, no. 24, p. 13,504-13,519, Dec. 2013, DOI: 10.1002/2013jd020257..*

[51] N. Kitagawa and M. Brook, «A comparison of intracloud and cloud-to-ground lightning discharges,» *J. Geophys. Res., vol. 65, no. 4, pp. 1189–1201, Apr. 1960, DOI: 10.1029/jz065i004p01189..*

[52] L. He et al., «An Analysis of Current and Electric Field Pulses Associated With Upward Negative Lightning Flashes Initiated from the Säntis Tower,» *J. Geophys. Res. Atmos., vol. 123, no. 8, pp. 4045–4059, Apr. 2018, DOI: 10.1029/2018jd028295..*

[53] X. M. Shao, P. R. Krehbiel, R. J. Thomas, and W. Rison, «Radio interferometric observations of cloud-to-ground lightning phenomena in Florida,» *J. Geophys. Res., vol. 100, no. D2, p. 2749, 1995, DOI: 10.1029/94jd01943..*

[54] X. Qie et al., « Propagation of positive, negative, and recoil leaders in upward lightning flashes,» *Earth and Planetary Physics, vol. 3, no. 2, pp. 102–110, 2019, DOI: 10.26464/epp2019014..*

[55] N. L. Aleksandrov, E. M. Bazelyan, R. B. Carpenter Jr, M. M. Drabkin, and Y. P. Raizer, «The effect of coronae on leader initiation and development under thunderstorm conditions and in long air gaps,» *J. Phys. D: Appl. Phys., vol. 34, no. 22, pp. 3256–326.*

[56] A. Sunjerga, M. Rubinstein, F. Rachidi, and V. Cooray, «On the Initiation of Upward Negative Lightning by Nearby Lightning Activity: An Analytical Approach - Source Code.,» *Zenodo, 2020. doi: 10.5281/ZENODO.4321780,* n° %1https://github.com/IToni93/other_triggered_lightning_analytical.git.

[57] M. Becerra, M. Long, W. Schulz, and R. Thottappillil, «On the estimation of the lightning incidence to offshore wind farms,» *Electric Power Systems Research, vol. 157, pp. 211–226, Apr. 2018, DOI: 10.1016/j.epsr.2017.12.008.*

[58] A. J. Eriksson, «The Incidence of Lightning Strikes to Power Lines,» *IEEE Trans. Power Delivery, vol. 2, no. 3, pp. 859–870, 1987, DOI: 10.1109/tpwrd.1987.4308191.*

[59] Eriksson, A., and D. Meal , «The incidence of direct lightning strikes to structures and overhead lines,» *IEE-Conference on Lightning and Power Systems. IEE-Conference Publications, Vol. 236, pp. 67–71 1984.*

[60] K. Yamamoto, S. Yanagawa, K. Yamabuki, S. Sekioka, and S. Yokoyama, «Analytical Surveys of Transient and Frequency-Dependent Grounding Characteristics of a Wind Turbine Generator System on the Basis of Field Tests,» *IEEE Trans. Power Delivery, vol. 25, no. 4, pp. 3035–3043, Oct. 2010, DOI: 10.1109/tpwrd.2010.2043748..*

[61] A. Sunjerga, Q. Li, D. Poljak, M. Rubinstein, and F. Rachidi, «Transient Impedance of Interconnected Wind Turbine Grounding Systems,» *presented at the 2018 26th International Conference on Software, Telecommunications and Computer Networks (SoftCOM), Sep. 2018. DOI: 10.23919/softcom.2018.8555790.*

[62] R. Alipio and S. Visacro, «Frequency Dependence of Soil Parameters: Effect on the Lightning Response of Grounding Electrodes,» *IEEE Trans. Electromagn. Compat., vol. 55, no. 1, pp. 132–139, Feb. 2013, DOI: 10.1109/temc.2012.2210227..*

[63] G. Burke, « Numerical Electromagnetics Code (NEC-4) – Method of Moments, Part II,» *Program Description – Theory, Lawrence Livermore National Laboratory, YCRLMA- 109338 PT. II. 1992..*

[64] H. M. L. Y. Z. a. W. C. Z. K. B. Tan, «Analysis of the Grounding Resistance of a Hemispheric Electrode Located on a Truncated Cone,» *IEEE Trans. Electromagn. Compat., vol. 62, no. 4, pp. 1361–1363, Aug. 2020, DOI: 10.1109/temc.2019.2940902..*

[65] «COMSOL Multiphysics,» *v.5.3, COMSOL AB, Stockholm, Sweden..*

ANTONIO SUNJERGA (1993)

Electrical Engineer, Physics

CONTACT

Address

Chemin des Triaudes 4 C221
1024 Ecublens, Switzerland

Phone

+385 92 186 9981

Web

sunjerga@yahoo.com

SKILLS

ELECTRICAL ENGINEERING

MATLAB

PYTHON, C++,C

COMSOL

- GIT
- AWS
- OFFICE PACKAGE
- WASM
- RUST
- LABVIEW, NODE-RED
- DATA ACQUISITION
- WINDOWS, LINUX
- RF HARDWARE
- RASPBERRY PI, ARDUINO
- ADOBE ILLUSTRATOR
- ADOBE PHOTOSHOP

PROJECTS

- PHYSICS OF LIGHTNING DISCHARGE
- UPWARD LIGHTNING STUDIES
- WIND TURBINE LIGHTNING PROTECTION
- LASER LIGHTNING ROD

ABOUT ME

Hello! My name is Antonio. I received my Electrical engineer master's degree in field of Wireless Communication in 2017. During the second year of five-year Electrical engineer study I started to study physics in parallel and successfully received Bachelor degree in Physics also last year. Currently I'm working as PhD student in field of electromagnetic compatibility at EPFL, EMC Lab.

EDUCATION

Wireless Communication / 2015 - 2017

MASTER OF SCIENCE

University of Split

The aim of this program is to acquire basic theoretical knowledge and practical skills and to train them for permanent adoption of new knowledge and technologies. In addition, the ability of developing creative thinking, independent and team work skills and decision-making at all levels is achieved. I finished my master thesis project as exchange student at EPFL, Switzerland.

Physics / 2014 - 2017

BACHELOR'S DEGREE

University of Split

The aim of this program is to develop strong logic in solving complex physical problems. Student will gain fundamental knowledge in all branches of physics such as classical mechanics, electrodynamics, thermodynamics optics, modern physics and quantum physics.

Electrical Engineering and Information Technology / 2012 - 2015

BACHELOR'S DEGREE

Bachelor of Science in Electrical Engineering and Information Technology

During first two years' students gain fundamental knowledge in mathematics, physics, electrical engineering, computing and efficient communication. Third year program is more focused on particular chosen branches from field of Information Technology.

EXPERIENCES

EPFL / 2018 to Present

PHD STUDENT

I have been working at this position since the start of 2018. My research topic is related to investigation of physics of lightning discharge process and lightning protection. This consist of monitoring and upgrade of state of the art lightning observation site Säntis Tower, analysis of observed data and development of new theoretical and numerical models.

CERN / 2017

SUMMER STUDENT

I was working with CERN as summer student for two months. My project was related to implementation of machine learning in field of high energy physics.

Paper I

Säntis Lightning Research Facility Instrumentation

A. Sunjerga, A. Mostajabi, M. Paolone, F. Rachidi*
EMC Laboratory
EPFL
Lausanne, Switzerland
*farhad.rachidi@epfl.ch

M. Azadifar, A. Rubinstein, M. Rubinstein
Institute for Information and Communication Technologies
University of Applied Sciences of Western Switzerland
Yverdon-les-Bains, Switzerland

C. Romero
Armasuisse
Bern, Switzerland

D. Pavanello
Institute of Sustainable Energy
University of Applied Sciences of Western Switzerland,
Sion, Switzerland

P. Hettiarachchi, V. Cooray
Department of Engineering Sciences
Uppsala University
Uppsala, Sweden

D. Smith
Institute for Particle Physics and Department of Physics,
University of California,
Santa Cruz, California

***Abstract*— The Säntis Tower was instrumented in May 2010 to measure currents of lightning discharges striking the tower. Since then the system has been recurrently updated and expanded. Currently, data associated with lightning strikes to the tower are collected at five different sites. The facility is equipped with a current measurement system, three electric field antennas, an electrostatic field mill, two x-rays sensors, a high-speed camera and four full HD cameras. This paper presents the latest measurement configuration at the facility.**

Keywords-lightning,measurements, Säntis Tower, upgrade, current, camera, high-speed, X-rays

I. INTRODUCTION

The Säntis Tower is a 124-m-tall tower sitting at the top of the 2502-m tall Säntis Mountain (see Fig. 1). The Säntis Mountain is located in the northeast of Switzerland in the Appenzell region (47°14’57” N, 9°20’32” E). The tower is struck by lightning about 100 times per year.

The tower has been instrumented for lightning current measurements since May 2010 [1-3]. In 2014, an electric field station was installed at about 15 km away from the tower [4]. Also, since 2014, the trigger has been sent using TCP/IP over the Internet to the 380 km distant electric field sensor location in Neudorf, northern Austria, operated by ALDIS. More details on the Neudorf station can be found in [5,6]. Here, we present for the first time new measurement stations installed since then.

This paper presents a summary of the measurement systems deployed at the tower and its vicinity. The paper is organized as follows. Section II presents an overview of all the measurement sites and sensors. Sections III to VI present in detail recent upgrades and newly installed equipment.

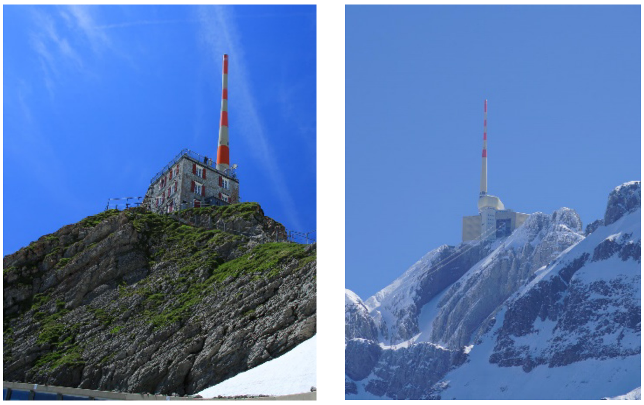

a.) b.)

Fig. 1. Säntis Tower at the top of the 2502-m tall Säntis Mountain. (a) Summer, (b) Winter.

I. OVERVIEW OF THE SÄNTIS RESEARCH FACILITY

A. Measurement Sites

Fig. 2 presents a simplified sketch of the seven measurement sites belonging to the Säntis research facility. The measurement systems deployed in each site are briefly described in what follows.

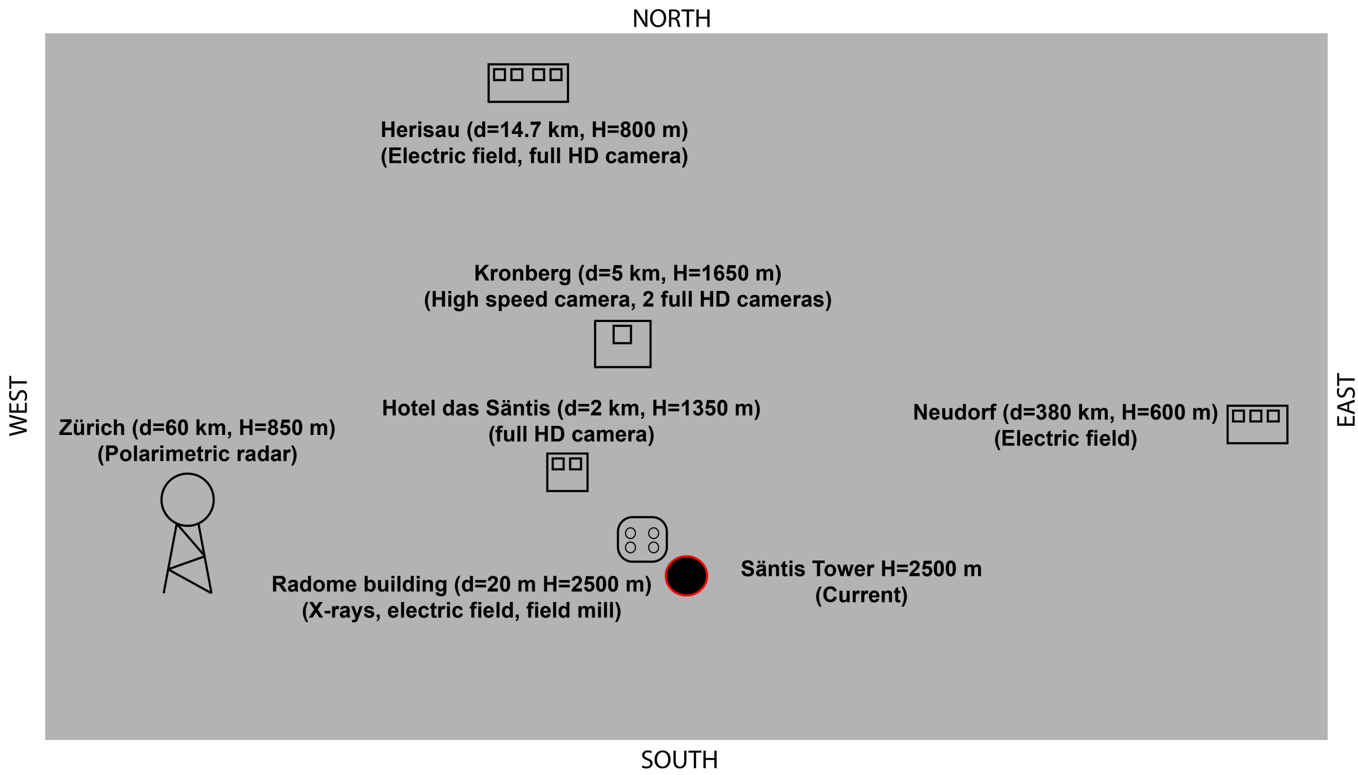

Fig. 2. Simplified sketch of different observational sites and measuring sensors including their distance to the tower and their geographical altitude. Not to scale.

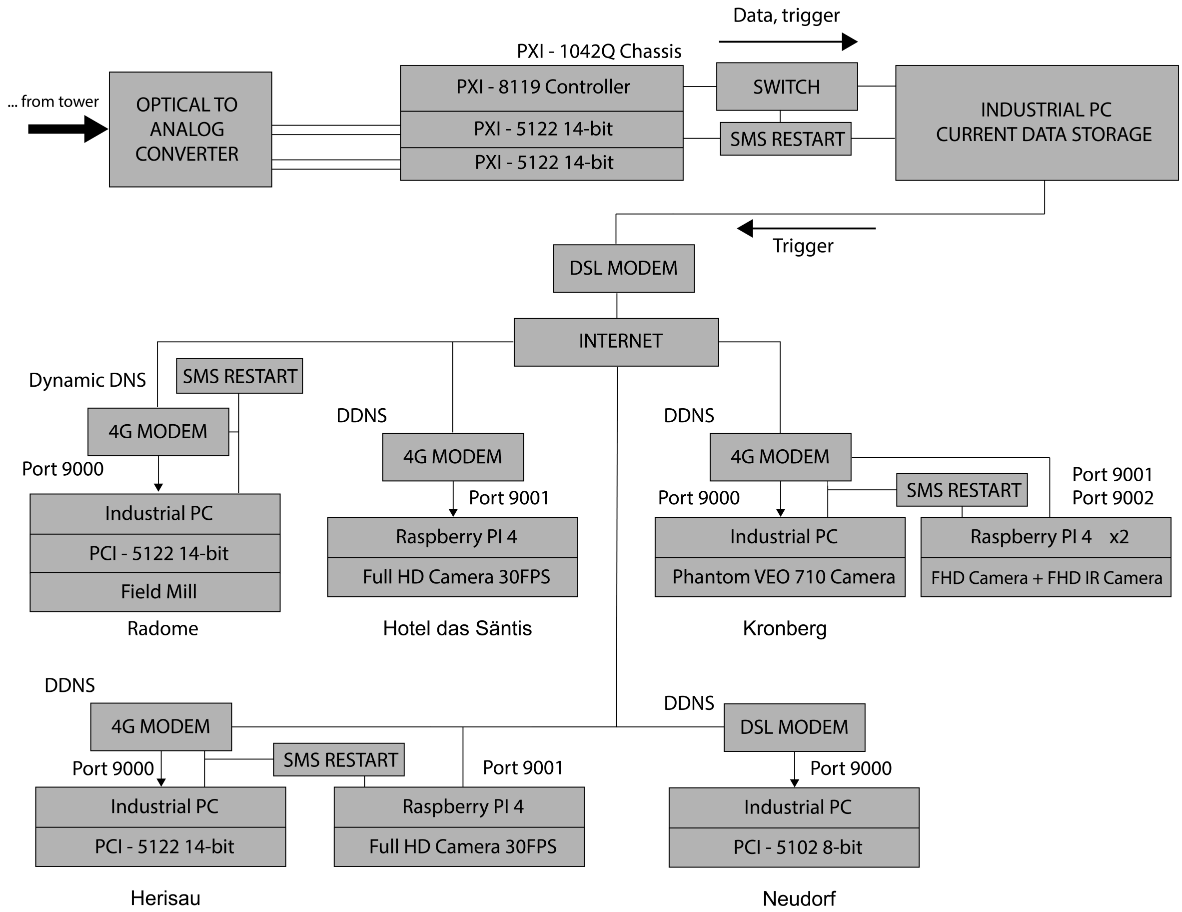

Fig. 3. Simplified graph of the measuring system. The TCP trigger is sent from the tower to all other trigger-based sites.

1. The Säntis Tower (2502 m ASL). Lightning current and its time derivative are measured at two different heights (24 m and 82 m above ground level), using at each location a Rogowski coil and a B-dot sensor. The measurement systems on the tower are thoroughly described in [1-3].
2. Radome (2500 m ASL). The radome is located about 20 m away from the tower (see Fig. 4). At this location, we have installed a fast electric field antenna, an electrostatic field mill, and two x-rays sensors, belonging to our partners from Uppsala University and the University of California at Santa Cruz.
3. Säntis - Das Hotel (1400 m ASL). Located about 2 km away from the tower on the slope of Mount Säntis, this station is equipped with a full HD camera.
4. Mount Kronberg (1663 m ASL) is about 5 km away from the tower. At this location, a high-speed video camera and two FHD cameras are installed. One of the FHD cameras operates in the visible spectrum, while the other one works in the infra-red (IR) spectrum.
5. Herisau (800 m ASL). This site is located at a distance of 14.7 km of the tower. A fast E-field antenna is installed on the top of a building belonging to the Huber+Suhner company.
6. Neudorf (600 m ASL). This station, operated by ALDIS, is located in Neudorf, northern Austria, 380 km away from the tower. The station is equipped with a fast E-field antenna.
7. Albis radar located near the city of Zurich, 60 km east from the Säntis area [7,8].

It is worth noting that the Säntis Tower area is also covered by the EUCLID lightning location network [9]. The Säntis area was also covered by a lightning mapping array (LMA) belonging to the Polytechnic University of Catalunya during an experimental campaign organized in the Summer of 2017 [8]. In addition, during the Summer of 2019 an interferometer belonging to the New Mexico Tech was installed near the Säntis Hotel and, as of the writing of this paper, it will be installed in the Summer of 2020.

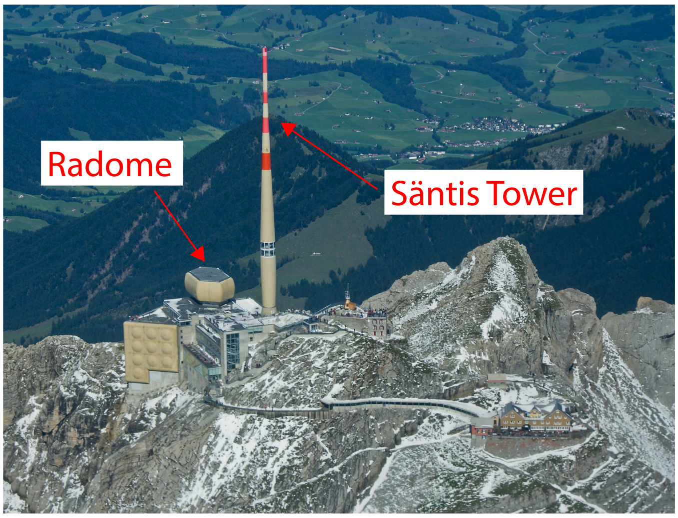

Fig. 4. Location of radome next to the tower.

At each measuring site, every relevant equipment is connected to the modem and has a fixed private local IP non-visible to the rest of the Internet. The modem is configured in such a way that one free port is allocated for each device with their static IP address. For example, in the case of the Kronberg site, three triggers will be sent from the current measuring site using TCP/IP to the URL belonging to the modem installed at this site but using different ports (e.g., 9000, 9001, 9002), one for each camera. This URL is pointing to the IP address of the modem and, in case of a change of IP address of the modem, this URL will be updated to point to the new IP address. This is achieved with the DDNS method and a client installed on one of the PCs connected to the modem. The modem is configured in such a way that the ports are forwarded to the static local IP address of each connected device.

Once each of the devices receives the data, they immediately trigger the corresponding measuring equipment. They all operate with appropriate pre-trigger times with data stored in the buffer. After receiving the trigger, they will continue to work for a time defined by the post-trigger window during which the data are recorded. Since most of the stations communicate over the 4G network, the latency is not always constant. However, most of the time the delay is no longer than 100 ms.

Since the location of the Säntis Tower is more than 200 km away from our laboratory and physical access to the tower and the radome is possible only three days per month, the remote control is of high importance. The remote control commands are transmitted over the Internet, with the inherent risk that a power failure and an interruption in the Internet access can cause disconnection. When the system at the tower is shut down (due to power outages or to voluntary power cycling operations at the tower), or when it loses its Internet connection, it is not able to send trigger signals to the other measuring sites. This can cause the loss of valuable data. In order to mitigate the problem of loss of Internet connection, we have added redundancy to the remote-control system using a GSM receiver. This system, shown in Fig. 5, can be controlled by sending codes in SMS messages to remotely power-cycle either one of the local PCs or the Internet modem since we have determined through experience that this solves most of the connection loss problems. The system is installed at four different locations as shown in Fig. 3.

In the following section, we will report on recent updates at the measuring stations. Details about the current measurement system as well as the remote electric field station in Neudorf can be found in previous literature [1-6]. The instrumentation in the three new stations (radome, Hotel and Kronberg) have not been reported elsewhere. We will give a summary of the instrumentation for each of these sites. Even though some information about the Herisau station has been already provided in [4], we will present here the latest upgrades made to that system.

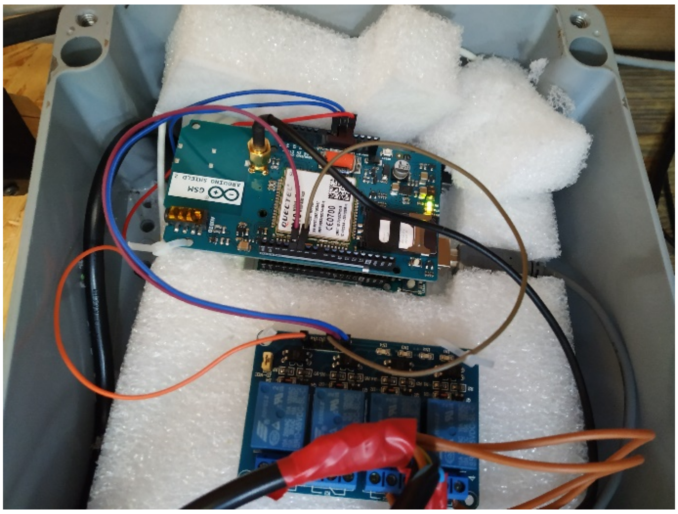

Fig. 5. Restart system. Arduino Uno with GSM module and 4 channel relays.

II. RADOME

This station is located 20 m away from the tower (see Fig. 4). It is equipped with an industrial PC with a two-channel PCI digitizer. One channel of the digitizer is connected to a fast E-field antenna while the second is connected to one of the X-ray sensors. The sampling rate is set to 50 MS/s with a pre-trigger delay of 1.2 s. Each record is 2.4 s long. The field mill is connected via USB to the same PC and the data are recorded in continuous mode. A Garmin GPS 18x LVC is connected to the serial port of the industrial computer and provides a time accuracy of several microseconds.

A commercial microphone is also installed and connected to the PC via USB cable. It is operated via LabView and provides recording for a duration of 100 s. The data will be saved only when a trigger is received.

A. *Fast antenna*

A commercial Thales (former Thomson CSF) Mélopée electric field sensor with a frequency range of 1 kHz to 150 MHz was installed during the Summer of 2018 (see Fig. 6). The output of this antenna is connected to the first channel of the digitizer. More information about the system can be found in [4]. Note that this antenna was initially located in Herisau and it was moved to the radome site in 2018. The antenna in Herisau was replaced with a flat plate antenna (see Section VI).

B. *X-ray sensors*

In July 2019, an X-ray sensor (see Fig. 7) from Uppsala University [11,12] was installed in the radome. In order to mitigate the coupling and interference of strong lightning electromagnetic fields to the measuring system, a battery power supply was installed in the metallic box containing the X-ray measuring device. This system consists of two batteries and a microcontroller that manages the charging of the batteries in such a way that the charging alternates between the two. While one battery is being charged, the other is used as the power supply, so that the system is never connected galvanically to the 230 V grid, preventing any conducted interference from reaching the equipment. Furthermore, the 230 V power supply is provided from an insulation transformer to further reduce noise in cables and possible field coupling. To further reduce the noise, the analog output of the X-ray sensor is relayed to the second channel of the digitizer via a fiberoptic link.

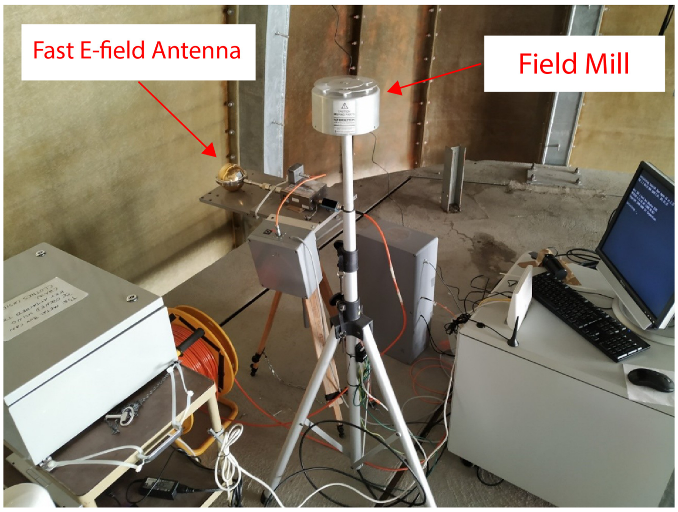

Fig. 6. Fast E-field antenna and field mill.

Another X-ray sensor belonging to the University of California, Santa Cruz (see Fig. 8) was also installed in July 2019. The detector is a 5-inch (diameter) x 5-inch (length) cylinder of BC-408 plastic mounted to a 5-inch PMT (photomultiplier tube). The PMT is negatively biased by ~850 Volts. The detector output is connected to a Bridgeport Instrument eMorpho MCA (Multi-Channel Analyzer) that uses a time-tagged event mode to record the integrated pulse area (with 16-bit resolution) and the arrival time (with 32-bit/12.5-ns resolution) of the detector output. This amounts to a 80-MHz sampling speed. The combination of the nanosecond decay time of the BC-408 and the sampling speed of the MCA is needed to record the high flux and sub-millisecond arrival times of TGF photons. In addition to the detector chain, there is also a GPS unit where a pulse-per-second signal is fed into the MCA's FPGA and incorporated into the data stream as a flagged event. This allows for a precise relative timing and low data usage since the periods without events are not saved, so the device can operate in continuous mode. This device is connected to a second computer on which the data are saved.

C. *Field Mill*

To measure the electrostatic field, an EFM-100 field mill has been installed in the same location since 15 July, 2016, as shown in Fig. 6. The field mill is connected via USB to the industrial PC and the data are recorded in continuous mode.

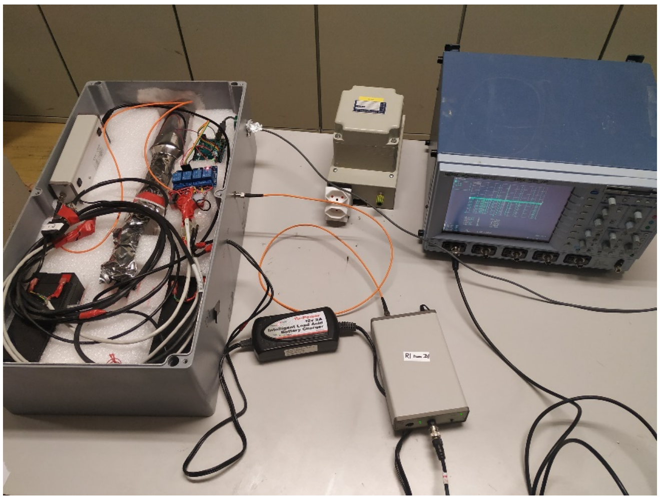

Fig. 7. X-ray sensor from Uppsala University

Fig. 8. X-ray sensor from the University of California, Santa Cruz working in the continuous mode.

III. HOTEL DAS SANTIS

In Spring 2020, a FHD camera was installed in the hotel located about 2 km of air distance away from the tower and 1150 m below the ASL of top of the mountain. A Raspberry PI 4 with a Camera Module v2 was used for this purpose. The camera has an optical size of 1/4" and a focal ratio equal to 2.0. It can operate in Full HD resolution with 30 FPS and can record images of 4K resolution. Currently the camera is set to an ISO equal to 100 and to record Full HD videos with 30 FPS.

Each Raspberry PI is equipped with a 32 GB SD card and it is connected to the Internet. The main code is written in Python and it consists of two threads. The first is waiting for the trigger over TCP/IP on the chosen port. The second is constantly recording the videos for a duration of 60 seconds. If the trigger is received, the video is saved. Otherwise, the video is deleted. Remote access of the raspberry PI is possible over the Internet.

Fig. 9. Four Raspberry PI 4 4G with the camera ready to be installed at three different sites.

IV. KRONBERG

A Phantom VEO 710L high-speed video camera is installed at this location. A view of the Säntis Tower from the camera is shown in Fig. 10. The camera can record up to 1,000,000 FPS at its lowest resolution of 8 x 8 pixels. To have a wider view of 512 x 512 pixels, the number of frames per second needs to be reduced to 10,000. These pixels are distributed over a view of about 2 km by 2 km. The camera records during a 3-second time window with a pre-trigger delay of 1.5 s. A GPS time stamp is provided with an Acutime 360 Multi-GNSS Smart Antenna and the synchronization error is within 15 nanoseconds.

Additionally, two FHD cameras as described in Section IV are installed at this location. The first camera works in the visible spectrum and the second on operates in infra-red.

Fig. 10. High speed Phantom VEO 710L camera installed at the top of the Kronberg mountain.

V. HERISAU

A flat plate antenna is installed in this location since 2017 and it has been updated several times since then. It has a two-battery system to ensure a noise-free power source since the charging and use of the batteries alternates to avoid having a galvanic connection to the mains as in the case of the X-ray sensor (Section III). An industrial computer with a two-channel digitizer is installed at the station. Integrator is located next to the antenna. Terahertz Technologies LTX-5515 analog to digital optical link was used to transfer the analog signal to the input of digitizer. The integrator output transferred by optical link and back converted to the analog signal is connected to the first channel of digitizer that can measure voltages from -5 V to 5 V with a 14-bit resolution. The time constant of the antenna is 8 ms and it can measure electric fields in the range from -200 V/m to 200 V/m.

The digitizer is set to a sampling rate of 10 MS/s with a time window of 6 s and a pre-trigger delay of 3 s. The second channel of the digitizer is connected to the pulse per second output of a Garmin GPS 18x LVC unit. This provides a time accuracy of about a microsecond. This site is also equipped with one FHD camera with the same specifications described in Section IV.

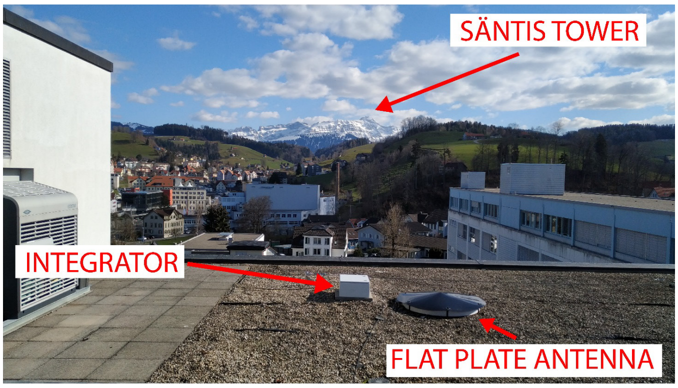

Fig. 11. Flat plate antenna installed at the Herisau site. The antenna is covered with a dielectric for precipitation protection.

VI. Conclusion

In this paper, we presented the measurement system deployed at the Säntis research facility, as well as its recent upgrades. Three new sites in the vicinity of the tower have been equipped with different sensors such a high-speed camera, four FHD cameras, two fast electric field antennas, an electric field mill and two X-rays sensors. The trigger signal is being sent to all stations from the current measurement system over the Internet. Each site can be accessed and controlled remotely. Broadband measurements can help us in future to better understand processes involved in upward lightning.

Acknowledgment

This work was supported in part by the Swiss National Science Foundation (Project No. 200020_175594) and the European Union's Horizon 2020 research and innovation program under grant agreement No 737033-LLR.

References

[1] C. Romero, “Measurement of Lightning Currents Using a Combination of Rogowski Coils and B-Dot Sensors,” Journal of Lightning Research, vol. 4, no. 1, pp. 71–77, Jul. 2012

[2] C. Romero et al., “A system for the measurements of lightning currents at the Säntis Tower,” Electric Power Systems Research, vol. 82, no. 1, pp. 34–43, Jan. 2012, doi: 10.1016/j.epsr.2011.08.011.

[3] Azadifar .M, M. Paolone, D. Pavanello, F. Rachidi, C. Romero, and M. Rubinstein (2014), "An Update on the Instrumentation of the Säntis Tower in Switzerland for Lightning Current Measurements and Obtained Results," in CIGRE International Colloquium on Lightning and Power

[4] D. Li et al., “On Lightning Electromagnetic Field Propagation Along an Irregular Terrain,” IEEE Transactions on Electromagnetic Compatibility, vol. 58, no. 1, pp. 161–171, Feb. 2016, doi: 10.1109/temc.2015.2483018.

[5] Azadifar, M., Li, D., Rachidi, F., Rubinstein, M., Diendorfer, G., Schulz, W., Pichler, H., Rakov, V. A., Paolone, M., & Pavanello, D. (2017). Analysis of lightning-ionosphere interaction using simultaneous records of source current and 380 km distant electric field. Journal of Atmospheric and Solar-Terrestrial Physics, 159, 48–56. https://doi.org/10.1016/j.jastp.2017.05.010

[6] Pichler, H., Diendorfer, G., & Mair, M. (2010). Some Parameters of Correlated Current and Radiated Field Pulses from Lightning to the Gaisberg Tower. IEEJ Transactions on Electrical and Electronic Engineering, 5(1), 8–13. https://doi.org/10.1002/tee.20486

[7] N. Pineda et al., “Meteorological Aspects of Self‐Initiated Upward Lightning at the Säntis Tower (Switzerland),” Journal of Geophysical Research: Atmospheres, vol. 124, no. 24, pp. 14162‐14183, Dec. 2019.

[8] J. Figueras i Ventura et al., “Analysis of the lightning production of convective cells,” Atmospheric Measurement Techniques, vol. 12, no. 10, pp. 5573–5591, Oct. 2019.

[9] W. Schulz, G. Diendorfer, S. Pedeboy, and D. R. Poelman, “The European lightning location system EUCLID – Part 1: Performance analysis and validation,” Natural Hazards and Earth System Sciences, vol. 16, no. 2, pp. 595–605, Mar. 2016, doi: 10.5194/nhess-16-595-2016

[10] A. Sunjerga et al., “LMA observations of upward lightning flashes at the Säntis Tower initiated by nearby lightning activity,” Electric Power Systems Research, vol. 181, p. 106067, Apr. 2020.

[11] P. Hettiarachchi, V. Cooray, G. Diendorfer, H. Pichler, J. Dwyer, and M. Rahman, “X-ray Observations at Gaisberg Tower,” Atmosphere, vol. 9, no. 1, p. 20, Jan. 2018, doi: 10.3390/atmos9010020.

[12] P. Hettiarachchi, M. Rahman, V. Cooray, and J. Dwyer, “X-rays from negative laboratory sparks in air: Influence of the anode geometry,” Journal of Atmospheric and Solar-Terrestrial Physics, vol. 154, pp. 190–194, Feb. 2017.

Paper II

Electric Power Systems Research 181 (2020) 106067

Contents lists available at ScienceDirect

Electric Power Systems Research

journal homepage: www.elsevier.com/locate/epsr

LMA observations of upward lightning flashes at the Säntis Tower initiated by nearby lightning activity

Antonio Sunjerga[a,*], Marcos Rubinstein[b], Nicolau Pineda[c,d], Amirhossein Mostajabi[a], Mohammad Azadifar[b], David Romero[d], Oscar Van der Velde[d], Joan Montanya[d], Jordi Figueras i Ventura[e], Nikola Besic[e], Jacopo Grazioli[e], Alessandro Hering[e], Urs Germann[e], Gerhard Diendorfer[f], Farhad Rachidi[a]

[a] Electromagnetic Compatibility Laboratory, Swiss Federal Institute of Technology (EPFL), Lausanne, 1015, Switzerland
[b] University of Applied Sciences of Western Switzerland (HES-SO), Yverdon-les-Bains, 1400, Switzerland
[c] Meteorological Service of Catalonia, Carrer Berlín 38-46, Barcelona, 08029, Spain
[d] Lightning Research Group, Technical University of Catalonia, Edifici TR1, Carrer Colom 1, Terrassa, 08222, Spain
[e] MeteoSwiss, Locarno, Switzerland
[f] OVE Service GmbH, Dept. ALDIS (Austrian Lightning Detection & Information System), Vienna, Austria

ARTICLE INFO

Keywords:
Lightning
Lightning Mapping Array
Other-triggered lightning
Current
Charge structure
Leader polarity
Radar
Electric field

ABSTRACT

We present in this paper lightning current measurements, LMA (Lightning Mapping Array) data and fast antenna electric fields associated with upward flashes observed at the Säntis Tower during summer of 2017. The LMA network consists of six stations that were installed in the vicinity of the tower at distances ranging from 100 m to 11 km from it. Out of 20 LMA recorded flashes here we analyze in detail three so-called 'other-triggered flashes', triggered by preceding activity. Based on the lightning activity derived from the European Lightning Detection Network (EUCLID) in an area within 30 km from the tower and within a 1-s time window before the start of the upward tower flashes, only one out of 20 flashes was classified as 'other-triggered'(OT). However, the investigations based on the LMA data reveal that 3 more flashes of the 20 analyzed were preceded by nearby activity and should therefore be classified as OT flashes. We analyze conditions conducive to the OT flashes, such as the charge structure of the clouds, polarity of preceding leaders and level of activity of the storm.

The LMA source active time period was on average seven times higher for the OT flashes than that for self-initiated flashes.

1. Introduction

The characteristics of upward lightning discharges based on tall structure measurements (e.g., Gaisberg, Peissenberg, Säntis) have been widely reported in the literature [1]. However, their initiation mechanisms are not well understood and are still under investigation. Wang et al. [2] proposed the classification of upward flashes into two categories: self-triggered (ST) and other-triggered (OT), based on the absence or the presence of other lightning activity in the geographical and temporal vicinity of the tower-initiated flash. The number of ST and OT flashes has been shown to vary depending on the geographical area (e.g., [3]). It has also been shown that the rate of ST versus that of OT flashes is correlated, to some extent, to atmospheric conditions [4,5]. Different observation methods have been used to classify flashes into the ST and OT categories, namely based on data from lightning location systems (LLS) [3], electric fields [6], and video observations [7].

OT flashes can be preceded (or triggered) by both in-cloud (IC) and cloud-to-ground (CG) flashes. IC flashes can occur on both large scales (a few tens of km) and small scales (a few hundreds of meters), while CG channels extend to a few kilometers [8]. Schumann et al. [9], using video observations, proposed different mechanisms conducive to the initiation of upward flashes, all of them associated with horizontally propagating leaders in the clouds over the towers.

A Lightning Mapping Array (LMA) is a 3D discharge location system pioneered by D. E. Proctor [10–12]. The detection is accomplished by measuring the VHF radiation from the discharges, while the location is determined using the measured arrival times of the common signal at each station to calculate the spatial position and emission time of the radiation source. Proctor used 5 stations to study small-scale

* Corresponding author.
E-mail address: antonio.sunjerga@epfl.ch (A. Sunjerga).

https://doi.org/10.1016/j.epsr.2019.106067
Received 10 April 2019; Received in revised form 18 July 2019; Accepted 9 October 2019
Available online 04 December 2019
0378-7796/

breakdowns of lightning. Clustering algorithms [13–15] can be used to automatically identify lightning flashes from LMA data.

In June 2017, a 3D LMA network [16,17], consisting of 6 stations belonging to the Lightning Research Group of the Polytechnic University of Catalonia (UPC) was installed around the Säntis Tower in Northeastern Switzerland. The covered range is typically about 60 km in diameter. The Säntis Tower is equipped with a direct current measuring system since May 2010. The LMA was operational during two months, July and August, 2017.

Out of a total of 20 recorded flashes, we analyze in detail in this paper three flashes for which simultaneous measurements of current and LMA sources associated with OT upward flashes from the Säntis Tower were obtained during the 2017 campaign. This paper is an extended version of paper [18].

2. Measurement setup

2.1. Lightning current and electric field measurements

The 124-m tall Säntis Tower, located at 47°14’57’’N and 9°20’32’’E, is by far the most frequently struck structure in Switzerland [19,20]. The tower has been instrumented since May 2010 using advanced equipment including remote monitoring and control capabilities for accurate measurement of lightning current parameters enabling a high-resolution sampling of lightning currents over long observation windows [19,21]. Lightning currents are measured using two sets of Rogowski coils and multigap B-dot sensors located at two different heights along the tower. The analog outputs of the sensors installed are relayed to a digitizing system by means of optical fiber links. The system is equipped with GPS and allows over-the-Internet remote maintenance, monitoring, and control. More details on the instrumentation can be found in Ref. [19,21–24]. The lightning current is recorded over a 2.4 s interval with a pre-trigger delay of 960 ms.

The Säntis measurement station includes also an electric field measurement station comprising a flat-plate antenna and an analog integrator with an overall frequency bandwidth of 30 Hz–2 MHz, located in Herisau at a distance of 14.7 km from the tower [25].

2.2. Lightning Mapping Array (LMA)

An LMA network was installed in the Säntis Tower region in June 2017 [26]. The system consists of six stations measuring VHF radiation in the 60–66 MHz band. The locations of the LMA stations were chosen considering several factors, namely:

1) The magnitude of the local noise within the frequency band,
2) The availability of reliable AC power and communication means,
3) The distance to the source (Säntis Tower), and,
4) A good combination of accessibility and security.

The selected locations correspond to mobile base stations belonging to Swisscom and Swisscom Broadcast and they are shown in Fig. 1. The measurement stations were deployed in the vicinity of the Säntis Tower, at distances ranging from 100 m to 11 km. The area of interest is located in eastern Switzerland and it covers parts of the cantons of Appenzell Inner-Rhodes, Appenzell Outer-Rhodes, and St. Gallen. The LMA takes the maximum power of VHF radiation within a time window of 80 ms and measures the time of arrival with 50 ns accuracy using a PC-based digitizer card coupled to a GPS receiver.

The LMA data were synchronized with the lightning current data using GPS time stamps. Results from the LMA network were transformed from global coordinates to the local coordinate system of the tower taking into account the curvature of the Earth. The coverage of the LMA system is about 30 km to the west of the tower, about 15 km to the east and 25 km to the south and north (for more details see [27]).

3. Observations of Other-triggerd flashes

3.1. Overall data

During the campaign, lightning currents, electric fields and LMA data were simultaneously recorded. In this paper, we present results for 20 analyzed flashes in the period from 29.06.2017 to 18.07.2017. The electric field system was operational only during three of the flashes (#18, #19 and #20 in Table 1). Using the data from the EUCLID network [28], the flashes were classified either as OT or ST, considering whether or not lightning activity was reported in an area within 30 km from the tower and within a 1-s time window before the start of the tower flash. The time interval criterion of 1-s was chosen because most of the flashes last less than a second [29] so we can take into account all the activity that could still occur after the recorded pulse by EUCLID. It is worth noting that the value of the inter-flash intervals recorded by EUCLID during the storms in the 30-km range around the Säntis Tower is observed to have a median of about 5 s [30]. Using these criteria, all 20 flashes (18 negative, 1 positive and 1 bipolar) were initially classified as ST in Ref. [18]. A high level of noise in the low frequency spectrum of the Rogowski coil lightning measuring system made it hard to determine the exact current onset time at the tower. A more detailed analysis with application of a lowpass filter in this paper showed that one flash in Ref. [18] was misclassified using EUCLID as an ST flash. That upward negative flash was preceded by a downward, single-stroke positive flash recorded about 100 ms before the start of the ICC (initial continuous current), about 22 km East and 11 km South of the tower, in an area without LMA coverage. Since the preceding event was not in the area of LMA coverage, the flash from the tower was not classified as OT using the LMA.

On the other hand, using the LMA, we could observe that 3 more flashes were of the OT type. Schumann et al. [31] observed three different types of preceding flashes from which the upward lightning can be triggered: (i) a return stroke (RS) that leads to an intensification of a horizontal leader over the tower that, in turn, triggers the upward lightning from the tower, (ii) an extension over the tower of the horizontal part of a leader during the continuing current (CC) phase of a nearby CG flash, and (iii) an in-cloud leader that develops over the tower, and whose other end may or may not terminate in the ground. All three LMA-recorded OT flashes belong to category (iii) and, consequently, are of the type not often recognized by lightning location systems, as they detect lightning in the LF frequency range and are mostly effective in detecting CG discharges and cloud discharges whose channel has a vertical orientation. It is unclear to which type the OT flash recognized by EUCLID belongs since the LMA did not detect any activity over the tower at the time of initiation of the upward flash. Note that the preceding RS is located outside of the coverage area of the LMA.

In what follows, we will present one positive OT flash and two negative OT flashes that occurred during a period of just 3 min. Data for the third negative OT flash classified by EUCLID will not be shown here since, as mentioned, the preceding flash was not covered by the LMA. However, the available data can be found in the attached materials. The time evolution of LMA sources for each flash can also be observed in the accompanying animations. We will analyze the charge structure of the cloud as well as the polarity of the leaders.

Since the negative leaders propagate through positive charge regions and radiate more strongly (compared to positive leaders) in the VHF spectrum [32], the LMA observations over longer periods can be used to infer the charge structure of the cloud. The average horizontal speed can be used to estimate the polarity of the leader. Van der Velde and Montanyà [33] showed that negative leaders propagate with an average speed of 10^5 m/s (during positive cloud to ground flashes, the speed can sometimes go up to 10^6 m/s), while the average speed for positive leaders is around 2×10^4 m/s. This can also be used to infer the charge structure since, in addition to the mentioned observation in [32] that negative leaders propagate through positive regions, positive

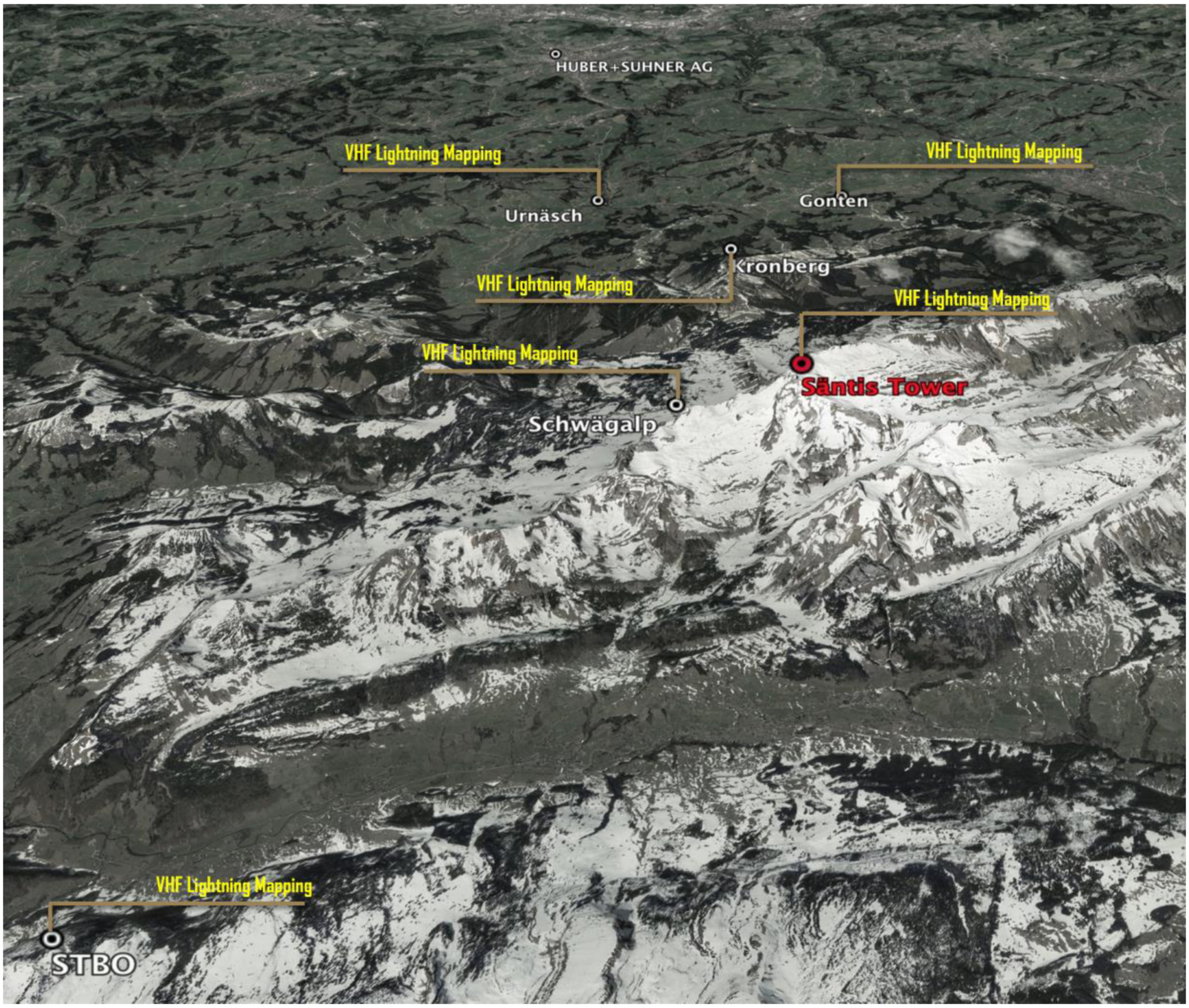

Fig. 1. Lightning Mapping Array stations around the Säntis Tower. The measurement stations were deployed in the vicinity of the Säntis Tower, at distances ranging from 100 m to 11 km. The electric field station is located 14.7 km north of the tower at the top of a building in Herisau belonging to the Huber + Suhner company.

Table 1
Percentage of LMA active period (period with no more than 100 ms without LMA sources) 20 min observations centered at time of flash.

Flash number	1	2	3	4	5	6	7	8	9	10
Date	29.06.17	29.06.17	29.06.17	29.06.17	29.06.17	29.06.17	29.06.17	29.06.17	29.06.17	29.06.17
UTC Time	13:38:27	14:06:13	14:08:39	14:11:09	15:05:42	15:10:52	15:36:50	15:39:46	15:45:52	15:47:31
Polarity	P	N	N	N	N	N	N	N	N	N
Type	OT	ST	ST	ST	ST	ST	ST	ST	ST	ST
LMA Active (%)	3.95	1.67	1.15	0.83	0.04	0.05	0.13	0.18	0.33	00.33
Flash number	**11**	**12**	**13**	**14**	**15**	**16**	**17**	**18**	**19**	**20**
Date	29.06.17	29.06.17	29.06.17	10.07.17	10.07.17	10.07.17	14.07.17	18.07.17	18.07.17	18.07.17
UTC Time	15:54:55	16:00:13	16:05:36	20:48:58	20:51:45	21:19:37	13:25:39	16:28:01	16:30:58	16:50:01
Polarity	N	N	N	N	N	N	B	N	N	N
Type	ST	ST	ST	ST	ST	ST	ST	OT	OT	OT
LMA Active (%)	0.24	0.13	0.07	0.19	0.10	0.01	0.13	2.42	2.38	0.68

leaders propagate through negative regions. In the following analysis, one has to bear in mind the limitation of the LMA. Mazur et al. [34] argued that the TOA lightning mapping technique does not allow the simultaneous processing of both the strong radiation signals from negative breakdowns and the much weaker radiation signals from positive breakdowns. Based on that assumption, it is not clear if any of the floating leaders occurred in a bidirectional [35] or a unidirectional manner. The LMA has also a low efficiency in detecting leaders such as dart leaders or K changes propagating along already ionized paths.

3.2. Negative flashes

3.2.1. Charge structure

Two negative OT flashes (#18 and #19 in Table 1) occurred in a time interval of just below 3 min and a third one (#20 in Table 1) followed about 22 min after the first one. The VHF activity in the 20-min period centered at the time of the first other-triggered flash is presented in Fig. 2, in which the inferred positive and negative charge regions are shown.

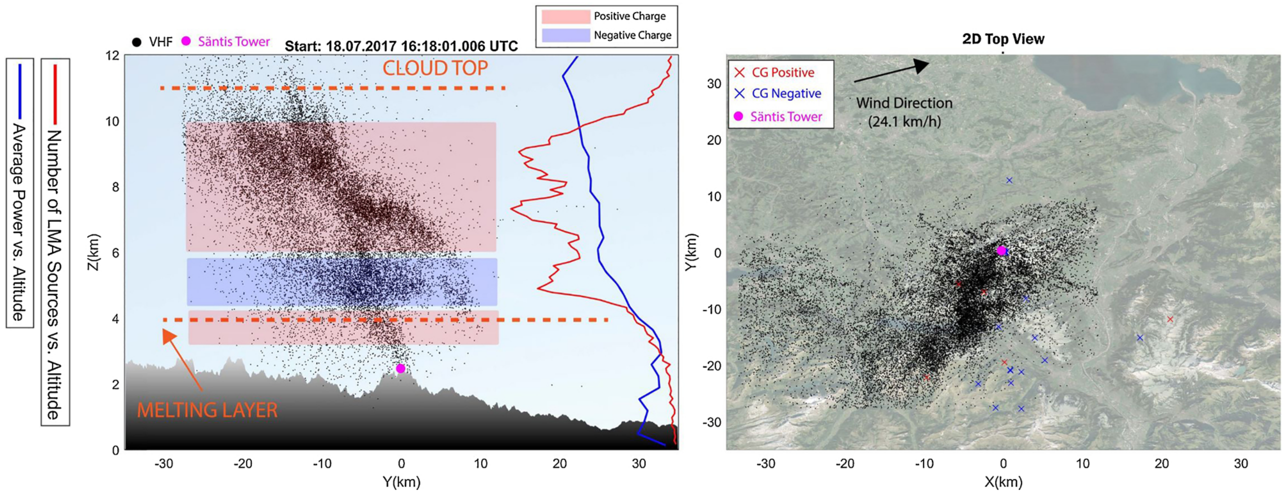

Fig. 2. VHF activity recorded by the LMA stations in the Säntis region over a 20-min time window starting 10 min prior to the initiation of two negative flashes to the tower. Left panel: 2D side view with histogram of LMA sources vs. altitude. Right panel: 2D top view. EUCLID recorded CG pulses are shown with crosses (blue for negative and red for positive). The negative and positive charge regions, inferred from the LMA source density, are shown, respectively, in blue and red in the left panel. The position of the tower is shown with a purple marker.

Radar data (see attached material) suggest that the cloud extended to a height of about 11 km and the melting layer can be observed at about 4 km. It is worth noting that, based on balloon observations, a change of the charge layer sign occurs at the level of the melting layer [36,37]. The wind speed at the location of the Säntis was 24.1 km/h with an angle of 253°, approximately from West (as shown with the black arrow in Fig. 2b). The temperature at the summit of the Säntis was measured to be 10.7 °C with a relative humidity of 75%. During the considered 20-min period, EUCLID recorded in total of 158 pulses which included 29 CG pulses and 129 IC pulses. Five out of 29 CG pulses were positive while there were 98 positive pulses out of 129 in the case of the IC pulses. Note that, even though most of the EUCLID detections are strokes, we have called EUCLID detections “pulses”. This is to account for the fact that EUCLID records may include, in addition to strokes, fast pulses superimposed on the ICC (the so-called ICC pulses).

In Fig. 2 we infer the charge polarity based on the density level of the LMA sources, the polarity of leaders propagating at different heights and the power of the LMA sources. A high number of LMA sources can be observed at altitudes ranging from 6 to 9.5 km, suggesting that these altitudes correspond to the main positive charge region. Negative leaders are observed in this region.

A negative charge region just below the main positive is characterized by a lower number and power of LMA sources. Further, we assume a shallow positive region below the main negative region due to the corona discharge from the ground. The exact charge structure might be much more complex than the one presented in Fig. 2, possibly with different charge polarities at the same altitude. The inferred charge structure in Fig. 2 is based on indirect measurements that could be affected by distance to the VHF radiation sources, polarization and other uncontrolled factors and it should therefore be taken with caution.

3.2.2. LMA observations

Fig. 3 presents the obtained data for the first upward negative OT flash. The start of the initial continuous current (ICC) occurs at about 100 ms as marked with a black arrow in Fig. 3c. The flash was preceded by in-cloud discharge activity as can be seen from the LMA data (red arrows marked with number 1). This activity was initiated at different altitudes (from about 2 to 10 km) west of the tower, propagating in different directions, south, north and east towards the tower, and presumably causing an electric field intensification at the tower tip, resulting in the initiation of an upward flash.

Fig. 4 presents the horizontal distance from the tower to the ground-plane projection of the detected LMA sources as a function of time. Blue and black straight lines were drawn in the plot of Fig. 4 with slopes corresponding to the typical positive leader speed (2×10^4 m/s) and negative leader speed (1×10^5 m/s). Using the speed criteria, we can infer the leader polarity. The estimation is made somewhat difficult by the relatively low number of detected LMA sources and leader branching. The trend in the data shown in Fig. 4 is not clear in the first 80 ms. Beyond this time, there is an indication of the characteristic horizontal speed of negative leaders. With reference to Fig. 3, the presence of the initial continuous current in the tower-base current indicates that the flash was of upward type. From the negative sign of the ICC, we can conclude that the leader was positive. No LMA sources associated with the upward leader are recorded, since they are probably obscured by stronger radiation from the negative leader (shown with the orange arrow #2 in Fig. 3) as discussed by Mazur et al. [34].

Observations for the complete duration of the flash are shown in Fig. 5. Note that the current in Fig. 5c is now shown in logarithmic scale. As can be seen from Fig. 5b, the length of the in-cloud leader was more than 40 km, covering a surface of about 800 km^2. The leader propagated in various directions and it probably obscured the activity of the flash at the tower, both during the ICC and during the RS’s phase. Most of the RSs were detected by EUCLID at the location of the tower. The extension of the in-cloud leader continued even after the last RS of the tower flash as can be seen from Fig. 5c. Interestingly, a positive CG flash, which presumably induced the fast current impulse at the tower, was observed by EUCLID. It is marked with the black arrow in Fig. 5c.

Observations on the first 350 ms of the second negative OT flash are shown in Fig. 6. The ICC current started at about 100 ms. Again, we can conclude from the ICC and current polarity that an upward positive leader was initiated from the tower. The LMA sources of the in-cloud leader started before the onset of the ICC (red arrows #1), at about 25 ms and the slope in Fig. 7 is typical of negative polarity leaders. As in the previous flash, most of the LMA sources from the preceding negative leader were detected at an altitude of 4–7 km, suggesting that the positive charge region was at that altitude range, consistent with Fig. 2. The upward positive leader was presumably obscured again by strong radiation from a negative in-cloud leader (orange arrow #2). The ICC ended before the onset of the first RS and only one LMA source was recorded during the six RSs. All six RSs were recorded by EUCLID at the location of the tower, not shown in Fig. 6c due to the limited range in the x and y axes.

3.2.3. Electric field vs. current

In Figs. 8 and 9 we present the time synchronized waveforms of the electric field measured at 14.7 km from the tower and the current

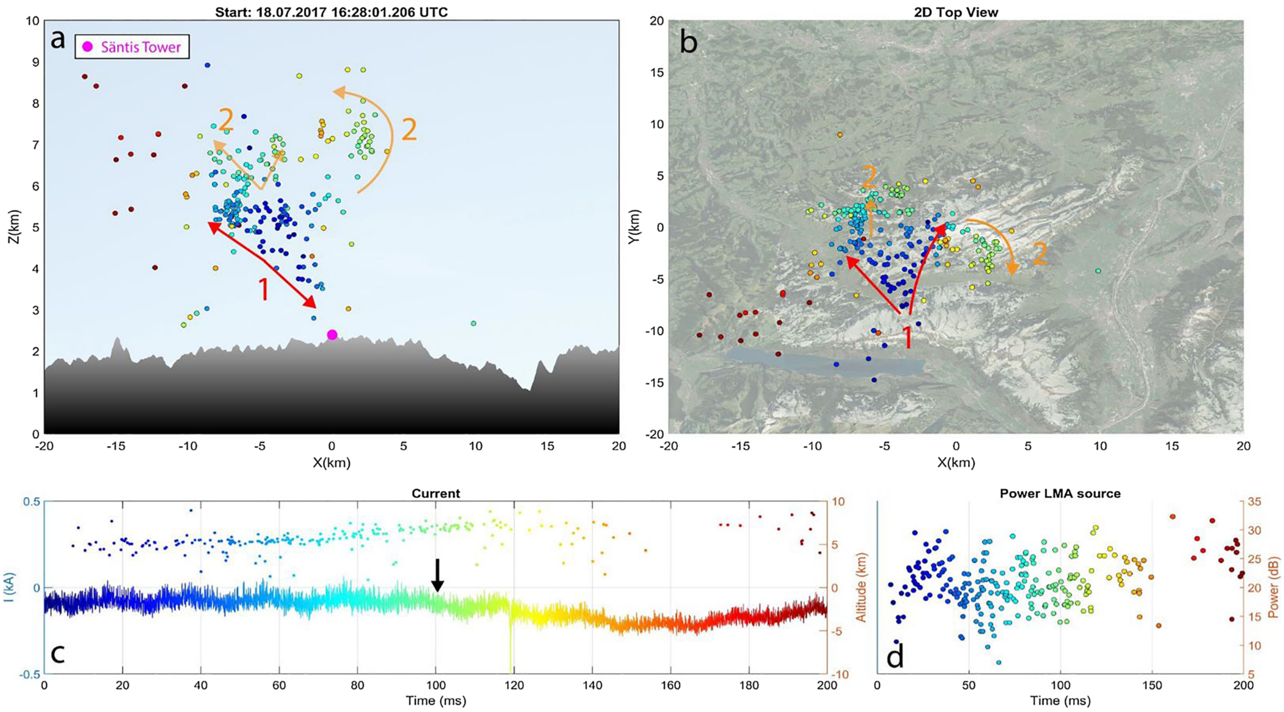

Fig. 3. Initial stage of an upward negative flash initiated from the Säntis Tower recorded on 18.07.2017 at 16:28:01 UTC. In the upper left panel, the location of the tower is shown with a purple marker and the LMA VHF sources are shown with time-color-coded circle markers. (a) 2D view of Z vs. X, (b) 2D view of X vs. Y, (c) current with VHF sources superimposed (1 kHz low-pass filter applied), (d) power vs. time for the VHF sources. Note that the colors of the arrows in (a) and (b) were selected for better contrast and do not bear a relation to the color-code used for timing. The start of the time axis corresponds to the time given in the title of subplot (a). The colored arrows show the development of in-cloud leaders.

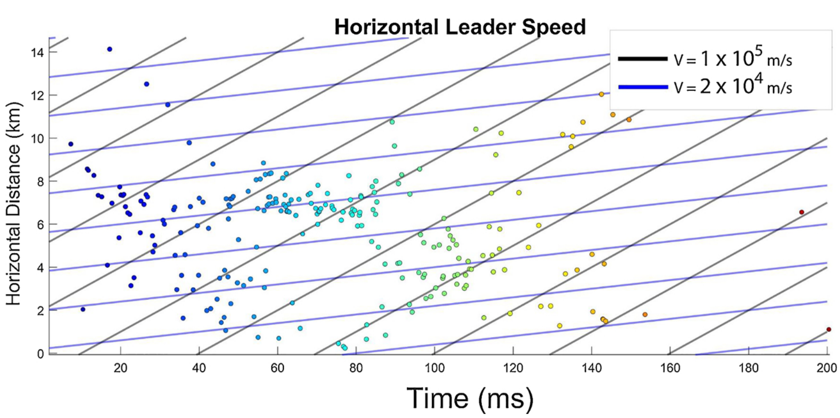

Fig. 4. Horizontal distance vs. time for LMA sources during the initial stage of the flash. The slopes of the blue and black straight lines correspond to the typical speeds of positive and negative leaders, respectively. Successive VHF sources (colored dots) are inferred to belong either to positive or to negative leaders depending on the straight line slope they roughly follow.

measured at the Säntis Tower. In both cases, we can observe the rise of the electric field, caused by the in-cloud leader, prior to the initiation of the current. The delay time of the current is consistent with the delay time from the first LMA sources measured in Figs. 3 and 6. The in-cloud leader propagated during the whole duration of the first negative flash. In the case of the second flash, the in-cloud leader ceased to exist prior to the RSs phase, which can be seen in Fig. 9.

3.2.4. *Skech of the process*

Figs. 10 and 11 show a simplified sketch of the initial stage of the two observed negative OT flashes. In the case of the first flash (Fig. 10), a leader started west of the tower at an altitude of about 5 km and it propagated in three different directions. Even though the polarity of the leader is not completely clear from the horizontal speed criteria, we have assumed it to be negative with possibly a positive branch to keep zero net charge [38].

The second flash started similarly west of the tower and it propagated in two directions, one horizontal above the tower and one both vertically up and horizontally. Again, we cannot rule out the existence of a positive leader in the opposite direction that was possibly obscured by the strong radiation of negative leaders. As the horizontal portion reached the region above the tower, a positive upward leader was initiated.

3.3. *Positive flash*

3.3.1. *Charge structure*

The high VHF activity in the 20-minute period centered at the time of the positive OT flash that occurred on 29.06.2017 at 13:28:27 UTC is presented in Fig. 12. Radar data (see attached material) suggest that the cloud extended to a height of about 8 km and the melting layer was at about 3 km. The wind speed at the location of the Säntis was 6.1 km/h with an angle of 186°, approximately from the South (as shown with a black arrow in Fig. 12b). The temperature at the altitude of the Säntis tower was 4.2 °C, with a relative humidity of 100%. During the considered 20-minute period, EUCLID recorded 70 CG pulses and 133 IC pulses. All 70 CG pulses where negative (some of them superimposed)

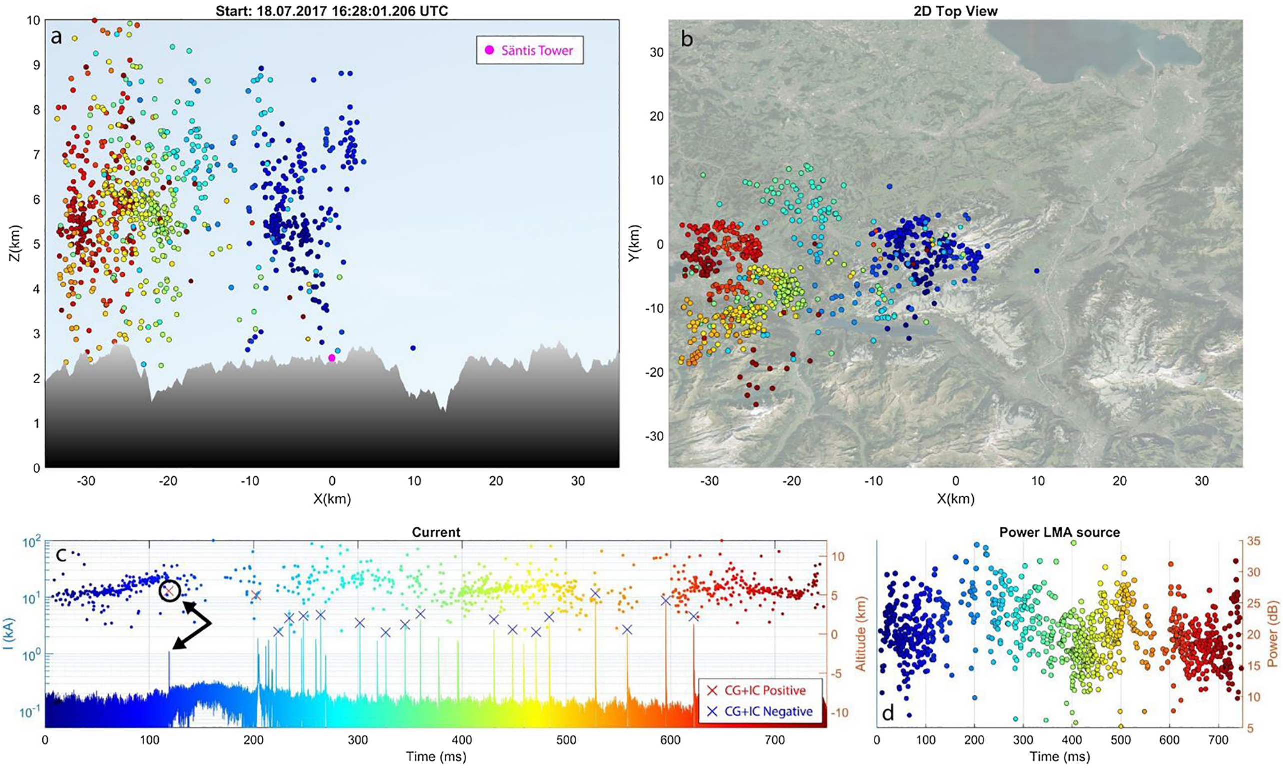

Fig. 5. Upward negative flash initiated from the Säntis tower that occured on 18.07.2017 16:28:01 UTC recorded over the flash's whole duration. In the upper left panel, the location of the tower is shown with a purple marker and the LMA VHF sources are shown with time-color-coded circle markers. (a) 2D view Z vs. Y, (b) 2D view of X vs. Y, (c) current magnitude in logarithmic scale with superimposed VHF sources, (d) power vs. time for the VHF sources.

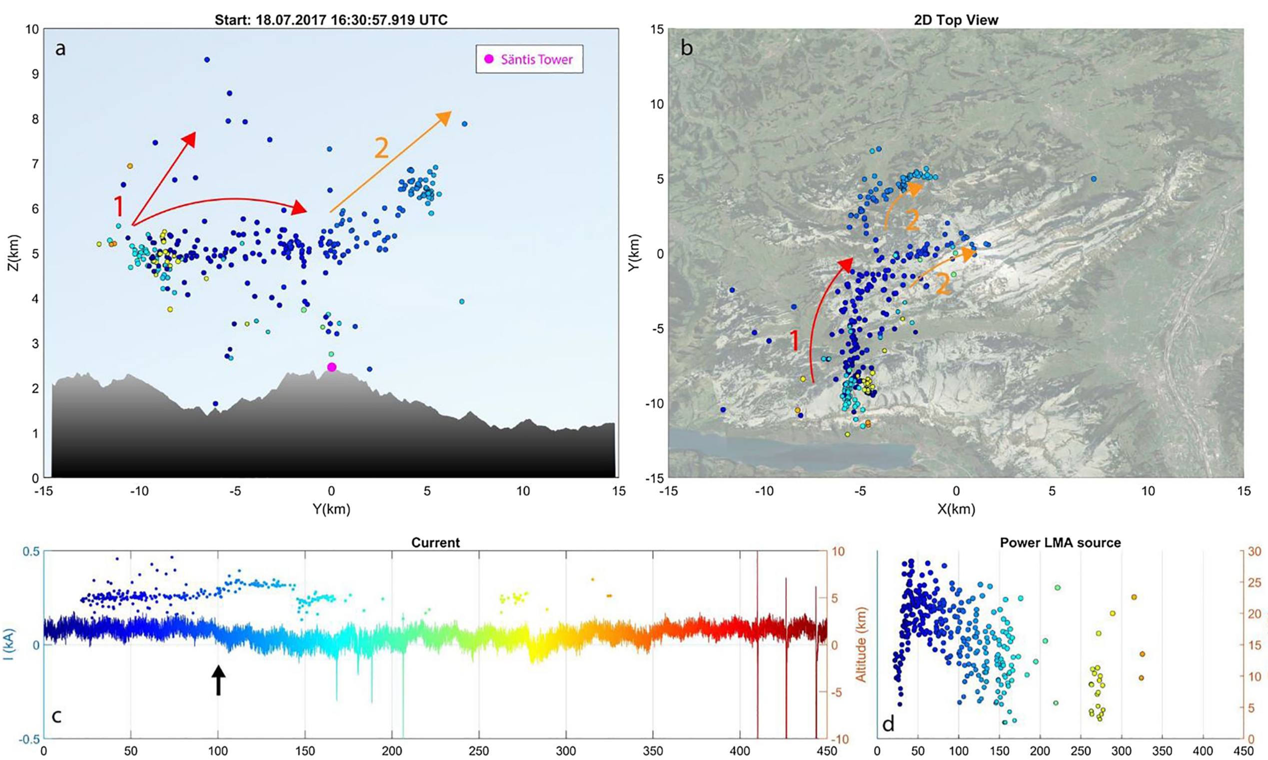

Fig. 6. First 350 ms of an upward negative flash initiated from the Säntis Tower recorded on 18.07.2017 at 16:30:57 UTC. In the upper left panel, the location of the tower is shown with a purple marker. The LMA VHF sources are shown with time-color-coded circle markers. (a) 2D view Z vs. X, (b) 2D view of X vs. Y, (c) current with superimposed VHF sources (1 kHz lowpass filter applied), (d) power vs. time for VHF sources. Note that the colors of the arrows were selected for better contrast and they are independent of the colors used in the time-code. The colored arrows show the development of in-cloud leaders.

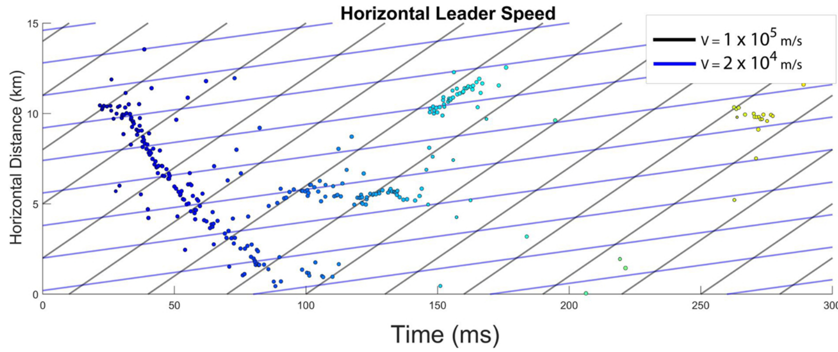

Fig. 7. Horizontal distance vs. time for LMA sources during the initial stage of the flash. The slopes of the blue and black straight lines correspond to the typical speeds of positive and negative leaders, respectively.

and 93 out of the 133 IC pulses were positive. In Fig. 12, the polarity of the charges was inferred based on the LMA sources density level, the polarity of the leaders propagating at different heights and the power of the LMA sources.

A high number of LMA sources can be observed at altitudes ranging from 3 to 5 km, suggesting that the positive charge region was located in that height range as illustrated in Fig. 12. The negative charge layer, inferred to be above that positive charge region is suggested by the lower LMA source density and slightly lower average power of LMA sources. It is possible that there exists a positive charge region above the negative region, making the structure be similar to the normal tripole structure observed by Qie et al. [39] with a larger-than-usual lower positive charge region that, also as in this study, did not produce downward positive CG. However, this larger than usual lower positive charge region might be conducive to upward positive lightning. Since the evidence used to infer the charges is indirect and essentially limited to LMA source characteristics, the charge structure in Fig. 12 should be taken with caution. The exact charge structure might be much more complex than the one presented in Fig. 12, possibly with different charge polarities at the same altitude.

3.3.2. LMA observations

Fig. 13 presents simultaneous measurements of current and LMA sources for the positive flash. The flash was preceded by an in-cloud leader marked with red arrows number (#1). This leader propagated vertically to ground and branched horizontally. It was classified as negative using the criteria for the horizontal velocity (same procedure as in Figs. 4 and 7). This leader was followed immediately by the upward negative leader from the tower (arrow #2). The polarity of this leader can be inferred from the current waveform. The positive current waveform at the tower lasted for about 6 ms. It should be noted that it is also possible that the flash was actually an aborted leader which never reached the positive cloud charge. This was followed by some LMA activity at the location of the preceding in-cloud flash. EUCLID did not record any CG or IC pulse either during or before the occurrence of the flash at the tower.

3.3.3. Skech of the process

Fig. 14 presents a simplified 2D sketch of the positive flash described in the previous section. The in-cloud negative leader started north from the tower and propagated vertically towards the ground. Again, the possibility of a positive leader propagating in the opposite direction and having been obscured by a stronger radiating negative leader cannot be ruled out. This positive end of leader might have been propagating in the direction of the tower and finally triggered the upward flash. When the in-cloud negative leader reached an altitude of about 3 km, another negative leader was initiated from the tower. Soon after, that LMA activity vanished.

4. Comparison with self-triggered flashes

During the 20 min centered around the first negative OT flash (#18), 24421 LMA sources were recorded. We define any period of 100 ms or longer without LMA sources in the covered range as a non-active period. During these 20 min, the no-activity period amounts to 97.6% of the total time, showing that the random overlapping of events

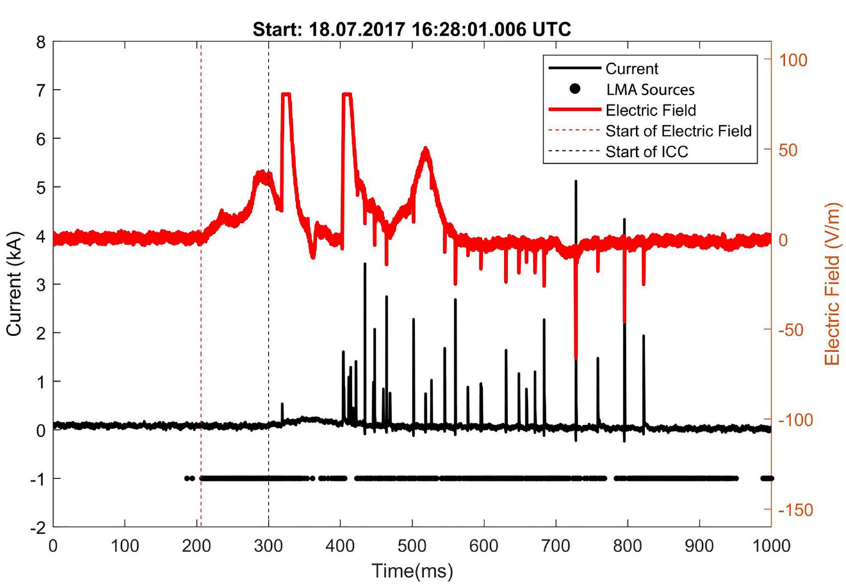

Fig. 8. Electric field at 14.7 km and current at the tower for the flash recorded on 18.07.2017 at 16:28:01 UTC. The current waveform shown in the figure was filtered with a 1-kHz lowpass filter to better emphasize the initial continuous current. Note that the sign of the current is inverted to emphasize syncronization with the electric field. The flat peak of the electric field plot is due to saturation.

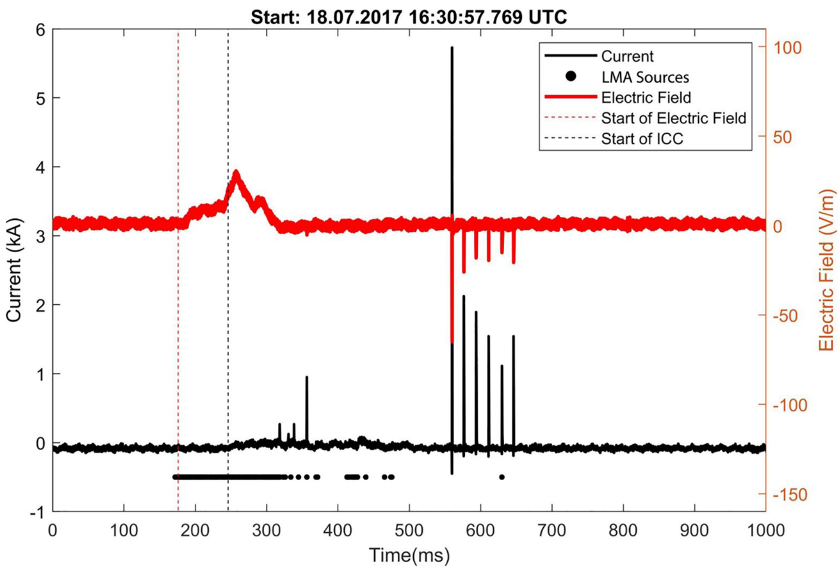

Fig. 9. Electric field at 14.7 km and current at the tower for the flash recorded on 18.07.2017 at 16:30:57 UTC. The current waveform shown in the figure was filtered with a 1-kHz lowpass filter to better emphasize the initial continuous current. Note that the sign of the current is inverted to emphasize syncronization with the electric field.

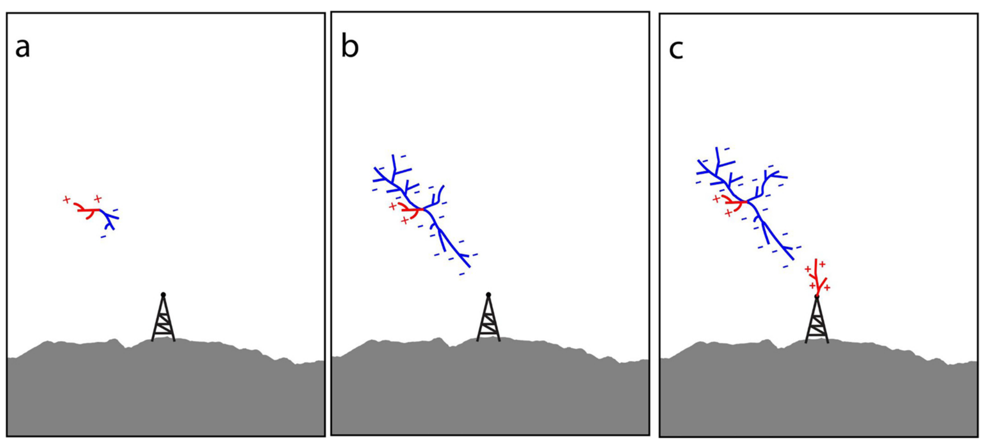

Fig. 10. Sketch of the initial phase of the flash initiated from the Säntis Tower on 18.07.2017 at 16:28:01 UTC. View from the South. Not to scale.

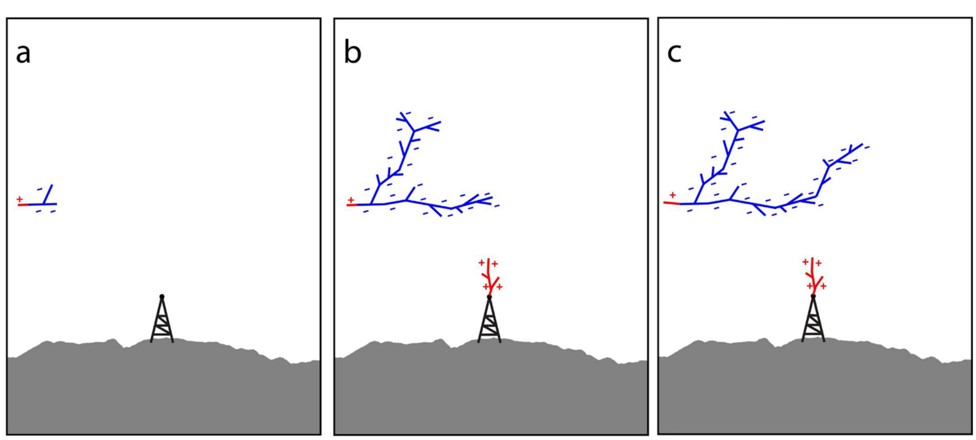

Fig. 11. Sketch of the initial phase of the flash initiated from the Säntis Tower recorded on 18.07.2017 at 16:30:57 UTC. View from the East. Not to scale.

has a probability of 2.4%. For the case of the third negative flash classified as OT based on EUCLID, some of the storm activity occurred outside of the LMA coverage range and we observed a lower LMA activity of 0.68 %. The positive OT flash was characterized by an LMA activity of 3.95%. The average LMA activity corresponding to the four OT flashes in the observed period is 2.35 %.

ST flashes occurred during less active thunderstorms. LMA activity ranged from 0.01 to 1.67% with an average value of 0.35%, almost seven times lower than in the case of OT flashes. Interestingly, two flashes (#5 and #7) occurred without any LMA activity 10 min prior to the flash.

The charge structure for the two negative OT flashes is characteristic of the typical tripole structure with a large upper positive region. The positive OT was observed during a thunderstorm characterized by a tripole charge structure and larger than usual lower positive region. A detailed analysis of the ST flashes during this campaign can be found in Ref. [40]. It was observed in Ref. [40] that the overall electrical

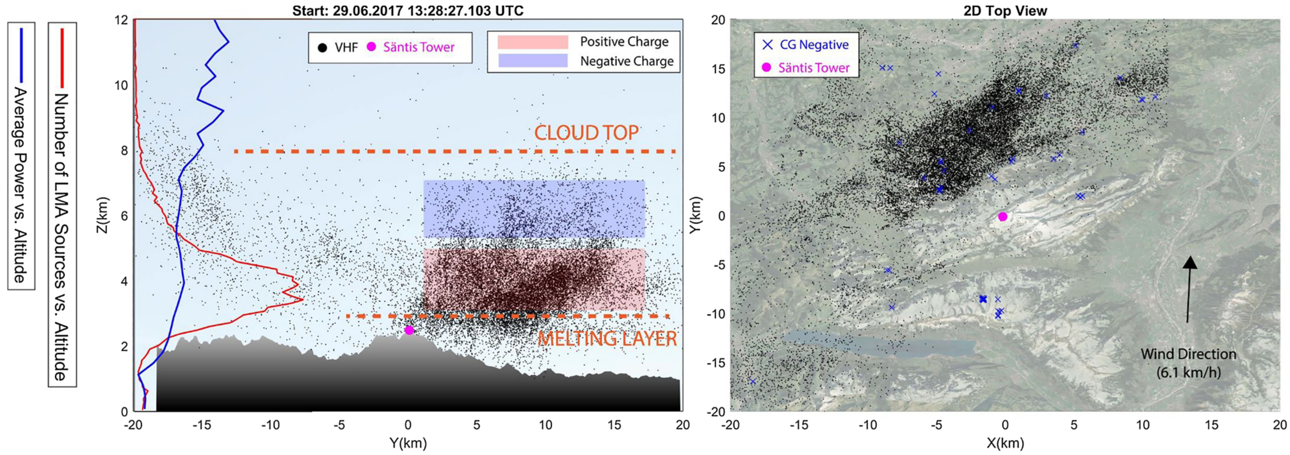

Fig. 12. VHF activity recorded by the LMA stations in the Säntis region over a 20-min time window starting 10 min prior to the initiation of an OT positive flash to the tower (29.06.2017 at 13:28:27 UTC). Left panel: 2D side view with histogram of LMA sources vs. altitude. Right panel: 2D top view. EUCLID recorded flashes are shown with crosses (blue for negative and red for positive). In the left panels, the negative and positive charge regions, inferred from the LMA source density, are shown, respectively, in blue and red. The position of the tower is shown with a purple marker.

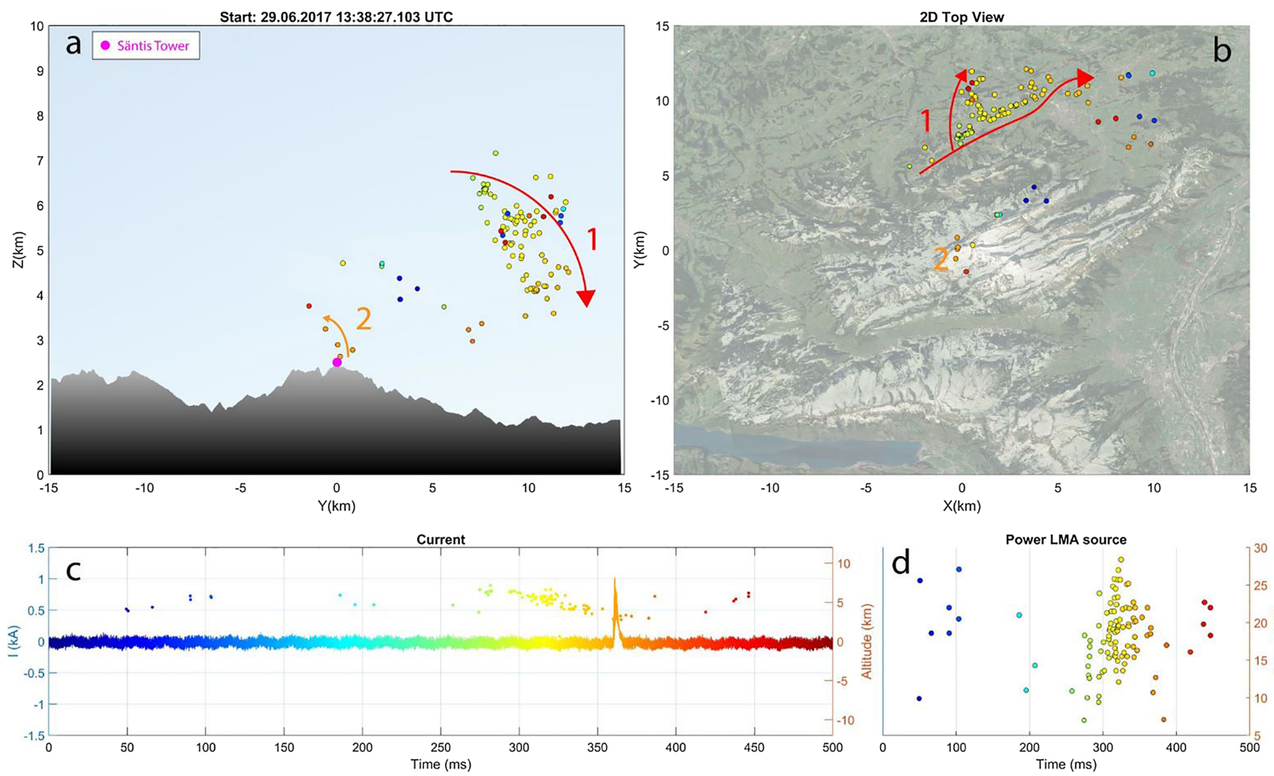

Fig. 13. Upward positive flash initiated from the Säntis Tower that occured on 29.06.2017 13:38:27 UTC recorded over the flash's whole duration. In the upper left panel, the location of the tower is shown with a purple marker and, in all of the panels, the LMA VHF sources are shown with time-color-coded circle markers. (a) 2D view Z vs. Y, (b) 2D view of X vs. Y, (c) current magnitude in logarithmic scale with superimposed VHF sources, (d) power vs. time for the VHF sources. Note that the colors were selected for better contrast and they bear no relation to the color-code used for timing. The colored arrows show the development of leaders.

structure consisted of a positive charge in the isothermal layer near the 0 °C, a main negative charge (~ 4 km/ − 5 °C) and a low density positive above (between − 10 °C and − 20 °C). This corresponds to the typical tripole charge structure [8]. The summary activity of the 20 analyzed flashes is shown in Table 1. The polarity row shows the polarity of charge transferred to ground.

5. Conclusions

We presented in this paper lightning current measurements and LMA data associated with upward flashes observed at the Säntis Tower during Summer 2017. The LMA network consisted of six stations located in the vicinity of the tower at distances ranging from 100 m to 11 km from it. We analyzed a total of 20 flashes that were simultaneously recorded by the current measurement system, fast electric field antenna, and LMA in the period from 29.06.2017 to 18.07.2017.

Based on the EUCLID lightning activity in an area within 30 km from the tower and in a 1-s time window before the start of the flash, only one of the 20 flashes was classified as OT. However, investigations based on the LMA data revealed that 3 more of the flashes were preceded by nearby activity. The results suggest that the number of OT flashes inferred from LLS data can be underestimated. The electric field measurements were available for three OT flashes and, in all of them, a preceding event can be observed. In the four observed OT flashes, the

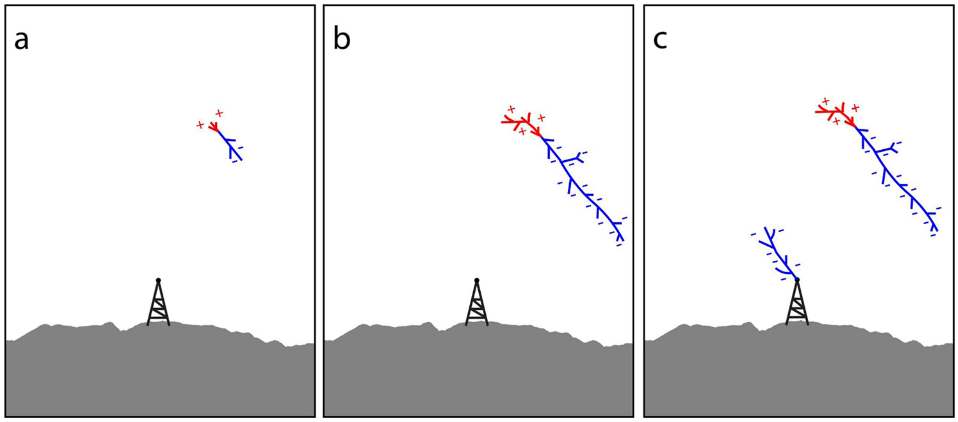

Fig. 14. Sketch of the positive flash initiated from the Säntis Tower recorded on 29.06.2017 at 13:28:27 UTC. View from the East. Not to scale.

events that preceded the tower flash either overlapped completely with the tower flash itself, or the delay between them was at most 100 ms.

We presented a detailed analysis of three OT flashes. The charge structure was inferred from the LMA measurements and the polarity of the leader from the horizontal speed of the leader and the current measurements at the tower. Simplified sketches for three OT flashes were presented. The OT flashes occurred during two different storms. The LMA activity, measured by the number of located sources, was, on average, almost seven times higher compared to that during the ST flashes.

Acknowledgments

This work was supported in part by the Swiss National Science Foundation (Project No. 200020_175594), the European Union's Horizon 2020 research and innovation program under grant agreement No 737033-LLR, the Spanish Ministry of Economy and the European Regional Development Fund (FEDER) ESP2015-69909-C5-5-R and ESP2017-86263-C4-2-R, and the European Union's Horizon 2020 research and innovation programme under the Marie Skłodowska-Curie grant agreement SAINT 722337.

Appendix A. Supplementary data

Supplementary material related to this article can be found, in the online version, at doi:https://doi.org/10.1016/j.epsr.2019.106067.

References

[1] A. Smorgonskiy, F. Rachidi, M. Rubinstein, G. Diendorfer, W. Schulz, On the proportion of upward flashes to lightning research towers, 2011 7th Asia-Pacific International Conference on Lightning (2011).
[2] D. Wang, N. Takagi, T. Watanabe, H. Sakurano, M. Hashimoto, Observed characteristics of upward leaders that are initiated from a windmill and its lightning protection tower, Geophys. Res. Lett. 35 (2008) 2008.
[3] A. Smorgonskiy, A. Tajalli, F. Rachidi, M. Rubinstein, G. Diendorfer, et al., An analysis of the initiation of upward flashes from tall towers with particular reference to Gaisberg and Säntis Towers, J. Atmos. Sol. Terr. Phys. 136 (2015) 46–51.
[4] H. Zhou, G. Diendorfer, R. Thottappillil, H. Pichler, M. Mair, The influence of meteorological conditions on upward lightning initiation at the Gaisberg Tower, 2014 International Conference on Lightning Protection (ICLP), Shanghai, China.
[5] A. Mostajabi, et al., On the impact of meteorological conditions on the initiation of upward lightning flashes from tall structures, 2018 34th International Conference on Lightning Protection (ICLP) (2018).
[6] F. Heidler, M. Manhardt, K. Stimper, Self-Initiated and Other-Triggered Positive Upward Lightning Measured at the Peissenberg Tower, Germany, paper presented at the 2014 International Conference on Lightning Protection (ICLP), 13-17 Oct, Shanghai, 2014.
[7] T. Warner, K. Cummins, R. Orville, Upward lightning observations from towers in Rapid City, South Dakota and comparison with National Lightning Detection Network data, 2004–2010, J. Geophys. Res. 117 (19) (2012).
[8] G.V. Cooray, The Lightning Flash IEE, Power & Energy Series, (2003).
[9] C. Schumann, M.M.F. Saba, T.A. Warner, M.A.S. Ferro, Upward flashes triggering mechanisms, 2017 International Symposium on Lightning Protection (XIV SIPDA), Natal, Brazil, 2nd–6th October, 2017.
[10] D.E. Proctor, A hyperbolic system for obtaining VHF radio pictures of lightning, J. Geophys. Res. 76 (February (6)) (1971) 1478–1489.
[11] D.E. Proctor, VHF radio pictures of cloud flashes, J. Geophys. Res. 86 (May (C5)) (1981) 4041.
[12] D.E. Proctor, R. Uytenbogaardt, B.M. Meredith, VHF radio pictures of lightning flashes to ground, J. Geophys. Res. 93 (October (D10)) (1988) 12683.
[13] B.R. Fuchs, et al., Environmental controls on storm intensity and charge structure in multiple regions of the continental United States, J. Geophys. Res. Atmos. 120 (July (13)) (2015) 6575–6596.
[14] E.W. McCaul, et al., Forecasting lightning threat using cloud-resolving model simulations, Weather Forecasting 24 (June (3)) (2009) 709–729.
[15] D.R. MacGorman, et al., TELEX the thunderstorm electrification and lightning experiment, Bull. Am. Meteorol. Soc. 89 (July (7)) (2008) 997–1013.
[16] W. Rison, R.J. Thomas, P.R. Krehbiel, T. Hamlin, J. Harlin, A GPS-based three-dimensional lightning mapping system: initial observations in central New Mexico, Geophys. Res. Lett. 26 (December (23)) (1999) 3573–3576.
[17] R.J. Thomas, et al., Accuracy of the lightning mapping array, J. Geophys. Res. 109 (July (D14)) (2004) D14207.
[18] A. Sunjerga, et al., On the classification of self-triggered versus othertriggered lightning flashes, 2018 34th International Conference on Lightning Protection (ICLP) (2018).
[19] C. Romero, et al., A system for the measurements of lightning currents at the Säntis Tower, Electr. Power Syst. Res. 82 (1) (2012) 34–43.
[20] C. Romero, F. Rachidi, M. Rubinstein, M. Paolone, Lightning currents measured on the Säntis Tower: a summary of the results obtained in 2010 and 2011, 2013 IEEE International Symposium on Electromagnetic Compatibility (2013) 825–828.
[21] M. Azadifar, M. Paolone, D. Pavanello, F. Rachidi, C. Romero, M. Rubinstein, An update on the instrumentation of the Säntis Tower in Switzerland for lightning current measurements and obtained results, CIGRE International Colloquium on Lightning and Power Systems (2014).
[22] C. Romero, F. Rachidi, M. Paolone, S. Member, Statistical distributions of lightning currents associated with upward negative flashes based on the data collected at the Säntis (EMC) Tower in 2010 and 2011, IEEE Trans. Power Deliv. 28 (3) (2013) 1804–1812.
[23] C. Romero, A. Mediano, A. Rubinstein, F. Rachidi, A. Rubinstein, M. Paolone, Measurement of lightning currents using a combination of Rogowski Coils and B-Dot Sensors, J. Light. Res. 4 (2012) 71–77.
[24] C. Romero, F. Rachidi, M. Rubinstein, M. Paolone, V.A. Rakov, D. Pavanello, Positive lightning flashes recorded on the Säntis Tower in 2010 and 2011, J. Geophys. Res. (2013) 12'879–12'892.
[25] D. Li, et al., On lightning electromagnetic field propagation along an irregular terrain, IEEE Trans. Electromagn. Compat. 58 (February (1)) (2016) 161–171.
[26] A. Mostajabi, et al., LMA observation of upward flashes at Säntis Tower: preliminary results, Joint IEEE International Symposium on Electromagnetic Compatibility & Asia-Pacific Symposium on Electromagnetic Compatibility (2018) 2–5.
[27] J. Figueras i Ventura, et al., Polarimetric radar characteristics of lightning initiation and propagating channels, Atmospheric Measurement Techniques Discussions, January, 2019, pp. 1–45.
[28] W. Schulz, G. Diendorfer, S. Pedeboy, D.R. Poelman, The European lightning location system EUCLID — part 1: performance analysis and validation, Nat. Hazards Earth Syst. Sci 16 (2016) 595–605.
[29] J.A. López, N. Pineda, J. Montanyà, O. van der Velde, F. Fabró, D. Romero, Spatiotemporal dimension of lightning flashes based on three-dimensional lightning mapping array, Atmos. Res. 197 (November) (2017) 255–264.
[30] A. Sunjerga, M. Rubinstein, G. Diendorfer, F. Rachidi, An analysis of the distribution of inter-flash time intervals in the area of the Säntis Tower, 2018 26th International Conference on Software, Telecommunications and Computer Networks (SoftCOM) (2018).
[31] C. Schumann et al., Analysis of the charge distribution and leaders inside the cloud for upward flash initiation 2018 25th ILDC an 7th ILMC Conference.
[32] J.T. Pilkey, et al., Rocket-triggered lightning propagation paths relative to

preceding natural lightning activity and inferred cloud charge, J. Geophys. Res. 119 (December (23)) (2014) p. 13,427-13,456.
[33] O.A. van der Velde, J. Montanyà, Asymmetries in bidirectional leader development of lightning flashes, J. Geophys. Res. 118 (December (24)) (2013) p. 13,504-13,519.
[34] V. Mazur, L.H. Ruhnke, T.A. Warner, R.E. Orville, Recoil leader formation and development, J. Electrostat. 71 (August (4)) (2013) 763–768.
[35] H.W. Kasemir, A contribution to the electrostatic theory of a lightning discharge, J. Geophys. Res. 65 (July (7)) (1960) 1873–1878.
[36] T.J. Schuur, S.A. Rutledge, Electrification of stratiform regions in mesoscale convective systems. part I: an observational comparison of symmetric and asymmetric MCSs, J. Atmos. Sci. 57 (July (13)) (2000) 1961–1982.
[37] W.D. Rust, R.J. Trapp, Initial balloon soundings of the electric field in winter nimbostratus clouds in the USA, Geophys. Res. Lett. 29 (October (20)) (2002) pp. 20-1-20–4.
[38] J. Montanyà, O. van der Velde, E.R. Williams, The start of lightning: evidence of bidirectional lightning initiation, Sci. Rep. 5 (October (1)) (2015).
[39] X. Qie, The lower positive charge center and its effect on lightning discharges on the Tibetan Plateau, Geophys. Res. Lett. 32 (5) (2005).
[40] N. Pineda, et al., Meteorological aspects of self-initiated upward lightning at the Säntis Tower (Switzerland), J. Geophys. Res.: Atmos. 124 (n.d.).

Paper III

ADVANCING EARTH AND SPACE SCIENCE

JGR Atmospheres

RESEARCH ARTICLE

10.1029/2021JD035238

Key Points:

- Recoil leaders main source of fast processes in negative lightning
- Recoil leaders initiate in bidirectional manner
- Mixed mode pulses connect directly to structure

Correspondence to:

A. Sunjerga,
antonio.sunjerga@epfl.ch

Citation:

Sunjerga, A., Rubinstein, M., Azadifar, M., Mostajabi, A., & Rachidi, F. (2021). Bidirectional recoil leaders in upward lightning flashes observed at the Säntis Tower. *Journal of Geophysical Research: Atmospheres*, *126*, e2021JD035238. https://doi.org/10.1029/2021JD035238

Received 13 MAY 2021
Accepted 23 AUG 2021

Author Contributions:

Conceptualization: Antonio Sunjerga, Farhad Rachidi
Data curation: Antonio Sunjerga, Mohammad Azadifar, Amirhossein Mostajabi, Farhad Rachidi
Formal analysis: Antonio Sunjerga, Farhad Rachidi
Funding acquisition: Marcos Rubinstein, Farhad Rachidi
Investigation: Antonio Sunjerga, Marcos Rubinstein
Methodology: Antonio Sunjerga, Marcos Rubinstein, Mohammad Azadifar
Project Administration: Marcos Rubinstein, Farhad Rachidi
Software: Antonio Sunjerga
Supervision: Marcos Rubinstein, Farhad Rachidi
Validation: Antonio Sunjerga
Visualization: Antonio Sunjerga
Writing – original draft: Antonio Sunjerga, Marcos Rubinstein, Farhad Rachidi

Bidirectional Recoil Leaders in Upward Lightning Flashes Observed at the Säntis Tower

Antonio Sunjerga[1], Marcos Rubinstein[2], Mohammad Azadifar[1], Amirhossein Mostajabi[1], and Farhad Rachidi[1]

[1]Electromagnetic Compatibility Laboratory, Swiss Federal Institute of Technology (EPFL), Lausanne, Switzerland,
[2]University of Applied Sciences of Western Switzerland (HES-SO), Yverdon-les-Bains, Switzerland

Abstract We report the observation of three negative upward flashes recorded by a high-speed camera at the Säntis Tower during the Summer of 2019. The camera was operating at 10,000 fps and an exposure time of 99 μs. Simultaneous measurements of the lightning current were obtained for all three flashes. The close electric field was measured for one of the observed flashes, which was analyzed in detail. In this flash, we observed 50 recoil leaders developing in the decayed channel with speeds characteristic of dart leader processes. Out of the 50 recoil leaders, 45 ended up as attempted leaders, three developed into M-component-type ICC (initial continuous current) processes, and two into return strokes. This study reveals that depending on the spatial and temporal properties of electric field in the area of the event and the main channel condition, recoil leaders can develop into different processes in upward negative lightning flashes such as attempted leaders, M-components, M-component-type ICC events, mixed mode pulses, or return strokes. We observed M-component-type ICC events with junction heights as low as 137 m, while all of the observed mixed mode pulses seemed to attach directly to the structure. Bidirectional propagation of the recoil leader was also observed.

1. Introduction

Upward lightning typically initiates from tall-grounded structures (greater than about 100 m) or from moderately tall structures (tens of meters) located in an elevated terrain. Understanding the mechanism of initiation of upward lightning is an important research topic because this type of lightning is predominant for tall structures such as telecommunications towers and wind turbines.

Several tall structures have been instrumented for lightning observations over the world (e.g., the Gaisberg, Peissenberg, Säntis, Skytree and CN towers). Measurements on these towers have led to reports on lightning current measurements (e.g., Diendorfer et al., 2009; Heidler et al., 2013; Hussein et al., 1995; and Romero et al., 2013; and Shinodo et al., 2014), electric field measurements (e.g., Azadifar et al., 2016; Heidler et al., 2013; and Zhou et al., 2015), and high-speed camera (HSC) observations (e.g., Mazur et al., 2013; Qie et al., 2017).

Different terms have been used to identify different processes in the lightning discharge, which are briefly summarized in what follows. In upward negative and downward negative lightning, one can observe subsequent return strokes (RSs) preceded by dart leaders (DLs) that propagate from the upper parts of the channel to the ground termination. If the DL stops before reaching the ground, the process is called an attempted leader (AL). Although no current is observed at the bottom of the channel in ALs, they do produce electric field changes that are known as K changes or K-events (Kitagawa & Brook, 1960). Note that a K-event can occur both in cloud-to-ground and in cloud lightning. M components occur when a floating leader connects to the upper part of the conducting channel created by the previous RS. Additionally, mixed mode (MM) pulses and M-component-type initial continuous current (ICC) pulses occur only in upward lightning (He et al., 2018; Zhou et al., 2015). These two types of pulses exhibit similarities, respectively, with the main pulse in the RS process and with the pulses that characterize the M component process, the main difference being that MM and M-component-type ICC (M-ICC) pulses occur during the ICC phase in upward negative lightning. Zhou et al. (2015) defined "mixed mode of charge transfer to ground" as an occurrence of RS like process in one of the branches of the UPL, while the channel is still conducting the ICC current. The corresponding pulse superimposed on the ICC current is called an MM pulse.

Writing – review & editing: Antonio Sunjerga, Marcos Rubinstein, Mohammad Azadifar, Amirhossein Mostajabi, Farhad Rachidi

Using an interferometer system, Shao et al. (1995) showed that RSs, M components, and ALs can be considered to belong to a single class of processes that start some distance beyond the flash origin (therefore extending the channel) and travel toward the main channel. The only difference between the M components and the RSs is that, in the case of RSs, the floating leader connects to a decayed main channel and reaches the ground (DL), while in M components, the floating leader connects to a conducting channel carrying a continuing or continuous current. The third and last member of the class, ALs, occur in the same manner as DLs but they stop before reaching the ground (Cooray, 2014, page 121). The observations of Shao et al. (1995) were confirmed by Mazur (2002), Mazur and Ruhnke (2011), and Mazur et al. (2013), who also attributed the same origin for these different phenomena further observing that floating leader was recoil leader (RL).

RLs are self-propagating discharges, moving along a previously ionized channel (Mazur, 2002) that occur in decayed positive leaders (as observed by means of lightning mapping arrays). They are thought to be the cause of K-changes (Mazur et al., 2013). Saba et al. (2008) made the first observation of recoil leaders with a high-speed camera.

It was suggested and observed (Mazur, 2002; Mazur & Ruhnke, 2011; Mazur et al., 2013) that these RLs occur in a bidirectional manner similar to observations in in-cloud lightning discharges and downward stepped leaders (Kasemir, 1950; Mazur & Ruhnke, 1993). The negative end of the RL travels toward the origin, which can be either a grounded structure or a branching point while the positive end propagates in the opposite direction outward and possibly extending the channel through virgin air propagation (Warner et al., 2016). Mazur (2002) argued that unidirectional propagation observed by lightning mapping array (LMA) systems is due to the fact that the negative leader radiates much more in the relevant frequency range of LMA systems (VHF) than the positive, and these systems are not able to measure both positive and negative leaders at the same time.

In later studies, a series of HSC observations of bidirectional RLs have been reported. Bidirectional RLs have been observed by Kotovsky et al. (2019) in rocket-triggered lightning during an M component event. They have also been observed to occur in ALs in both tower-initiated lightning (Jiang et al., 2014) and rocket-triggered lightning (Qie et al., 2017). Wu et al. (2019) and Zhu et al. (2019) observed bidirectional propagation in the DL phase of a tower-initiated upward flash preceding the RS phase. Warner et al. (2012) reported one of the biggest HSC data sets of upward lightning recording 81 upward flashes during a period of 6 years from 10 different towers. Bidirectional propagation was unambiguously observed both in RLs connecting to the conducting main channel and directly to the towers. Unfortunately, due to the lack of current measurements, it is not possible to distinguish MM and M-ICC pulses. Furthermore, the authors did not report that any of the RLs reaching either the conducting main channel or the tower tip occurred while some other upward branch was active suggesting that all RLs connecting to the conducting main channel are either M-ICC or M-component-type pulses. Zhou et al., 2015 using HSC observations and current measurements observed a difference in the junction height between M-ICC or M-component-type pulses. However, their relatively high exposure time of 2 ms did not allow to observe the RL mechanism.

Using an interferometer, Yoshida et al. (2012) observed that AL can be started both by RLs in the decayed branches and by virgin air breakdown (propagating toward the pre-existing channel). Later, Warner et al. (2016) observed that AL initiated in virgin air starts in a similar way as AL caused by RL with bidirectional propagation.

In this paper, we report simultaneous measurements of current, close electric field and HSC images for three upward negative flashes initiated from the Säntis Tower in Switzerland. The close-range electric field was only measured in one of the flashes, which we analyze in detail. We observed parts of the upward positive leader (UPL) propagation during the ICC phase that reveal different processes that started as RLs. The aim of the present study is to identify and analyze the role of RLs in upward negative flashes using HSC observations, simultaneously with lightning current and electric field measurements.

The rest of this paper is organized as follows. In Section 2, we briefly describe the Säntis Tower facility and the measurement sensors. The obtained data for the considered flashes are presented in Section 3. Section 4 is devoted to the analysis of the observed RLs and their role in the various processes in upward negative

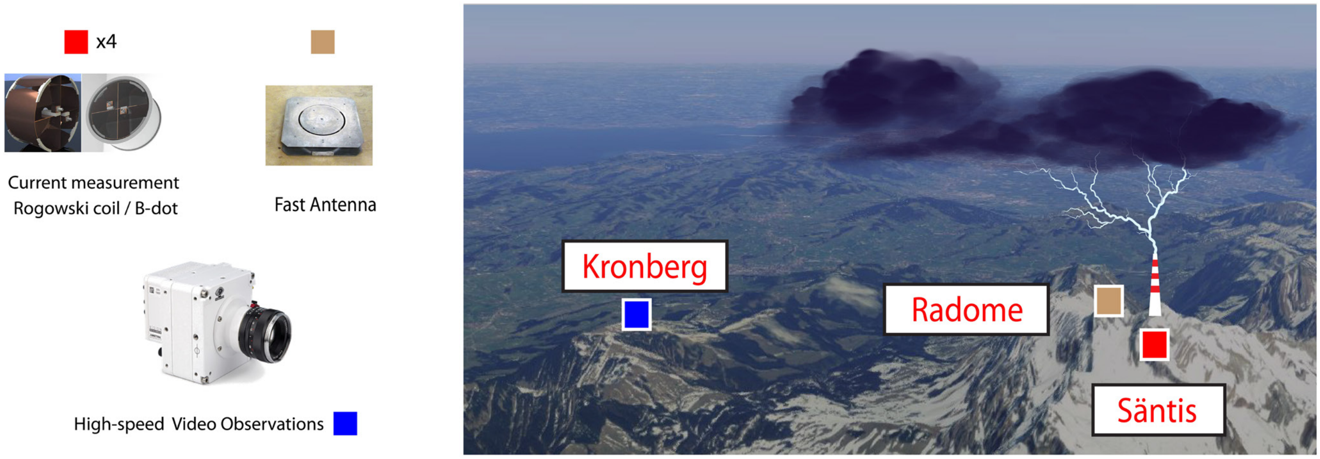

Figure 1. Sketch of location of the tower, close electric field station and high-speed camera (HSC). Not to scale.

flashes. The observed bidirectional propagation in three RLs is discussed in Section 5. The paper ends with a general discussion (Section 6) and concluding remarks (Section 7).

2. Measurement Setup

The 124-m tall Säntis Tower, located in the Northeastern part of Switzerland, is by far the most frequently struck structure in Switzerland (Romero et al., 2012). The tower has been instrumented for current measurements since May 2010. Throughout the years, the station has been upgraded and enhanced with electromagnetic field and optical measurement systems. More details about the station and its instrumentation can be found in (Azadifar et al., 2014; Romero et al., 2010, 2012). Locations of the equipment used in this study can be seen in Figure 1.

A wideband Mélopée electric field sensor, purchased from the now-defunct company Thomson-CSF, was installed and connected to a digitizer with 5 MS/s sampling rate during the Summer of 2018 (some information on the sensor can be found in Li et al., 2016). The sensor was installed about 23 m away from the tower in the radome (structural, weatherproof enclosure transparent for electromagnetic waves) building next to the tower used commercially for broadcasting signals in different bandwidths. The estimated time constant of the sensor is about 20 μs, which as explained later in Section 3, was compensated to 400 μs. The electric field antenna does not have GPS time synchronization and its output was manually aligned with the current measurements. Note that the electric field measurements are to some extent affected by the shadowing effect of the tower (Smorgonskiy et al., 2015). An evaluation of this effect is beyond the scope of this paper.

A Phantom VEO 710L HSC is installed on the Kronberg mountain about 5 km away from the tower. The camera can record up to 1,000,000 FPS at its lowest resolution of 8 × 8 pixels. To have a wider view of 512 × 512 pixels, the number of frames per second has been reduced to 10,000. These pixels are distributed over a view of about 1,700 m by 1,700 m in the plane of the tower, perpendicular to the view with a resolution of about 3.4 m per pixel. The camera records during a 3-s time window with a pretrigger delay of 1.5 s. A GPS time stamp is provided by an Acutime 360 Multi-GNSS Smart Antenna. However, it was not operational at the time of the observed flashes, so that the time synchronization was obtained manually.

During 2019, only three negative flashes could be observed with the HSC, all of the other flashes to the tower having been obscured by the clouds. The first flash, referred to as Flash #1 in this work, occurred on July 18, 2019 at 17:58 UTC. The second, Flash #2, occurred the day after, on July 19, 2019 at 21:01 UTC, followed about 4 min later by the third, Flash #3, at 21:05 UTC. For all three flashes, the system recorded the current. The electric field was obtained only for Flash #3, which will be analyzed in detail in this study.

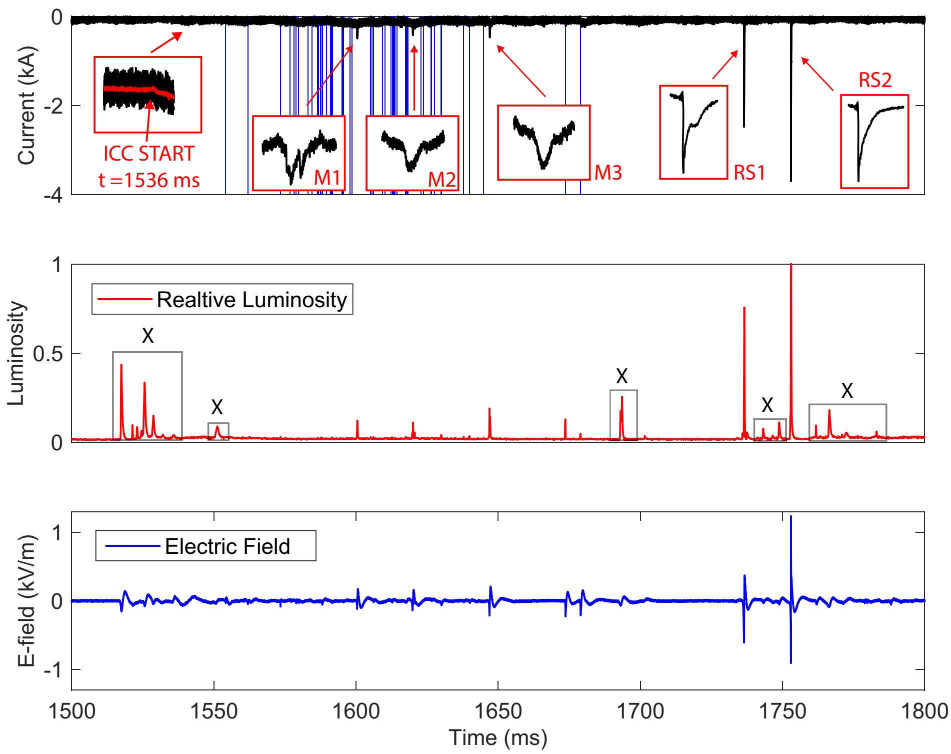

Figure 2. Measured waveforms for the duration of the whole Flash#3. Top: Current waveform. Blue vertical lines indicate attempted leaders (ALs) observed on the high-speed camera (HSC). Middle: Relative luminosity of each frame with distant events shown in gray boxes and marked with the letter X. Bottom: Electric field measured at a distance of 23 m with the fast antenna (atmospheric sign convention). Note that the start of the initial continuous current (ICC), marked with the red line in the top subplot, was determined by filtering the current waveform (lowpass 1 kHz and band-stop 50 Hz filter).

3. Summary of Obtained Data for Flash #3

Figure 2 presents the simultaneously measured waveforms for Flash #3. The time is relative to the start of the record. The upper plot presents the current waveform measured with the Rogowski coil at 24 m above the tower base, the middle plot presents the sum of luminosity of all pixels in relative units versus time measured by the camera and, finally, in the bottom plot we can observe the electric field measured by the fast antenna 23 m away from the tower. As mentioned in Section 2, the amplitude of the electric field measurements is affected by the shadowing effect of the nearby tower (Smorgonskiy et al., 2015).

During the flash, we recorded 50 RLs. Forty five out of the 50 ended up as ALs as they did not reach the ground, three developed into M-ICC processes, and two into RSs. The times of initiation of ALs are indicated with blue lines in the top subplot of Figure 2. The luminosity of the channel is shown in the middle subplot where events that are not directly related to the tower flash (either cloud or nearby lightning) are framed in a gray box and marked with the letter X.

Figure 3 presents selected frames from the Flash #3 and simultaneous measurements of the current and the electric field. In the electric field plots, the black line represents original waveforms obtained from the fast antenna with a 20 μs decay time constant. Since the decay time is in the same order of magnitude of the recorded events, we also present, in red, the waveform compensated to a decay time constant of 400 μs, centered at the timestamp of each frame, based on the method proposed by Rubinstein et al. (2012). Note that the vertical scale in the compensated electric field waveforms is bigger than the scale in the uncompensated ones; as a result, the fast changes are less discernible. The red shaded time intervals in the field plots are 160 μs wide and they represent a 99 μs exposure of each frame and an extra 61 μs estimated uncertainty due to the manual time synchronization. The red vertical segment in the bottom of the frames represents

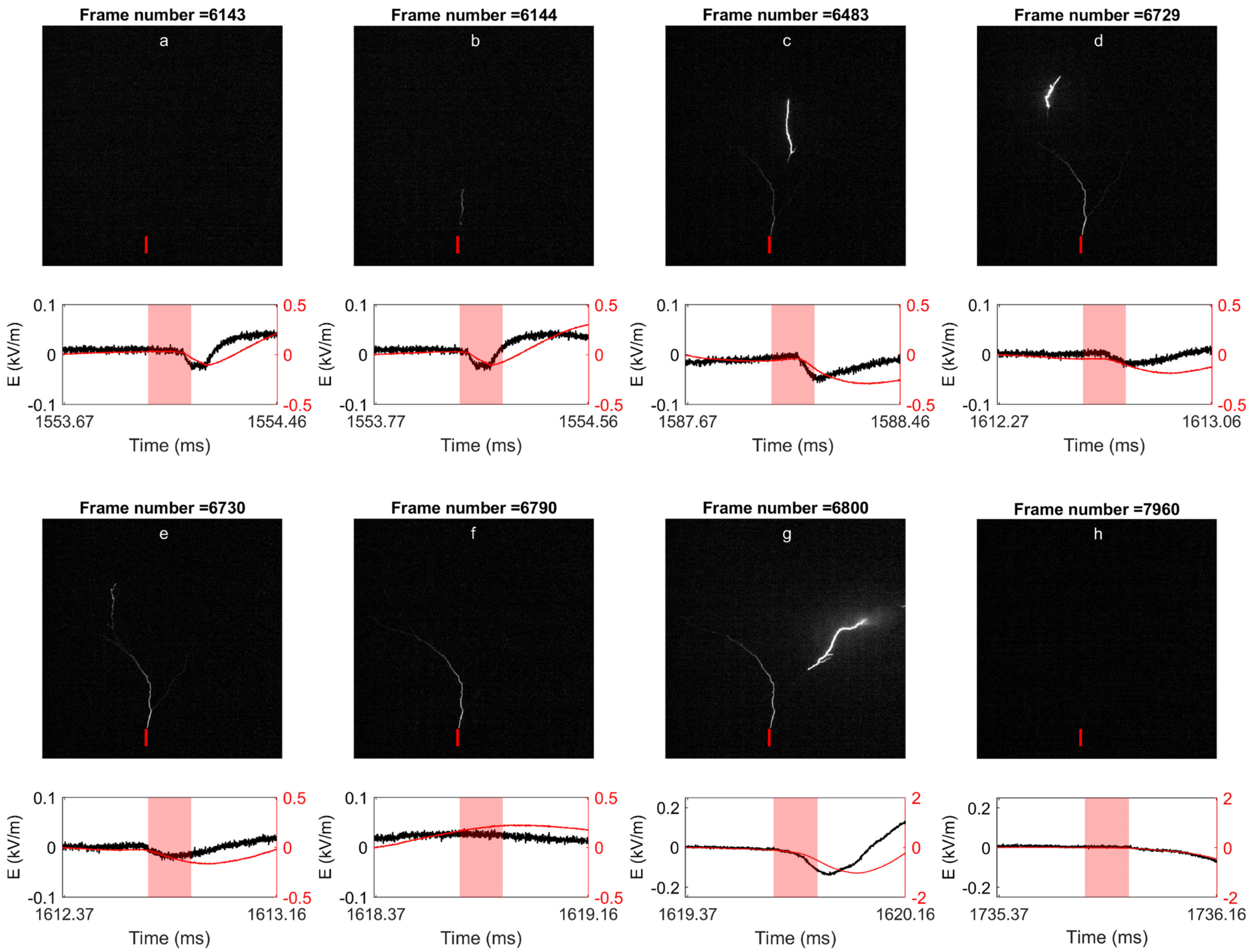

Figure 3. Selected high-speed camera (HSC) frames for the upward negative Flash #3 (top panels). The associated electric field changes at 23 m are shown in the respective bottom panels. The red shaded time intervals in the field plots are 160 µs wide and they represent a 99 µs exposure of each frame and an extra 61 µs estimated uncertainty due to the manual time synchronization. The red vertical segment in the bottom of the frames represent the 124-m tall Säntis Tower. The black line represents waveforms obtained from the fast antenna with a 20 µs decay time and the red line is the waveform compensated to a decay time of 400 µs centered at the timestamp of each frame based on the method proposed by Rubinstein et al. (2012).

the 124-m tall Säntis Tower. The above description is valid for all the following figures presenting multiple HSC frames.

The ICC current started somewhere after the time 1,536 ms. A slight intensification of the luminosity, probably due to nearby lightning, was observed at about 1,551 ms. The first RL was recorded at time 1,554 ms (see Figure 3b), before which (Figure 3a) we were not able to observe the propagation of the upward positive leader due to low luminosity. Only after the first RL, was the UPL channel heated, making it visible in subsequent frames. At later times, the UPL channel was extending and, since it was heated by RLs, the ICC current and M-component type processes, some part of it remained continuously visible as shown in Figures 3c–3h. Most of the RLs lasted less than the duration of one frame (99 µs). In Figure 3g, we can observe the start of an M-ICC event (M1) illuminating the channel on the right side of the frame.

The ICC channel decayed at about 1,736 ms (as shown in Figure 3h) when the RS1 (see Figure 2) was initiated. At that time, the first subsequent RS occurred and its channel decayed about 15 ms later. The RS1 channel was barely visible when the following subsequent RS2 (see Figure 2) was initiated. About 10 ms later, the channel was no longer visible and some distant activity followed. In Figure 4, we present the time-integrated image for the duration of the whole flash. The first branching of the channel occurs at a

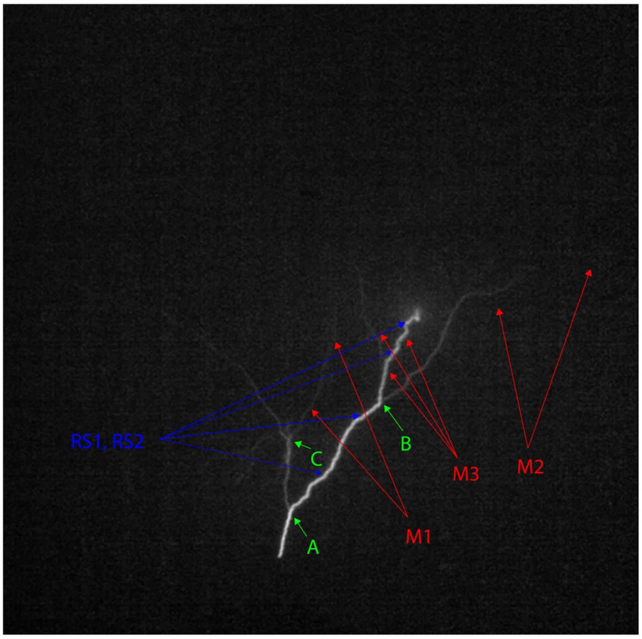

Figure 4. Time integrated image for the duration of whole Flash#3 (Altitudes of branching points: A 137 m, B 422 m, and C 325 m). Channels that were involved in each one of the RSs (RS1 and RS2) and M components (M1, M2, and M3) are pointed to with arrows.

height of about 137 m above the tower tip (labeled A in Figure 4). Note that, as previously observed in the literature (Krehbiel et al., 1979), for each subsequent stroke, the lightning leaders will propagate further away than the preceding leader. In this specific case, since the flash had only two RSs, most of the processes were located in the view of the camera (about 1,700 × 1,700 m). A similar behavior was observed at the Säntis Tower by LMA observations (Sunjerga et al., 2020).

4. Recoil Leaders

In this section, we discuss the RLs observed in Flash #3. These RLs can be classified as different transient events: (a) ALs, (b) M-ICC pulses, or (c) DLs, based on whether they reached the ground or if they attached to the conducting channel. We have also observed classical M components and MM pulses in two other flashes data provided in the supplementary material in Sunjerga, Rachidi, and Rubinstein (2021) that are not analyzed here in detail. It is worth noting that, in the literature, these different transient events could be either due to a RL propagating along a previously ionized channel (e.g., Mazur et al., 2013) or due to a newly ionized channel (Warner et al., 2016; Yoshida et al., 2012); however, all of the events observed in our three flashes were due to RLs. We classify them as RLs based on the fact that they all develop with speeds characteristic of propagation along a previously ionized channel while, additionally, for most of them, we can observe from camera frames that they propagate indeed along a previously ionized channel. It is worth noting that our measurements could be somehow biased by the fact that, in some cases, leaders extend out of the camera view or they are obscured by the clouds.

4.1. Attempted Leaders

Figure 5 presents four representative samples of ALs that occurred during the flash by order of occurrence. The associated electric field changes at 23 m are also shown. We can observe that the electric field is strongest in the first event shown in Figure 5a since the leader is close to the tower. The leaders in Figures 5a and 5c are much brighter compared to those in Figures 5b and 5d.

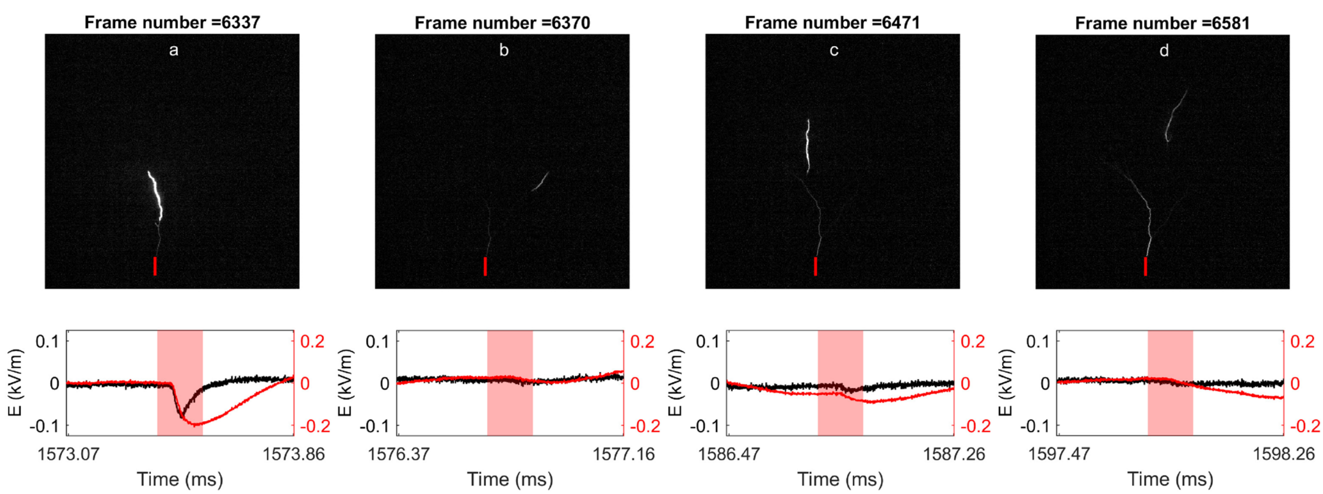

Figure 5. Video frames of representative samples of attempted leaders (ALs) and the electric field at 23 m. See more detailed description of subplots in the caption of Figure 3.

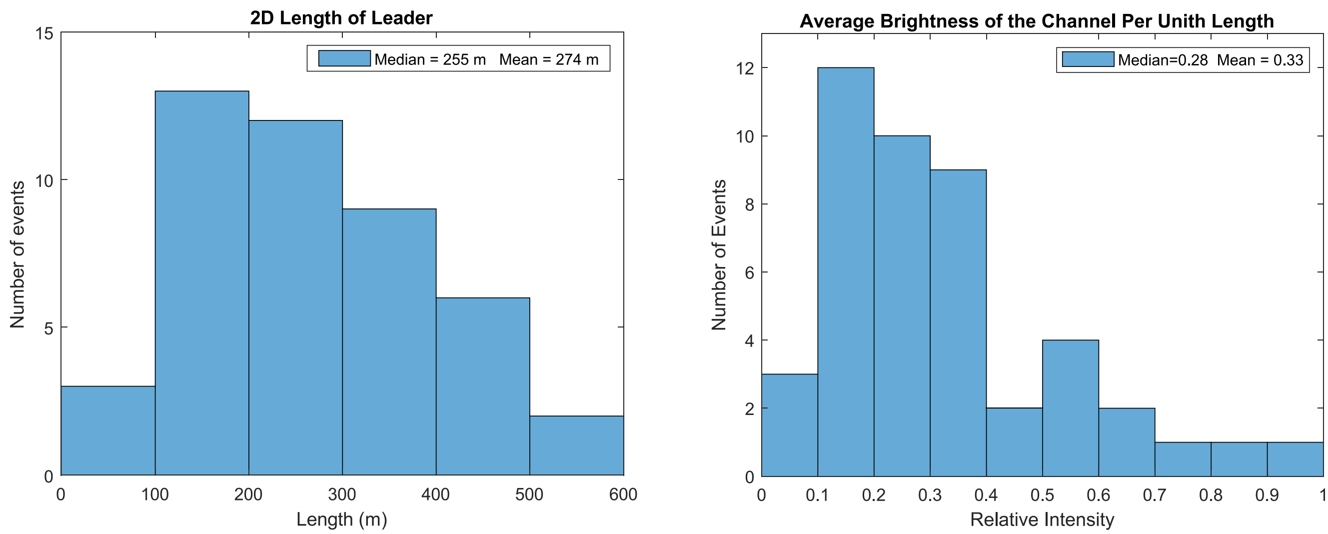

Figure 6. Attempted leaders (ALs) histograms. (a) Length of the leader (b) Average brightness of the channel per unit length.

Most of the ALs were visible only in one frame and the 2D-inferred length was typically in the range of 100–500 m as shown in Figure 6a. The propagation speed of the leaders could not be accurately estimated because of the limited number of frames. The observations allow only to conclude that the speed is at least higher than 10^6 m/s, probably in the range of about 10^7 m/s, which is typically the speed of leaders reactivating decayed channels (e.g., Qie et al., 2017). The median 2D length of the ALs was about 255 m. In the later stages of the flash, five of the ALs were characterized by longer lengths than reported here since the leaders extended beyond the camera view. The reported lengths may be further underestimated because of the possible clouds obscuring the view.

Figure 6b presents the histogram of average light brightness per unit length of each event. The average brightness per unit length is calculated by taking, for each horizontal line containing the leader, the brightest pixel. We then averaged the pixel intensities along the 2D leader length and divided it by the 2D leader length. The calculated average brightness per unit length shows a wide spread: the brightest observed leaders are about 14 times brighter than the darkest ones.

The Pearson correlation coefficient ($R = 0.5025$) with statistical significance ($P = 0.0004$) indicates some positive correlation between the length of the leader and the average brightness per unit length. The longer the leader, the brighter it is. The length of the RL as well as its brightness could depend on multiple parameters such as the conditions in the decayed channel, and the spatial and temporal distribution of the total electric field.

4.2. M-Component-Type ICC Pulses

In this section, we discuss three M-ICC events. All three were characterized by a relatively low-peak current (about 500 A). The first event is shown in Figure 7. It started with two RLs as seen in Figure 7c, one of them reached in Figure 7d the branching point C (see Figure 4). The total electric field in this case is the sum of the contributions from the downward propagating negative charge due to the first RL and, once it connects to the channel, from the M-ICC pulse. The stationary point of the compensated electric field (shown with a red arrow in Figure 7e) occurs when the contribution in the electric field change at location of measurements of the positive charge supplied by the tower to the channel becomes higher than the contribution due to the negative charge flowing downward from the charge sources in the cloud. After the RL attached the channel and initiated an M-ICC event, the luminosity intensified across the whole channel (Figure 7e), presumably due to the M-ICC pulse propagation. Another RL connected to the visible channel in the upper part of Figure 7e that caused another subpeak and another M-ICC pulse in the current waveform.

10.1029/2021JD035238

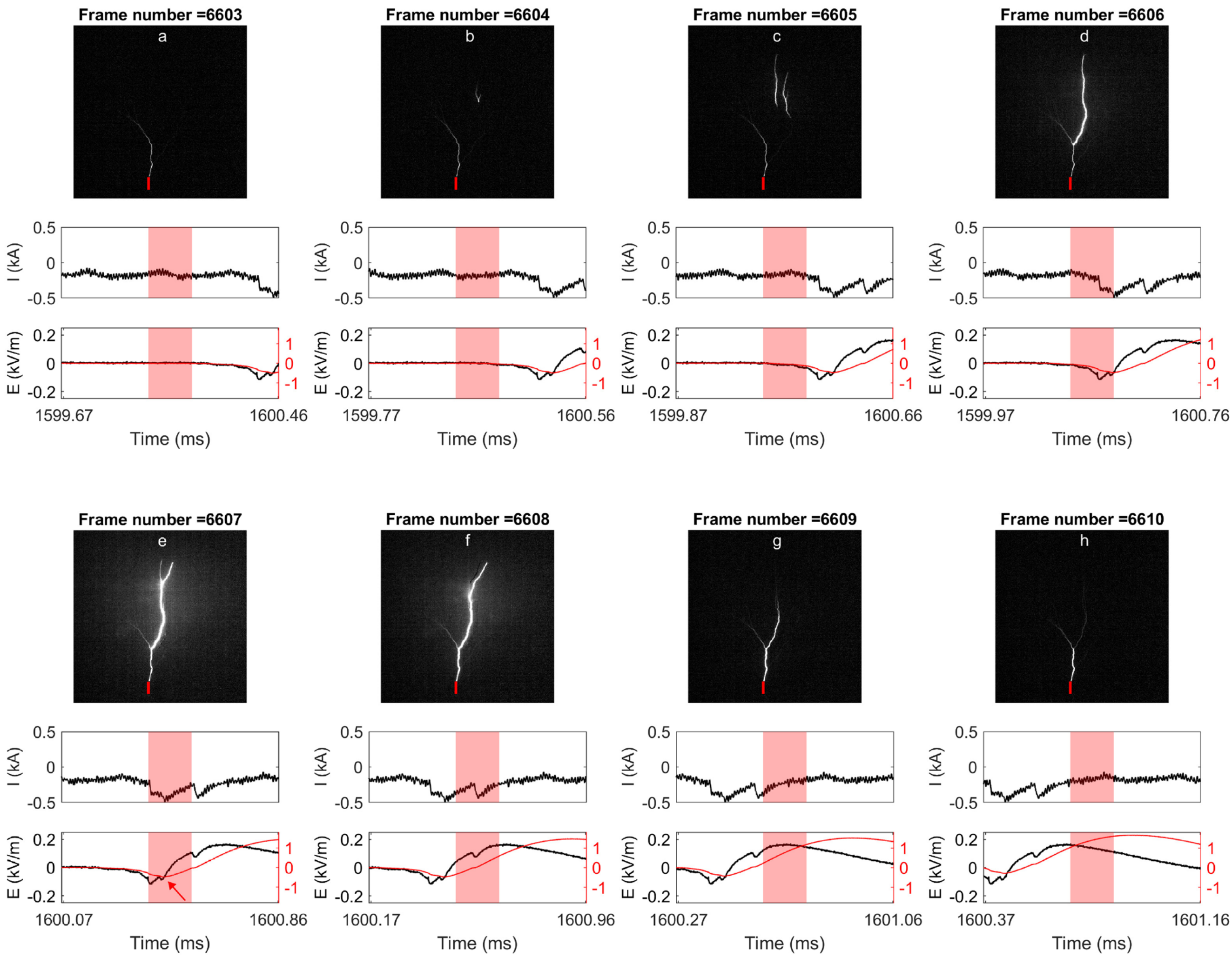

Figure 7. The first M-initial continuous current (ICC) pulse in Flash #3. In parts (a) through (h), frames from the HSC are shown at the top, the current waveform plot in the middle and the electric field plot at the bottom. See more detailed description of subplots in the caption of Figure 3.

The second M-ICC event, shown in Figure 8, occurred about 20 ms later. The initiation of the RL is discernible on the right-hand side of the video frame in Figure 8b. The RL extended further in Figure 8c. In the next frame (Figure 8d), the RL was not propagating further, even though the luminosity of the decayed channel just below the RL slightly increased (it is possible that the propagation occurred during the last few microseconds of the exposure time of this frame). In the following frame, Figure 8e, the RL attached to the channel and a current was measured at the tower.

The third and last M-ICC event occurred about 25 ms after the second one. The start of the RL can be observed as a bright spot in Figure 9b. It further extended in the next frame (Figure 9c) and connected to the branching point B as shown in Figure 9d. The 2D speed of the leader between the frames in Figures 9b and Figure 9(c) is estimated to be 1.8×10^6 m/s.

In these three events, we can observe the following mechanism. First, due to the electric field, the RL is initiated in the decayed channel creating negative charge density in the lower part of the leader. When this RL connects to the conducting channel, the M-ICC event is initiated, and it propagates down the conducting channel. Once the M-ICC event reaches the tower tip, the whole channel becomes highly conductive and a pulse superimposed on the ICC current can be observed at the tower. The low current peaks in these three cases can be due to the small length of these RLs (Cooray et al., 2020). There is no clear relation between the current risetime (about 60 μs for all the three events) and the junction height (137, 325, and 422 m).

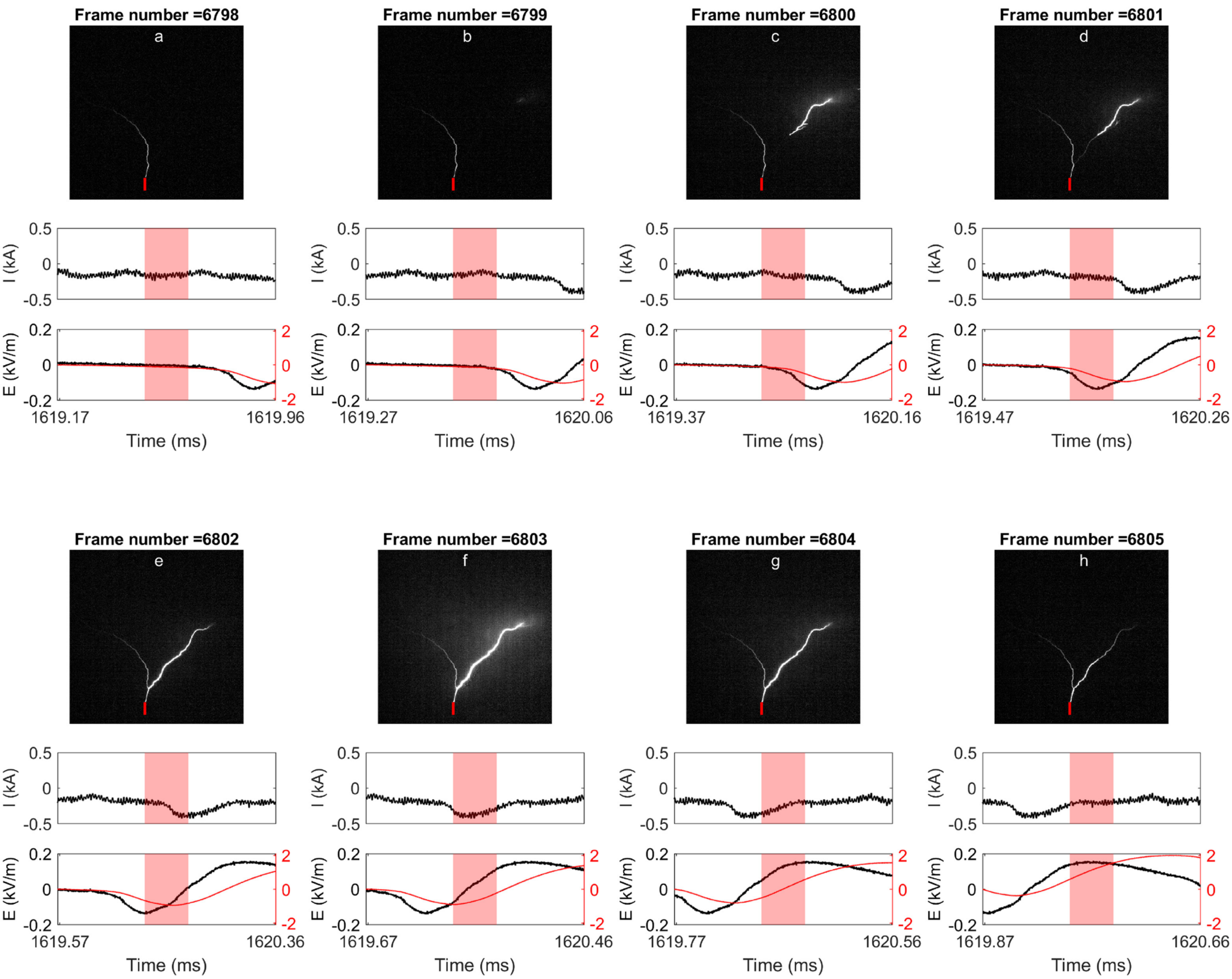

Figure 8. The second M-initial continuous current (ICC) pulse. See description of subplots in the captions of Figures 3 and 7.

Zhou et al. (2015) observed that: "When the connection point is a kilometer or more above the tower top (inside the cloud), the M-component mode takes place, and if it is very close to the tower top (say, 10 m), the mixed mode (involving two channels below the cloud base) is likely." Note that in the case of the Säntis and Gaisberg towers (Zhou et al., 2015), due to the high altitude above sea level of the mountains on which the towers are constructed, thunderclouds are frequently very close to the structure.

All three M-ICC events observed in Flash#3 connected to the channel at a relatively low altitude of a few hundred meters, in one case less than 150 m above the tower tip (137 m), providing evidence that the junction point of M-ICC events can be significantly lower than the 1-km threshold suggested by Zhou et al. (2015).

On the other hand, in agreement with Zhou et al. (2015), we observed in Flash #2 (data in supplementary material, Sunjerga, Rachidi, & Rubinstein, 2021) that RLs associated with MM pulses connected either directly to the structure top, or to the conducting channel only a few meters above the tower tip (the resolution of the observation system does not allow a clear distinction).

Also, it is worth noting that, in the three observed cases, we clearly see that the channel branch above the junction point is much brighter and thicker (similar to RSs, but less bright) than the lower part of the channel (below the junction point), which is consistent with the M-component model proposed by Azadifar

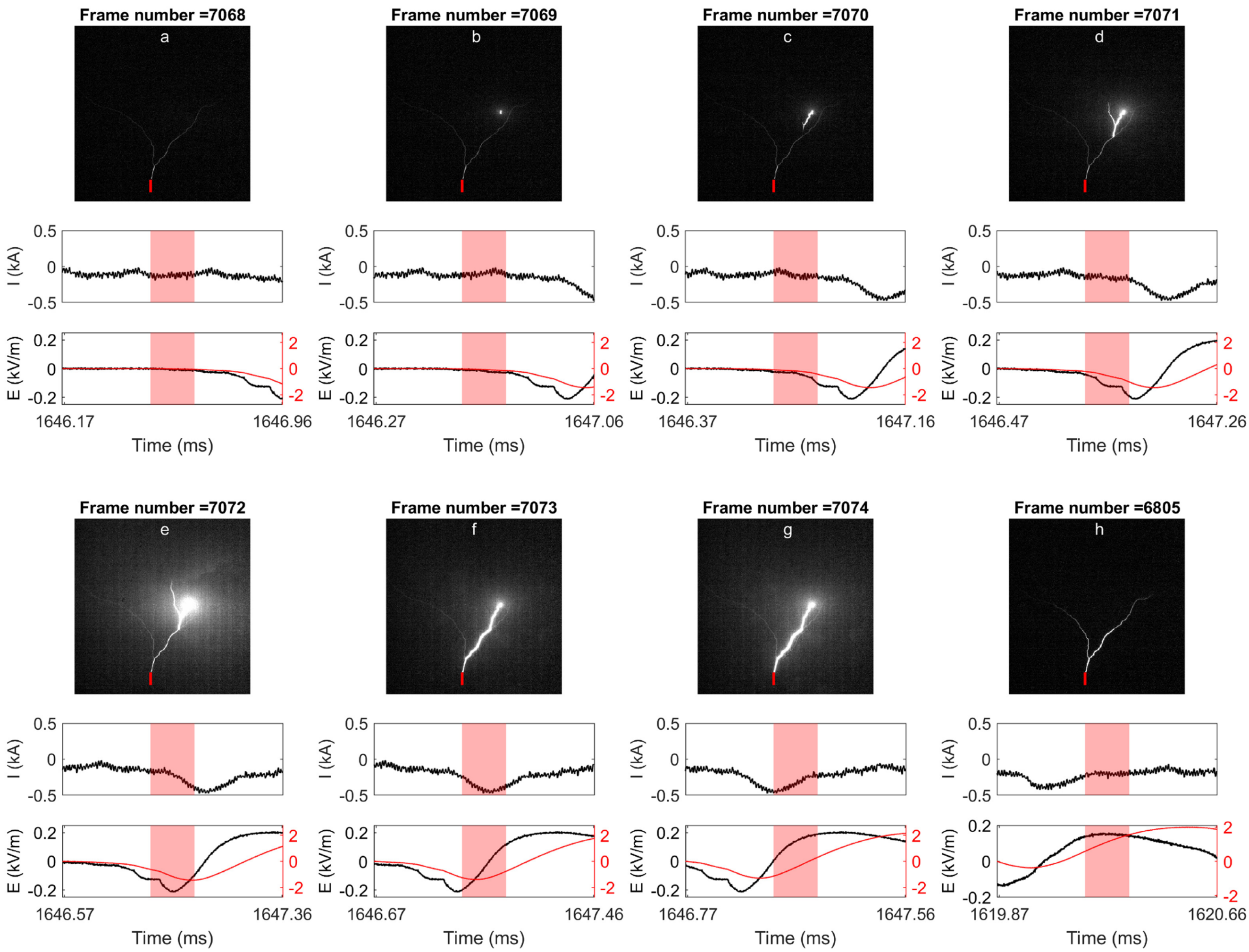

Figure 9. The third M-initial continuous current (ICC) pulse. See description of subplots in the captions of Figures 3 and 7.

et al. (2019). Note that three observed events have relatively low current peaks, which could explain the lower brightness.

4.3. Dart Leaders

In this section, we discuss two RSs belonging to Flash #3, which occurred after the extinction of the ICC. The observed images, current and electric field waveforms for the first are shown in Figure 10. Figure 10a shows the start of a RL. Since it was relatively slow, we were able to estimate the average 2D speed for Figure 10b frame to be 6.55×10^6 m/s. The peak value of the current is only about 2.5 kA with a risetime of about 3.7 μs. The characteristic asymmetrical V-shape (Rubinstein et al., 1995) can be seen in the uncompensated waveform, the bottom of which corresponds to the start of the RS.

The second RS was initiated about 15 ms after the previous one and it is shown in Figure 11. In Figure 11a, we can observe some in-cloud activity, which was not sensed by the E-field sensor. In the following frames, the RL reached the tower, initiating the RS. Distant activity can still be observed in Figure 11e–11f. The peak value of the current is about 3.7 kA with a risetime of about 4 μs.

In both cases, the initiation point is stationary and there is no observed upward extension even after the RS phase. However, one can again observe in both cases (see Figures 10d and 11e) that in the area around the initiation point, the light is highly dispersed, presumably indicating the presence of clouds.

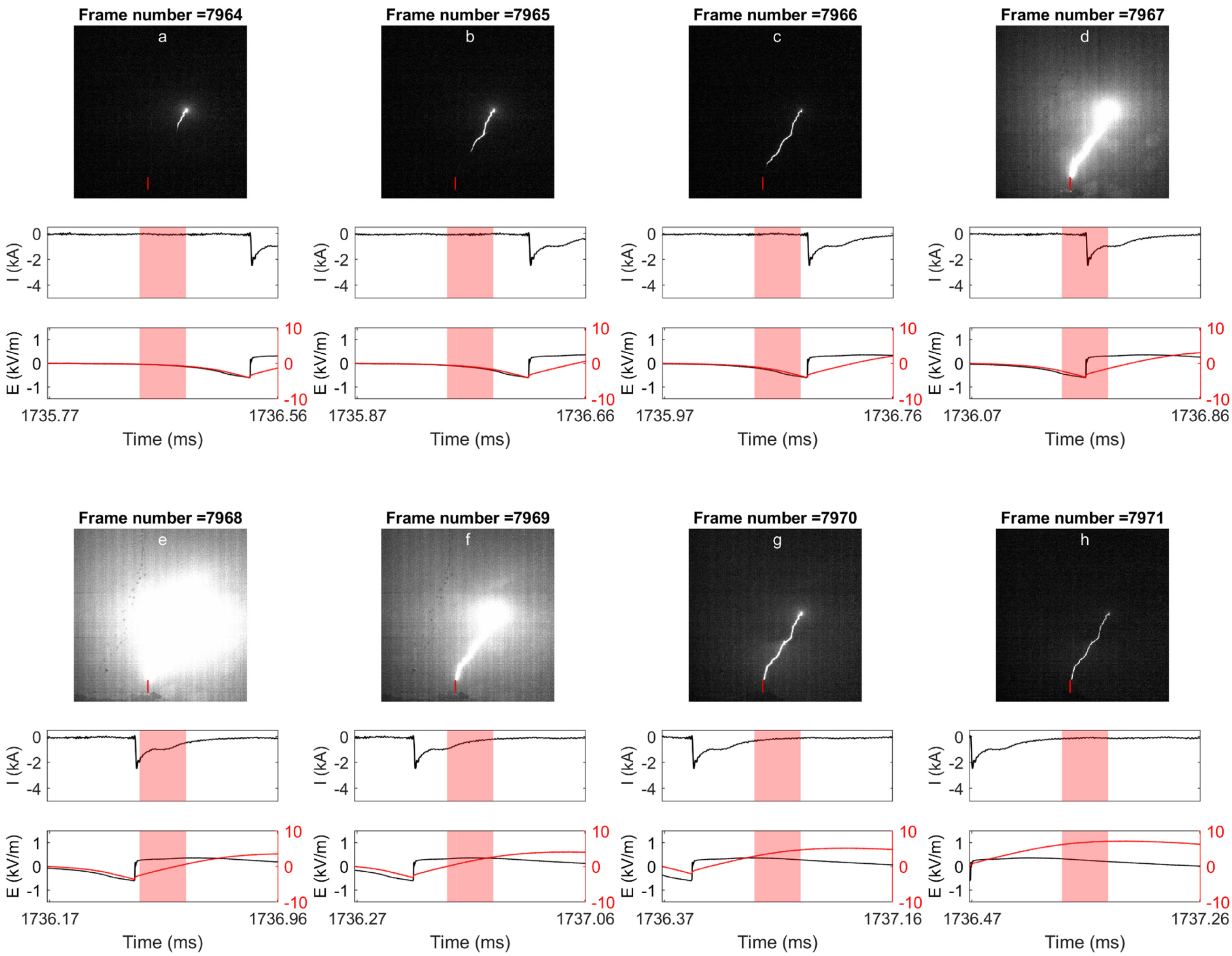

Figure 10. First return stroke (RS) event. See description of subplots in the captions of Figures 3 and 7.

4.4. Comparison of the Recoil Leader Luminosity Brightness in Different Phenomena

In Figure 12, we present the average luminosity brightness per unit length of all RLs for the observed ALs, M-ICC events and RSs. We can observe that M-ICC events and RSs are initiated by bright RLs. One of the M-ICC RLs had a relatively low luminosity. However, in this case, we had two RLs at the same time as can be seen in Figure 7c. We could expect brighter RLs to be initiated in the case of a stronger electric field. It is reasonable to assume that a stronger field would also result in a longer RL and, therefore, a higher probability of reaching the ground. A strong field could also initiate more than one RL at the same time, as in the case of Figure 7c.

5. Bidirectional Recoil Leader Propagation

We have not observed any bidirectional propagation in the analyzed RLs of Flash #3. This can be explained by the fact that our FPS rate (10 k) was smaller than that of Mazur et al. (2013) (54 k). In most cases, we had only one frame for the whole RL. Even in the cases for which we did have more than one frame, it is also possible that the positive end was no longer propagating after the first frame. It was indeed observed in Mazur et al. (2013) (see Figure 4) and (Wu et al., 2019) that, in the beginning, the positive end was propagating slower than the negative, and after some time, the positive leader seems to cease to propagate.

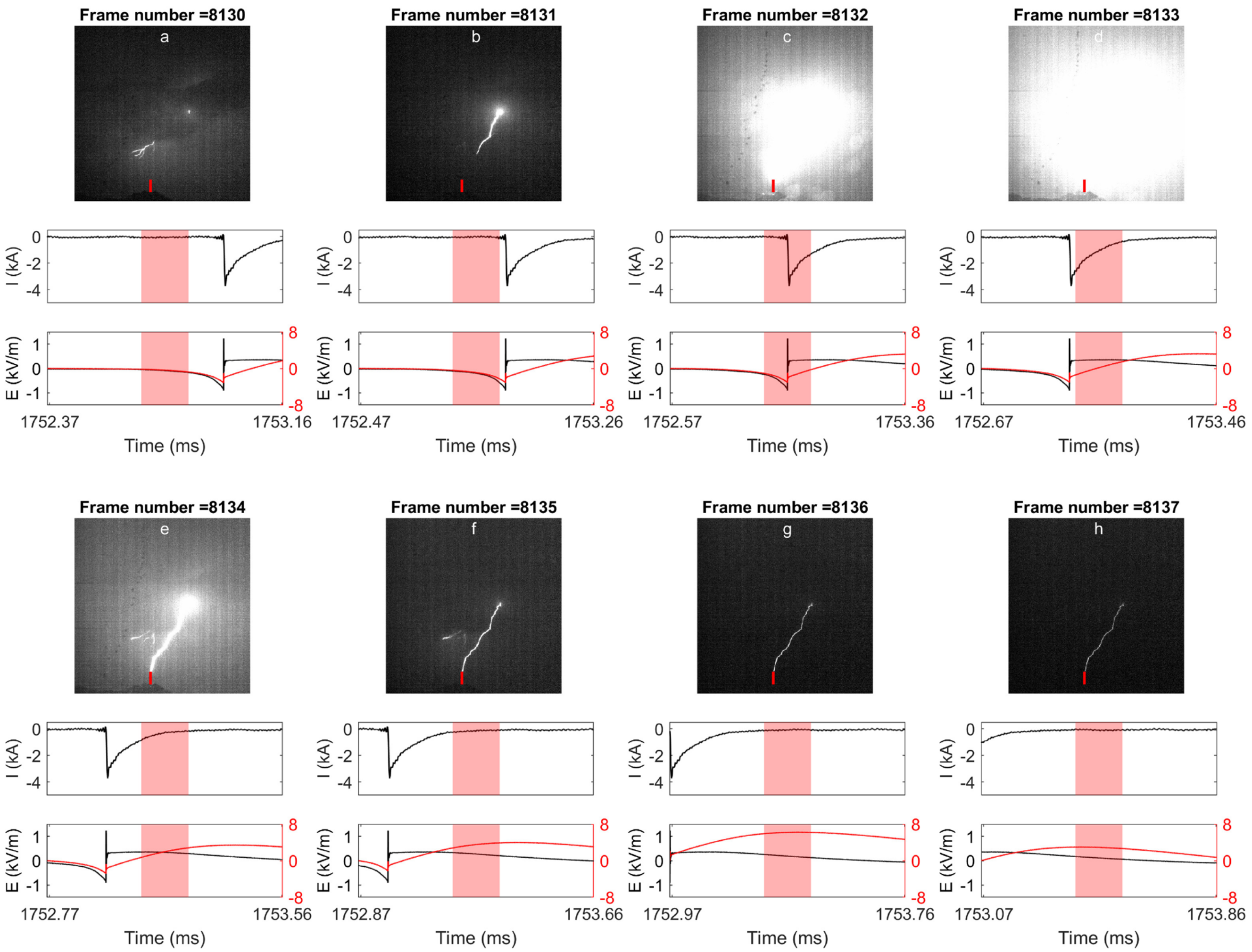

Figure 11. Second return stroke (RS) event. See description of subplots in the captions of Figures 3 and 7.

However, we have observed bidirectional propagation in three RLs belonging to Flash #2: one AL and two RSs (see Figure 13). Figure 14 presents the bidirectional propagation in an AL that occurred along the decayed ICC channel. We can observe bidirectional propagation from Figure 14b to Figure 14c.

Figure 15 and Figure 16 present the observations associated with the two RSs belonging to Flash #2, for which we can observe bidirectional propagation of the RL in Figure 15b to 15c and Figures 16b to 16c. It can be seen that in later stages (Figures 15c to 15d and Figures 16c to 16d), the positive end is no longer observed to propagate, presumably because either it was obscured by the clouds, or the critical electric field condition was no longer satisfied. This fact could explain why in some cases with a limited number of frames, we were not able to confirm a bidirectional propagation as the positive end could have ceased to propagate already by the end of the exposure time of the first observed frame.

6. Discussion

HSC observations of different processes, namely RSs, M-ICC events, and ALs, characterized by different current and electric field waveforms were discussed. The observations show that all these processes start as RLs, based on the fact that they propagate with speeds characteristic of DLs and they propagate along a decayed channel as observed from HSC video. It is worth noting that in our observations, RLs always start at the extremity of decayed channels. Although we did not observe any M components or MM pulses in the flash that was analyzed in detail, we did observe them in the two other flashes, which are presented in

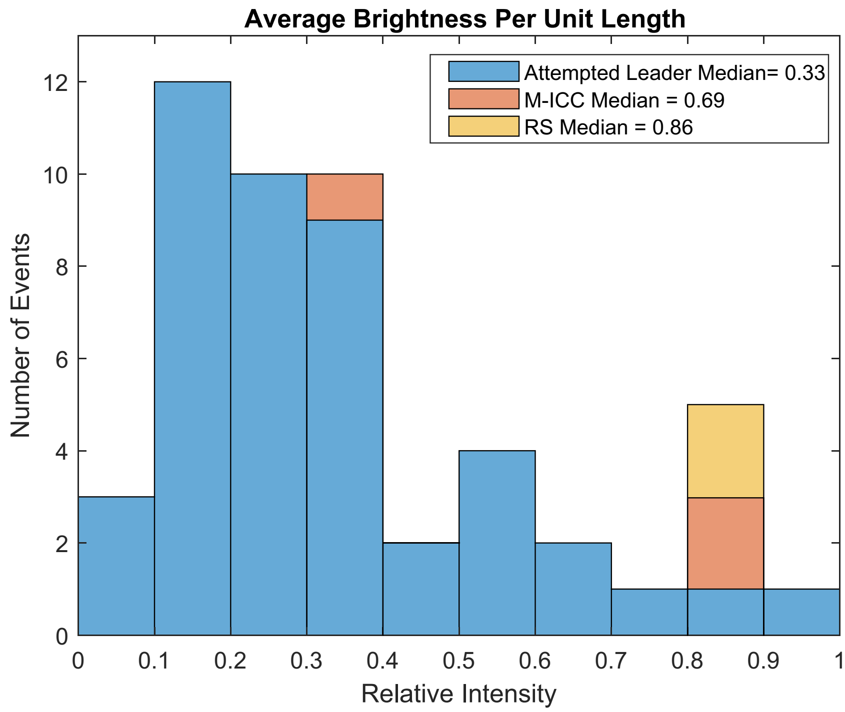

Figure 12. Histogram of the average luminosity brightness per unit length for recoil leaders (RLs) resulting in different phenomena.

the supplementary material (Sunjerga, Rachidi, & Rubinstein, 2021). Both M components and MM pulses propagated with speeds characteristic of DLs and not those of dart stepped leaders (that develop along previously created but decayed channels), suggesting that they are also originating from RLs propagating along ionized paths.

An illustrated summary of the observations presented in this work is shown in Figure 17. Note that we assume that the negative part of the RL is longer (see [Sunjerga, Rubinstein, et al., 2021] for more details) than the positive part, and that the positive end stops to extend at a certain point (see [Mazur et al., 2013]). The figure can be described as follows.

In our observations, all the processes start with a RL. Note that this might be partially due to the fact that the camera view was concentrated in proximity of the tower tip and there might be part of a recoil leader out

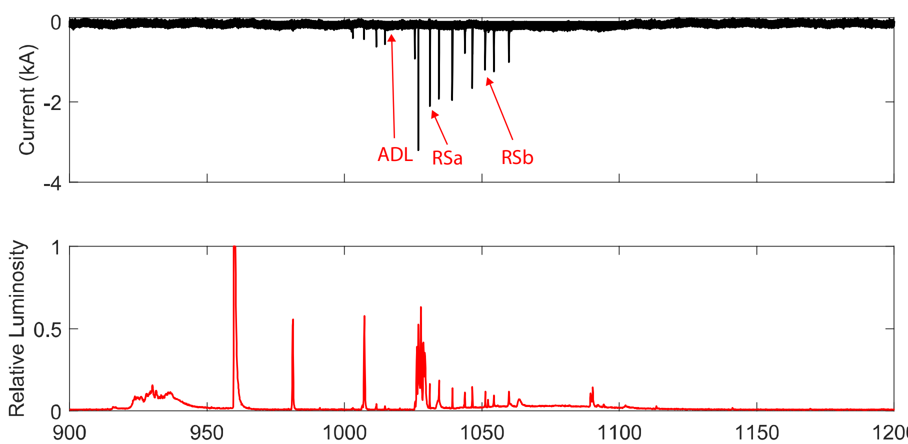

Figure 13. Current and relative luminosity for Flash #2. Bidirectional recoil leaders (RLs) were observed with an attempted leader (AL) and two return strokes (RSs) marked in the figure.

10.1029/2021JD035238

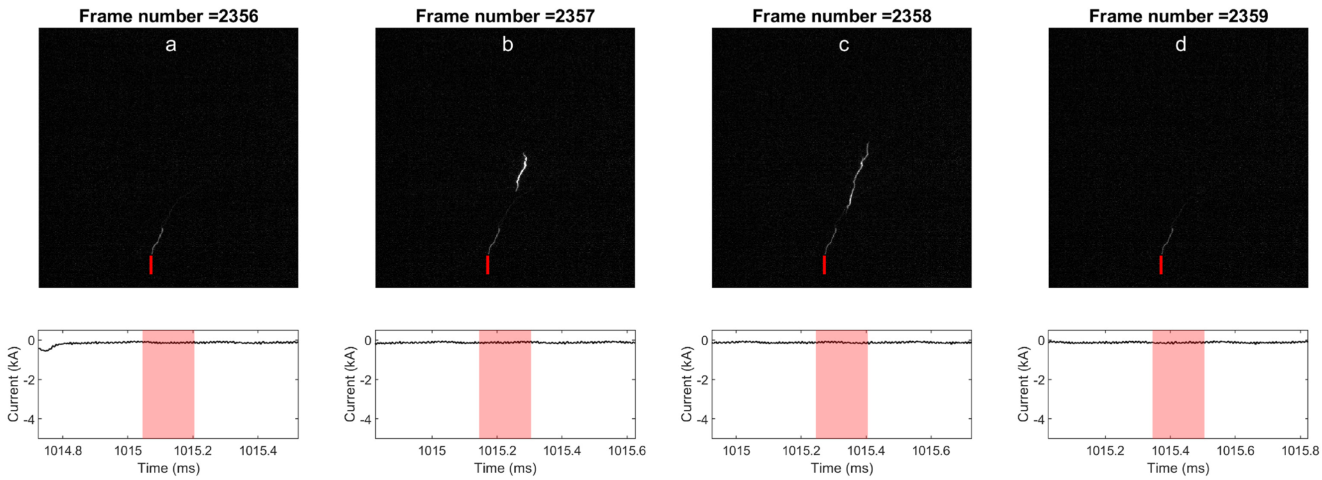

Figure 14. Attempted leader (AL) in Flash #2 with bidirectional propagation of the recoil leader (RL). Frames from the high-speed camera (HSC) are shown on the top and the corresponding current waveform on the bottom. The red shaded time intervals in the field plots are 160 μs wide and they represent a 99 μs exposure of each frame and an extra 61 μs estimated uncertainty due to the manual time synchronization.

of the view propagating as virgin air breakdown and extending the channel. A DL is created when the RL or virgin air breakdown retraces the old channel and reaches either (a) the ground (or the tip of the tower), resulting in a subsequent stroke or a MM pulse, or (b) a conducting channel, resulting in an M-component or an M-ICC pulse. What follows after will depend on the type of junction (to the structure or to a conducting channel) and the presence of another conducting branch. This confirms once again (Shao et al., 1995; and Mazur, 2002) that a RL is the main cause for the sequence of different events observed in upward and downward negative lightning.

7. Conclusion

We analyzed three upward negative flashes at the Säntis Tower using a high-speed video camera. The channel-base lightning current was also observed using direct measurements on the tower. In one of the flashes, simultaneous records of electric fields at 23 m distance were also obtained. A detailed analysis of this flash was presented in the paper. During the flash, 50 recoil leaders were observed, 45 of which ended up as attempted leaders, three developed into M-component-type ICC processes, and two into return strokes.

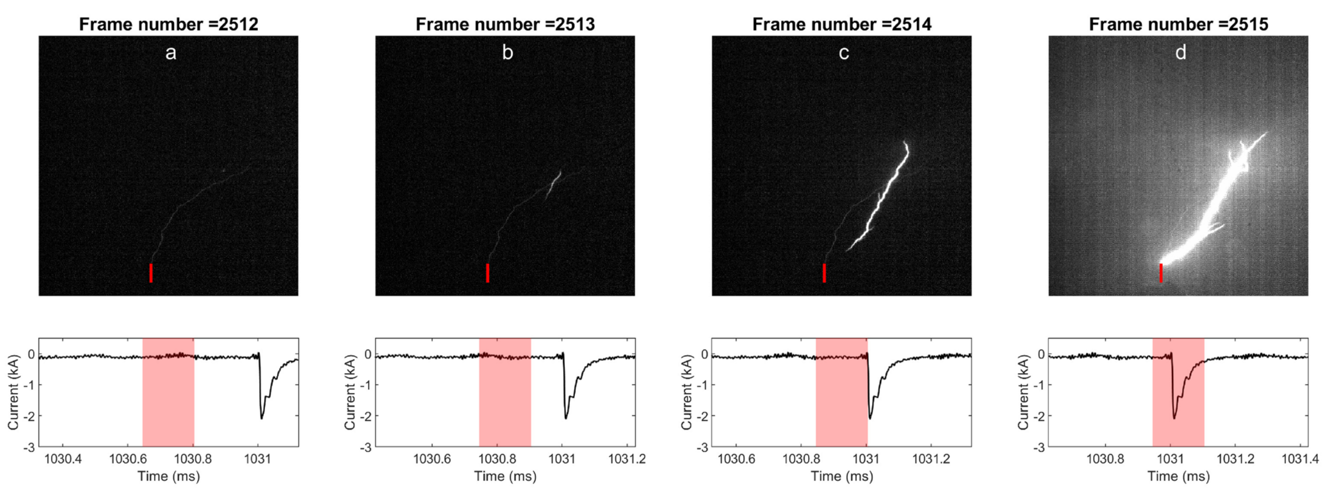

Figure 15. Return stroke (RS) *a* from Flash #2 with bidirectional propagation of the recoil leader (RL). The description is the same as in Figure 14.

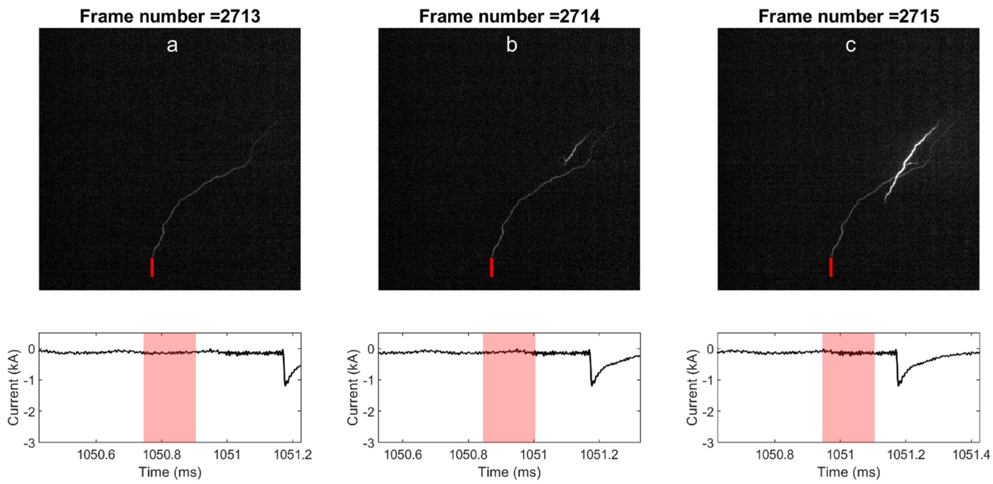

Figure 16. Return stroke (RS) *b* from Flash #2 with bidirectional propagation of the recoil leader (RL). The description is the same as in Figure 14.

We observed that different processes occurring in upward negative flashes, including the return stroke, mixed-mode pulses, M-components, M-component-type ICC events, and attempted leaders all started as recoil leaders. Depending on the spatial and temporal properties of the electric field in the area of the event and the main channel condition, the recoil leader can develop into one of these phenomena.

Our observations suggest that mixed-mode pulses occur only when the dart leader connects directly to the structure, while junction to the conducting channel at any height will cause M-component-type ICC pulses.

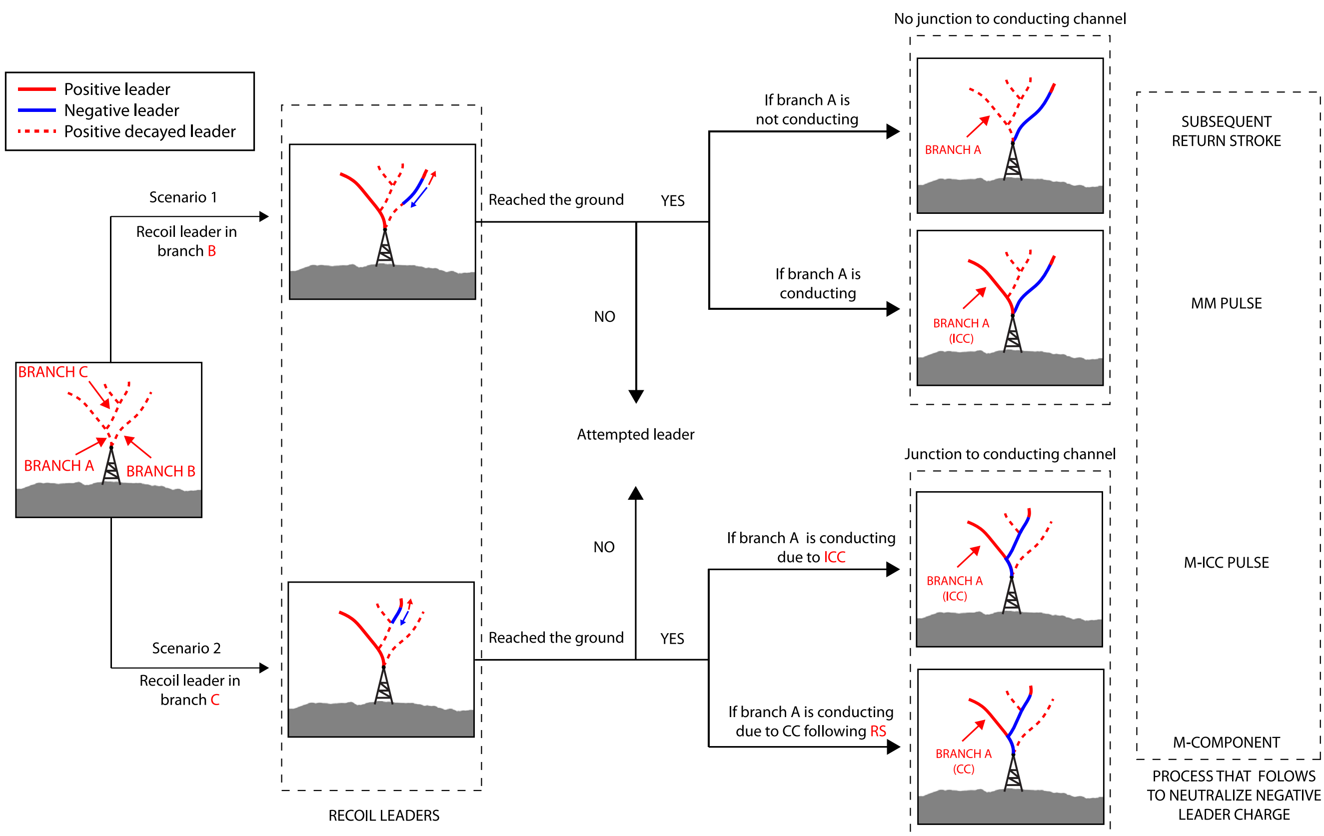

Figure 17. Sketch of mechanisms involved in the initiation of different charge transfer modes in upward negative flashes, all of them starting from recoil leaders (RLs), as observed at Säntis. Not to scale.

Furthermore, our observations suggest that not only return strokes and mixed-mode pulses consist of the dart leader/return stroke phase. A similar phase can be also observed in M-components and M-component-type ICC events in parts of channel above the junction point.

All the observed M-component-type ICC events connected to the channel at a relatively low altitude of a few hundred meters, providing evidence that the junction points of M-component-type ICC events can be significantly lower than the 1-km threshold suggested earlier in literature (Zhou et al., 2015).

Bidirectional propagation of recoil leaders was also observed in three recoil leaders leading to an attempted leader and in two return strokes. Observations suggest that in later stages of the recoil leader development, the positive end ceases to propagate.

Data Availability Statement

Supplementary data are available at Sunjerga, Rachidi, & Rubinstein, 2021.

Acknowledgments
This work was supported in part by the Swiss National Science Foundation (Project No. 200020_175594). Open access funding enabled and organized by Projekt DEAL.

References

Azadifar, M., Paolone, M., Pavanello, D., Rachidi, F., Romero, C., & Rubinstein, M. (2014). "An update on the instrumentation of the Säntis Tower in Switzerland for lightning current measurements and obtained results". In CIGRE international colloquium on lightning and power systems.

Azadifar, M., Rachidi, F., Rubinstein, M., Rakov, V. A., Paolone, M., Pavanello, D., & Metz, S. (2016). Fast initial continuous current pulses versus return stroke pulses in tower-initiated lightning. *Journal of Geophysical Research: Atmospheres*, *121*(11), 6425–6434. https://doi.org/10.1002/2016jd024900

Azadifar, M., Rubinstein, M., Li, Q., Rachidi, F., & Rakov, V. (2019). A New Engineering Model of Lightning M Component That Reproduces Its Electric Field Waveforms at Both Close and Far Distances. *Journal of Geophysical Research: Atmospheres*, *124*(24), 14008–14023. https://doi.org/10.1029/2019jd030796

Cooray, G. V. (2014). *The lightning flash IEE, power & energy series* (2nd ed.).

Cooray, V., Rubinstein, M., & Rachidi, F. (2020). Latitude and topographical dependence of lightning return stroke peak current in natural and tower-initiated negative ground flashes. *Atmosphere*, *11*(6), 560. https://doi.org/10.3390/atmos11060560

Diendorfer, G., Pichler, H., & Mair, M. (2009). Some parameters of negative upward-initiated lightning to the Gaisberg Tower (2000–2007). *IEEE Transactions on Electromagnetic Compatibility*, *51*, 443–452. https://doi.org/10.1109/temc.2009.2021616

He, L., Azadifar, M., Rachidi, F., Rubinstein, M., Rakov, V. A., Cooray, V., et al. (2018). An analysis of current and electric field pulses associated with upward negative lightning flashes initiated from the Säntis Tower. *Journal of Geophysical Research: Atmospheres*, *123*(8), 4045–4059. https://doi.org/10.1029/2018jd028295

Heidler, F. H., Manhardt, M., & Stimper, K. (2013). The slow-varying electric field of negative upward lightning initiated by the Peissenberg Tower, Germany. *IEEE Transactions on Electromagnetic Compatibility*, *55*(2), 353–361. https://doi.org/10.1109/temc.2012.2209121

Hussein, A. M., Janischewskyj, W., Chang, J.-S., Shostak, V., Chisholm, W. A., Dzurevych, P., & Kawasaki, Z.-I. (1995). Simultaneous measurement of lightning parameters for strokes to the Toronto Canadian National Tower. *Journal of Geophysical Research*, *100*(D5), 8853. https://doi.org/10.1029/95jd00543

Jiang, R., Wu, Z., Qie, X., Wang, D., & Liu, M. (2014). High-speed video evidence of a dart leader with bidirectional development. *Geophysical Research Letters*, *41*(14), 5246–5250. https://doi.org/10.1002/2014gl060585

Kasemir, H. W. (1950). Qualitative ubersicht uber potential-, feld- und ladungsverhaltnisse bei einer blitzentladung inder gewitterwolke (qualitative survey of the potential, field and charge conditions during a lightning dischargein the thunderstorm cloud). In H. Israel (Ed.), *Das Gewitter*. Leipzig: Akadem. Verlagsgesellschaft.

Kitagawa, N., & Brook, M. (1960). A comparison of intracloud and cloud-to-ground lightning discharges. *Journal of Geophysical Research*, *65*(4), 1189–1201. https://doi.org/10.1029/jz065i004p01189

Kotovsky, D. A., Uman, M. A., Wilkes, R. A., & Jordan, D. M. (2019). High-speed video and lightning mapping array observations of in-cloud lightning leaders and an M component to ground. *Journal of Geophysical Research: Atmospheres*, *124*(3), 1496–1513. https://doi.org/10.1029/2018jd029506

Krehbiel, P. R., Brook, M., & McCrory, R. A. (1979). An analysis of the charge structure of lightning discharges to ground. *Journal of Geophysical Research*, *84*(C5), 2432. https://doi.org/10.1029/jc084ic05p02432

Li, D., Azadifar, M., Rachidi, F., Rubinstein, M., Paolone, M., Pavanello, D., et al. (2016). On lightning electromagnetic field propagation along an irregular terrain. *IEEE Transactions on Electromagnetic Compatibility*, *58*(1), 161–171. https://doi.org/10.1109/temc.2015.2483018

Mazur, V. (2002). Physical processes during development of lightning flashes. *Comptes Rendus Physique*, *3*(10), 1393–1409. https://doi.org/10.1016/s1631-0705(02)01412-3

Mazur, V., & Ruhnke, L. H. (1993). Common physical processes in natural and artificially triggered lightning. *Journal of Geophysical Research*, *98*(D7), 12913. https://doi.org/10.1029/93jd00626

Mazur, V., & Ruhnke, L. H. (2011). Physical processes during development of upward leaders from tall structures. *Journal of Electrostatics*, *69*(2), 97–110. https://doi.org/10.1016/j.elstat.2011.01.003

Mazur, V., Ruhnke, L. H., Warner, T. A., & Orville, R. E. (2013). RL formation and development. *Journal of Electrostatics*, *71*(4), 763–768. https://doi.org/10.1016/j.elstat.2013.05.001

Qie, X., Pu, Y., Jiang, R., Sun, Z., Liu, M., Zhang, H., et al. (2017). Bidirectional leader development in a preexisting channel as observed in rocket-triggered lightning flashes. *Journal of Geophysical Research: Atmospheres*, *122*(2), 586–599. https://doi.org/10.1002/2016jd025224

Romero, C., Mediano, A., Rubinstein, A., Rachidi, F., Rubinstein, M., Paolone, M., et al. (2010). Measurement of lightning currents using a combination of Rogowski coils and B-dot sensors. *2010 30th international conference on lightning protection (ICLP)*. https://doi.org/10.1109/iclp.2010.7845959

Romero, C., Paolone, M., Rubinstein, M., Rachidi, F., Rubinstein, A., Diendorfer, G., et al. (2012). A system for the measurements of lightning currents at the Säntis Tower. *Electric Power Systems Research*, *82*(1), 34–43. https://doi.org/10.1016/j.epsr.2011.08.011

Romero, C., Rachidi, F., Paolone, M., & Rubinstein, M. (2013). Statistical distributions of lightning currents associated with upward negative flashes based on the data collected at the Säntis Tower in 2010 and 2011. *IEEE Transactions on Power Delivery*, *28*(3), 1804–1812. https://doi.org/10.1109/tpwrd.2013.2254727

Rubenstein, M., Rachidi, F., Uman, M. A., Thottappillil, R., Rakov, V. A., & Nucci, C. A. (1995). Characterization of vertical electric fields 500 m and 30 m from triggered lightning. *Journal of Geophysical Research*, *100*(D5), 8863. https://doi.org/10.1029/95jd00213

Rubinstein, M., Bermdez, J., Rakov, V., Rachidi, F., & Hussein, A. (2012). Compensation of the instrumental decay in measured lightning electric field waveforms. *IEEE Transactions on Electromagnetic Compatibility*, *54*(3), 685–688. https://doi.org/10.1109/temc.2012.2198482

Saba, M. M. F., Cummins, K. L., Warner, T. A., Krider, E. P., Campos, L. Z. S., Ballarotti, M. G., et al. (2008). Positive leader characteristics from high-speed video observations. *Geophysical Research Letters*, *35*(7). https://doi.org/10.1029/2007gl033000

Shao, X. M., Krehbiel, P. R., Thomas, R. J., & Rison, W. (1995). Radio interferometric observations of cloud-to-ground lightning phenomena in Florida. *Journal of Geophysical Research*, *100*(D2), 2749. https://doi.org/10.1029/94jd01943

Shindo, T., Miki, T., Saito, M., Tanaka, D., Asakawa, A., Motoyama, H., et al. (2014). Lightning observations at Tokyo Skytree. In *2014 international symposium on electromagnetic compatibility - EMC EUROPE*. https://doi.org/10.1109/emceurope.2014.6930973

Smorgonskiy, A., Egüz, E., Rachidi, F., Rubinstein, M., & Cooray, V. (2015). A model for the evaluation of the electric field associated with the lightning-triggering rocket wire and its corona. *Journal of Geophysical Research: Atmospheres*, *120*(20), 10964–10973. https://doi.org/10.1002/2015jd023373

Sunjerga, A., Rachidi, F., & Rubinstein, M. (2021). *Bidirectional recoil leaders in upward lightning flashes observed at the Säntis Tower.zip*. figshare. Dataset. https://doi.org/10.6084/m9.figshare.14588346.v2

Sunjerga, A., Rubinstein, M., Pineda, N., Mostajabi, A., Azadifar, M., Romero, D., & Rachidi, F. (2020). LMA observations of upward lightning flashes at the Säntis Tower initiated by nearby lightning activity. *Electric Power Systems Research*, *181*, 106067. https://doi.org/10.1016/j.epsr.2019.106067

Sunjerga, A., Rubinstein, M., Rachidi, F., & Cooray, V. (2021). On the initiation of upward negative lightning by nearby lightning activity: An analytical approach. *Journal of Geophysical Research: Atmospheres*, *126*. https://doi.org/10.1029/2020jd034043

Warner, T. A., Cummins, K. L., & Orville, R. E. (2012). Upward lightning observations from towers in Rapid City, South Dakota and comparison with National Lightning Detection Network data, 2004-2010. *Journal of Geophysical Research*, *117*(D19). https://doi.org/10.1029/2012jd018346

Warner, T. A., Saba, M. M. F., Schumann, C., Helsdon, J. H., Jr, & Orville, R. E. (2016). Observations of bidirectional lightning leader initiation and development near positive leader channels. *Journal of Geophysical Research: Atmospheres*, *121*(15), 9251–9260. https://doi.org/10.1002/2016jd025365

Wu, B., Lyu, W., Qi, Q., Ma, Y., Chen, L., Jiang, R., et al. (2019). High-speed video observations of recoil leaders producing and not producing return strokes in a Canton-Tower upward flash. *Geophysical Research Letters*, *46*(14), 8546–8553. https://doi.org/10.1029/2019gl083862

Yoshida, S., Biagi, C. J., Rakov, V. A., Hill, J. D., Stapleton, M. V., Jordan, D. M., et al. (2012). The initial stage processes of rocket-and-wire triggered lightning as observed by VHF interferometry. *Journal of Geophysical Research*, *117*(D9). https://doi.org/10.1029/2012jd017657

Zhou, H., Rakov, V. A., Diendorfer, G., Thottappillil, R., Pichler, H., & Mair, M. (2015). A study of different modes of charge transfer to ground in upward lightning. *Journal of Atmospheric and Solar-Terrestrial Physics*, *125–126*, 38–49. https://doi.org/10.1016/j.jastp.2015.02.008

Zhu, Y., Ding, Z., Rakov, V. A., & Tran, M. D. (2019). Evolution of an upward negative lightning flash triggered by a distant +cg from a 257-m-tall tower, including initiation of subsequent strokes. *Geophysical Research Letters*, *46*(12), 7015–7023. https://doi.org/10.1029/2019gl083274

Paper IV

JGR Atmospheres

RESEARCH ARTICLE

10.1029/2020JD034043

Key Points:

- Analytical formulas are derived to describe the electrostatic field changes associated with horizontal and vertical leaders
- The derived formulas are used to evaluate the electric fields in different scenarios leading to the triggering of an upward flash
- Upward lightning can be triggered by nearby lightning activity, either during leader propagation phase, or after the return stroke phase

Correspondence to:

A. Sunjerga,
antonio.sunjerga@epfl.ch

Citation:

Sunjerga, A., Rubinstein, M., Rachidi, F., & Cooray, V. (2021). On the initiation of upward negative lightning by nearby lightning activity: An analytical approach. *Journal of Geophysical Research: Atmospheres*, *126*, e2020JD034043. https://doi.org/10.1029/2020JD034043

Received 7 OCT 2020
Accepted 2 FEB 2021

Author Contributions:

Conceptualization: Antonio Sunjerga
Data curation: Antonio Sunjerga
Formal analysis: Antonio Sunjerga
Funding acquisition: Marcos Rubinstein, Farhad Rachidi
Investigation: Antonio Sunjerga, Marcos Rubinstein, Farhad Rachidi
Methodology: Antonio Sunjerga, Marcos Rubinstein, Farhad Rachidi
Project administration: Farhad Rachidi
Resources: Antonio Sunjerga, Marcos Rubinstein, Farhad Rachidi
Software: Antonio Sunjerga
Supervision: Marcos Rubinstein, Farhad Rachidi
Validation: Antonio Sunjerga, Vernon Cooray
Writing – original draft: Antonio Sunjerga, Farhad Rachidi
Writing – review & editing: Antonio Sunjerga, Marcos Rubinstein, Farhad Rachidi, Vernon Cooray

On the Initiation of Upward Negative Lightning by Nearby Lightning Activity: An Analytical Approach

Antonio Sunjerga[1], Marcos Rubinstein[2], Farhad Rachidi[1], and Vernon Cooray[3]

[1]Electromagnetic Compatibility Laboratory, Swiss Federal Institute of Technology (EPFL), Lausanne, Switzerland, [2]University of Applied Sciences of Western Switzerland (HES-SO), Yverdon-les-Bains, Switzerland, [3]Department of Engineering Sciences, Uppsala University, Uppsala, Sweden

Abstract Upward lightning occurs generally from tall structures. The mechanism of the initiation of upward lightning is not yet fully understood. Upward lightning can be classified into two categories based on either the absence or the presence of other lightning activity prior to the upward flash. This work proposes an explanation of how upward lightning flashes can be triggered by nearby lightning activity. It is generally thought that the lightning activity prior to the flash will intensify the electric field at the tip of the tall structures. However, to the best of our knowledge, no attempt has been made to evaluate theoretically this hypothesis. In this paper, we derive analytically the electric field enhancement on the ground (or at the top of tall structures) based on different triggering scenarios. These fields are later used in a simplified corona model to evaluate if they are able to trigger upward lightning. It is shown that both slow processes such as leader propagation and faster return strokes can trigger an upward negative flash from relatively short structures of a few tens of meters, even without any slowly varying background electric field. This study confirms theoretically experimental observations and it provides new insights into the mechanisms of initiation of upward flashes from tall structures.

1. Introduction

The characteristics of upward lightning discharges observed on tall towers (e.g., Gaisberg, Peissenberg, Säntis) have been widely reported in the literature (e.g., Smorgonskiy et al., 2011). However, their initiation mechanisms are not well understood and are still under analysis.

Knowing the background thunderstorm electric field, the electric field at the tip of the tower can be estimated by electrostatic modeling. However, once the electric field reaches the critical breakdown value, corona discharges will be initiated reducing the electric field in the vicinity of the tower tip. In case of a positive corona discharge, the electric field will ionize the air and electrons will move toward the tower tip, while positive ions will drift in the electric field creating positive ion space charge near the tip of the tower, reducing the value of electric field. It is well known that a moving rocket in rocket-triggered lightning is more likely to initiate upward lightning at a given altitude than a tall structure of the same height as the altitude of the rocket (Uman, 1987), presumably because the corona charges are left behind the tip of the rocket.

Similarly, it has been hypothesized (Rachidi et al., 2008) and later confirmed by observations (Montanyà, 2014) that a rotating wind turbine blade is more likely to initiate upward lightning compared to a still one. This is due to the fact that there is less time for the corona charge to build up as the object is moving and any corona charges that are generated are left behind by the moving blade tip.

The electric field distribution is governed by coupled electrostatic and charge balance equations. In order to have an upward leader initiated from the tip of a tower, the electric field has to exceed a critical value not only at the tip of the tower, but also along some critical distance (Cooray, 2013). The electric potential of the tall structure has to be high enough for the initiated leader to be sustained and for it to escape from the corona charge cloud; otherwise, it will end up as what is known as an aborted leader (Wang et al., 2008).

Based on a simplified model, Aleksandrov et al. (2001) derived analytical equations to determine the conditions for the development of an upward leader. The main input to their model is the induced voltage at the tip of the tower with respect to the ground, which is directly related to the background electric field and the height of the structure. The main conclusion of their work was that beyond a certain value of the background electric field for a given geometry, a sustained upward leader will be initiated. However, as shown in Aleksandrov et al. (2001), this value depends not only on the peak electric field, but also on its waveform. Electric field waveforms with fast risetimes are capable of initiating a sustained upward leader at lower values of the maximum electric field. Assuming a background electric field of 10 kV/m and a rise-time of about 10 s, the structure would need to be taller than 400 m to initiate a sustained upward leader. Based on their analysis, Aleksandrov et al. concluded that it is more likely that an upward leader be triggered by preceding nearby in-cloud or cloud-to-ground lightning activity than by the slow varying background electric field. Since in-cloud and cloud-to-ground flashes contain processes characterized by risetimes lower than few milliseconds, they would be able to initiate a sustained upward leader even from moderately tall structures with the same value of the electric field. This was first suggested by Berger and Vogelsanger (1969). It is worth noting that electric field changes caused by lightning are hypothesized to trigger discharges in the middle and upper atmosphere such as red sprites and elves (see Chapter 14 of Rakov & Uman, 2003).

Wang et al. (2008) proposed the classification of upward flashes into two categories: self-triggered (ST) and other-triggered (OT), based on either the absence or the presence of prior lightning activity in the geographical and temporal vicinity of the tower-initiated flash. The relative number of ST and OT flashes has been shown to vary depending on the geographical area (see e.g., Smorgonskiy et al., 2015). For example, at the Gaisberg Tower (Smorgonskiy, Tajalli, et al., 2015), only 13% of the flashes occur after prior lightning activity in the vicinity of the tower. On the other hand, in Rapid City (Warner et al., 2012), observations from 10 tall towers have shown that out of 81 upward flashes, only one was not preceded by other lightning activity, as determined by optical observations. The reported statistics on the percentage of triggered flashes could be underestimated since some of the preceding flashes could be missed depending on the type of data used for the classification (Sunjerga et al., 2018; Sunjerga, Rubinstein, Pineda, et al., 2020). It is worth noting that ST flashes have been observed at structures with much shorter height than those suggested by Aleksandrov et al. This might be due to the fact that the electric field can significantly exceed the value of 10 kV/m for some short period of time. Also, some of the structures are located on mountaintops, causing further enhancement of the field. The concept of effective height was introduced to account for the increased number of upward flashes from a tower located on a mountaintop (Rakov & Uman, 2013; Smorgonskiy et al., 2012).

OT flashes can be preceded (or triggered) by both in-cloud and cloud-to-ground (CG) flashes. Schumann et al. (2019), using video observations, proposed different mechanisms conducive to the initiation of upward flashes, all of them associated with horizontally propagating leaders in the clouds over the towers. It was assumed that the horizontal leaders produce an enhancement of the electric field at the tip of the tower, initiating an upward flash. To the best of our knowledge, no quantitative analysis has been performed to evaluate the field enhancement. The aim of this paper is to estimate the salient parameters (such as peak value and risetime) of the electric field waveforms associated with the different nearby lightning triggering scenarios observed by Schumann et al. Furthermore, we investigate to which extent the estimated electric fields are able to initiate a sustained upward leader. The analysis is performed for an upward negative lightning and a positive corona discharge. A simplified, closed-form formula for the electric field at ground level as a function of time is derived that is applicable both, to the case of a horizontal and of a vertical leader. The ground is assumed to be a perfect electric conductor. To evaluate the criterion for the leader initiation, the electric field at ground level is then used as an input to the simplified, analytical corona discharge model for tall structures that was proposed by Aleksandrov et al. (2001).

The rest of the paper is organized as follows. Section 2 presents a brief description of the triggering scenarios proposed by Schumann et al. (2019). Section 3 presents simulations of the vertical electric field for each of these scenarios. In Section 4, we evaluate if these typical electric field changes can trigger an upward flash from a tower-like structure. Discussion is given in Section 5 and conclusions in Section 6.

2. Description of Scenarios

Saba et al. (2016) and Schumann et al. (2019) observed different scenarios leading to the triggering of an upward flash from a tower. All of them are characterized by a horizontal leader propagation over the tower. Some scenarios additionally include the presence of a vertical channel approaching the ground.

10.1029/2020JD034043

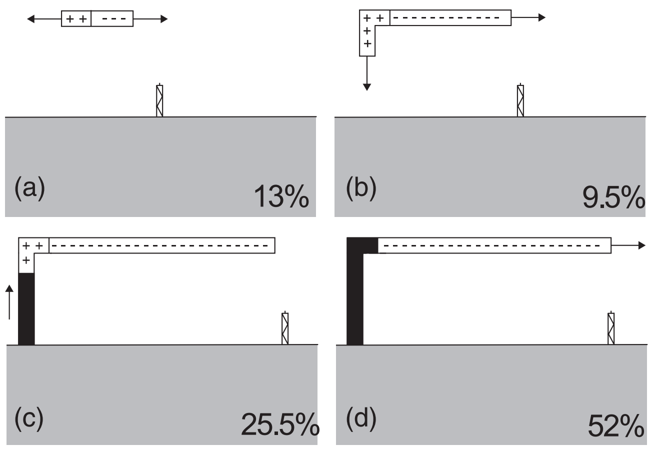

Figure 1. Typical scenarios leading to the triggering of a negative upward flash from a tower. (a) In-cloud leader above the tower, (b) in-cloud leader prior to a positive RS, (c) positive RS, (d) CC extending the negative leader above the tower. Not to scale. The percentage of occurrence of these scenarios as observed by Schumann et al. (2019) is given in each panel. CC, continuous current; RS, return stroke.

Figure 1 presents simplified sketches of the four scenarios observed to trigger upward negative lightning from the tip of the tower with the occurrence statistics. Schumann et al. (2019) reported occurrence statistics from both hemispheres at two observations sites in Rapid City and in Sao Paulo. Relatively similar occurrence statistics have been observed at these two sites (see Table 2 of Schumann et al., 2019). The reported values in Figure 1 are average values taking in account sample sizes from these two sites.

In the first scenario (Figure 1a), a bidirectional in-cloud leader is initiated near the tower and develops horizontally with its negative end approaching the tower while its positive end stretches away from the tower. Note that the positive leader part is shorter in length compared to the negative part since the positive leader speed has been observed to be smaller than the negative leader speed (van der Velde & Montanyà, 2013).

Upward lightning was also observed to occur prior to the attachment to ground of these leaders (Scenario 2), as shown in Figure 1b.

If the mechanisms described in scenarios 1 and 2 did not trigger an upward flash, this could happen after the connection of the downward leader to the ground and the initiation of the positive return stroke (RS), as illustrated in Figure 1c.

Finally, if none of the previous stages of the CG flash started as a horizontal in-cloud bidirectional leader trigger an upward flash, this could happen during the continuous current (CC) phase after the RS while the negative leader is extending in the direction of the tower as shown in Figure 1d.

Note that we assume that the positive RS neutralizes only the positive end of the leader while the negative one remains negatively charged. Once the downward leader reaches the ground Figure 1c the return stroke will neutralize the positive charges while the negative ones will be kept in place by cloud positive charges. Furthermore, if the charge from the negative cloud leader was also removed, since a bidirectional in-cloud leader is believed to have a zero-net charge, one would measure zero charge transfer in the channel-base current measurements which was not observed in measured downward positive flashes. If the negative charge were also to be neutralized by the positive RS, this would cause an electric field change at the tower opposite to the one leading to a negative upward flash, making the initiation of an upward leader according to the scenario 3 in Figure 1c even less likely. The removal of the positive charge of the leader could actually enable the negative part of the leader to spread even more freely and rapidly, as observed, at least for an opposite polarity flash in Stock et al. (2017).

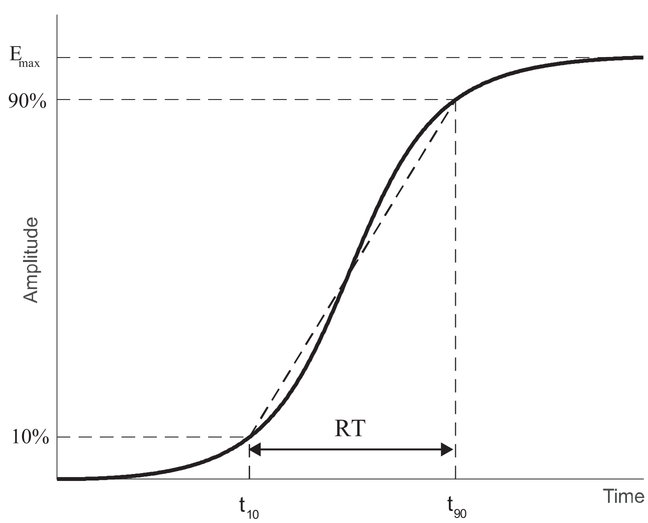

Figure 2. Definition of the electric field waveform parameters: 10%–90% risetime (RT) and field peak.

The four scenarios illustrated in Figure 1 are arranged in a chronological order of occurrence. However, the scenarios in Figure 1a, 1b, and 1d share similar physical properties as they are all caused by relatively slow leader propagation. On the other hand, the scenario in Figure 1c is governed by the RS process that can be three orders of magnitude faster than leader processes.

3. Electric Field Characteristics of the Considered Scenarios for the Triggering Events

The aim of this section is to evaluate the electric fields caused by the considered triggering scenarios. We will consider possible ranges of the 10%–90% risetime and peak (Figure 2) of the electric field by varying the geometrical properties, the velocity of propagation and the charge density of the leader.

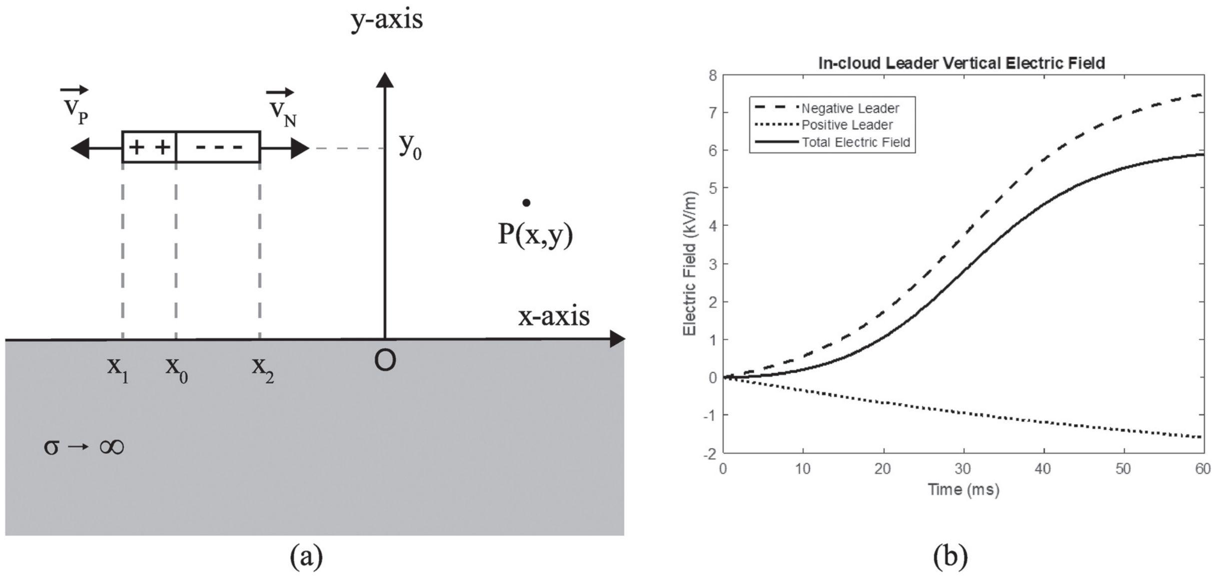

Figure 3. In-cloud leader. (a) Geometry of problem. (b) Vertical electric field on the ground surface at the origin of the coordinate system. The computation parameters correspond to Case 2 of Table 1. The contributions of the negative and positive leaders are also presented. The origin of time ($t = 0$) corresponds to the initiation of the bidirectional leader.

Note that we are only considering scenarios for the initiation of an upward negative lightning (upward positive leader). Similar mechanisms have been observed in the case of an upward positive lightning (upward negative leader), in which an approaching positive leader leads to the initiation of an upward negative leader (for example, see Figure 14 in Sunjerga, Rubinstein, Pineda, et al., 2020). In this section, we present the electric field expressions derived for each considered scenario. The full derivation can be found in the Appendix. Physics sign convention for the electric field was used in this paper (upward directed field is positive). It is worth noting that here we present a limited number of cases that are representative of common processes, having in mind uncertainties in input variables, including the input geometry, line charge density (e.g., Gao et al., 2020; Shen et al., 2019) and velocity of leaders (e.g., Campos et al., 2014; Proctor, 1997). An open-source code with a graphical interface is provided as supporting information. Interested readers can use it to run any specific case.

3.1. Scenario 1: In-Cloud Leader

Figure 3a presents the geometry of the problem. The vertical electric field associated with this scenario at a given point $P(x,y)$ is given by:

$$E_{ysc1}\left(x,y,t\right) = \frac{\lambda_N\left(y-y_0\right)}{4\pi\varepsilon_0}\left(f_{2H}\left(x,y,x_0,x_0+v_N t,y_0\right) - \frac{v_N}{v_P} f_{2H}\left(x,y,x_0-v_P t,x_0,y_0\right)\right), \tag{1}$$

where ε_0 is the vacuum permittivity, λ_N is the negative charge density, v_N and v_p are the propagation speeds of the negative and positive leader branches, and the function f_{2H} is defined in Equations (A.9–A.13) in the Appendix.

Note that the adopted line charge density of the positive leader is such that the overall zero charge condition (Kasemir, 1960) along the whole bidirectional leader is satisfied.

The resulting electric field waveform will depend on many input parameters, of either geometrical or physical nature. For example, we can directly see from (1) that the electric field has a linear dependence on the charge density. On the other hand, the amplitude will also depend on the height of the leader above the ground as well as the starting point of the bidirectional leader ($x = x_0$ in Figure 3). The risetime will be

Table 1
Input Parameters and the Resulting Rise Time (τ) and Peak Electric Field (E_{max}) for Scenario 1: In-Cloud Leader

	λ_N (C/km)	H (km)	v_P (m/s)	v_N (m/s)	x_0 (km)	RT (ms)	E_{max} (kV/m)
Case 1	−0.1	4	1×10^4	5×10^4	−1.5	39	0.06
Case 2	−0.5	2	2×10^4	1×10^5	−3	31	5.8
Case 3	−1.5	1	4×10^4	2×10^5	−6	12	52

governed by the velocities of the positive and negative leaders. Note that, in our model, we do not consider any branching of the channel.

We will analyze three different cases as described in Table 1. Case 2 corresponds to typical values expected from in-cloud bidirectional leaders at an altitude of 2 km above the ground (van der Velde & Montanyà, 2013). Case 1 corresponds to a low charge density leader characterized by the smallest expected propagation velocities and initiated at a height of 4 km above the ground. Case 3 corresponds to the highest expected line charge density and propagation velocities for a leader located only 1 km above the ground. The charge density obtained for this maximum charge density case (1.5 C/km) is similar to the values observed by Proctor (1997) from measurements of stepped leaders. The charge density values for the other cases are similar to those obtained by Shen et al. (2018).

Figure 3b presents the contributions of the positive and the negative leaders to the total electric field at the origin of the coordinate system for Case 2. At early times, the contributions of the positive and negative leaders are similar in magnitude because of their similar relative distance to the observation point (origin of coordinate system). However, as the negative leader progresses to the right and approaches the origin, it becomes dominant. A comparison of the electric field waveforms associated with the three different cases is shown in Figure 4a. Differences in both peak amplitude and waveshape can be observed. Figure 4b presents the two-dimensional (2-D) distribution of the vertical electric field for Case 2, 60 ms after the initiation.

3.2. Scenario 2: Positive Leader Approaching the Ground

Figure 5a presents the geometry of the scenario. The vertical electric field at a given point $P(x,y)$ is given by:

$$E_{y\,sc2}\left(x,y,t\right)=\begin{cases}E_{y\,sc1}\left(t\right), t \le T_1\\ E_{y2}\left(t\right), \quad t > T_1\end{cases}, \tag{2}$$

where T_1 is the moment in time when the positive leader starts to propagate toward the ground, and $E_{ysc1}(t)$ is the field associated with Scenario 1 given by (1). E_{y2} is given by

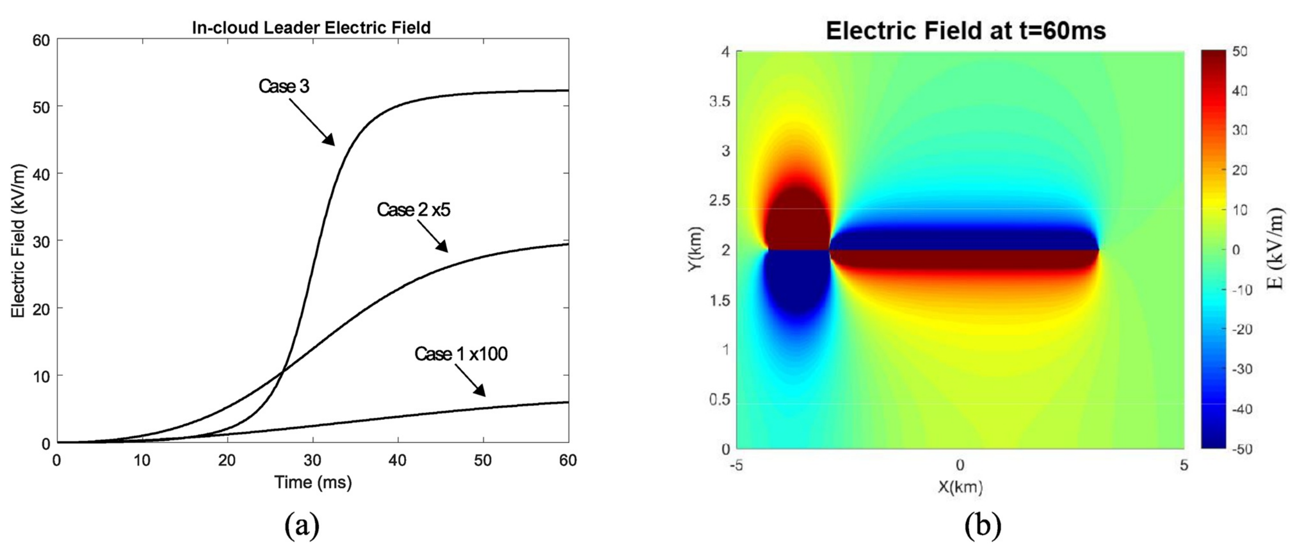

Figure 4. Scenario 1: (a) Vertical electric field waveforms at the origin of the coordinate system for the three considered cases. (b) 2D distribution of the vertical electric field for Case 2 at 60 ms.

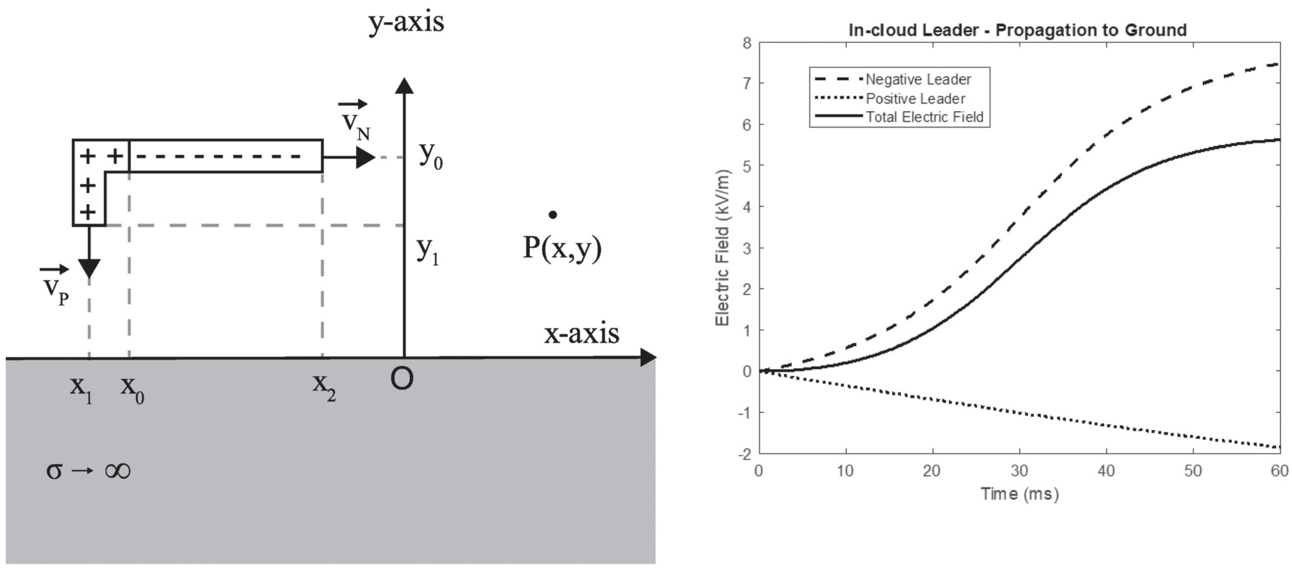

(a) (b)

Figure 5. Scenario 2: In-cloud leader propagation to ground. (a) Geometry of problem. (b) Components of the vertical electric field at the origin of the coordinate system for Case 2a. The origin of time ($t = 0$) corresponds to the initiation of the bidirectional leader.

$$E_{y2}\left(x,y,t\right) = \frac{\lambda_N\left(y-y_0\right)}{4\pi\varepsilon_0}\left(f_{2H}\left(x,y,x_0,x_0+v_N t,y_0\right)-\frac{v_N}{v_P}f_{2H}\left(x,y,x_0-v_P,T_1,x_0,y_0\right)\right) - \frac{\lambda_N v_N}{4\pi\varepsilon_0 v_P}f_{2V}(x,y,x_{T_1},y_0-v_P\left(t-T_1\right). \quad (3)$$

The functions f_{2H} and f_{2V} are defined in the equations (A.9–A.13) and (A.24–A.28) in the Appendix. Note that the line charge density of the positive leader is such that the overall zero charge condition along the whole leader is satisfied.

Three different cases are considered whose parameters are presented in Table 2. These cases are similar to Case 2 in Scenario 1 (in terms of leader charge density, propagation speeds, height) with the difference that, here, we vary the location along the *x*-axis of the initiation of the bidirectional leader and the time T_1 after which the positive leader veers toward the ground. It is also worth mentioning that the velocity of a downward stepped leader increases as it approaches the ground (Campos et al., 2010). However, for the sake of simplicity, we consider it to be constant in this study.

As can be seen from the results presented in Figure 5b, the vertical positive leader will result in a smaller overall peak electric field compared to Scenario 1. As expected, it can be seen on Figure 6a that the closer the positive leader to the observation point, the higher the decrease in the field. If the leader gets sufficiently close to the observation point, the electric field could even change sign and become negative. Figure 6b presents the 2D distribution of the vertical electric field for Case 2a, 60 ms from the initiation of the leader.

Table 2
Input Parameters and the Resulting Rise Time (RT) and Peak Electric Field (E_{max}) for Scenario 2: In-Cloud Leader Propagation to the ground

	x_0 (km)	RT (ms)	E_{max}(kV/m)
Case 2a	−3	31	5.75
Case 2b	−2	22	3.5
Case 2c	−1	18	1

Note. For $\lambda_N = -0.5$ C/km, $H = 2$ km, $v_P = 2 \times 10^4$ m/s, $v_N = 1 \times 10^5$ m/s and $T_1 = 10$ ms.

3.3. Scenario 3: Positive Return Stroke

Positive flashes are less common than negative flashes. Their current waveform is typically characterized by slower risetimes and it can have an order of magnitude higher peak value compared to negative flashes (Rakov, 2013). Cooray (1995, 2000) was the first to develop a model for positive return strokes. For the sake of simplicity and considering the relatively small distance to the observation point, we will consider here only

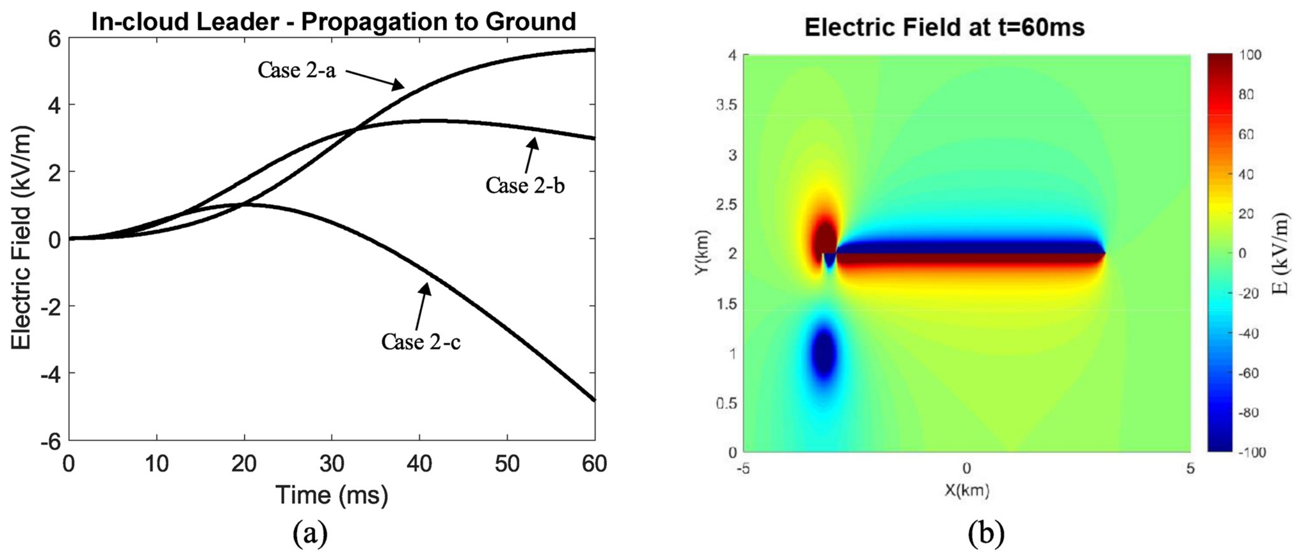

Figure 6. (a) Electric field waveforms at the origin of the coordinate system for the three considered cases (Table 2) in Scenario 2. (b) 2D distribution of the vertical electric field for Case 2a at 60 ms.

the electrostatic field of the return stroke. At distances not exceeding a few kilometers, the late-time electric field is mostly due to the electrostatic field component in case of negative return strokes as discussed by Lin et al. (1979). We assume here that the electrostatic assumption would hold for a positive return strokes due to its slower risetime.

Figure 7a presents the geometry of the problem. The vertical electric field at a given point $P(x,y)$ is given by:

$$E_{ysc3}(x,y,t) = \begin{cases} E_{y1}(t), & t \le T_2 \\ E_{y2}(t) = E_{y1}(T_2) + E_{y2}(t), & t > T_2 \end{cases}, \tag{4}$$

where T_2 is the moment in time when the return stroke reaches the maximum altitude y_0 and starts to propagate in the horizontal direction. E_{y1} and E_{y2} are given by

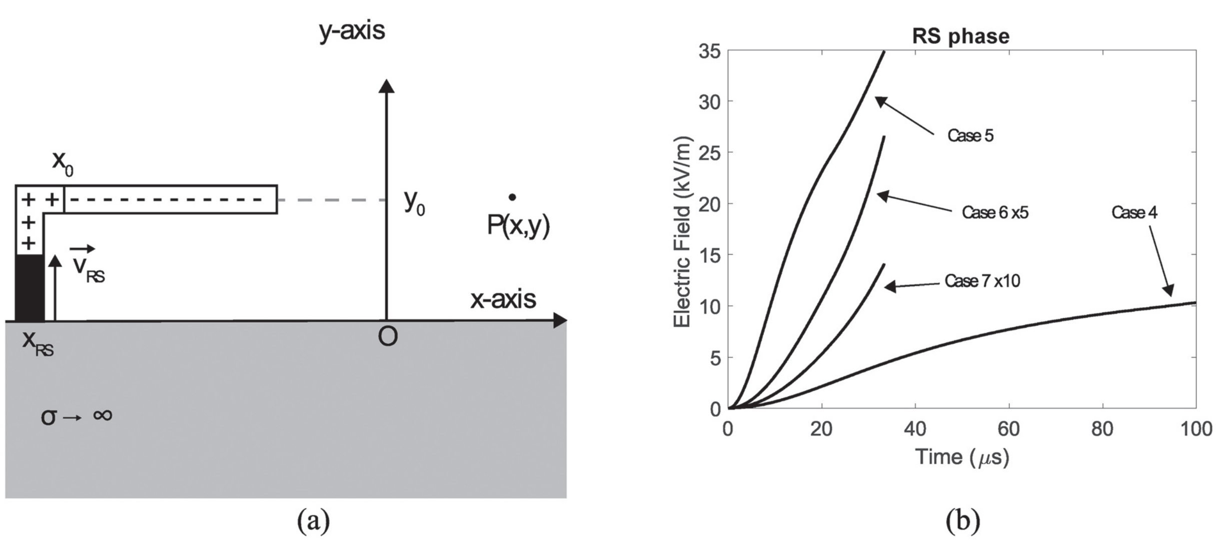

Figure 7. Scenario 3: Positive RS (a) Geometry of the problem. (b) Vertical electric field at the origin of the coordinate system for the considered cases in Table 4. The origin of time ($t = 0$) corresponds to the initiation of the return stroke. RS, return stroke.

Table 3
Input Parameters and the Resulting Rise Times (RT) and Electric Fields (E_{max1} and E_{max2}) for Scenario 3: Positive RS

	H (km)	x_{RS} (km)	x_0 (km)	RT (μs)	E_{max1} (kV/m)	E_{max2} (kV/m)
Case 4	8	−3	−2	68.2	9.7	10.3
Case 5	2	−1	0	25.2	24.8	34.9
Case 6	2	−3	−2	22.6	2.5	5.32
Case 7	2	−5	−4	21.7	0.64	1.4

Note. For $\lambda_P = 2.5$ C/km and $v_{RS} = 0.9 \times 10^8$ m/s.
RS, return stroke.

$$E_{y1}\left(x,y,t\right) = -\frac{\lambda_P}{4\pi\varepsilon_0} f_{2V}\left(x,y,x_{RS},0,v_{RS}t\right), \tag{5}$$

$$E_{y2}\left(x,y,t\right) = -\frac{\lambda_P}{4\pi\varepsilon_0}\left(f_{2V}\left(x,y,x_{RS},0,v_{RS}T_2\right) + \left(y-y_0\right) f_{2H}\left(x,y,x_{RS},x_{RS}+v_{RS}\left(t-T_2\right),y_0\right)\right), \tag{6}$$

in which the geometrical functions f_{2H} and f_{2V} are defined in equations (A.9–A.13) and (A.24–A.28) in the Appendix.

We will consider three different distances from the vertical leader, as specified in Table 3. The assumed charge density is 2.5 C/km (Thomson et al., 1985). The assumed return stroke speed is 0.9×10^8 m/s, which corresponds to typical observed speeds (Cooray, 2000). We consider two different heights for the return stroke (or altitudes for the horizontal leader). The lower one could be associated with positive flashes caused by the lower positive charge pocket, and the higher to flashes caused by the upper main positive charge region (Rakov, 2013). Note that, in Table 3, E_{max1} is the field observed at the origin at the moment when the return stroke reaches the point (x_{RS},y_0), while E_{max2} is the field at the moment when the return stroke reaches the initiation point of the bidirectional leader (x_0,y_0).

The magnitude of the electric field will mostly depend on the distance to the observation point. The observed risetimes are much smaller compared to risetimes associated with leader fields, since the return stroke speed is much faster than the leader propagation speed.

Figure 8 presents the spatial distribution of the vertical electric field at the time instant when the whole positive leader is neutralized for cases 4 and 5 in Table 3. As expected, the maximum value of the electric field occurs at the base of the vertical leader since the contribution of the channel elements and their images add-up constructively to yield a maximum value.

3.4. Scenario 4: Developing Horizontal Leader During the Continuous Current Phase

Figure 9a presents a sketch of Scenario 4, according to which a horizontal leader develops above the tower during the CC phase following a positive return stroke. Note that the positive part of the leader is already neutralized by the return stroke preceding the CC phase. We evaluate here the electric field change caused by the extension of the negative leader from its location right after the RS.

With reference to Figure 9a, the vertical electric field a given point $P(x,y)$ is given by:

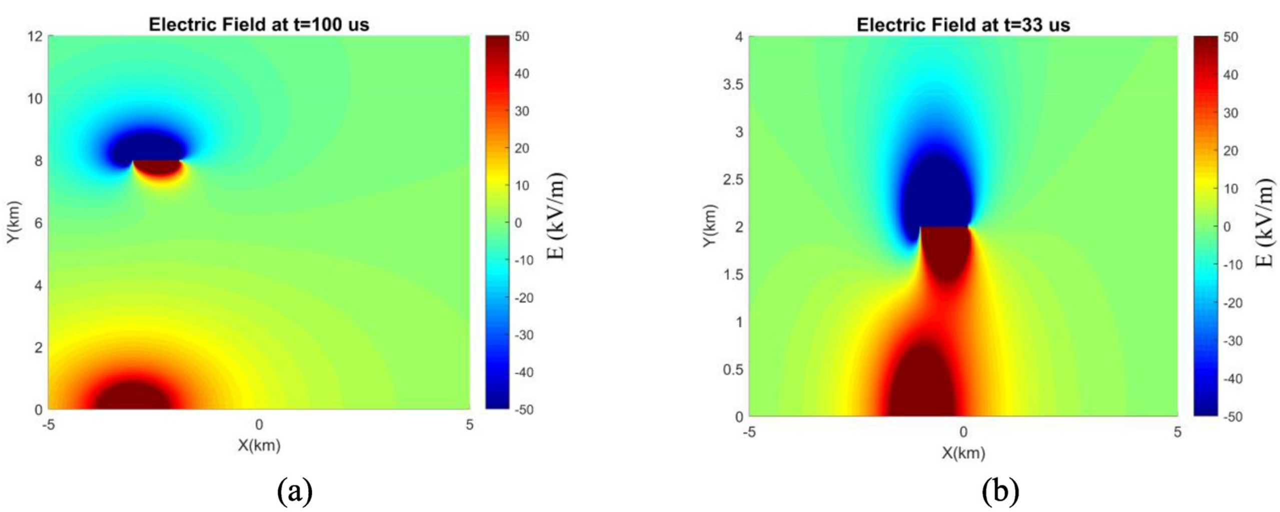

Figure 8. 2D distribution of the vertical electric field at the time instant when the whole positive leader is neutralized. (a) Case 4. (b) Case 5.

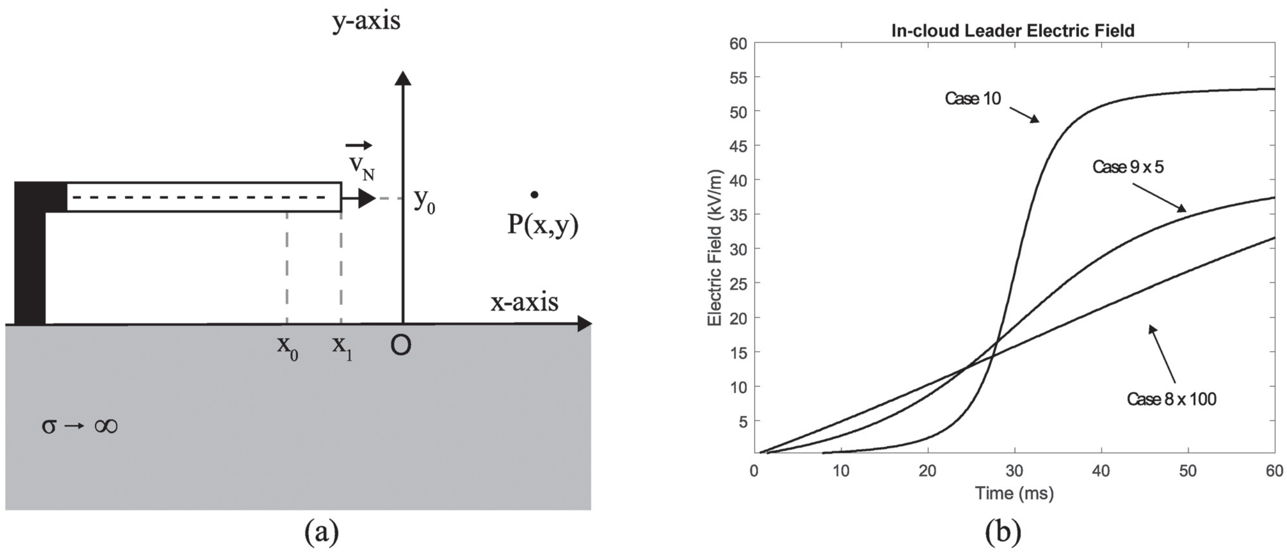

Figure 9. Scenario 4: Horizontal leader during the continuous current phase following a positive return stroke. (a) Geometry of problem. (b) Vertical electric field at the origin of the coordinate system for the three considered cases (cases 7, 8, and 9). The origin of time ($t = 0$) corresponds to the start of the horizontal leader extension during the continuous current phase.

$$E_{ysc1}\left(x,y,t\right) = \frac{\lambda_N\left(y-y_0\right)}{4\pi\varepsilon_0} f_{2H}\left(x,y,x_0,x_0+v_N t,y_0\right), \tag{7}$$

where the geometrical function f_{2H} is given in equations A.9–A.13 in the Appendix.

The resulting electric fields are calculated for three different cases with the same leader parameters (see Table 4) as in Scenario 1 (In-cloud leader). The resulting waveforms are somewhat similar to the ones obtained in Scenario 1 (In-cloud leader) with higher peaks in Scenario 4 because the absence of the positive end of the leader increases the value of the field. This latter reason is particularly evident in Case 1 (Case 8 in Scenario 4), where the leader is at a high altitude above the ground and the contribution of the positive leader is close to the one of the negative leader, as their distances to the observation point are similar. The risetimes observed in Scenario 4 are similar to those in Scenario 1 (In-cloud leader) since they are mostly governed by the velocity of the negative leader.

Table 4
Input Parameters and the Resulting Rise Time (RT) and Peak Electric Field (E_{max}) for Scenario 4: Horizontal Leader During the CC Phase

	λ_N (C/km)	H (km)	v_N (m/s)	x_0 (km)	RT (ms)	E_{max}(kV/m)
Case 8	−0.1	4	5×10^4	−1.5	46.8	0.32
Case 9	−0.5	2	1×10^5	−3	35.6	7.47
Case 10	−1.5	1	2×10^5	−6	12.8	53.2

4. Upward Lightning Initiation Criteria

4.1. Aleksandrov et al. Model for the Corona Discharge

This section is based on the simplified analytical model developed by Aleksandrov et al. (2001) where the corona discharge from the tip of a tall structure (Figure 10a) is represented by a spherical electrode in free space as shown in Figure 10b (r_1, which tends to infinity, denotes the distance to the reference for the potential difference calculation), imposing the condition that the total potential on the surface of the sphere is at the same potential as the ground. This model neglects the contribution of the charges along the structure. Assuming a constant electric field along the z-axis, the background potential at the location of the sphere at the altitude h is $-Eh$, so that, in order to satisfy zero total potential condition, the potential due to the charge on the sphere is given by:

$$U \approx E_y h. \tag{8}$$

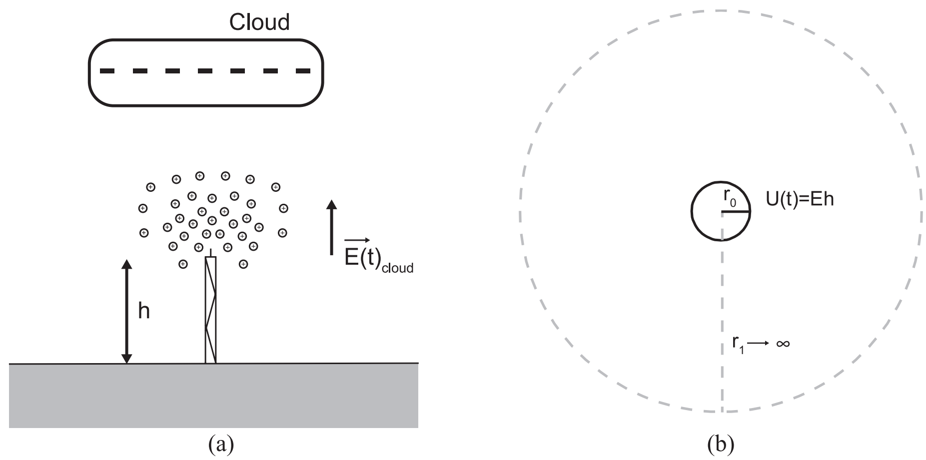

Figure 10. Corona discharge from the tip of a tall structure. (a) Positive corona discharge at the tip of a tall structure in the electric field of the cloud (adapted from Aleksandrov et al., 2001). (b) Simplified model representing the corona discharge using a spherical electrode in free space.

Now, assuming that the background electric field is not significant near the sphere compared to the electric field due to the charge on the sphere, this simple corona model can be used, as a first approximation, to evaluate the electric field on the top of a tall structure in the presence of corona charges. A more rigorous approach would require discretizing the structure and its image into elementary parts and imposing the zero-potential condition on each element. This procedure is used in the charge simulation method developed by Singer et al. (1974). That approach, although more accurate, is not used here because it does not allow a fully analytical solution. Aleksandrov et al. (2002) estimated the accuracy of the simplified sphere model by comparing it to a more realistic model of a grounded rod of height h and a hemispherical top of the same radius as the sphere, and they observed that the simple sphere model overestimates the electric field by a factor of less than two.

This simplified model is good enough for the analysis of the field near the electrode and it can yield more insights into the upward triggering mechanism using a qualitative analysis. If one were interested in obtaining the electric field at ground level next to the structure, the elaboration of a more realistic model of the structure would be needed. Such analysis was done analytically by Smorgonskiy, Egüz, et al. (2015) and numerically by Arcanjo et al. (2018), both based on the charge simulation method. Observations show that, depending on the height of the object, the measured electric field could be more than 10 times lower than the background electric field.

Note that, in our analysis, the background electric field will be caused either by the leader or by the return stroke, depending on the particular scenario being considered (see Figure 1). Here, we will briefly summarize the approach presented by Aleksandrov et al. (2001). The interested reader is referred to the original paper for more details.

If the electric field on the surface of the sphere is lower than the critical breakdown electric field, then the electric potential at a distance r from the center of the sphere in space outside of the sphere is obtained by solving Poisson's equation and the solution is:

$$U_{\text{no corona}}(r) = \frac{Ehr_0}{r}, \tag{9}$$

As soon as the field on the surface of the sphere exceeds the breakdown electric field (around 3 MV/m under standard conditions for an electrode with a radius bigger than a few centimeters), streamer-free corona discharge (electron avalanche), and therefore a current will be initiated. In order to evaluate the electric field, one has to solve the electrostatic Poisson's equation coupled with the balance equation for the space

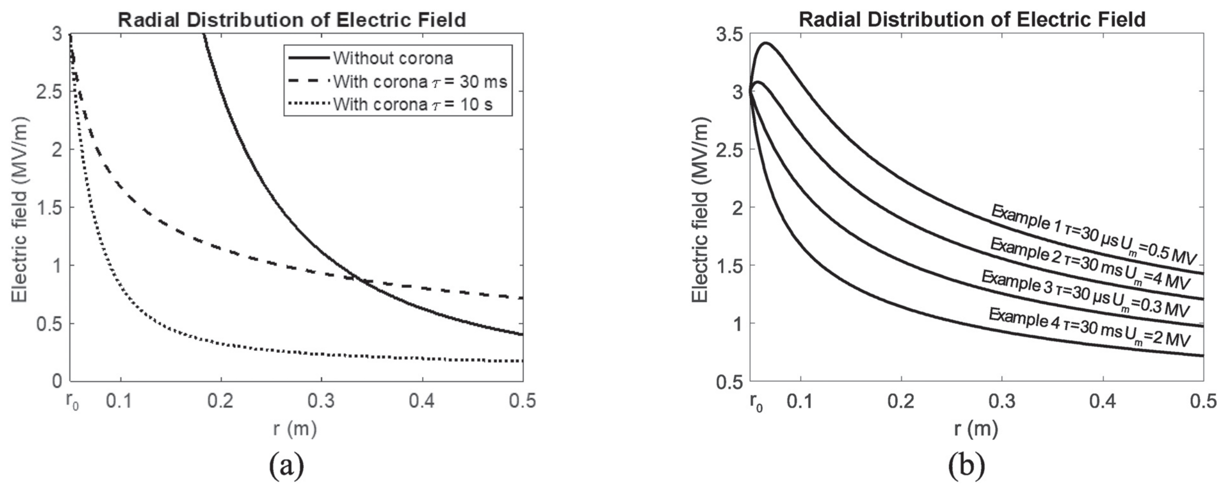

Figure 11. Electric field at the time of maximum voltage as a function of the radial distance. (a) 10-s risetime and 30-ms risetime $U_m = 2$ MV, $r_0 = 5$ cm. (b) 30-ms and 30-μs risetime for different peak voltages.

charge. Aleksandrov et al. (2001) obtained the following solution for the electric field as a function of the radial distance r outside of the sphere:

$$E(r) = \frac{1}{r^2}\sqrt{E_C^2 r_0^4 + \frac{i(t)\left(r^3 - r_0^3\right)}{6\pi\varepsilon_0\mu}}, \tag{10}$$

where μ is permeability of the vacuum, E_C is the threshold corona field and $i(t)$ is the current that can be obtained for the case of a voltage applied to the sphere as a result of the background electric field, of the form $U = U_m t^k$ at $t \le \tau_A$ and $U = U_m$ at $t > \tau_A$ as:

$$i(t) = 2\pi\varepsilon_0 U^{3/2}(t)\sqrt{\frac{(k+1)\mu}{6t}}, \tag{11}$$

the radius of the expanding ion cloud is given by:

$$R(t) = \sqrt{\frac{2\mu U(t)t}{3(k+1)}}, \tag{12}$$

in which $\mu = 1.5\ \text{cm}^2\text{V}^{-1}\text{s}^{-1}$ is the ion mobility (Chauzy & Rennela, 1985), r_0 is the radius of the sphere, and U is the voltage between the sphere and infinity (see Figure 10b) with peak value of U_m.

Figure 11a presents the electric field as a function of the radial distance considering two different risetimes for U. The voltage U is assumed to be linearly rising ($k = 1$) up to the maximum voltage $U_m = 2$ MV, beyond which it stays constant. The radius of the sphere is $r_0 = 5$ cm. This voltage could be for example induced on a 200-m tall structure under a background electric field of 10 kV/m (see Equation 8). We can observe from Figure 11a that the electric field is reduced significantly by the influence of the corona charges, both in the case of slow (10-s risetime) and fast (30-ms risetime) changes. In both cases, the predicted field without taking into account the effect of the corona charge is equal to 40 MV/m at $r = r_0$ (not seen in Figure 11a since it is out of the scale). When the corona charge is taken into account, the electric field on the surface of the sphere is equal to 3 MV/m in both cases. The analysis also shows that the reduction of the electric field is about four times more significant at a distance of $r = 0.5$ m for the case of a slow process (10-s risetime) compared with a faster process (30-ms risetime). At farther distances, the predicted electric field disregarding the corona charges will become smaller than those taking into account corona, since most of the voltage drop occurs close to the sphere.

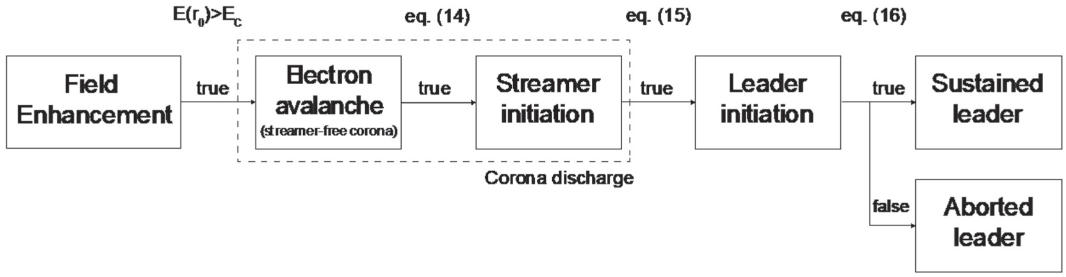

Figure 12. Conditions for sustained upward leader initiation.

4.2. Criteria for the Initiation of a Sustained Leader

In order for the streamers to be initiated from streamer-free corona discharge, the electric field has to be higher than the breakdown level over some critical length in front of the electrode. Note that corona discharge consists of both electron avalanches and streamers while Aleksandrov et al. (2001) refers to electron avalanche without streamers as streamer-free corona (see Figure 12). Aleksandrov et al. (2001) assumed that the condition

$$\frac{\partial E(r,t)}{\partial r}\Big|_{r=r_0} > 0, \tag{13}$$

is sufficient for the streamers to be initiated.

Figure 11b presents four examples with different voltage risetimes and peaks. The two considered risetimes are characteristic of the cases analyzed in the previous section, namely the leader propagation and the return stroke. Example 1 and Example 2 satisfy condition (13). Note that, for low risetimes, which are characteristic of return strokes, much lower voltages are required to satisfy condition (13) than in a case of the longer risetimes associated with leader propagation (see Figure 13 for more details).

In this section, we will discuss different criteria that have to be satisfied in order to have a sustained leader development. Once the electric field on the surface of the electrode reaches the critical breakdown electric field, streamer-free corona discharge will be initiated. This could lead to streamer initiation which is a necessary condition for the leader generation.

Further, if specific conditions are met, a leader will be initiated and, depending on the conditions, it can end up either as an aborted leader or continue to develop as a sustained leader. A graphical representation

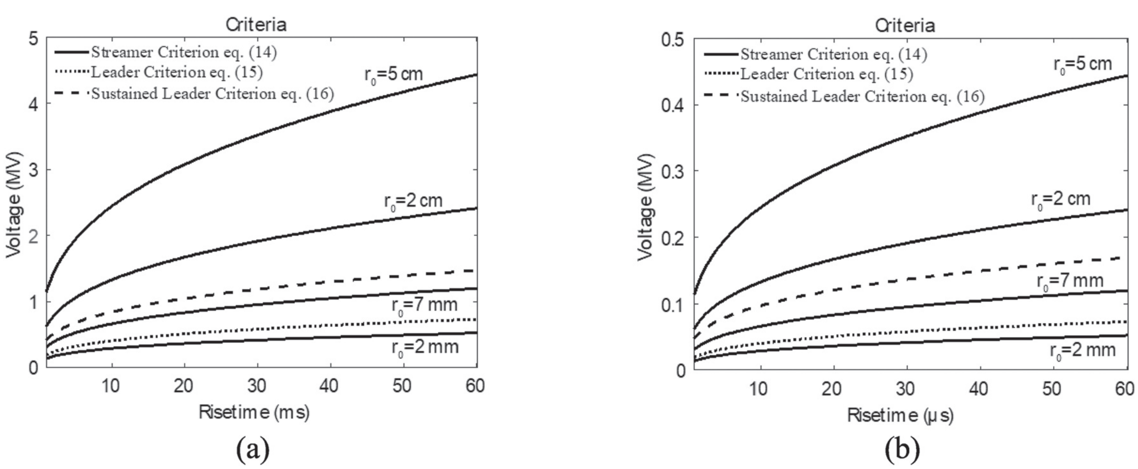

Figure 13. Minimum voltage criteria for upward leader development from a tall structure as a function of the field risetime. (a) Risetime characteristic of leader processes. (b) Risetime characteristic of return stroke processes.

illustrating the necessary conditions leading to the leader initiation and development is shown in Figure 12, which refers to equations that are given below.

In what follows, we will provide criteria for a sustained upward positive leader development as obtained by Aleksandrov et al. (2001). First, the electric field has to be higher than the critical breakdown electric field for the start of the streamer-free corona discharge.

Further, inserting (10) into (13), one can obtain a criterion for corona discharge (streamer-free) to streamer initiation for the case of a linearly rising voltage as:

$$U_m \geq 2E_C r_0 \left(\frac{6\mu E_C \tau}{r_0} \right)^{1/3}, \tag{14}$$

where τ is the risetime of the voltage and E_C is the critical electric field for the streamer-free corona discharge initiation.

Based on the fact that the minimum necessary length of the streamer zone for that streamer to evolve into leader called critical length (d_{cr}) is about 1 m (Bazelyan & Raizer Yu, 1998; Gallimberti, 1979; Meek & Craggs, 1978), and that the voltage drop (ΔU_{min}) along that distance has to be at least 400 kV (Aleksandrov et al., 2001; Bazelyan & Raizer Yu, 1998, 2000) derived the following condition for the upward leader initiation:

$$U_m \geq \frac{3}{2} \left(\frac{\Delta U_{min}^4 \mu}{2d_{cr}^2} \right)^{1/3} \approx 1.86\, \tau^{1/3} \left[MV \right]. \tag{15}$$

This condition can be satisfied by a voltage with either sufficiently high magnitude or a sufficiently low risetime. Furthermore, Aleksandrov et al. (2001) derived a criterion that has to be satisfied by an upward leader to escape the space charge cloud and not end up as aborted leader. This criterion is derived based on the condition that the background electric field is higher than the channel electric field opposing the former, so that the potential of the tip remains always higher than the background electric field potential. The criterion reads

$$U_m \geq 3.54\, \tau^{5/16} \left[MV \right]. \tag{16}$$

If (16) is not satisfied, the leader will stop propagating once the potential of the leader tip becomes equal to U_m. Note that (14–16) are derived for the case of a linearly rising voltage. In the following analysis, we use $E_c = 3$ MV/m.

4.3. Criteria Evaluation

In this section, we will use the initiation criteria (inequalities (14), (15), and (16)) to assess the ability of the scenarios discussed in Section 3 to initiate upward lightning from a tall structure. We will only discuss the field changes caused by these processes and we will not take into account the background electric field, which usually has much slower risetimes in the order of several seconds. This assumption is supported by the fact that corona charges at the tall structure will have had enough time to neutralize the slow background field in the proximity of the tower.

In our model, Scenario 2 (Positive leader approaching the ground) is taking into account the field change due to the prior Scenario 1 process. In Scenario 3 (Positive RS), the influence of the prior two scenarios (1 and 2) is omitted since the risetime of the positive RS is three orders of magnitude lower than that of the prior processes. Moreover, in the case of Scenario 3, the leader in these prior scenarios does not necessarily have to be passing above the tower as shown in Figure 1c, they could be directed away from the structure of interest. Finally, in Scenario 4, prior processes are again omitted since we assume that if the RS was close to the tall structure, it would have already triggered an upward flash before the CC phase.

Table 5
Minimum Height of the Structure for the Initiation of a Sustained Upward Leader

Case	E_m (kV/m)	τ	H (m)
1	0.06	39 ms	26,759
2	5.8	31 ms	254
3	52	12 ms	21
2a	5.75	31 ms	260
2b	3.5	22 ms	384
2c	1	18 ms	1260
4	10.3	68 µs	21.4
5	35	25 µs	4.6
6	5.3	23 µs	29.4
7	1.4	22 µs	110
8	0.21	47 ms	5312
9	5	36 ms	209
10	50.1	13 ms	21

These assumptions are made in order to use the derived analytical solution to assess each scenario individually. For a more thorough analysis, numerical methods can be used to estimate the background electric field resulting from the different prior processes. Note finally that the contribution from the background electric field could either support or oppose the triggering of the upward flash. It is not unconceivable that for some cases in Scenarios 3 and 4 that do not generate the required conditions to initiate an upward flash, the field contribution from prior processes could add constructively to support the initiation of an upward flash.

Criteria (15) and (16) only depend on the risetime and, for the risetimes of interest, the voltage given by criterion (16) is always higher that that given by (15). On the other hand, (14) depends also on the radius of the sphere.

The criteria for the minimum voltage for each of the processes (streamer, leader, sustained leader) are shown in Figure 13 as a function of the risetime. For the streamer criterion, the results are shown considering four different radiuses for the equivalent spherical electrode. If we consider the radius of the sphere to be in the range of about 3–10 mm, all of the streamers will develop at least to aborted leaders. If the radius is less than about 3 mm, the leader initiation will require a higher field than that required for the streamer. It is worth also noting that for sphere radiuses of less than 1 cm, a higher error in the analytical model is expected as discussed in Aleksandrov et al. (2001).

Considering that the lightning rods are sharp, it is reasonable to assume that the sphere radius is less than 1 cm. According to the above analysis, for a sphere radius less than 1 cm, condition (16) for the sustained upward leader requires higher fields than those required for streamer and leader initiation. Table 5 presents for all the considered cases, the minimum height of the structure so that condition (16) for a sustained leader is satisfied.

In order to obtain the excitation voltage given as:

$$U(t) = \begin{cases} U_m t, & t \le \tau \\ U_m, & t > \tau \end{cases}, \tag{17}$$

from the simulated results in Section 3, we made the following assumptions. The simulated waveforms are linear in the range from t_{10} to t_{90} (see Figure 2). We assume that E_m is equal to the electric field difference from t_{10} to t_{90} or 80% of E_{max} (see Figure 2). The risetime τ is equal to RT ($t_{90} - t_{10}$).

Further, we assume that the vertical electric field is constant along the height of the object so that U_m is simply given as the product of E_m with the height h. The resulting minimum heights of the structure to initiate a sustained upward leader are presented in Table 5 for the various considered cases.

We can observe that a weakly charged leader as those analyzed in cases 1 and 8 are not likely to trigger a sustained upward lightning during the leader propagation phase. In Case 2c, a sustained leader is unlikely because of the decrease of the field due to the presence of a positive leader close to the observation point. All other cases shown can trigger an upward flash from a tower with a reasonable height. Strongly charged leaders such as those in Cases 3 and 10 are also very likely to trigger a sustained upward leader. Also, all the Cases 4–7 with a fast risetime corresponding to the return stroke phase are capable of triggering lightning from relatively low structures. Note that, for some cases, the assumption of a constant electric field along the structure is questionable because of the high value of the minimum height (Cases 1, 2c, and 8). However, these high values suggest that no upward flashes can be initiated under such conditions.

Figure 14 presents the critical value of the electric field change as a function of the risetime for structures of different heights. These heights are representative of modern wind turbines. We assume that the lightning rod is sharp enough so that the criterium in Equation (16) is the most rigid one. Fast changes of about

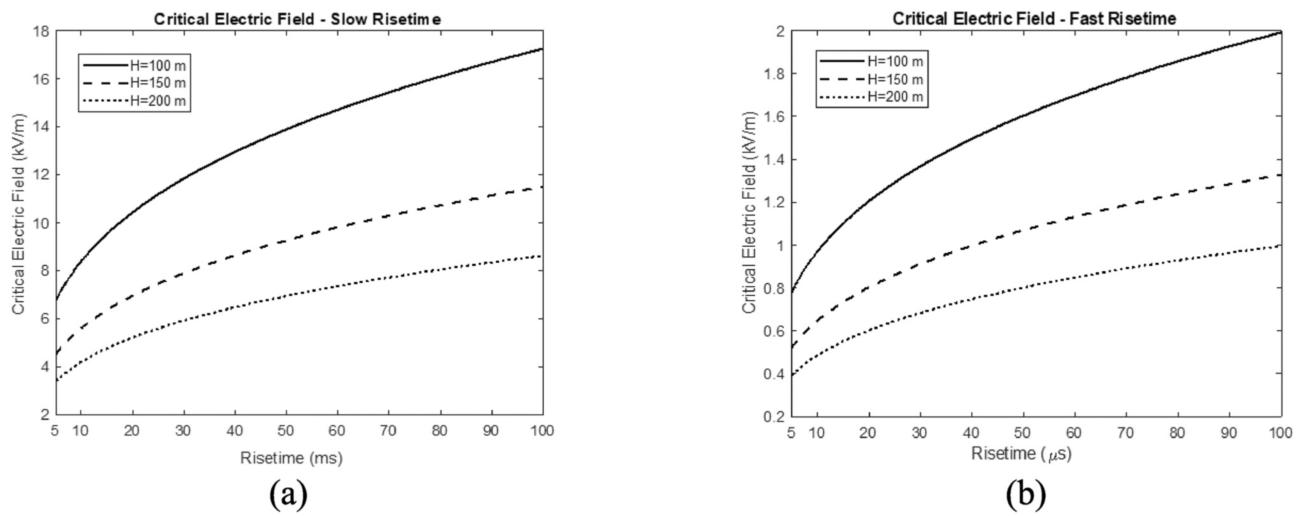

Figure 14. Critical electric field change for development of sustained leader as a function of the risetime for different tall structure heights. (a) Risetime characteristic of leader processes. (b) Risetime characteristic of return stroke processes.

1 kV/m typical for the nearby return strokes (distances of few km) can initiate a sustained leader while, in the case of slow risetimes typical of the nearby leader propagation, the electric field has to be several times higher. Note that these values could be significantly lower if the background cloud charge electric field was also considered. Also, it is worth noting that the simplified sphere model overestimates (by a factor of about 2) the fields in the vicinity of the sphere. As a result, the critical electric field to initiate an upward flash might be higher.

5. Discussion

A discussion is in order on the statistical occurrence of the observed scenarios, as reported by Schumann et al. (2019). For example, the lowest occurrence (9.5%) was observed for Scenario 2 (Positive leader approaching the ground), for which we observed the lowest magnitudes of the electric field. The fact that Scenario 4 (CC phase) has a much higher occurrence (52%) than Scenario 1 (In-cloud leader) with 13% can be explained by the higher amplitude of electric field and processes occurring prior to Scenario 4 (CC phase). Scenario 4 (CC phase) is preceded by scenarios 2 (Positive leader approaching the ground) and 3 (Positive RS), the contributions of which add up to the field enhancement at the tower. On the other hand, the relatively high occurrence of upward flashes after the RS phase might be due to its fast risetime and also to Scenario 2 (Positive leader approaching the ground) preceding it. Cloud-to-cloud lightning is about 2–10 times (Soriano & de Pablo, 2007) more common than cloud-to-ground lightning and this could explain the occurrence ratio of scenarios 1 (In-cloud leader) and 2 (Positive leader approaching the ground). For a more detailed analysis, one would have to take into account the general occurrence statistics of each scenario as well as the spatial extent. For example, while the RS is occurring at a given location, leaders can extend to several tens of km. We will not pursue this analysis since it is beyond the scope of this study.

The obtained results presented in Figure 14a suggest that electric fields in the order of only 1 kV/m from return strokes of positive flashes can potentially initiate an upward flash from a 100-m tall structure. Such field intensities are typical of return strokes at distances as far as a few kilometers. This finding is supported by experimental observations. Warner et al. (2012) observed upward lightning flashes to 10 communication towers with heights ranging from 91 to 191 m, which were preceded by positive CG flashes that occurred at distances ranging from 3.5 to 49 km from the towers. Smorgonskiy, Tajalli, et al. (2015) reported upward flashes to the 100-m tall Gaisberg Tower preceded by positive CG lightning at distances ranging from 300 m to 48.3 km from the tower. The observed cases involving preceding CG flashes at longer distances (of some tens of km) could be due to different reasons such as

- the presence of a strong background electric field.
- errors in the estimates of the locations of the preceding CG flashes provided by lightning location systems.
- some of these distant preceding events might have happened by chance without any causality relation to the upward flashes (Rubinstein et al., 2016).
- the fact that negative leaders during the CC phase can propagate several tens of kilometers. The propagation of the negative leader along the cloud base during tens (sometimes hundreds) of milliseconds were frequently observed by high-speed cameras and/or lightning mapping arrays for most of the cases analyzed in Brazil and the US (Saba et al., 2016; Schumann et al., 2019).

The above results are of significance for lightning protection of tall structures. For example, for a 200-m tall tower (typical of modern wind turbines), located in an area with a yearly ground flash density of about 3 flash/km^2, one would expect using Eriksson's empirical formula (Eriksson, 1987) 3.75 upward flashes, and a total of 37 flashes in the 1.5-km-radius area of around the tower (12.5 km^2). Assuming that on average 7.5% of the flashes are positive (Rakov, 2003) and taking into account that positive flashes tend to exhibit a single return stroke, we would have, out of the 37 flashes in this area, about 3 positive return strokes, which are able to produce fields that are high enough to initiate upward flashes. This reasoning applies if the considered structure is the only one in the area and located on a flat ground. If the tower is located on a mountainous area, the resulting number of upward flashes initiated by nearby positive strokes can be even higher. It is also worth noting that we do not consider the background electric field in this study, the effect of which can be very complex. For example, one could expect in the case when the positive CG flash is close to the tall structure that the cloud charge distribution above the tower creates an opposite field to that created by the return stroke in the positive flash, therefore impeding the initiation of an upward positive leader from the tower. On the other hand, if the return stroke location is far away, it is less likely that the cloud charge distribution above the tower would impede the upward leader initiation. Note also that in the case of the three leader scenarios (I, II and IV), the amplitude of the electric field change will depend strongly on the altitude of the leader above the ground.

It is finally important to note the limitations of both the model used for the field calculation and the simplified corona model. The field calculation is based on an electrostatic assumption, which can be considered as reasonable for the leader processes and the considered distances (see also, Rachidi et al., 1997; Rubinstein et al., 1995). The application of the electrostatic model to the faster RS process is more questionable, even though positive return strokes (considered in this work) are characterized by slower risetimes compared to negative return strokes. Furthermore, we use a fairly simple geometry of horizontal and vertical leaders without taking into account any branching. A more complex leader geometry can be represented with a combination of horizontal and vertical leaders or by discretizing the leader and obtaining numerical solution.

The corona discharge model is based on a simplified spherical electrode representation. As previously noted, the electric fields predicted by such model could overestimate the fields by a factor as high as 2. The criteria for leader and sustained leader development are based on a combination of results obtained by the model and by observations. Some other external parameters, such as the wind speed, atmospheric conditions and the air chemistry might also play a role. We also do not consider electric field changes prior to any specific event. Despite the above-mentioned limitations, the proposed model can provide a qualitative insight into the mechanisms of upward leader initiation from tall structures. Note finally that the derived electrostatic model is valid for estimating the electric field enhancement in case of both positive and negative upward lightning, while the corona model is based on a positive corona discharge and it is only valid for modeling a negative upward lightning.

6. Summary and Conclusion

We have derived analytical formulas to describe the electrostatic field changes associated with horizontal and vertical leaders. These formulas were then used to evaluate the field in four different scenarios leading to the triggering of an upward flash from a tower, as observed by Schumann et al. (2019). The obtained results indicate that the three scenarios in which the initiation of the upward lightning occurs during the leader propagation phase exhibit similar peak values and risetimes. Scenarios 1 (In-cloud leader) and 4 (CC phase) result in almost the same waveform (see Figure 4 and 9), mainly due to the fact that most of the field at the observation point is due to the closest part of the leader. Scenario 2 (Positive leader approaching the ground) results in a slightly lower field peak compared to scenarios 1 (In-cloud leader) and 4 (CC phase), depending on how far the downward propagating leader is from the observation point. The order of magnitude of the electric field change associated with a 3-km away return stroke is similar to that of a horizontal leader passing above the tower, however with different risetimes.

We then used the criteria for an upward negative leader initiation obtained from a simplified corona model to estimate the minimum height of a tall structure for an upward flash to be initiated. Due to its relatively fast risetimes, the return stroke phase can trigger upward flashes with fields that are about 10 times lower than in the case of slower leader propagation processes for a structure of a given height.

It is worth noting that the simplified criteria used to evaluate the initiation of the upward leader can only be used in the case of one linear excitation with respect to time. We have considered only the field change associated with each scenario and disregarded the background electric field, which might have an appreciable effect on the initiation of an upward flash. We can assume that even the cases with less favorable geometrical and electrical properties could trigger an upward flash depending on how close the value of the background electric field was to the value necessary for the so-called self-initiated upward lightning.

The main contributions of this paper can be summarized as follows:

(i) We derived analytical solutions for leader/RS geometries associated with the observed scenarios leading to the initiation of upward flashes from a tall structure. The resulting field enhancement was used in a simplified corona model at the tip of a tall structure.
(ii) The obtained results suggest that it is possible for an upward negative lightning to be triggered by nearby lightning activity, either during a relatively slow leader propagation phase, or after the faster return stroke phase. In most of the analyzed cases, the field change due to nearby lightning activity was high enough to trigger an upward flash from a structure of moderate height, even without the background electric field.
(iii) Slow processes of leader propagation have the fastest risetime and highest amplitude as the leader is passing just above the observation point since the tangential component of the speed with respect to the ground surface is at its maximum and the distance to the leader is at its minimum.
(iv) Nearby return strokes with relatively fast risetimes (some tens of microseconds) are able to trigger upward negative flashes even for field enhancements about 10 times lower than in the case of slower leader propagation processes (risetime of some tens of milliseconds).
(v) The obtained results suggest that electric fields in the order of only 1 kV/m from nearby positive return strokes can potentially initiate an upward flash from a 100-m tall structure. Such field intensities are typical of return strokes at distances as large as a few kilometers.

Appendix: Derivation of the Fields Associated with the 4 Scenarios Leading to the Initiation of an Upward Lightning from a Tall Structure

Let us start with the derivation of the electric field of a horizontal line charge above a perfectly conducting ground as shown in Figure 14a. The electric potential of an arbitrary charge distribution at a given point (x,y) in free space can be calculated as:

$$V = \frac{1}{4\pi\varepsilon_0}\int\frac{\mathrm{d}q}{r}. \tag{A.1}$$

In the case of a horizontal linear charge density λ, (1) can be expressed as

$$V_H\left(x,y\right) = \frac{1}{4\pi\varepsilon_0}\int_{x_1'}^{x_2'}\frac{\lambda\left(x'\right)\mathrm{d}x'}{\sqrt{\left(x-x'\right)^2+\left(y-y'\right)^2}}. \tag{A.2}$$

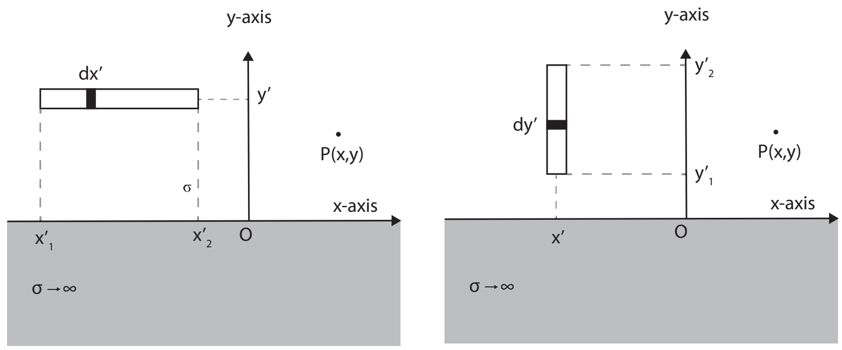

Figure A1. Geometry of problem. Leader above a perfectly conducting ground. (a) Horizontal leader. (b) Vertical leader. The leader channel radius is assumed to be infinitesimally small.

Note that y′ is constant for a specific geometry of the leader. For the time being, we are ignoring the presence of the perfectly conducting ground. This will be taken into account later using image theory. If we assume a constant linear charge density, the integral in (A.2) can be solved analytically. Note that (A.2) can also be solved analytically for some other simplified charge distributions such as a linear distribution. The solution for a constant linear charge density is:

$$V\left(x,y\right)=\frac{-\lambda}{4\pi\varepsilon_0}\ln\left(\left|\frac{x-x_2'+\sqrt{\left(x-x_2'\right)^2+\left(y-y'\right)^2}}{x-x_1'+\sqrt{\left(x-x_1'\right)^2+\left(y-y'\right)^2}}\right|\right). \tag{A.3}$$

Note that the minus sign comes from solving the integral and using the substitution t = x−x′. The components of the electric field can be obtained as follows:

$$\overrightarrow{E_{xH}}\left(x,y\right)=-\frac{\partial V\left(x,y\right)}{\partial x}\widehat{e_x}, \tag{A.4}$$

$$\overrightarrow{E_{yH}}\left(x,y\right)=-\frac{\partial V\left(x,y\right)}{\partial y}\widehat{e_y}. \tag{A.5}$$

Plugging (A.3) into (A.4) and (A.5), we obtain:

$$E_{xH}\left(x,y\right)=\frac{\lambda}{4\pi\varepsilon_0}\left(\frac{1}{R_{2H}}-\frac{1}{R_{1H}}\right)=\frac{\lambda}{4\pi\varepsilon_0}f_{1H}\left(x,y,x_1',x_2',y'\right), \tag{A.6}$$

$$E_{yH}\left(x,y\right)=\frac{\lambda\left(y-y'\right)}{4\pi\varepsilon_0}\left(\frac{1}{A_HR_{1H}}+\frac{1}{B_HR_{2H}}\right)=\frac{\lambda\left(y-y'\right)}{4\pi\varepsilon_0}f_{2H}\left(x,y,x_1',x_2',y'\right), \tag{A.7}$$

where f_{1H} and f_{2H} are:

$$f_{1H}\left(x,y,x_1',x_2',y'\right)=\left(\frac{1}{R_{2H}}-\frac{1}{R_{1H}}\right), \tag{A.8}$$

$$f_{2H}\left(x,y,x_1',x_2',y'\right)=\left(\frac{1}{A_HR_{1H}}+\frac{1}{B_HR_{2H}}\right), \tag{A.9}$$

and the coefficients R_{1H}, R_{2H}, A_H, and B_H are:

$$R_{1H}=\sqrt{\left(x-x_1'\right)^2+\left(y-y'\right)^2}, \tag{A.10}$$

$$R_{2H} = \sqrt{\left(x - x_2'\right)^2 + \left(y - y'\right)^2}, \tag{A.11}$$

$$A_H = x - x_1' + R_{1H}, \tag{A.12}$$

$$B_H = x - x_2' + R_{2H}. \tag{A.13}$$

Note that (A.12) or (A.13) can be zero in the particular case when

$$y = y', \tag{A.14}$$

and when either

$$x - x_1' < 0, \tag{A.15}$$

Or

$$x - x_2' < 0. \tag{A.16}$$

which leads to a field solution tending to infinity. This singularity comes from the fact that the analytical solution of the integral in (A.2) is not defined at points $y = y'$. Note that this does not impose any limitation to the model since the line charge density is assumed to be infinitely thin, so the singularity can be avoided.

We will now take into account the presence of a perfectly conducting ground. Using image theory, the total electric field at any point with positive y coordinate will simply be the sum of the original source and the image source (denoted with the superscript *) with the same charge density of the source but with an opposite polarity.

$$E_{xHPCG}\left(x, y\right) = E_{xH}\left(x, y\right) + E_{xH}^{*}\left(x, y\right), \tag{A.17}$$

$$E_{yHPCG}\left(x, y\right) = E_{yH}\left(x, y\right) + E_{yH}^{*}\left(x, y\right). \tag{A.18}$$

The electric field components of the image source can be readily calculated making the following substitutions in Equations (A.6–A.13)

$$\lambda \rightarrow -\lambda, \tag{A.19}$$

$$y' \rightarrow -y', \tag{A.20}$$

to take into account the change of charge polarity and the location of the image.

A similar procedure can be followed in the case of a vertical leader shown in Figure A.1b. Note that this is the same problem in free space since only the source has been rotated. The electric field (ignoring the presence of the ground) can be obtained as:

$$E_{xV}\left(x, y\right) = \frac{\lambda\left(x - x'\right)}{4\pi\varepsilon_0}\left(\frac{1}{A_V R_{1V}} + \frac{1}{B_V R_{2V}}\right) = \frac{\lambda\left(x - x'\right)}{4\pi\varepsilon_0} f_{1V}\left(x, y, x', y_1', y_2'\right), \tag{A.21}$$

$$E_{yV}\left(x, y\right) = \frac{\lambda}{4\pi\varepsilon_0}\left(\frac{1}{R_{2V}} - \frac{1}{R_{1V}}\right) = \frac{\lambda}{4\pi\varepsilon_0} f_{2V}\left(x, y, x', y_1', y_2'\right), \tag{A.22}$$

where f_{1V} and f_{2V} are:

$$f_{1V}\left(x, y, x', y_1', y_2'\right) = \left(\frac{1}{A_V R_{1V}} + \frac{1}{B_V R_{2V}}\right), \tag{A.23}$$

$$f_{2V}\left(x, y, x', y_1', y_2'\right) = \left(\frac{1}{R_{2V}} - \frac{1}{R_{1V}}\right), \tag{A.24}$$

and the coefficients R_{1V}, R_{2V}, A_V, and B_V are given by:

$$R_{1V} = \sqrt{\left(x - x'\right)^2 + \left(y - y_1'\right)^2}, \tag{A.25}$$

$$R_{2V} = \sqrt{\left(x - x'\right)^2 + \left(y - y_2'\right)^2}, \tag{A.26}$$

$$A_V = y - y_1' + R_{1V}, \tag{A.27}$$

$$B_V = y - y_2' + R_{2V}. \tag{A.28}$$

Again, the presence of a perfectly conducting ground is accounted for with the use of image theory. The total electric field at any point with positive y coordinate will be the sum of the field from the original source and the field from the image source with the same charge density of the original source but with an opposite polarity:

$$E_{xVPCG}\left(x, y\right) = E_{xV}\left(x, y\right) + E_{xV}^{*}\left(x, y\right), \tag{A.29}$$

$$E_{yVPCG}\left(x, y\right) = E_{yV}\left(x, y\right) + E_{yV}^{*}\left(x, y\right). \tag{A.30}$$

The electric field components of the image source can be readily calculated from (A.6) to (A.7) making the following substitutions:

$$\lambda \rightarrow -\lambda, \tag{A.31}$$

$$y_1' \rightarrow -y_2', \tag{A.32}$$

$$y_2' \rightarrow -y_1', \tag{A.33}$$

Let us derive the electric field as a function of time for the geometry shown in Figure 3a. In order to obtain the time-domain waveform of the electric field, we will consider the leader propagation as a series of electrostatic steps. Defining the points x_1 and x_2 as:

$$x_1 = x_0 - v_P t, \tag{A.34}$$

$$x_2 = x_0 + v_N t. \tag{A.35}$$

We can now obtain $E_y\left(x, y, t\right)$ from Equation (A.7) for both the positive and the negative leader by setting, for the positive leader:

$$x_1' = x_1, \tag{A.36}$$

$$x_2' = x_0, \tag{A.37}$$

and, for the negative leader:

$$x_1' = x_0, \tag{A.38}$$

$$x_2' = x_2, \tag{A.39}$$

with:

$$y' = y_0, \tag{A.40}$$

for both positive and negative leaders.

We choose the value of the linear charge density for the positive charge to be:

$$\lambda_P = -\frac{v_P}{v_N}\lambda_N, \tag{A.41}$$

so that the overall net charge along the leader is equal to zero. The vertical field at any point (x, y) is then given by:

$$E_{ysc1}\left(x,y,t\right) = \frac{\lambda_N\left(y-y_0\right)}{4\pi\varepsilon_0}\left(f_{2H}\left(x,y,x_0,x_0+v_2t,y_0\right)-\frac{v_N}{v_P}f_{2H}\left(x,y,x_0-v_1t,x_0,y_0\right)\right) \tag{A.42}$$

Figure 5a presents the sketch of the second scenario where the positive end of the initially horizontal leader bends toward the ground. We will assume that this happens at a time T_1. The electric field for times smaller than T_1 can be obtained using the expression derived in the previous subsection. The total vertical electric field due to the positive leader can be expressed as

$$E_{y\,sc2}\left(x,y,t\right) = \begin{cases} E_{y\,sc1}\left(t\right), & t \le T_1 \\ E_{y2}\left(t\right), & t > T_1 \end{cases}. \tag{A.43}$$

At time T_1, the positive leader will reach the coordinate:

$$x_{\mathrm{TD}} = x_0 - v_P T_1. \tag{A.44}$$

The negative part of the leader will be treated as in previous section. The field due to the positive part of the leader in the vertical channel will be given by Equation (A.22) with:

$$x' = x_{T_1}, \tag{A.45}$$

$$y_1' = y_0 - v_P\left(t - T_1\right), \tag{A.46}$$

$$y_2' = y_0\,. \tag{A.47}$$

Finally, the electric field E_{y2} can be obtained as:

$$\begin{aligned} E_{y2}\left(x,y,t\right) \;=\; & \frac{\lambda_N\left(y-y_0\right)}{4\pi\varepsilon_0}\left(f_{2H}\left(x,y,x_0,x_0+v_2t,y_0\right)-\frac{v_N}{v_P}f_{2H}\left(x,y,x_0-v_1,T_1,x_0,y_0\right)\right) \\ & -\frac{\lambda_N v_N}{4\pi\varepsilon_0 v_P}f_{2V}\left(x,y,x_{T_1},y_0-v_P\left(t-T_1\right)\right) \end{aligned} \tag{A.48}$$

The return stroke is represented by a negative line charge propagating upward from the ground to the initiation point as shown in Figure 7a with the same line charge density as in the preceding downward positive leader but with an opposite sign. The vertical electric field due to the return stroke is given by:

$$E_{y\,sc3}\left(x,y,t\right) = \begin{cases} E_{y1}\left(t\right), & t \le T_2 \\ E_{y2}\left(t\right) = E_{y1}\left(T_2\right) + E_{y2}'\left(t\right), & t > T_2 \end{cases}, \tag{A.49}$$

where T_2 is the time when the return stroke front reaches the maximum height y_0 given by:

$$T_2 = \frac{y_0}{v_{\mathrm{RS}}}. \tag{A.50}$$

$E_{y1}(t)$ can be calculated using Equation (A.22) with the following substitutions:

$$x' = x_{\mathrm{RS}}, \tag{A.51}$$

$$y_1^{'} = 0, \tag{A.52}$$

and:

$$y_2^{'} = v_{\mathrm{RS}} t, \tag{A.53}$$

We obtain:

$$E_{y1}\left(x, y, t\right) = -\frac{\lambda_P}{4\pi\varepsilon_0} f_{2V}\left(x, y, x_{\mathrm{RS}}, 0, v_{\mathrm{RS}} t\right), \tag{A.54}$$

where the negative sign is due to the fact that the positive return stroke is neutralizing positive charges along the channel.

After the return stroke front reaches the maximum altitude, the contribution of the horizontal part can be taken into account by plugging the following expressions

$$x_1^{'} = x_{\mathrm{RS}}, \tag{A.55}$$

$$x_2^{'} = x_{\mathrm{RS}} + v_{\mathrm{RS}}\left(t - T_2\right), \tag{A.56}$$

$$y' = y_0, \tag{A.57}$$

into Equation (A.7), which yields

$$E_{y2}\left(x, y, t\right) = -\frac{\lambda_P}{4\pi\varepsilon_0}\left(f_{2V}\left(x, y, x_{\mathrm{RS}}, 0, v_{\mathrm{RS}} T_2\right) + \left(y - y_0\right) f_{2H}\left(x, y, x_{\mathrm{RS}}, x_{\mathrm{RS}} + v_{\mathrm{RS}}\left(t - T_2\right), y_0\right)\right), \tag{A.58}$$

To evaluate the electric field associated with Scenario 4 illustrated in Figure 9a, we can use again Equation (A.7) with the following parameters:

$$x_1^{'} = x_0, \tag{A.59}$$

$$x_2^{'} = v_N t, \tag{A.60}$$

with:

$$y' = y_0. \tag{A.61}$$

The final expression can be straightforwardly obtained as:

$$E_{y\,sc4}\left(x, y, t\right) = \frac{\lambda_N\left(y - y_0\right)}{4\pi\varepsilon_0} f_{2H}\left(x, y, x_0, x_0 + v_N t, y_0\right). \tag{A.62}$$

Data Availability Statement

The source code for the analytical solutions can be found online at https://github.com/IToni93/other_triggered_lightning_analytical.git (Sunjerga, Rubinstein, Rachidi, & Cooray, 2020). An interactive interface can also be found at https://IToni93.github.io/other_triggered_lightning_analytical/.

Acknowledgments
This work was supported in part by the Swiss National Science Foundation (Project No. 200020_175594). The authors would like to thank Prof. Marcelo Saba and two anonymous reviewers for their careful review of our manuscript and their many insightful comments and suggestions that helped us improve the quality of the paper.

References

Aleksandrov, N. L., Bazelyan, E. M., Carpenter, R. B., Jr, Drabkin, M. M., & Raizer, Y. P. (2001). The effect of coronae on leader initiation and development under thunderstorm conditions and in long air gaps. *Journal of Physics D: Applied Physics*, *34*(22), 3256–3266. https://doi.org/10.1088/0022-3727/34/22/309

Aleksandrov, N. L., Bazelyan, E. M., Drabkin, M. M., Carpenter, R. B., Jr, & Raizer, Y. P. (2002). Corona discharge at the tip of a tall object in the electric field of a thundercloud. *Plasma Physics Reports*, *28*(11), 953–964. https://doi.org/10.1134/1.1520289

Arcanjo, M., Mazala, K., Guimaraes, M., & Visacro, S. (2018). *Estimating the electric field above the top of grounded structures upon UCL initiation in CG lightning from close E-field measured over the ground*. Presented at the 2018 34th International Conference on Lightning Protection (ICLP). IEEE. https://doi.org/10.1109/iclp.2018.8503316

Bazelyan, E. M., & Raizer Yu, P. (1998). *Spark discharge*. Boca Raton, FL: CRC Press.

Bazelyan, E. M., & Raizer Yu, P. (2000). *Lightning physics and lightning protection*. Bristol: IOPP.

Berger, K., & Vogelsanger, E. (1969). New results of lightning observations. In S. C. Coroniti, & J. Hughes (Eds.), *Planeteary electrodynamics* (pp. 498–510). New York, NY: Gordon and Breach.

Campos, L. Z. S., Saba, M. M. F., Warner, T. A., Pinto, O., Jr, Krider, E. P., & Orville, R. E. (2014). High-speed video observations of natural cloud-to-ground lightning leaders—A statistical analysis. *Atmospheric Research*, *135–136*, 285–305. https://doi.org/10.1016/j.atmosres.2012.12.011

Campos, Z. S., Saba, M. M., Warner, T. A., Krider, E. P., Cummins, K. L., & Orville, R. E. (2010). Does the average downward speed of a lightning leader change as it approaches the ground? – An observational approach. *Paper presented at International. Conferences on Lightning. Vaisala*.

Chauzy, S., & Rennela, C. (1985). Computed response of the space charge layer created by corona at ground level to external electric field variations beneath a thundercloud. *Journal of Geophysical Research*, *90*(D4), 6051. https://doi.org/10.1029/jd090id04p06051

Cooray, V. (1995). A model for positive return strokes Inst. *Journal of Physics Conference Series*, *143*, 363–371.

Cooray, V. (2000). The modelling of positive return strokes in lightning flashes. *Journal of Atmospheric and Solar-Terrestrial Physics*, *62*(3), 169–187. https://doi.org/10.1016/s1364-6826(99)00056-5

Eriksson, A. J. (1987). The incidence of lightning strikes to power lines. *IEEE Transactions on Power Delivery*, *2*(3), 859–870. https://doi.org/10.1109/tpwrd.1987.4308191

Gao, Y., Chen, M., Lyu, W., Qi, Q., Qin, Z., Du, Y., & Zhang, Y. (2020). Leader charges, currents, ambient electric fields, and space charges along downward positive leader paths retrieved from ground measurements in metropolis. *Journal of Geophysical Research: Atmosphere*, *125*(19). https://doi.org/10.1029/2020jd032818

Kasemir, H. W. (1960). A contribution to the electrostatic theory of a lightning discharge. *Journal of Geophysical Research*, *65*(7), 1873–1878. https://doi.org/10.1029/jz065i007p01873

Lin, Y. T., Uman, M. A., Tiller, J. A., Brantley, R. D., Beasley, W. H., Krider, E. P., & Weidman, C. D. (1979). Characterization of lightning return stroke electric and magnetic fields from simultaneous two-station measurements. *Journal of Geophysical Research*, *84*(C10), 6307. https://doi.org/10.1029/jc084ic10p06307

Meek, J. M., & Craggs, I. D. (1978). *Electrical breakdown of gases*. New York, NY: Wiley.

Montanyà, J. (2014). Turbines shoot upside-down lightning. *Nature*, *506*(7488), 268. https://doi.org/10.1038/506268a

Proctor, D. E. (1997). Lightning flashes with high origins. *Journal of Geophysical Research: Atmosphere*, *102*(D2), 1693–1706. https://doi.org/10.1029/96jd02635

Rachidi, F., Rubinstein, M., Guerrieri, S., & Nucci, C. A. (1997). Voltages induced on overhead lines by dart leaders and subsequent return strokes in natural and rocket-triggered lightning. *IEEE Transactions on Electromagnetic Compatibility*, *39*(2), 160–166. https://doi.org/10.1109/15.584939

Rachidi, F., Rubinstein, M., Montanya, J., Bermudez, J.-L., Rodriguez Sola, R., Sola, G., & Korovkin, N. (2008). A review of current issues in lightning protection of new-generation wind-turbine blades. *IEEE Transactions on Industrial Electronics*, *55*(6), 2489–2496. https://doi.org/10.1109/tie.2007.896443

Rakov, V. A. (2003). A review of positive and bipolar lightning discharges. *Bulletin of the American Meteorological Society*, *84*(6), 767–776. https://doi.org/10.1175/bams-84-6-767

Rakov, V. A., & Uman, M. A. (2003). *Lightning: Physics and effects*. Cambridge: Cambridge University Press.

Rubinstein, M., Zuber, J., Smorgonskiy, A., Rachidi, F., & Diendorfer, G. (2016). Correlation vs. causality in other-triggered upward lightning in tower flashes. *Paper presented at 2016 33rd International Conference on Lightning Protection (ICLP)*. IEEE. https://doi.org/10.1109/iclp.2016.7791360

Saba, M. M. F., Schumann, C., Warner, T. A., Ferro, M. A. S., de Paiva, A. R., Helsdon, J., Jr, & Orville, R. E. (2016). Upward lightning flashes characteristics from high-speed videos. *Journal of Geophysical Research: Atmosphere*, *121*(14), 8493–8505. https://doi.org/10.1002/2016jd025137

Schumann, C., Saba, M. M. F., Warner, T. A., Ferro, M. A. S., Helsdon, J. H., Jr, Thomas, R., & Orville, R. E. (2019). On the triggering mechanisms of upward lightning. *Scientific Reports*, *9*(1). https://doi.org/10.1038/s41598-019-46122-x

Shen, Y., Chen, M., Du, Y., & Dong, W. (2019). Line charge densities and currents of downward negative leaders estimated from VHF images and VLF electric fields observed at close distances. *IEEE Transactions on Electromagnetic Compatibility*, *61*(5), 1507–1514. https://doi.org/10.1109/temc.2018.2864199

Singer, H., Steinbigler, H., & Weiss, P. (1974). A charge simulation method for the calculation of high voltage fields. *IEEE Transactions on Power Apparatus and Systems, PAS-*, *93*(5), 1660–1668. https://doi.org/10.1109/tpas.1974.293898

Smorgonskiy, A., Egüz, E., Rachidi, F., Rubinstein, M., & Cooray, V. (2015). A model for the evaluation of the electric field associated with the lightning-triggering rocket wire and its corona. *Journal of Geophysical Research: Atmosphere*, *120*(20), 10–964. https://doi.org/10.1002/2015jd023373

Smorgonskiy, A., Rachidi, F., Rubinstein, M., Diendorfer, G., & Schulz, W. (2011). On the proportion of upward flashes to lightning research towers. *Presented at the 2011 7th Asia-Pacific International Conference on LightningAPL*. Elsevier. https://doi.org/10.1109/apl.2011.6110248

Smorgonskiy, A., Tajalli, A., Rachidi, F., Rubinstein, M., Diendorfer, G., & Pichler, H. (2015). An analysis of the initiation of upward flashes from tall towers with particular reference to Gaisberg and Säntis Towers. *Journal of Atmospheric and Solar-Terrestrial Physics*, *136*, 46–51. https://doi.org/10.1016/j.jastp.2015.06.016

Soriano, L. R., & de Pablo, F. (2007). Total flash density and the intracloud/cloud-to-ground lightning ratio over the Iberian Peninsula. *Journal of Geophysical Research: Atmosphere*, *112*(D13). https://doi.org/10.1029/2006jd007624

Stock, M. G., Krehbiel, P. R., Lapierre, J., Wu, T., Stanley, M. A., & Edens, H. E. (2017). Fast positive breakdown in lightning. *Journal of Geophysical Research: Atmosphere*, *122*(15), 8135–8152. https://doi.org/10.1002/2016jd025909

Sunjerga, A., Mostajabi, A., Rachidi, F., Pineda, N., Romero, D., Van der Velde, O. A., et al. (2018). On the classification of self-triggered versus OtherTriggered lightning flashes. *Presented at the 2018 34th International Conference on Lightning Protection ICLP*. IEEE. https://doi.org/10.1109/iclp.2018.8503322

Sunjerga, A., Rubinstein, M., Pineda, N., Mostajabi, A., Azadifar, M., Romero, D., et al. (2020). LMA observations of upward lightning flashes at the Säntis Tower initiated by nearby lightning activity. *Electric Power Systems Research*, *181*, 106067. https://doi.org/10.1016/j.epsr.2019.106067

Sunjerga, A., Rubinstein, M., Rachidi, F., & Cooray, V. (2020). *On the initiation of upward negative lightning by nearby lightning activity: An analytical approach – Source code (v1.0.0)*. Zenodo. https://doi.org/10.5281/ZENODO.4321780

Thomson, E. M., Uman, M. A., & Beasley, W. H. (1985). Speed and current for lightning stepped leaders near ground as determined from electric field records. *Journal of Geophysical Research: Atmospheres*, *90*(D5), 8136–8142. https://doi.org/10.1029/jd090id05p08136

Uman, M. A. (1987). *The lightning discharge*. New York, NY: Academic.

van der Velde, O. A., & Montanyà, J. (2013). Asymmetries in bidirectional leader development of lightning flashes. *Journal of Geophysical Research: Atmosphere*, *118*(24), 13–504. https://doi.org/10.1002/2013jd020257

Wang, D., Takagi, N., Watanabe, T., Sakurano, H., & Hashimoto, M. (2008). Observed characteristics of upward leaders that are initiated from a windmill and its lightning protection tower. *Geophysical Research Letters*, *35*(2). https://doi.org/10.1029/2007gl032136

Warner, T. A., Cummins, K. L., & Orville, R. E. (2012). Upward lightning observations from towers in Rapid City, South Dakota and comparison with national lightning detection network data, 2004–2010. *Journal of Geophysical Research: Atmosphere*, *117*(D19). https://doi.org/10.1029/2012jd018346

Paper V

35th International Conference on Lightning Protection
XVI International Symposium on Lightning Protection
20th to 26th September 2021 - Sri Lanka
ICLP-SIPDA SRI LANKA 2021

Incidence of Upward Lightning Triggered by Nearby Lightning: A Monte Carlo Simulation

Antonio Sunjerga*, Farhad Rachidi
EMC Laboratory
EPFL
Lausanne, Switzerland
*antonio.sunjerga@epfl.ch

Marcos Rubinstein
University of Applied Sciences and Arts of Western Switzerland
Yverdon-les-Bains, Switzerland

Vernon Cooray
Department of Engineering Sciences,
Uppsala University
Uppsala, Sweden

***Abstract*— Upward lightning is the dominant type of lightning discharge to tall structures. It has been observed that a significant number of these upward flashes are initiated by nearby lightning activity. The aim of this study is to estimate the incidence of upward lightning flashes from tall structures caused by nearby lightning based on Monte Carlo simulations and using a simplified electrostatic and corona model. We present the spatial distribution of different nearby lightning events that can potentially trigger upward lightning from a given structure. Our results suggest that Eriksson's empirical formulas might significantly underestimate the total number of flashes to a tall structure.**

Keywords—lightning, upward, triggered, other-triggered, Monte Carlo, incidence

I. Introduction

Upward lightning initiation has been observed either due to the slowly rising background electric field caused by cloud charges (the so-called 'self-triggered' or 'self-initiated'), or due to the faster electric field changes caused by nearby lightning ('other-triggered') [1], superimposed on the slow background electric field. The estimation of the number of upward flashes from a given structure is of high importance for determining the risk level for vulnerable structures such as tall wind turbines built from nonconducting materials.

Simple empirical equations exist to estimate the number of downward and upward lightning flashes to a structure of a given height, such as the formula derived by Eriksson [2] or the one defined in the IEC standard 61400-24:2010 for lightning protection of wind turbines [3]. However, field observations suggest that these formulas underestimate the number of flashes [4-6]. Becerra et al. [7] estimated that both downward and self-initiated upward lightning can be responsible for only a limited number of flashes, 8 to 20% of observed events.

Saba et al. [8] and Schumann et al. [9] observed four different scenarios leading to the triggering of an upward flash from a tower (see Figure 6-8 in [9]). One of them is due to intracloud discharges, and three are due to different phases in a positive cloud to ground (CG) flash. All of them are characterized by a horizontal leader propagation over the tower.

In their study, Becerra et al. [7] estimated the proportion of positive CG flashes that are capable to trigger upward lightning, by interpolating the number of triggering events as a function of distance from [8]. Further, they assumed different probabilities for those events to produce a critical electric field resulting in a triggered upward lightning. It is worth noting that Becerra et al. [7] only considered relatively slow electric field changes associated with leader propagation, as observed in [1]. However, faster field changes of return strokes can also trigger upward lightning with much smaller field magnitudes [10].

In this paper, we present a method to estimate the number of upward flashes from a tower triggered by nearby lightning. Based on the analytical model presented in [10,11], we employ Monte Carlo simulations considering a possible range of values for the electrical and geometrical parameters of positive cloud to ground (CG) lightning. We take into account both, relatively slow processes due to the leader propagation and faster return stroke processes. The adopted geometrical parameters are based on the scenarios observed by Schuman et al. [9]. Similar to [7], one of the scenarios in which cloud discharges are the triggering mechanism was not considered because of the low efficiency of lightning location systems to detect these events and lack of available statistical data. This omission would, however, not significantly impact the overall prediction since this scenario represents only 13% of the observed cases [8,9].

II. Method

A. Electrostatic Model

The full derivation of the electrostatic field due to horizontal and vertical line charge densities involved in triggering processes as observed in [8,9] can be found in the

978-1-6654-2346-5/21/$31.00 ©2021 IEEE

appendix of [10]. Here, for the sake of conciseness, we only present the general ideas. The electric potential of any charge distribution at an arbitrary observation point (*x*,*y*,*z*) in free space can be calculated as:

$$V = \frac{1}{4\pi\varepsilon_0}\int\frac{dq}{r} \tag{1}$$

Integrating along the leader, one can obtain the electric potential at each point in space. The components of electric field are given by:

$$\overrightarrow{E_x}(x,y,z) = -\frac{\partial V(x,y,z)}{\partial x}\,\widehat{e_x} \tag{2}$$

$$\overrightarrow{E_y}(x,y,z) = -\frac{\partial V(x,y,z)}{\partial y}\,\widehat{e_y} \tag{3}$$

$$\overrightarrow{E_z}(x,y,z) = -\frac{\partial V(x,y,z)}{\partial x}\,\widehat{e_z} \tag{4}$$

The influence of the flat ground can be taken into account with image theory. The expressions for the electric fields were derived for the scenarios observed by Schuman et al. [9] shown in Fig. 1 associated with a nearby CG positive flash. For more details see the Appendix of [10].

B. *Sustained Leader Criteria*

The electrostatic model is capable of predicting the electric field (*E*) due to a nearby lightning event in the case of a flat ground. These fields can later be used in simplified corona models to evaluate whether the conditions for a sustained leader initiation are satisfied [10]. In case of lightning protected objects with sharp lightning rods, the following condition has to be satisfied to initiate a sustained leader [11]:

$$U_m \geq K * 3.54\,\tau^{\frac{5}{16}}\,[MV] \tag{5}$$

where K is a coefficient that takes into account the complexity of the structure geometry, τ is the 10-90% risetime of the electric field *E* and U_m is 80% of the peak voltage induced on a structure of height *h*. Assuming that the electric field is constant along its height, U_m can be evaluated as:

$$U_m = 0.8E_m h \tag{6}$$

Note that Eq. (5) is obtained using a simple geometry of a sphere located at an altitude *h* and connected to ground with a wire, neglecting the charge distribution along the wire. It was estimated that a more realistic structure consisting of a rod with hemispheric top would differ by a factor of about two [11]. Therefore, we choose K = 2. Further for the chosen coefficient critical electric field for sustained leader initiation is similar to one obtained using numerical modeling in n Fig. 6 of [7] for the case of zero background field. Note that the simplified approach used here aims to provide a rough estimate of the total number of other-triggered flashes, rather than an accurate representation of the complex mechanisms involved. For more details, see Section 4 of [10].

C. *Monte Carlo Model*

In order to estimate the incidence of upward lightning triggered by nearby events, we will use Monte Carlo simulations.

The general geometry applied to the three different scenarios is shown in Fig. 2. The structure is located at the origin of the coordinate system S and it is along the y axis. The location of the nearby lightning flash ground termination point is at coordinates (xl,zl) in S and at the origin of the coordinate system S'. The red line denotes a horizontal leader with an arbitrary angle Φ with respect to the x axis of the coordinate system S.

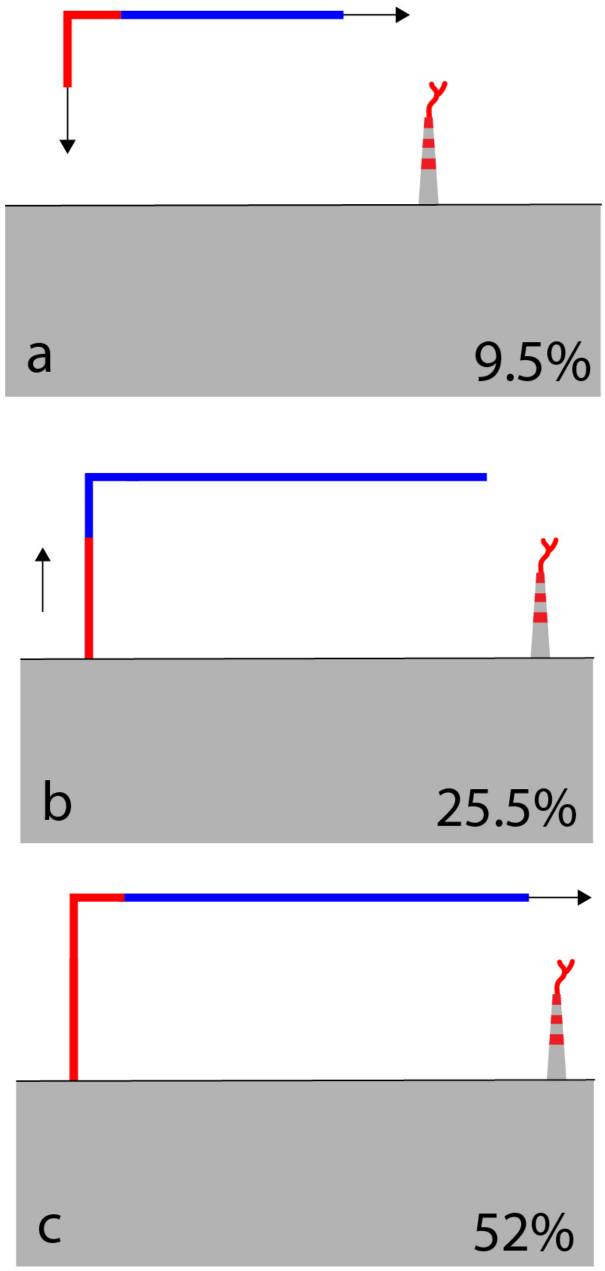

Fig. 1. Upward lightning triggered by different subsequent phases of a nearby CG positive flash. Positive discharges are represented in red and negative in blue. a) Positive leader approaching the ground, b) positive RS, c) during the CC phase.

Note that the formulas for the electric fields derived in [10] are defined for a coordinate system in which the x axis is parallel to the leader direction. In order to apply the same formulas in [10] to horizontal leaders with an arbitrary orientation, we will first transform location of structure to one from the coordinate system S to S' with its x axis parallel to the negative leader and with the ground termination point of the positive CG at its origin:

$$\begin{bmatrix} x_S' \\ y_S' \end{bmatrix} = \begin{bmatrix} cos\phi & sin\phi \\ -sin\phi & cos\phi \end{bmatrix} \begin{bmatrix} x_S - x_L \\ y_S - y_L \end{bmatrix} \qquad (7)$$

Now we can calculate the vertical electric field by directly using the equations from [10].

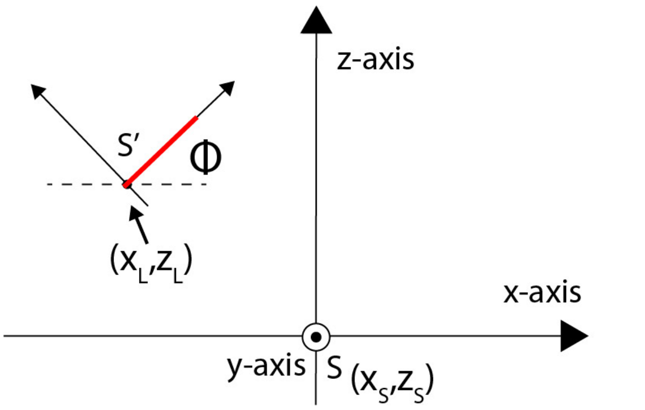

Fig. 2. Geometry of problem. Location of the structure (x_S,y_S) and ground termination point of the positive lightning flash (x_L,y_L).

The range of values considered for our Monte Carlo simulations is presented in Table 1. These values are chosen based on some typical values observed experimentally [e.g., 12-16]. The input parameters of our model are the leader angle, the initiation altitude above the ground, the speed of the positive leader end, the speed of the negative leader end, the return stroke velocity, the duration of the horizontal propagation before the leader veers down to ground, the duration of the continuous current phase, and the line charge density of the negative leader end. Note that the line charge density of the positive end is obtained by assuming a zero net charge along the leader (see [10] for more details). For the sake of simplicity and due to lack of experimental data, we use a uniform distribution for each random experiment. More advanced models can be built by using more representative distributions for each parameter.

Table 1 – Input parameters and considered ranges of variation.

	MIN	MAX
Φ [°]	0	360
altitude [km]	1.5	5
$v_{Positive}$ [10^4 m/s]	1	4
$v_{Negative}$ [10^5 m/s]	0.5	2
$v_{return\ stroke}$ [10^8 m/s]	0.7	1.2
Horizontal duration [ms]	30	200
CC duration [ms]	200	700
$\lambda_{negative}$ [C/km]	0.5	2

The aim of each random experiment is to evaluate the criterion given by Eq. (5) for each successive scenario related to the process of a positive lightning flash, as shown in Fig. 3. For the scenario of a positive leader approaching the ground (Fig 1.a), Eq. (5) is evaluated just prior to the attachment to the ground. The criterion for the positive return stroke (Fig. 1b) is evaluated when the whole positive charge is neutralized. Finally, the criterion for the continuous current (CC), which has a given duration, is evaluated at five equally distant points in time since, in some cases, the criterion might be satisfied at earlier times rather than late times.

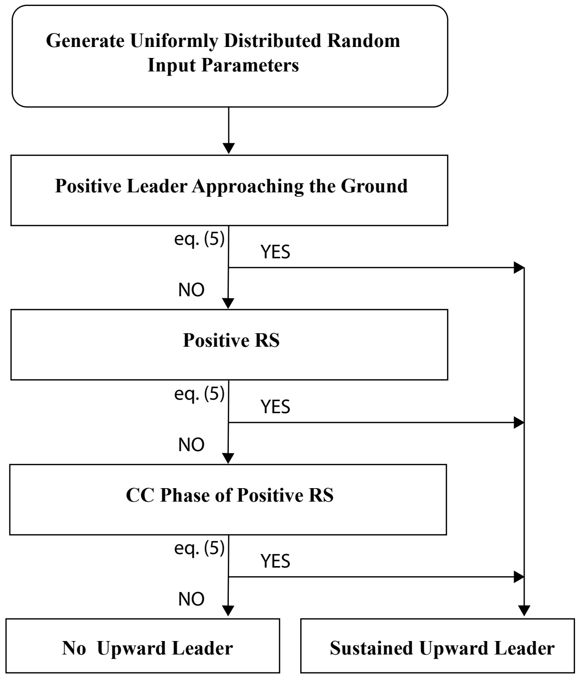

Fig. 3. Flowchart for each random experiment.

III. Results

In this section, we present the results of Monte Carlo simulations for structures of different height. We analyzed an area of 60 x 60 km^2 around the structure. The x and y coordinates of each flash are randomly generated. We assumed a flash density N_g = 2 flashes/km^2 year. Furthermore, we assume that only 7.5 % of flashes are positive. This results in 540 positive flashes per year in the considered 60 x 60 km^2 area.

Fig. 4 and Fig. 5 present the spatial distribution of ground termination points for positive flashes with respectively a 100-m and a 200-m tall structure at the origin for a period of 100 years. The adopted analytical approach enables us to simulate 54000 events in less than two minutes on a typical modern personal computer without any specific optimization or parallelization. Note that in figures we presented 60 x 60 km^2 area centered around the structure since the majority of events that result in sustained leader initiation are within it, but the statistical results are obtained for a 120 x 120 km^2 area to take into account less likely distant events. Grey colored markers denote positive flashes that did not cause the initiation of upward lightning from the tall structure.

The red colored dots represent ground termination points of positive flashes that initiated upward lightning during the initial phase of the positive leader approaching the ground (Fig. 1a). About 90% of these events are within a radius of about 25 km around the 100-m structure and about 28 km in the case of the 200-m tall structure.

Blue color denotes ground termination points of positive return strokes initiating an upward flash (Fig. 1b). About 90% of them are located within a radius of 9 km around the 100-m tall structure and a radius of 10 km around the 200-m tall structure.

CC phase events shown in green can have the most distant ground termination points since, if their horizontal propagation is in the direction of the structure, they can reach its proximity. About 90% of these events are located within a radius of 53 km around the 100-m tall structure and 55 km around the 200-m tall structure. Note that there is no CC events in very close proximity to the tower since these would have already triggered upward lightning by their preceding processes.

Note finally that in our modelling we did not take into account the fact that a small fraction of the positive flashes in the immediate proximity of the structure might connect directly to it.

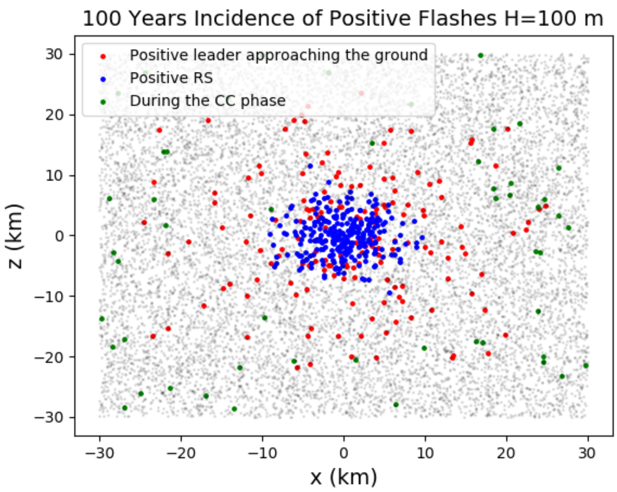

Fig. 4. Distribution of positive lightning flashes in a 60 x 60 km^2 flat ground area with a 100-m tall structure at the origin. Grey markers denote events that did not cause a sustained upward leader. The red, blue and green dots correspond to the scenarios in Fig. 1a, 1b and 1c, respectively.

Fig. 6 presents the reverse cumulative distribution of CC phase events that triggered an upward lightning versus the distance from the structure. We can observe that there are no events with a distance less than 10 km. Furthermore, a similar distribution is observed for both heights.

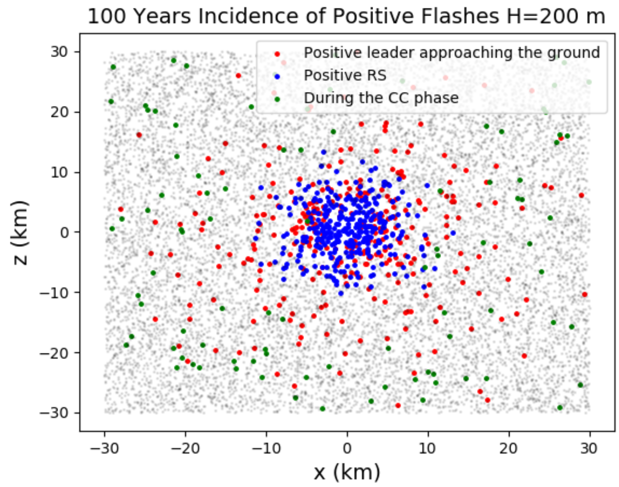

Fig. 5. Distribution of positive lightning flashes in a 60 x 60 km^2 flat ground area with a 200-m tall structure at the origin. Grey markers denote event that did not cause a sustained upward leader. The red, blue and green dots correspond to the scenarios in Fig. 1a, 1b and 1c, respectively.

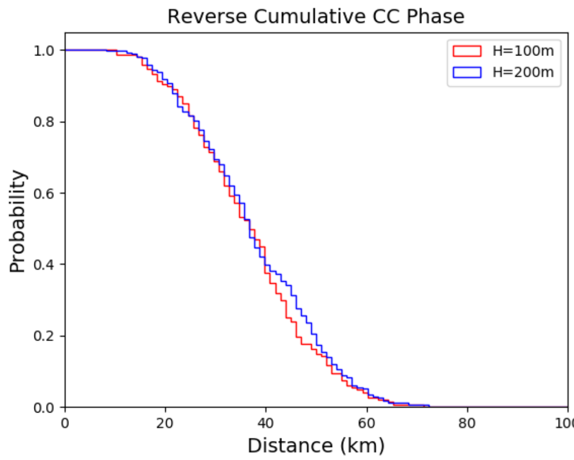

Fig. 6. Reverse cumulative distribution of CC phase events that triggered an upward lightning versus the distance from the structure.

The total number of both downward and upward flashes to a structure of height h can be estimated using the well-known Eriksson's empirical formula [2]:

$$N_T = 24 * N_g * h^{2.05} * 10^{-6} \tag{8}$$

The percentage of upward lightning can be obtained using [17]:

$$P_U = 24 * N_g * h^{2.05} * 10^{-6} \tag{9}$$

Note that in both equations, the structure is assumed to be located on flat ground; in case of an elevated terrain, the physical height has to be replaced by the effective height of the object (e.g. [18]).

Table 2 presents the total number of expected flashes to structures of different heights using eqs. (8) and (9). We also present the total estimated number of other-triggered (OT) flashes obtained by using the Monte Carlo model averaged over a period of one year. We can observe that the number of estimated OT flashes is 3 to 10 times (depending on the structure height) higher than the number of flashes predicted using Equation (8), and the percentage of upward flashes is about 4 to 80 times higher than the number predicted by Equation (9). In line with [7], we observe a significant underestimation of Eriksson's empirical formulas, just by considering upward flashes caused by nearby lightning without contribution of downward lightning and self-initiated upward lightning.

Table 2 – Statistics for a 60 x 60 km^2 observation area, and comparison with equations (8) and (9). N_g= 2 flashes / km^2

Height [m]	100	125	150	175	200	250
N_T from (8)	0.6	0.95	1.39	1.9	2.5	3.95
P_U [%] from (9)	13.2	25	34.6	42.7	49.8	61.5
Scenario a [%]	33	33	33	34	34	35
Scenario b [%]	43	42	40	39	36	35
Scenario c [%]	24	25	27	27	30	30
Total number OT flashes per year	6.2	6.66	7.75	8.33	9.46	11.42

Note that the estimated number of OT flashes does not take into account the contribution of intracloud processes to which 13% of OT flashes are attributed [8,9]. Furthermore, in order to obtain more accurate predictions, more exact statistics of the parameters in Table 1 should be used.

Note also that the percentage of occurrence of each of the three scenarios is somehow different to those observed in [8,9]. This might be explained by the fact that our model does not include the electric field change due to the preceding events (see [10] for more details), which could increase the occurrence of scenarios (b) and (c) (Fig. 1), so that they might become more similar to the observations reported in [8,9].

IV. Conclusion

Using a simplified electrostatic model coupled with a simplified corona model, Monte Carlo simulations were carried out to estimate the incidence of upward lightning flashes from a tall tower caused by nearby positive cloud to ground flashes.

The study allowed for the first time to obtain spatial distributions of triggering events based on their nature. Our results suggest that Eriksson's empirical formulas could significantly underestimate the total number of flashes to tall structures. Based on our analysis, the number of upward flashes triggered by nearby lightning could be, depending on the height of the structure, as much as three to ten times as high as the total number of both upward and downward lightning flashes estimated using conventional empirical formulas.

Acknowledgment

This work was supported by the Swiss National Science Foundation under Grant 200020_175594.

References

[1] Wang, D., Takagi, N., Watanabe, T., Sakurano, H., & Hashimoto, M. (2008). Observed characteristics of upward leaders that are initiated from a windmill and its lightning protection tower. Geophysical Research Letters, 35(2). https://doi.org/10.1029/2007gl032136

[2] A. J. Eriksson, "The Incidence of Lightning Strikes to Power Lines," IEEE Trans. Power Delivery, vol. 2, no. 3, pp. 859–870, 1987, doi: 10.1109/tpwrd.1987.4308191.

[3] IEC 61400: Wind turbines — Part 24: Lightning Protection, IEC, 2011, 2017.

[4] S.F. Madsen, Interaction between Electrical Discharges and Materials for WindTurbine Blades — Particularly Related to Lightning Protection, PhD Thesis,DTU, The Technical University of Denmark, 2007.

[5] V. Peesapati, I. Cotton, T. Sorensen, T. Krogh, and N. Kokkinos, "Lightning protection of wind turbines – a comparison of measured data with required protection levels," IET Renew. Power Gener., vol. 5, no. 1, p. 48, 2011, doi: 10.1049/iet-rpg.2008.0107.

[6] M. Saito, M. Ishii, A. Ohnishi, F. Fujii, M. Matsui, and D. Natsuno, "Frequency of Upward Lightning Hits to Wind Turbines in Winter," Electr Eng Jpn, vol. 190, no. 1, pp. 37–44, Sep. 2014, doi: 10.1002/eej.22358.

[7] M. Becerra, M. Long, W. Schulz, and R. Thottappillil, "On the estimation of the lightning incidence to offshore wind farms," Electric Power Systems Research, vol. 157, pp. 211–226, Apr. 2018, doi: 10.1016/j.epsr.2017.12.008.

[8] M. M. F. Saba et al., "Upward lightning flashes characteristics from high-speed videos," J. Geophys. Res. Atmos., vol. 121, no. 14, pp. 8493–8505, Jul. 2016, doi: 10.1002/2016jd025137.

[9] C. Schumann et al., "On the Triggering Mechanisms of Upward Lightning," Scientific Reports, vol. 9, no. 1, Jul. 2019.

[10] A. Sunjerga, M. Rubinstein, F. Rachidi, and V. Cooray, "On the Initiation of Upward Negative Lightning by Nearby Lightning Activity: An Analytical Approach," Geophys Res Atmos, vol. 126, no. 5, Mar. 2021, doi: 10.1029/2020jd034043.

[11] N. L. Aleksandrov, E. M. Bazelyan, R. B. Carpenter Jr, M. M. Drabkin, and Y. P. Raizer, "The effect of coronae on leader initiation and development under thunderstorm conditions and in long air gaps," J. Phys. D: Appl. Phys., vol. 34, no. 22, pp. 3256–3266, Nov. 2001, doi: 10.1088/0022-3727/34/22/309.

[12] Y. Shen, M. Chen, Y. Du, and W. Dong, "Line Charge Densities and Currents of Downward Negative Leaders Estimated From VHF Images and VLF Electric Fields Observed at Close Distances," IEEE Trans. Electromagn. Compat., vol. 61, no. 5, pp. 1507–1514, Oct. 2019, doi: 10.1109/temc.2018.2864199.

[13] Y. Gao et al., "Leader Charges, Currents, Ambient Electric Fields, and Space Charges Along Downward Positive Leader Paths Retrieved From Ground Measurements in Metropolis," J. Geophys. Res. Atmos., vol. 125, no. 19, Sep. 2020, doi: 10.1029/2020jd032818.

[14] D. E. Proctor, "Lightning flashes with high origins," J. Geophys. Res., vol. 102, no. D2, pp. 1693–1706, Jan. 1997, doi: 10.1029/96jd02635.

[15] L. Z. S. Campos, M. M. F. Saba, T. A. Warner, O. Pinto Jr., E. P. Krider, and R. E. Orville, "High-speed video observations of natural cloud-to-ground lightning leaders – A statistical analysis," Atmospheric Research, vol. 135–136, pp. 285–305, Jan. 2014, doi: 10.1016/j.atmosres.2012.12.011.

[16] G.V. Cooray "The Lightning Flash" IEE, Power & Energy Series (2003)

[17] Eriksson, A., and D. Meal (1984), The incidence of direct lightning strikes to structures and overhead lines, IEE-Conference on Lightning and Power Systems. IEE-Conference Publications, Vol. 236, pp. 67–71

[18] A. Smorgonskiy, F. Rachidi, M. Rubinstein, and N. Korovkin, "On the evaluation of the effective height of towers: The case of the Gaisberg tower," presented at the 2012 International Conference on Lightning Protection (ICLP), Sep. 2012, doi: 10.1109/iclp.2012.6344388.

Paper VI

Electric Power Systems Research 173 (2019) 230–239

Contents lists available at ScienceDirect

Electric Power Systems Research

journal homepage: www.elsevier.com/locate/epsr

Isolated vs. Interconnected Wind Turbine Grounding Systems: Effect on the Harmonic Grounding Impedance, Ground Potential Rise and Step Voltage

Antonio Sunjerga[a,*], Quanxin Li[a,b], Dragan Poljak[c], Marcos Rubinstein[d], Farhad Rachidi[a]

[a] Electromagnetic Compatibility Laboratory, Swiss Federal Institute of Technology (EPFL), 1015 Lausanne, Switzerland
[b] School of Electrical Engineering, Wuhan University, Wuhan 430072, China
[c] Faculty of Electrical Engineering, Mechanical Engineering and Naval Architecture, University of Split, Split 21000, Croatia
[d] University of Applied Sciences of Western Switzerland (HES-SO), 1400 Yverdon-les-Bains, Switzerland

ARTICLE INFO

Keywords:
Grounding impedance
Wind turbine
Interconnected
Ground potential rise
Step voltage
Frequency dependent

ABSTRACT

Wind turbines are very vulnerable to lightning strikes due to their height, sharp edges and remote locations often with high soil resistivity. In this paper we present numerical simulations of the impedance of a typical wind turbine grounding geometry. We analyze the influence of interconnecting grounding systems of different wind turbines. IEC TR61400-24 suggests interconnection of grounding electrodes of wind turbines through horizontal electrodes (in the form of insulated or bare conductors) to achieve low steady-state grounding resistance. The analysis takes into account the frequency dependence of the soil electrical parameters. We show that the low frequency grounding impedance can be reduced by a factor of two or more as a result of interconnecting grounding systems. However, the reduction is significantly lower at higher frequencies because of the interconnection wire's inductance. We analyze the spatial distribution of the ground potential rise and step voltage in response to typical first and subsequent lightning return stroke current waveforms. It is shown that both, ground potential rise and step voltage can be significant along the wire, especially for high resistivity soil, and placing sensitive equipment near the interconnecting wire should be either avoided, or insulated wire should be used.

1. Introduction

Damages to wind turbines caused by lightning strikes account for approximately 80% of wind turbine (WT) insurance claims [1]. Wind turbines are very vulnerable to lightning because of their height, sharp edges and remote and hilly locations often with low soil conductivity [2–4]. Tall structures not only attract downward discharges but, perhaps more importantly, they also initiate upward discharges [5]. There is some evidence that the probability of lightning incidence can be increased by the rotation of the blades [6]. Somewhere between 4% and 8% of wind turbines in Europe suffer damages due to lightning strikes each year [3].

The heights of wind turbines have been constantly increasing over the past years. As a result, they are more exposed to lightning and the design of a proper lightning protection system (LPS), which includes the grounding system, is of high importance. The lightning discharge current has a frequency spectrum ranging from DC up to a few MHz [7]. Proper grounding for the protection of the WT should be designed so that the impedance remains within acceptable limits. According to IEC, the grounding DC resistance should be preferably below 10 Ω [8].

IEC TR61400-24 [8] recommends interconnecting the grounding systems of adjacent wind turbines through horizontal electrodes (in the form of either insulated or bare conductors) to achieve low steady-state grounding resistance and to reduce interference injected into the electrical links. In the case of a single wind turbine, the length of horizontal wires used for impedance reduction is recommended to be limited to 80 m [8]. Of course, in the case of the interconnection of adjacent wind turbine grounding systems, the length of the cable will depend on the distance between the wind turbines and it can exceed the limit for individual turbines. The influence of an interconnecting wire has been analyzed in several studies [9–11]. In Refs. [9,11], beneficial effects of an interconnection in terms of the reduction of the early time response and the peak value of the grounding impedance have been observed. On the other hand, in Ref. [10], no significant difference was observed when adding an interconnecting wire, either connected or not to an adjacent wind turbine grounding system. This is probably due to the fact that the grounding system that was considered in Refs. [10,12] was significantly more extensive than those used in Refs. [9,11], so that the presence of an additional wire did not make any noteworthy effect.

In this paper, which is an extended version of the preliminary study

* Corresponding author.
E-mail address: antonio.sunjerga@epfl.ch (A. Sunjerga).

https://doi.org/10.1016/j.epsr.2019.04.010
Received 8 November 2018; Received in revised form 18 March 2019; Accepted 10 April 2019
Available online 03 May 2019

presented in Ref. [13], we present numerical simulations for the impedance of a typical wind turbine grounding geometry. We also analyze the effects of interconnecting grounding systems of adjacent wind turbines. The presented analysis is based on a full-wave approach in which the frequency dependence of the soil parameters is taken into account. The influence of including the frequency dependence of the soil parameters has been considered in grounding analyses (e.g. [14,15]), but it has never been applied to the analysis of interconnected wind turbine grounding systems. Nonlinear effects associated with soil ionization [16] are expected to be significant only for peak currents higher than 100 kA and for very poorly conducting soils [17] and they are therefore disregarded in this study.

2. Geometry of problem

Typical grounding systems [18–20] consist of several rings connected with horizontal and vertical rods. The depth of the rings is usually a few meters and they are located within a foundation made of concrete [18]. Vertical or horizontal rods are often added to reduce the overall impedance. The effects of adding different rod geometries and the effect of additional rings are discussed in Refs. [19,20], respectively. The simplified geometry used in this paper is shown in Fig. 1 while the related geometrical parameters are listed in Table 1. The geometry consists of 5 rings and four interconnecting wires. The current is injected into the center of the grounding system (origin of the coordinate system). Table 2 presents the electrical parameters of the soil for two different cases studied in this paper. It is worth noting that soil parameters are highly dependent on humidity [21,22] and this dependence can be expressed with empirical formulas (e.g., [23]).

We will consider the interconnection of two wind turbine grounding systems separated by 100 m (center to center) and connected with a 100-m long bare cable buried at a 1 m depth. All the wires are considered to be perfect electric conductors with 1-cm radius. The presence of concrete in the foundation has been disregarded by assuming that its parameters are the same as those of the surrounding medium (soil).

3. Analysis method

3.1. Full wave simulations

The full-wave calculations were carried out using the NEC-4 code, which is based on the numerical solution of the Pocklington integro-differential equation (for the case of wire structures) by means of the Method of Moments (MoM) [24]. A rigorous Sommerfeld integral

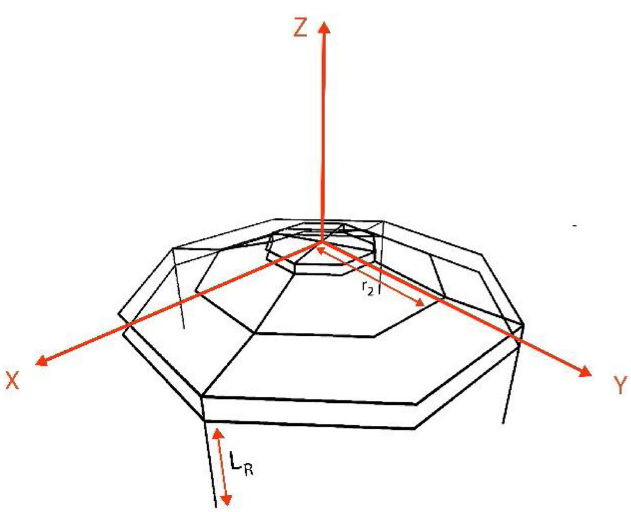

Fig. 1. Geometry of the simplified five rings grounding system configuration used in the study.

Table 1
Geometry of model.

		r_i (m)	Z_i (m)
Ring #1		2.6	−0.05
Ring #2		2.6	−1
Ring #3		5.8	−1.5
Ring #4		9	−2
Ring #5		9	−3
	L_R(m)	Z_1 (m)	Z_2 (m)
Vertical rod	4	−3	−7

Table 2
Soil parameters. ρ_{DC} and ε_∞ are the parameters of the frequency-dependent soil model given by Eqs. (10) and (11).

	ρ_{DC} (Ωm)	ε_∞
Case #1	1000	10
Case #2	100	10

approach was used in the evaluation of the current distribution. Once the current distribution is evaluated solving the Pocklington equation [25], the total electric field at an arbitrary point in space is calculated by summing the contributions of each wire segment.

The ground potential rise (GPR) at a given point on the ground surface can be evaluated as the line integral of the electric field:

$$V_{GPR}(x, y, f) = \int_{x,y\,z=0}^{x,y\,z=-\infty\,(remote\ earh)} \vec{E}\,(\vec{r}, f)\cdot\vec{ds} \tag{1}$$

The path to the remote earth is chosen vertically along the z direction to obtain faster convergence of the results. It is worth noting that the voltage is dependent on the chosen path at higher frequencies [26]. In this paper, the abbreviation GPR is used as the ground potential rise, also known as earth potential rise. This should not be confused with the grounding potential rise commonly referred to with the same GPR abbreviation (e.g. [27]), which relate only to the potential rise at the point of current injection and not at any arbitrary point on the ground surface.

The impedance of the grounding system can be calculated as

$$Z = \frac{V_{GPR}(x = 0, y = 0, f)}{I(f)} \tag{2}$$

where $V_{GPR}(x = 0, y = 0, f)$ is the ground potential rise at the feeding point, and $I(f)$ is the injected current.

3.2. Frequency dependent soil parameters

There are several experimentally obtained formulas for modeling frequency dependence of the soil parameters. In this paper, we take into account the frequency dependent soil parameters in terms of the Smith and Longmire empirical formula [28], which is valid for the simulated frequency range (1 kHz– 10 MHz). The model of Smith-Longmire was selected essentially because of two reasons: (i) it provides results which are in good agreement with experimental results obtained by Bigelow and Eberle [29] and He et al. [30], and (ii) the equations satisfy causality [31]. Other models, such as the model of Messier [32] or that of Alipo and Visacro [33] could also have been used. According to Smith and Longmire, the soil parameters at a given frequency can be calculated using the following empirical formulas:

$$\varepsilon_R(f) = \varepsilon_\infty + \sum_{i=1}^{13} \frac{a_i}{1 + \left(\frac{f}{F_i}\right)^2} \tag{3}$$

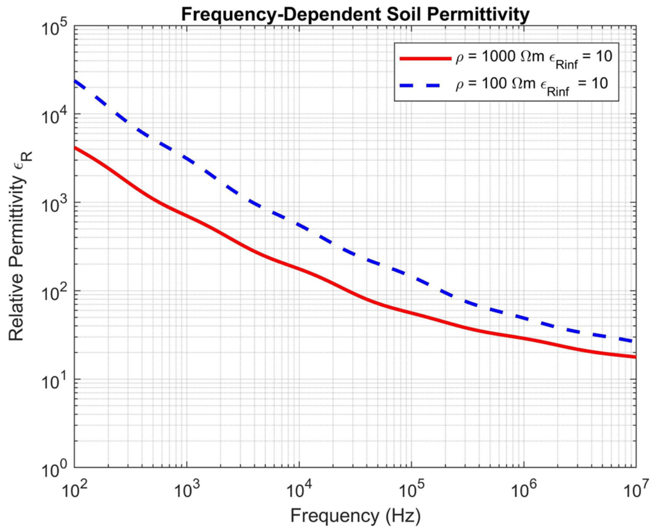

Fig. 2. Frequency-dependence of the soil relative permittivity. Case 1 (red solid line) and Case 2 (dashed blue).

$$\sigma(f) = \sigma_{DC} + 2\pi\varepsilon_0 \sum_{i=1}^{13} \frac{a_i F_i \left(\frac{f}{F_i}\right)^2}{1 + \left(\frac{f}{F_i}\right)^2} \tag{4}$$

where:

$$F_i = F(\sigma_{DC}) \cdot 10^{i-1} \tag{5}$$

$$F(\sigma_{DC}) = (125\sigma_{DC})^{0.8312} \tag{6}$$

and $\sigma_{DC} = 1/\rho_{DC}$ and ε_∞ are values of these parameters at zero frequency and asymptotic value at infinite frequency, respectively. The original expressions in Ref. [28] is adapted here in such a way that the input parameter is the DC conductivity instead of the moisture content.

The expressions for the coefficients a_i can be found in Ref. [31]. Figs. 2 and 3 show the frequency dependence of the soil relative permittivity and resistivity for the two cases considered in Table 2. The implementation of this model is straightforward in the frequency domain. The NEC4 engine was embedded in MATLAB script, in which the soil parameters for each frequency step are calculated using (3)–(6) and used as input in NEC4.

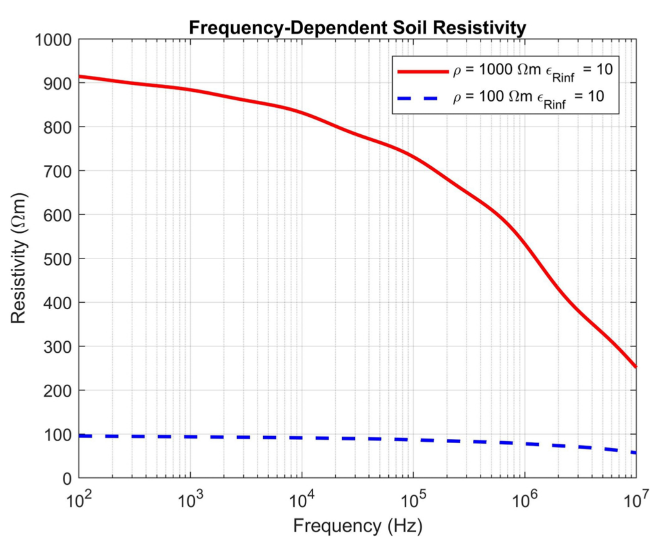

Fig. 3. Frequency-dependence of the soil resistivity. Case 1 (red solid line) and Case 2 (dashed blue).

3.3. Time-domain analysis

In order to evaluate the influence of the injected current waveform on the ground potential rise, two waveforms corresponding to typical first and subsequent return strokes were considered. The waveforms were represented using Heidler's functions, defined as [34]:

$$I_H(t) = \frac{I_0}{\eta} \frac{\left(\frac{t}{\tau_1}\right)^n}{1 + \left(\frac{t}{\tau_1}\right)^n} e^{-\frac{t}{\tau_2}} \tag{7}$$

where η can be calculated as:

$$\eta = e^{\left(-\frac{\tau_1}{\tau_2}\left(n\frac{\tau_2}{\tau_1}\right)^{-n}\right)} \tag{8}$$

The parameters of the Heidler's functions used to represent, respectively, a typical first return stroke and a typical subsequent return stroke are the same as those used in Ref. [35] and they are given in Table 3. The subsequent stroke is represented using the sum of two Heidler's functions. The early-time behavior of the two waveforms is shown in Fig. 4. The front time of the first and subsequent stroke are 4.125 μs and 0.5 μs respectively.

The ground potential rise at a point (x, y) on the surface of the ground due to the first or the subsequent return stroke waveforms represented by the Heidler's functions is given by:

$$V_{GPR}(x, y, t) = \mathscr{F}^{-1}[Z_{tr}(x, y, f) I_H(f)] \tag{9}$$

$I_H(f)$ is the injected current in frequency domain, $V_{GPR}(x, y, t)$ is the time-domain GPR at (x, y), and $Z_{tr}(x, y, f)$ is the transfer function determined as:

$$Z_{tr}(x, y) = \frac{V_{0\,GPR}(x, y, f)}{I_0(f)} \tag{10}$$

in which $V_{0GPR}(x, y, f)$ is the response to a Dirac excitation current $I_0(f)$ (1 A at every frequency through the 1-MV voltage source in series with 1-MΩ impedance). The Inverse Fourier transforms are evaluated by way of the Inverse Fast Fourier Transform (IFFT) algorithm [36]. The transfer function is calculated at discrete frequencies from 1 kHz to 10 MHz with a non-uniform and adaptive sampling (more points in frequencies at which the transfer function changes more rapidly). The number of points varied from case to case with an average of about 80 points. Simulated impedances are interpolated using the Spline algorithm [37] to obtain a uniform frequency-domain sampling required for the IFFT algorithm.

4. Frequency-domain response

The effect of the frequency dependence of the soil parameters on grounding systems has been analyzed previously in frequency-domain simulations (e.g., [14,15] for the particular case of the grounding of wind turbines). On the other hand, the effect of interconnecting wind turbine grounding systems was analyzed using the finite-difference time-domain (FDTD) approach (e.g., [9,10]) and in the frequency domain using the method of moments [11]. Here, we consider and discuss both of these effects for the same model solved in the frequency domain. It is worth noting that the three dimensional ground potential rise and step voltage have been reported only for the case of single wind turbines with constant soil parameters [19,20].

First, we will examine the transient response of a single wind turbine grounding system. In a second case, we will analyze the effect of connecting the grounding system to that of an adjacent wind turbine using a 100-m long horizontal bare wire buried at 1 m depth. Finally, a third case will be examined, considering the grounding system and the 100-m long buried wire but without connection to the adjacent grounding system.

Figs. 5 and 6 show the magnitude of the harmonic grounding impedance, respectively for the case of a high resistivity soil (Case #1) and

Table 3
Heidler's function parameters for the representation of typical first and subsequent return strokes (from Ref. [35]).

	I_{01} (kA)	T_{11} (μs)	T_{21} (μs)	n_1	I_{02} (kA)	T_{12} (μs)	T_{22} (μs)	n_2
First stroke	28	1.8	95	2	–	–	–	–
Subsequent stroke	10.7	0.25	2.5	2	6.5	2	230	2

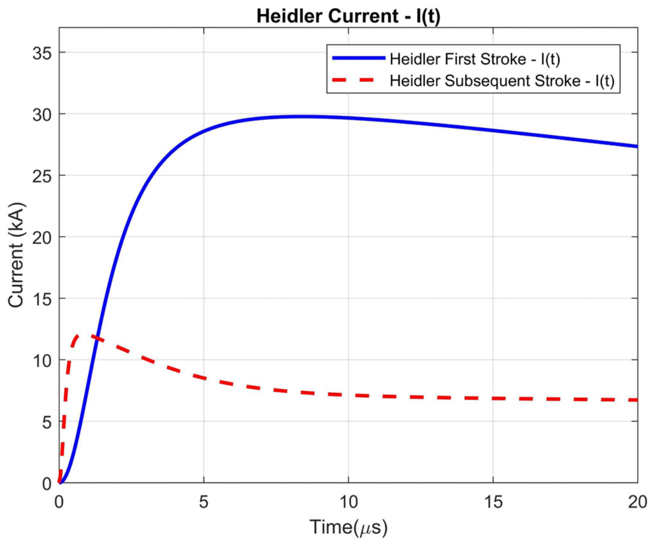

Fig. 4. Injected lightning current waveforms represented using Heidler's functions. First return stroke (solid blue); subsequent return stroke (dashed red).

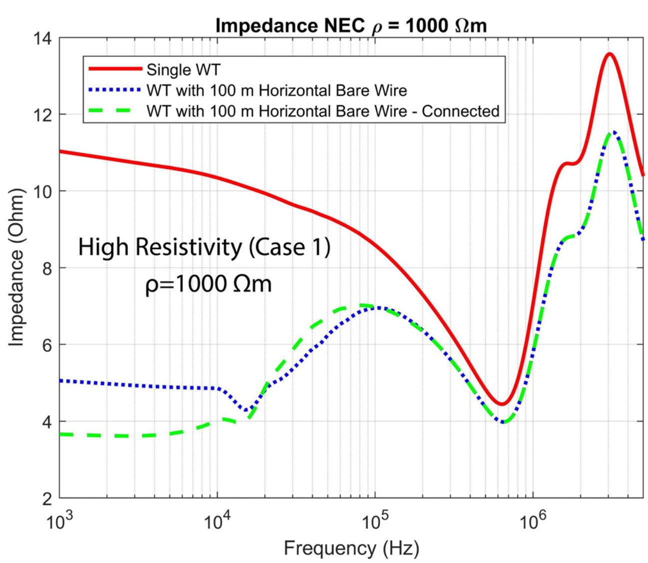

Fig. 5. Magnitude of the harmonic grounding impedance. Frequency-dependent soil parameters: ρ_{DC} = 1000 Ωm, ε_∞ = 10. Single WT (solid red), WT with 100-m long buried horizontal wire (dotted blue) and WT with 100-m long buried horizontal wire connected to an adjacent grounding system (dashed green).

a low resistivity soil (Case #2).

It can be seen that at low frequencies, the connection to an adjacent grounding system through a 100-m long wire results in a significant reduction of the harmonic grounding impedance. For higher frequencies (about 100 kHz for Case #1 and 10 kHz for Case #2), the effect of the adjacent grounding impedance becomes insignificant and the results for the grounding impedance of the whole system (WT connected to an adjacent one) coincide with those of a single WT with only the horizontal wire.

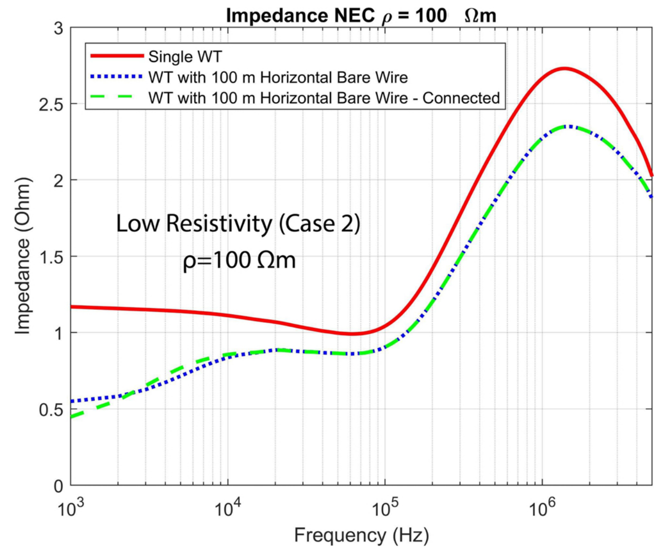

Fig. 6. Magnitude of the harmonic grounding impedance. Frequency-dependent soil parameters: ρ_{DC} = 100 Ωm, ε_∞ = 10. Single WT (solid red), WT with 100-m long buried horizontal wire (dotted blue) and WT with 100-m long buried horizontal wire connected to an adjacent grounding system (dashed green).

The influence of the connection wire can be understood intuitively from circuit theory. The current attenuation along the connecting wire is essentially due to:

(i) The leakage to the earth (conductance to remote earth), which results in the attenuation of the current along the wire. The lower the soil resistivity, the higher the attenuation.

(ii) The inductance of the wire, which is not significantly affected by the soil resistivity, and has an effect on the current as the frequency increases.

Considering the above, in the case of a low resistivity soil where the leakage is the main factor attenuating the current, the adjacent wind turbine grounding system becomes irrelevant, even at low frequencies. For the case of a high resistivity soil, the connection to an adjacent wind turbine grounding system will be beneficial in reducing the grounding impedance at low frequencies, since both grounding systems can be considered to be in parallel. As the frequency increases, the impedance of the wire will also increase. This will result in reducing the effective length of the wire. As a result, a negligible current will reach adjacent wind turbine grounding.

In Fig. 7, we compare the results assuming constant soil parameters versus frequency-dependent soil parameters, for a single WT (Fig. 7a), and for two interconnected WTs using a 100-m long bare wire (Fig. 7b). The results are presented for the case of a high ground resistivity (ρ_{DC} = 1000 Ωm), for which the effect of the soil frequency-dependent parameters is more significant on the grounding impedance. We can see that the frequency dependence of the soil electrical parameters affects the grounding impedance over the whole frequency range in both cases. At very low frequencies, there is no displacement current and the impedance is only governed by the soil resistivity and not the permittivity. As the frequency goes to zero, the soil resistivity becomes the same for both models (Eq. (4)). For example, at 100 Hz in the case of Fig. 7a and b, the models converge to 12.49 Ω and 4.18 Ω, respectively.

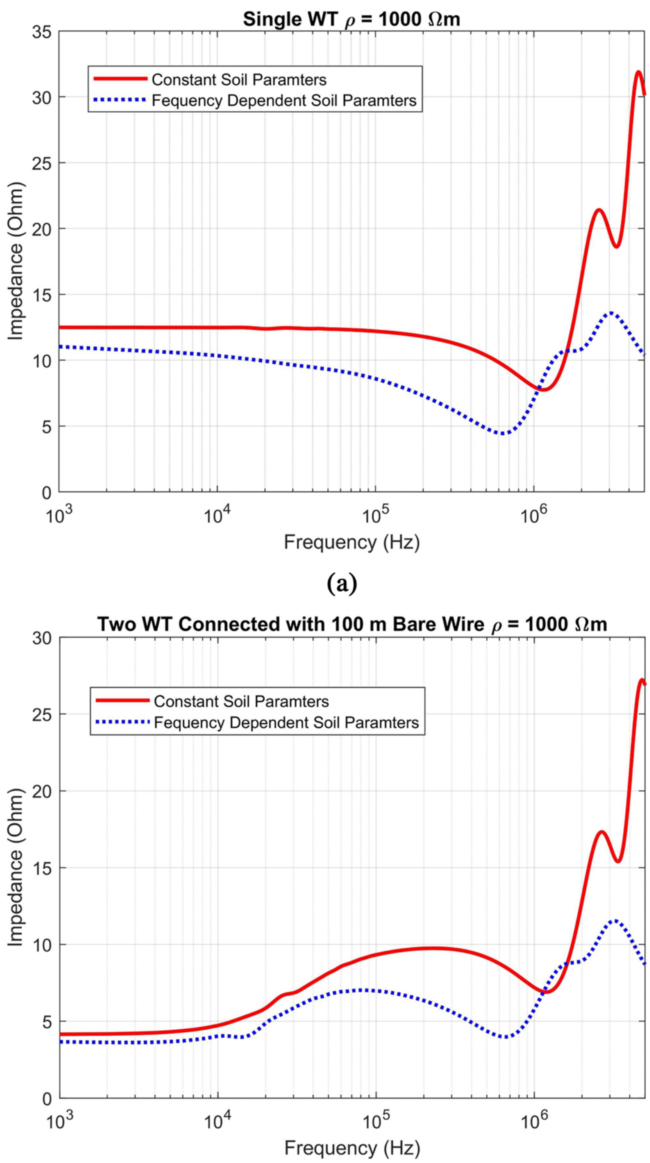

Fig. 7. Magnitude of the harmonic grounding impedance for the case of high resistivity soil ρ_{DC} = 1000 Ωm, ε_∞ = 10. Constant soil parameters (solid red), frequency dependent parameters (dashed blue). (a) Single WT, (b) Two WT connected with a 100-m bare wire.

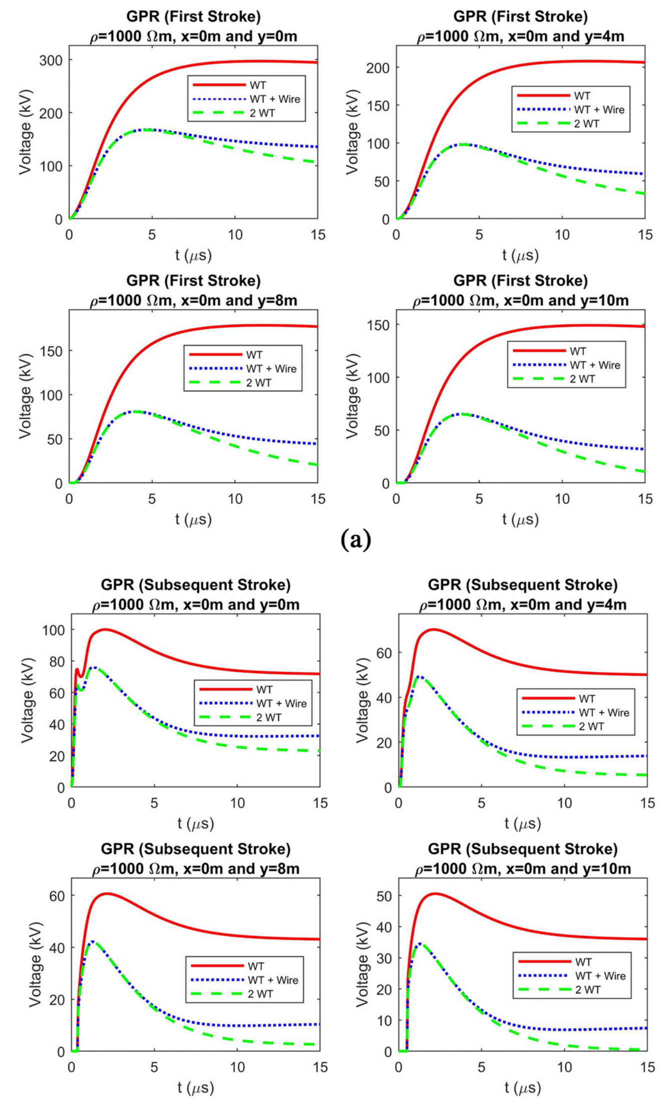

Fig. 8. Time evolution of the ground potential rise for the case of high resistivity soil and for the three considered geometries: single WT (solid red), WT with a 100-m long buried horizontal wire (dotted blue), and WT with a 100-m long buried horizontal wire connected to an adjacent grounding system (dashed green). (a) First stroke, (b) subsequent stroke.

5. Time domain

In this Section, we will examine the GPR time evolution and spatial distribution as well as the step voltage spatial distribution for the two considered cases of soil resistivity, and for the first and subsequent stroke waveforms. As in the previous section, we will consider the cases of a single WT, a WT with a 100-m long bare wire, and two WTs connected with a 100-m long bare wire. We show the spatial distribution of GPR and step voltage at the time instant of its maximum. The full spatial time evolution can be seen in the attached animations.

5.1. Time evolution of the ground potential rise

In this section, we present the time evolution of the GPR at specific locations along the axis perpendicular to the interconnecting wire and horizontal.

Figs. 8 and 9 present the ground potential rise for the case of high and low resistivity soils, respectively. The time evolution is plotted at four different points, including the current injection point at the origin of the coordinate system (x = 0, y = 0) and at distances of 4, 8 and 10 m away in the direction perpendicular to the connecting wire. As expected, moving away from the injection point, we observe a decrease

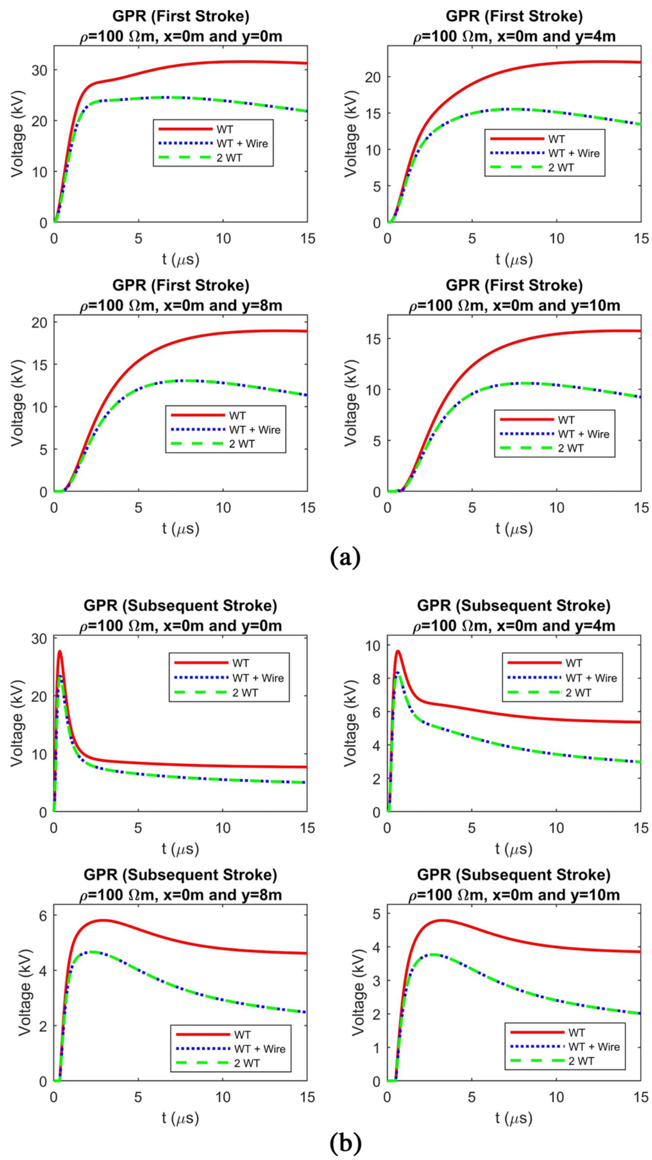

Fig. 9. Time evolution of the ground potential rise for the case of low resistivity soil and for the three considered geometries: single WT (solid red), WT with a 100-m long buried horizontal wire (dotted blue), and WT with a 100-m long buried horizontal wire connected to an adjacent grounding system (dashed green). (a) First stroke, (b) subsequent stroke.

of the potential. The observed waveforms are qualitatively in agreement with the results of Yamamoto et al. [12,38], having in mind the differences in the considered geometries and adopted models. In Refs. [12,38], the multi-layer soil model results in the appearance of reflections in the voltage waveform. In Ref. [38], the measured peak GPR values are lower than the simulated ones by a few tens of percent. This might be due to the fact that the simulations presented in Ref. [38] are based on the assumption of constant soil parameters. In both considered soil resistivity cases, a decrease of the peak GPR is observed for the case when an interconnected wire is used, whether alone or connected to an adjacent WT grounding system. It can be seen that the decrease of the peak value is only due to the interconnecting wire. The adjacent WT grounding system will only decrease the late-time response in the case of a high resistivity soil, in agreement with what was observed in the previous section in the frequency domain.

5.2. Spatial distribution of the ground potential rise

Figs. 10 and 11 show the ground potential rise for the case of a high resistivity soil with a single WT grounding, and a system of two WT groundings separated by 100 m and connected with bare wire, respectively. We can see that the connection to an additional WT leads to a maximum GPR that is significantly reduced and that it occurs much earlier in time. On the other hand, the level of GPR along the connecting wire in Fig. 9 is significant and comparable to the maximum level at the feeding point.

Figs. 12 and 13 show the GPR for the case of a low resistivity soil. Again, it can be seen that the interconnection of the grounding systems results in an overall reduction of the GPR. Furthermore, it can be seen that the maximum GPR at the feeding point occurs at an earlier time compared to the case of a highly resistive soil.

The GPR reduction as a result of interconnecting grounding systems is more significant for first return strokes (characterized by slower waveforms) compared to subsequent return strokes. In the case of a low resistivity soil, the GPR is, as expected, more localized around the grounding center.

5.3. Step voltage

The step voltage is calculated as a potential difference between two points on the earth surface at a distance of 1 m. Figs. 14 and 15 show the step voltage for the case of high resistivity soil with a single WT grounding, and two WT grounding systems connected with a 100-m long bare wire, respectively. Similar to the GPR, we can see that for interconnected WT grounding systems, the maximum step voltage is significantly reduced and it occurs much earlier. However, the step voltage along the connecting wire and at location of vertical rods can be significant and comparable to the maximum level at the feeding point.

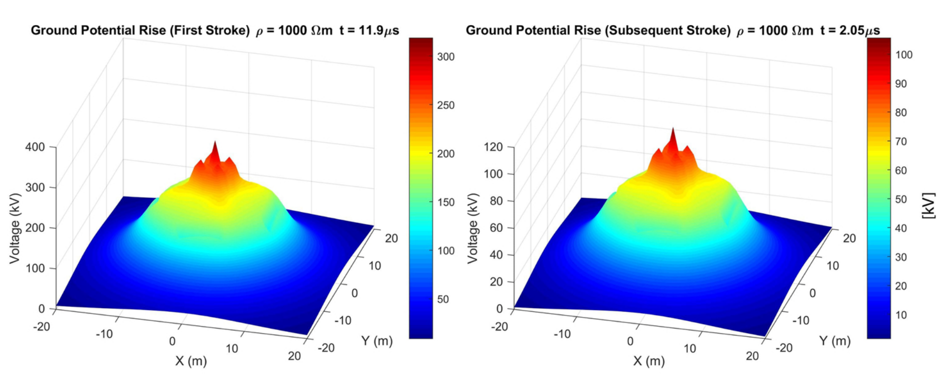

Fig. 10. Ground potential rise for single wind turbine grounding at the time when it attains its maximum at the feeding point. Case #1, ρ_{DC} = 1000 Ωm. (a) First stroke, (b) subsequent stroke.

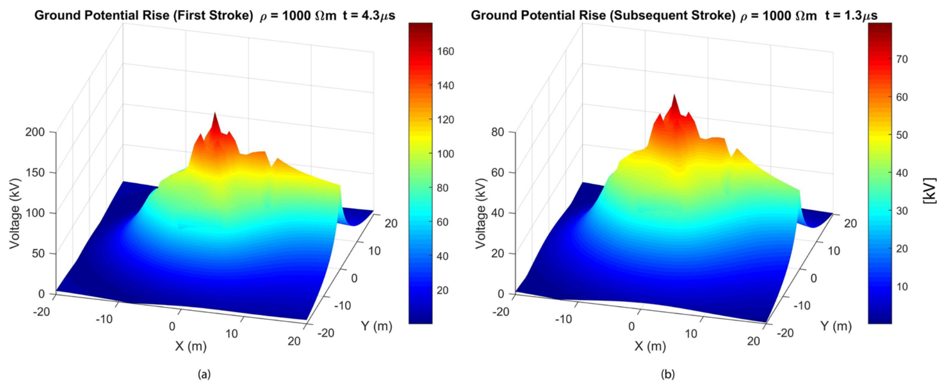

Fig. 11. Ground potential rise at the time when the maximum value is attained at the feeding point for two 100-m separated wind turbine groundings connected with 100 m of bare wire. Case #1, ρ_{DC} = 1000 Ωm. (a) First stroke, (b) subsequent stroke.

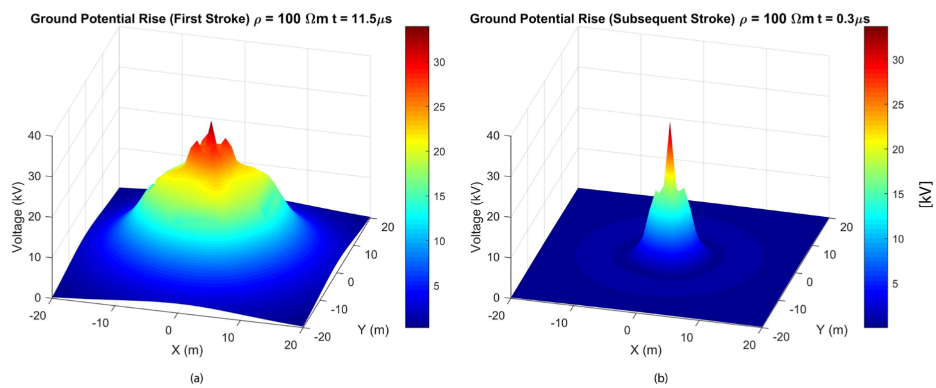

Fig. 12. Ground potential rise for single wind turbine grounding at the time when the maximum value is reached at the feeding point. Case #2, ρ_{DC} = 100 Ωm. (a) First stroke, (b) subsequent stroke.

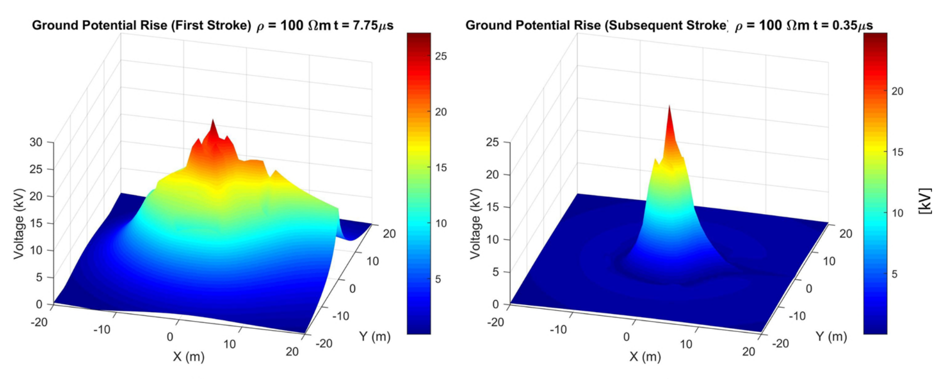

Fig. 13. Ground potential rise at the time when the maximum is reached at the feeding point for two 100 m separated wind turbine grounding connected with 100 m bare wire. Case #2, ρ_{DC} = 100 Ωm. (a) First stroke, (b) subsequent stroke.

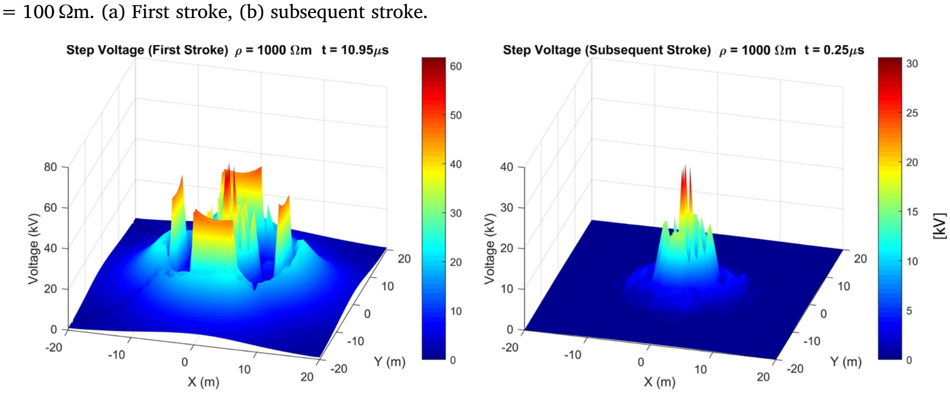

Fig. 14. Step voltage for a single wind turbine grounding at the time when the maximum is reached at the feeding point. Case #1, ρ_{DC} = 1000 Ωm. (a) First stroke. (b) subsequent stroke.

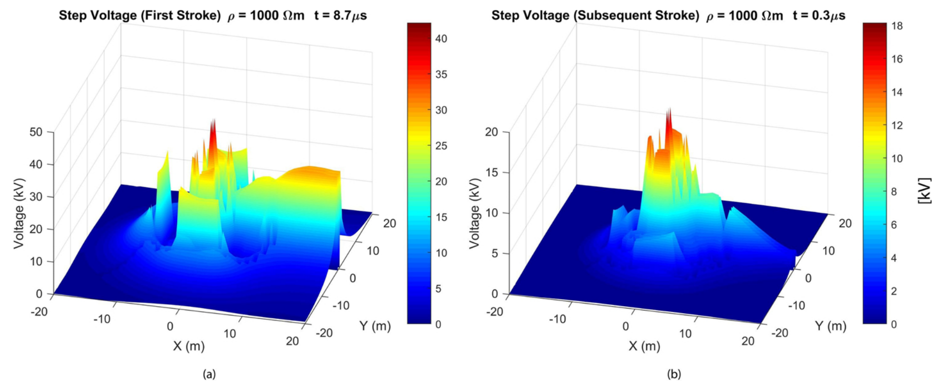

Fig. 15. Step voltage at the time when the maximum is reached at the feeding point for two 100-m separated wind turbine groundings connected with a 100-m bare wire. Case #1, ρ_{DC} = 1000 Ωm. (a) First stroke. (b) subsequent stroke.

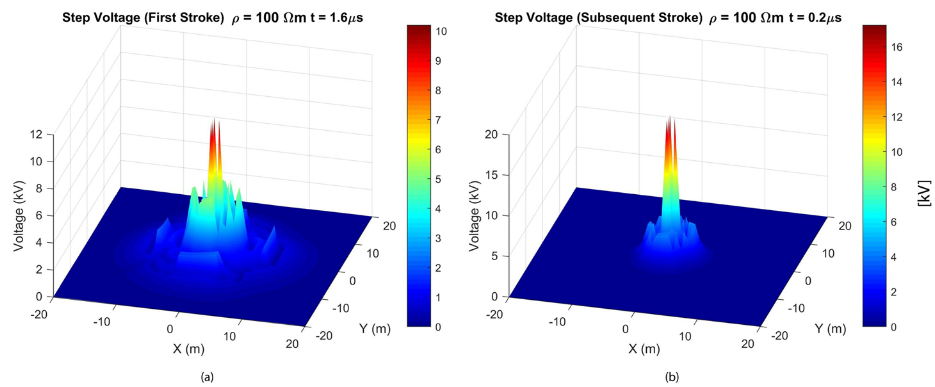

Fig. 16. Step voltage for single wind turbine grounding at the time when the maximum is reached at the feeding point. Case #2, ρ_{DC} = 100 Ωm. (a) First stroke. (b) subsequent stroke.

Figs. 16 and 17 show the step voltage for the case of a low resistivity soil. Again, it can be seen that the interconnection of grounding systems results in the reduction of the overall step voltage. However, in this case, and unlike the case of a highly resistive soil, the step voltage along the interconnecting wire is much smaller compared it to the maximum at the feeding point.

The step voltage reduction as a result of interconnecting grounding systems is more significant for first return strokes (characterized by slower waveforms) compared to subsequent return strokes. In the case of a low resistivity soil, as expected, the step voltage is more localized around the grounding center.

The step voltage along the wire is less significant in case of low resistivity, but it is comparable to the maximum value at late times (see attached animation).

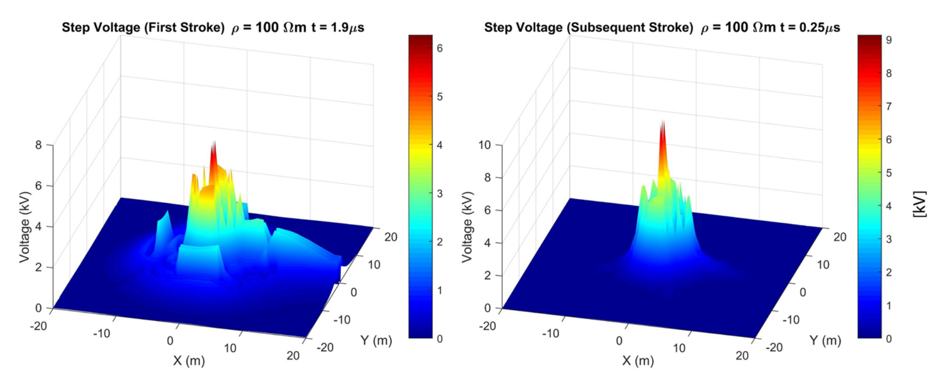

Fig. 17. Step voltage at the time when the maximum is reached at the feeding point for two 100-m separated wind turbine grounding connected with a 100-m bare wire. Case #2, ρ_{DC} = 100 Ωm. (a) First stroke, (b) subsequent stroke.

6. Conclusions

We presented numerical simulations for the impedance of a typical wind turbine grounding geometry, focusing on the effect of interconnecting grounding systems for different wind turbines, as recommended by IEC (TR61400-24). In the case of a single wind turbine, the length of horizontal wires used for impedance reduction is recommended by IEC to be limited to 80 m. Modern wind turbines have blades with lengths of 60 m and longer. Therefore, the distance between adjacent wind turbines is in practice much higher than 80 m. The analysis accounts for the frequency dependent soil electrical parameters.

It was shown that the low frequency grounding impedance could be reduced by a factor of two or more as a result of interconnecting two grounding systems separated by a 100-m distance. However, the reduction is significantly lower at higher frequencies due to influence of the interconnecting wire's inductance.

The results of this study show that the reduction of the GPR peak values in interconnected WTs is essentially due to the interconnecting wire. Adjacent wind turbines can only reduce the late-time response for the case of low resistivity soils since, in the early time, the effective length of the interconnecting wire is lower than the typical distance between wind turbines.

We analyzed the spatial distribution of ground potential rise and the step voltage in response to typical first and subsequent lightning return stroke current waveforms. We showed that both, the ground potential rise and the step voltage could be significant along the wire, in particular for the highly resistive soil. We also observed a high step voltage at locations of vertical rods that are a potential risk to the personnel. Furthermore, placing of sensitive equipment near the interconnecting wire should be either avoided, or insulated wire should be used.

Future work will include the taking into account of the presence of concrete in the foundation of the wind turbine.

Acknowledgments

Special thanks to four anonymous reviewers whose constructive comments improved this paper. This work was supported in part by the Swiss National Science Foundation (Project No. 200020_175594).

Appendix A. Supplementary data

Supplementary material related to this article can be found, in the online version, at doi:https://doi.org/10.1016/j.epsr.2019.04.010.

References

[1] D.I.B. Djalel, M. Mourad, S. Ghoudelbourk, Protection of wind turbine against the lightning damage, IREC2015 The Sixth International Renewable Energy Congress, (2015).

[2] D. Poljak, D. Čavka, Properties and Characterization of Modern Materials, Chapter Electromagnetic Compatibility Aspects of Wind Turbine Analysis and Design July 2016.

[3] F. Rachidi, M. Rubinstein, J. Montanyà, J. Bermúdez, R. Sola, G. Solà, N. Korovkin, A review of current issues in lightning protection of new-generation wind-turbine blades, IEEE Trans. Ind. Electron. 55 (June (6)) (2008).

[4] A. Sunjerga, F. Rachidi, M. Rubinstein, D. Poljak, Calculation of the grounding resistance of structures located on elevated terrain, IEEE Trans. Electromagn. Compat. (2018) 1–5.

[5] F. Rachidi, M. Rubinstein, A. Smorgonskiy, Lightning protection of large wind-turbine blades, Wind Energy Conversion Systems, Springer, 2012, pp. 227–242.

[6] J. Montanyà, O. van der Velde, E.R. Williams, Turbines shoot upside-down lightning, Nature 506 (February (7488)) (2014) 268–268.

[7] CIGRE Working Group C4.407 (Convener: V.A. Rakov), Lightning Parameters for Engineering Applications, Technical Brochure 549, CIGRE, 2014.

[8] IEC International Standard, Lightning protection. IEC 61400e61424, Wind Turbine Generation System vol. 24, International Electro-technical Commission, Geneva, 2010.

[9] M.R. Ahmed, M. Ishii, Effectiveness of interconnection of wind turbine grounding influenced by interconnection wire, 2012 International Conference on Lightning Protection (ICLP), (2012).

[10] J. Niihara, A. Ametani, K. Yamamoto, Transient grounding characteristics of wind turbine with counterpoise, 2012 Asia-Pacific Symposium on Electromagnetic Compatibility, (2012).

[11] B. Markovski, Transient performance of interconnected wind turbine grounding systems, Przegląd Elektrotechniczny 1 (June (6)) (2015) 74–77.

[12] K. Yamamoto, S. Yanagawa, K. Yamabuki, S. Sekioka, S. Yokoyama, Analytical surveys of transient and frequency-dependent grounding characteristics of a wind turbine generator system on the basis of field tests, IEEE Trans. Power Deliv. 25 (October (4)) (2010) 3035–3043.

[13] A. Sunjerga, Q. Li, D. Pojak, M. Rubinstein, F. Rachidi, Transient impedance of interconnected wind turbine grounding systems, 2018 26th International Conference on Software, Telecommunications and Computer Networks (SoftCOM), (2018).

[14] R. Alipio, S. Visacro, Frequency dependence of soil parameters: effect on the lightning response of grounding electrodes, IEEE Trans. Electromagn. Compat. 55 (February (1)) (2013) 132–139.

[15] M. Akbari, K. Sheshyekani, M.R. Alemi, The effect of frequency dependence of soil electrical parameters on the lightning performance of grounding systems, IEEE Trans. Electromagn. Compat. 55 (August (4)) (2013) 739–746.

[16] M. Mokhtari, Z. Abdul-Malek, G.B. Gharehpetian, A critical review on soil ionisation modelling for grounding electrodes, Arch. Electr. Eng. 65 (January (3)) (2016).

[17] B. Markovski, L. Grcev, V. Arnautovski-Toseva, Transient characteristics of wind turbine grounding, 2012 International Conference on Lightning Protection (ICLP). IEEE (2012), https://doi.org/10.1109/iclp.2012.6344413.

[18] D.S. Gazzana, A. Smorgonskiy, N. Mora, A. Šunjerga, M. Rubinstein, F. Rachidi, An experimental field study of the grounding system response of tall wind turbines to impulse surges, Electr. Power Syst. Res. 160 (July) (2018) 219–225.

[19] D. Cavka, D. Poljak, V. Doric, R. Goic, Transient analysis of grounding systems for wind turbines, Renew. Energy 43 (July) (2012) 284–291.

[20] B. Markovski, L. Grcev, V. Arnautovski-Toseva, Step and touch voltages near wind turbine grounding during lightning strokes, International Symposium on Electromagnetic Compatibility – EMC EUROPE, (2012).

[21] G.C. Topp, J.L. Davis, A.P. Annan, Electromagnetic determination of soil water content: measurements in coaxial transmission lines, Water Resour. Res. 16 (June (3)) (1980) 574–582.

[22] Roberta Porretta, Fabio Bianchi, Profiles of relative permittivity and electrical conductivity from unsaturated soil water content models, Ann. Geophys. 59 (July (3)) (2016).

[23] J.H. Scott, Electrical and magnetic properties of rock and soil, Open-File Report. US Geological Survey, 1983.

[24] G.J. Burke, Numerical Electromagnetics Code (NEC-4) – Method of Moments, Part II: Program Description – Theory, Lawrence Livermore National Laboratory, YCRL-MA-109338 PT. II. 1992.

[25] D. Poljak, Advanced Modeling in Computational Electromagnetic Compatibility, Wiley, N.J, 2007.

[26] A. Sunjerga, et al., Tower and path-dependent voltage effects on the measurement of grounding impedance for lightning studies, IEEE Transactions on Electromagnetic Compatibility, (2018), pp. 1–10.

[27] S. Visacro, R. Alipio, M.H. Murta Vale, C. Pereira, The response of grounding electrodes to lightning currents: the effect of frequency-dependent soil resistivity and permittivity, IEEE Trans. Electromagn. Compat. 53 (May (2)) (2011) 401–406.

[28] C.L. Longmire, H.J. Longley, Time domain treatment of media with frequency dependent parameters, Theoretical Notes 113, Defense Nuclear Agency (1973) [Online]. Available: https://www.ece.unm.edu/summa/notes/Theoretical.html.

[29] R.C. Bigelow, W.R. Eberle, Empirical predictive curves for resistivity and dielectric constant of earth materials: 100 Hz to 100 MHz, Open-File Report 83-911, U.S. Geological Survey, 1972.

[30] J. He, R. Zeng, B. Zhang, Methodology and Technology for Power System Grounding, Wiley, Singapore, 2013 p. 35.

[31] D. Cavka, N. Mora, F. Rachidi, A comparison of frequency-dependent soil models: application to the analysis of grounding systems, IEEE Trans. Electromagn. Compat. 56 (February (1)) (2014) 177–187.

[32] M.A. Messier, The Propagation of an Electromagnetic Impulse Through Soil: Influence of Frequency Dependent Parameters, Mission Res. Corp., Santa Barbara, CA, USA, 1980 Tech. Rep. MRC-N-415.

[33] R. Alipio, S. Visacro, Modeling the frequency dependence of electrical parameters of soil, IEEE Trans. Electromagn. Compat. 56 (October (5)) (2014) 1163–1171.
[34] F. Heidler, Analytische Blitzstromfunktion zur LEMP – Berechnung, Proc. 18th Int. Conf. Lightning Protection (1985) 63–66 paper 1.9.
[35] F. Rachidi, W. Janischewskyj, A.M. Hussein, C.A. Nucci, S. Guerrieri, B. Kordi, J. Chang, Current and electromagnetic field associated with lightning-return strokes to tall towers, IEEE Trans. Electromagn. Compat. 43 (3) (2001).
[36] M. Frigo, S.G. Johnson, FFTW: an adaptive software architecture for the FFT, Proceedings of the International Conference on Acoustics, Speech, and Signal Processing vol. 3, (1998) 1381–1384.
[37] Carl de Boor, A Practical Guide to Splines, Springer-Verlag, New York, 1978.
[38] K. Yamamoto, S. Sumi, Transient grounding characteristics of a wind turbine foundation with grounding wires and plates, 2014 IEEE International Symposium on Electromagnetic Compatibility (EMC), (2014).

Paper VII

Calculation of the Grounding Resistance of Structures Located on Elevated Terrain

Antonio Sunjerga, Farhad Rachidi, *Fellow*, IEEE, Marcos Rubinstein, *Fellow*, IEEE and Dragan Poljak, *Senior Member*, IEEE

***Abstract*— We present an analysis of the response of a grounding electrode located on top of a mountain. Specifically, we derive an analytical solution for the low-frequency response of a hemispheric grounding electrode buried on the top of a cone-shaped mountain characterized by its apex angle. The derived equation is validated using numerical simulations based on the Finite Element Method obtained using COMSOL.**

Simulation results show that, for the same ground electrical parameters, the grounding resistance of such an electrode for steep mountains can be significantly higher than that obtained if the electrode is on flat ground. Such situations can occur in particular for the case of telecommunication towers or wind turbines located on mountaintops.

The study emphasizes the importance of considering the terrain profile in the evaluation of the grounding resistance of structures located in elevated locations.

***Index Terms*—Lightning, grounding resistance, hilly, elevated terrain, grounding electrode**

I. INTRODUCTION

Tall structures such as wind turbines and mobile phone base stations are often installed in remote and hilly locations. Those locations are very likely to be struck by lightning due to their geographical elevation [1,2] and to the initiation of upward flashes [3,4] from them.

These hilly areas are often very rocky with low soil conductivity (0.001 S/m and lower). Therefore, the design of proper grounding systems is of high importance.

The evaluation of the impedance of grounding electrodes requires, in general, the application of numerical methods (e.g., [5]), or simplified transmission-line-based or circuit-based models (e.g., [6]). On the other hand, analytical expressions are available for the grounding resistance for various electrode geometries, such as a hemisphere, buried ring, and vertical or horizontal rods (see, e.g., Appendix D of [7]). All these analytical expressions have been derived assuming that the earth is a homogeneous half space and its surface is flat.

To the best of our knowledge, no previous studies have discussed the influence of a non-flat ground on the impedance of grounding electrodes. In this paper, we derive an analytical solution for the case of a hemispheric electrode located on top of a mountain represented by a conical shape. We compare the derived analytical solution to numerical simulations for validation purposes.

II. LOW-FREQUENCY RESPONSE OF A GROUNDING ELECTRODE

A. Basic Equations

The low-frequency response of a grounding system is governed by Ohm's law and the current continuity equation. Ohm's law in differential form, also called point form, can be written as:

$$\vec{J} = \sigma \vec{E} \tag{1}$$

where σ is the conductivity of the medium at a given point and $\vec{J}$ is the current density.

The continuity equation in cases where the time derivative of the volume charge density can be neglected, can be written as:

$$\vec{\nabla} \cdot \vec{J} = 0 \tag{2}$$

Using (1) and expressing the electric field in terms of the electric potential for the considered low frequency regime, (2) can be rewritten as

$$-\vec{\nabla} \cdot \left(\sigma \vec{\nabla} \cdot \varphi \right) = 0 \tag{3}$$

Current sources at the boundary with a non-conducting medium can be imposed through Neumann boundary condition. In the analysis, the numerical simulations will be carried out using the AC/DC module of the commercial tool COMSOL [8].

B. Hemispheric Grounding Electrode in a Flat Ground

The geometry of the problem is shown in Figure 1. We consider a metallic hemispheric electrode of radius R_0 buried in a flat ground, characterized by its electric conductivity and relative permittivity. The derivation of the grounding resistance is classical and has been carried out elsewhere [9,10]. However, for the sake of completeness, we will present it here.

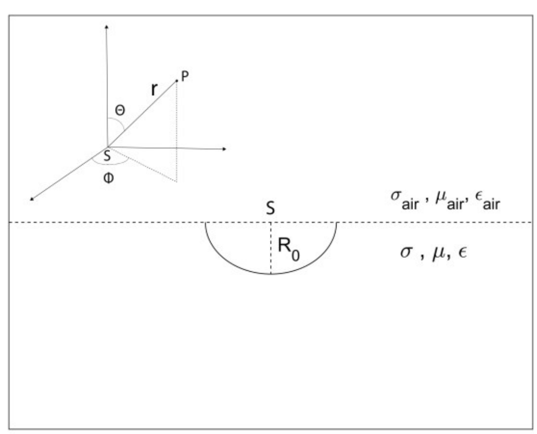

Fig. 1. Hemispheric electrode buried in a flat ground. The origin of the spherical coordinate system is at the center of the hemisphere.

A current I is impressed at the center of the hemisphere. The resistance of the grounding electrode is defined as the ratio of the ground potential rise (GPR) at the feeding point and the injected current I:

$$R = \frac{V_\infty}{I} \tag{4}$$

Due to the symmetry of the problem, the magnitude of the current density $\vec{J}$ is constant at points in the ground that are at a given distance r from the origin and it is collinear with the radial vector. Therefore, the current at a distance r is simply given by:

$$\vec{J} = \frac{I}{A}\hat{e_r} = \frac{I}{2\pi r^2}\hat{e_r} \tag{5}$$

where A is the surface of the hemisphere at a given distance r. Now, from Ohm's law (1), one obtains:

$$\vec{E} = \frac{I}{2\pi\sigma r^2}\hat{e_r} \tag{6}$$

The GPR is defined as the voltage difference from the feeding point to the remote earth:

$$V_\infty = \int_{r=0}^{r=\infty} \vec{E}\,\overrightarrow{dr} = \\ = \int_{r=0}^{r=R_0} \frac{I}{2\pi\sigma_{hemisphere} r^2} dr + \int_{r=R_0}^{r=\infty} \frac{I}{2\pi\sigma r^2} dr \tag{7}$$

The hemisphere being made of metal ($\sigma_{hemisphere}$ in the order of 10^6 S/m), the first integral on the right-hand side of the equation can be neglected (the voltage is constant along the conductor). The final result reads:

$$V_\infty \approx \frac{I}{2\pi\sigma R_0} \tag{8}$$

Thus, the resistance is given by:

$$R_{flat} = \frac{V_\infty}{I} = \frac{1}{2\pi\sigma R_0} \tag{9}$$

C. Hemispheric Grounding Electrode in a Cone-Shaped Ground

Let us now consider the geometry shown in Figure 2. In this case, a hemispheric grounding electrode of radius R_0 is buried on the top of a truncated cone-shaped earth characterized by an angle φ. We assume that the hemispheric electrode reaches the edges of the truncated cone, a situation which does not necessarily correspond to a realistic case, but will allow us to derive an analytical solution for the grounding resistance, providing insight into the effect of a non-flat terrain on the low-frequency response of a grounding system. A more realistic situation will be considered in Section II.E and analyzed numerically using COMSOL.

The current is assumed to be applied at the center of the hemisphere. In this case, the current density in the spherical coordinate system will be a function of both r and the azimuth angle.

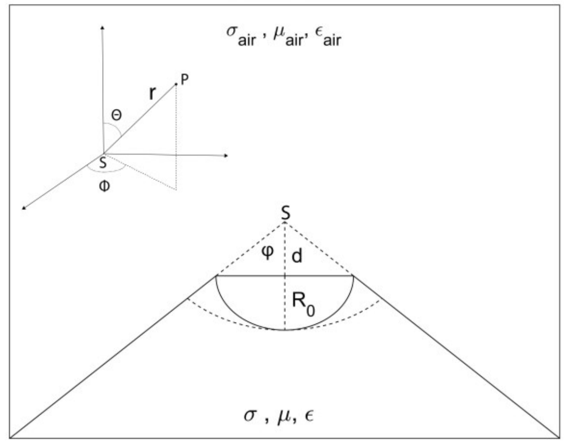

Fig. 2. Hemispheric electrode buried on the top of a truncated cone-shaped ground. The center of the spherical coordinate system is at the tip of the untruncated cone.

In order to be able to derive an analytical solution for the grounding resistance, let us approximate the original hemispheric electrode by a spherical sector delimited by the dotted line and centered at the tip of the cone (Fig. 2). The radius of this sphere is given by

$$R_1 = R_0 + d \tag{10}$$

in which d is defined in Fig. 2. R_1 can be expressed in terms of the apex angle φ as follows:

$$R_1 = R_0(1 + ctg(\varphi)) \tag{11}$$

As can be seen from Fig. 2, the approximated electrode covers a larger area compared to the original one. Thus, the resulting grounding resistance would be an underestimate of the original one. A curved surface area of a spherical sector of radius r is given by:

$$A = \Omega r^2 \tag{12}$$

where Ω is the solid angle which can be calculated from the apex angle as:

$$\Omega = 2\pi(1 - \cos(\varphi)) \tag{13}$$

Because of the symmetry of the approximate geometry, the current density depends only on the variable r and it is always collinear with the radial vector. The current density at a given distance r is given by

$$\vec{J} = \frac{I}{A}\hat{e_r} = \frac{I}{2\pi(1 - \cos(\varphi))r^2}\hat{e_r} \tag{14}$$

The GPR at the feeding point can be calculated as:

$$V_\infty = \int_{r=0}^{r=\infty} \vec{E}\,\overrightarrow{dr} \approx \int_{r=R_1}^{r=\infty} \frac{I}{2\pi\sigma(1 - \cos(\varphi))r^2} dr \tag{15}$$

where, as in (7), the potential drop across the conductor is considered to be negligible. The final expression for the voltage is given by

$$V_\infty = \frac{I}{2\pi\sigma R_0(1 - \cos(\varphi))(1 + ctg(\varphi))} \tag{16}$$

which can be used in (4) to calculate the resistance of the grounding electrode as follows:

$$R_{cone} = \frac{1}{2\pi\sigma R_0(1-\cos(\varphi))(1+ctg(\varphi))} \tag{17}$$

To express the increase of the grounding resistance as a function of the ground profile, let us define a coefficient k given by the ratio of the resistance for a flat ground and the one for a conical ground:

$$k = \frac{R_{cone}}{R_{flat}} = \frac{1}{(1-\cos(\varphi))(1+ctg(\varphi))} \tag{18}$$

As can be seen from (18), this ratio depends only on the apex angle φ. For the case of a flat ground, φ =90º, (17) reduces to (9) and k tends to 1. Fig. 3 presents the coefficient k as a function of the apex angle.

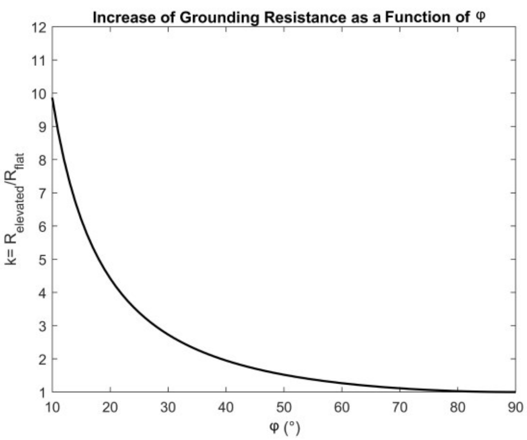

Fig. 3. Coefficient of increase of the grounding resistance as a function of the apex angle.

It can be seen that for very steep profiles, the ratio can take significant values, corresponding to an appreciable increase in the grounding resistance. As an example, for φ = 60º, the resistance is increased by about 30 %, and for φ = 40º, the increase is almost 100%. For very steep profiles, namely for angles smaller than 20º, the resistance can be increased by a factor of 5 or more.

D. Comparison with Numerical Simulations

Fig. 4 shows the distribution of the potential to remote earth obtained by solving (3) numerically using COMSOL. A current source of 1 A was applied at the center of the 20-m radius hemispheric electrode. The Dirichlet boundary condition is set at the bottom of the cone as φ = 0 V, and the Neumann boundary condition, $\vec{J}_{normal} = 0$, is set on the surface of the cone. The height of the cone is taken such that it is far enough for the results to converge (200 to 2000 m, depending on the apex angle). Let us consider a hemisphere with a radius R_0 = 20 m, which would represent as a first approximation the grounding system of a wind turbine. Considering a grounding conductivity of σ = 0.001 S/m and an apex angle of $\varphi = 45^o$, we obtain a grounding resistance of 13,68 **Ω**, while using the analytical approximation (18), we obtain a value of 13,58 **Ω**.

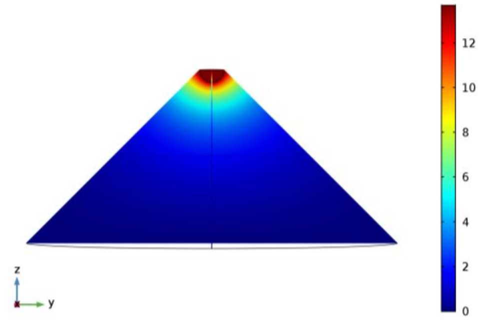

Fig. 4. Potential to remote earth for the case of R_0=20 m, σ=0.001S/m, φ=45° and 1 A current source applied at the center of the hemisphere. Simulated in the commercial tool COMSOL [8].

Fig 5 shows the values of the grounding resistance as a function of the apex angle, obtained using the proposed analytical solution and the COMSOL numerical results. It can be seen that the proposed analytical approximation yields values which are in excellent agreement with numerical results, for all considered angles.

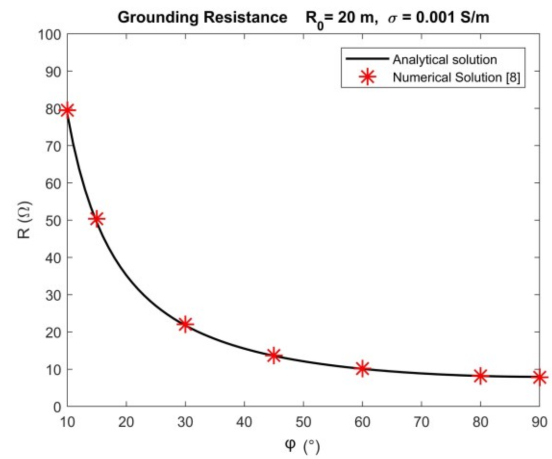

Fig. 5. Grounding resistance for σ = 0.001 S/m and R_0 = 20 m. Analytical solution and discrete numerical solution as a function of apex angle.

Fig 6 shows similar results for the case of a hemispheric grounding electrode of radius R_0 = 5 m. Again, it can be seen that the results obtained using the proposed analytical expression agree well with the numerical results obtained using COMSOL.

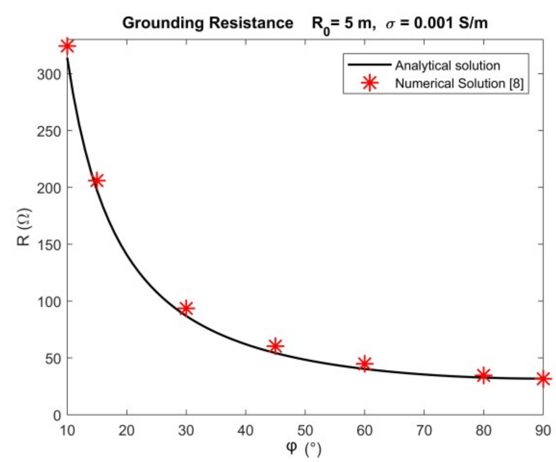

Fig. 6. Grounding resistance for σ = 0.001 S/m and R_0 = 5 m. Analytical solution and discrete numerical solution as a function of the apex angle.

E. Variation of Cone Top Radius

As mentioned earlier, the considered case of a hemispheric electrode that reaches the edges of the truncated cone-shaped mountain (as opposed to one that is smaller) is not a realistic case. Here, we will consider the geometry shown in Fig. 7 in which the top radius of the cone is bigger than the radius of hemispheric grounding electrode. The distance between the center of the hemisphere and edge of cone is r_{top} and the apex angle is φ.

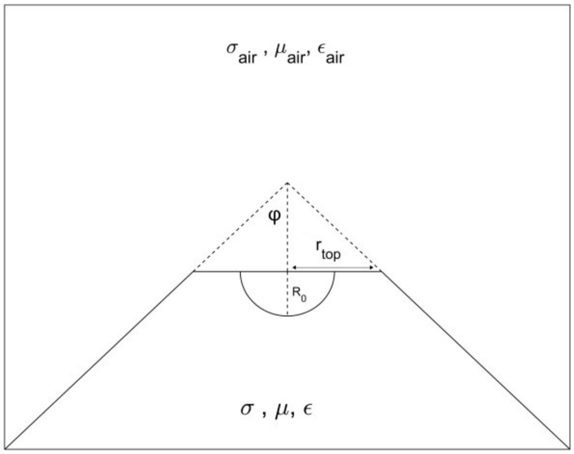

Fig. 7. Hemispheric electrode buried on the top of a truncated cone-shaped ground. The center of the spherical coordinate system is at the tip of the truncated cone prolongation.

Table 1 shows the COMSOL computed values for the grounding resistance of a 5-m radius hemispheric grounding electrode, with a ground conductivity of σ = 0.001 S/m, as a function of the apex angle and the distance r_{top} to the cone edge. The grounding resistance of the same electrode buried in a flat ground would be 31.8 Ω.

Table 1 – Grounding resistance of a 5-m radius hemisphere grounding electrode buried in a cone-shaped ground of conductivity σ = 0.001 S/m, as a function of the apex angle φ and the distance r_{top} to the cone edge.

Apex angle (φ)	Resistance (Ω)			
	r_{top}= R_0	r_{top}= $2R_0$	r_{top}= $4R_0$	r_{top}= $10R_0$
60°	44.8	38	34.5	32.4
45°	60.4	46.2	38.6	34.1
30°	93.5	62.9	46.6	36.8
15°	206	121	75.7	48.7
10°	324.4	188.7	108.7	67.9

It can be seen that, even for the case when the top radius is four times the radius of the grounding electrode, the increase in the grounding resistance with respect to the case of a flat ground would be as high as 50% for an apex angle of 30°. For the case of an apex angle of 60° and r_{top}=$10R_0$, the resulting grounding resistance approaches the value for a flat ground. Similar relative increase as in Table 1. was observed for the case of vertical rod and it will be further discussed in future studies.

III. Conclusion

In this study, we analyzed the response of a grounding electrode located on top of a hill or a mountain top. Specifically, we derived an analytical solution for the low-frequency response of a hemispheric grounding electrode buried on top of a cone-shaped mountain characterized by its apex angle. The derived equation was validated using numerical simulations based on the Finite Element Method obtained using COMSOL.

Results show that, for the same ground electrical parameters, the grounding resistance of such an electrode can increase significantly for steep mountains. Such situations can occur in particular for the case of telecommunication towers or wind turbines located on mountaintops. These conclusions can be extended to any geometry of grounding system.

The study emphasizes the importance of considering the terrain profile in the evaluation of the grounding resistance or structures located in elevated locations.

Acknowledgments – This work was supported in part by the Swiss National Science Foundation (Project No. 200020_175594).

References

[1] R. M. Reap, "Evaluation of Cloud-to-Ground Lightning Data from the Western United States for the 1983–84 Summer Seasons," Journal of Climate and Applied Meteorology, vol. 25, pp. 785–799, Jun. 1986.
[2] A. Smorgonskiy, F. Rachidi, M. Rubinstein, and G. Diendorfer, "On the relation between lightning flash density and terrain elevation," in 2013 International Symposium on Lightning Protection (XII SIPDA), 2013.
[3] F. Rachidi, M. Rubinstein and A. Smorgonskiy, Lightning Protection of Large Wind-Turbine Blades, in Wind Energy Conversion Systems, Springer, p. 227-242, 2012.
[4] J. Montanyà, O. van der Velde, and E. R. Williams, "Lightning discharges produced by wind turbines," Journal of Geophysical Research: Atmospheres, vol. 119, no. 3, pp. 1455–1462, Feb. 2014.
[5] L. Grcev and V. Arnautovski-Toseva, "Grounding systems modeling for high frequencies and transients: some fundamental considerations," in 2003 IEEE Bologna Power Tech Conference Proceedings
[6] L. D. Grcev, A. Kuhar, V. Arnautovski-Toseva, and B. Markovski, "Evaluation of High-Frequency Circuit Models for Horizontal and Vertical Grounding Electrodes," IEEE Transactions on Power Delivery, pp. 1–1, 2018.
[7] F. M. Tesche, M. Ianoz, T. Karlsson EMC Analysis Methods and Computational Models, N.J. Wiley, 1997.
[8] COMSOL Multiphysics® v.5.3. www.comsol.com. COMSOL AB, Stockholm, Sweden.
[9] E. D. Sunde, Earth Conduction Effects in Transmission Systems. New York: Van Nostrand, 1949.
[10] D. Poljak Advanced modeling in computational electromagnetic compatibility, N.J. Wiley, 2007.

Paper VIII

Grounding Resistance of a Hemispheric Electrode Located on the Top of a Finite-Height, Cone-Shaped Mountain

Antonio Sunjerga, Marcos Rubinstein, *Fellow*, IEEE, Dragan Poljak, *Senior Member*, IEEE, Hamidreza Karami and Farhad Rachidi, *Fellow*, IEEE

***Abstract*— In this study, we present an analytical solution for the resistance of a hemispheric grounding electrode located on the top of a mountain. The mountain is modeled as a truncated cone with a finite height. Recently, a closed-form solution for the grounding resistance was derived first for a hemispheric electrode on top of a cone, and later for a more realistic case of a truncated cone with a flat region at its top. The height of the cone was considered infinite in those studies. Here, we extend these studies for the case of a truncated cone with finite height. The analytical solution is compared with numerical simulations and the results agree reasonably well.**

***Index Terms*— Lightning, grounding resistance, hilly terrain, elevated terrain, grounding electrode, finite height**

I. Introduction

Mountain tops are ideal locations for placing either telecommunication towers to obtain line of sight, or wind turbines to maximize the generated power. These locations have a higher risk of being struck by lightning due to the geographical elevation and the height of the tower itself [1-3]. Furthermore, tall structures located on mountaintops can also initiate upward flashes [4]. Furthermore, these areas being often characterized by low soil conductivities, lightning protection of these structures is a challenging task [5,6].

The effectiveness of a grounding system depends mostly on its geometry and its surrounding soil properties, such as the electrical properties of the ground, their frequency dependence and the soil stratification (e.g., [7,8 and 9]), as well as soil ionization [e.g., 10].

It has recently been shown that the grounding resistance can be significantly increased in the case of a non-flat terrain that effectively reduces the conductive volume for the injected current [11]. A similar degree of increase was obtained for both, hemispheric grounding electrodes [11] and vertical rods [12], suggesting that the increase in the grounding resistance is mostly governed by the soil geometry and not by the geometry of grounding electrode. Remote grounding can be one effective way of reducing the grounding resistance of structures located on mountaintops [13].

Analytical solutions for the calculation of the grounding resistance of electrodes buried in the soil are available in the case of a flat terrain (e.g. [14-17]). Recently, analytical solutions for the low-frequency response of a hemispheric grounding electrode buried on the top of a cone-shaped mountain characterized by its apex angle were derived [11, 18]. In these studies, the height of the mountain was assumed to be infinite.

In this letter, we present an analytical solution for the grounding resistance of a hemispheric grounding electrode located on the top of a truncated cone, characterized by a finite height.

II. Analytical Solutions

Fig. 1 presents three different simplified geometries representing a hemispheric grounding electrode located on the top of a mountain. The models shown in Fig. 1-a and Fig. 1-b have been considered in [11]. In these models, the height of the cone-shaped mountain was assumed to be infinite. In this study, we will relax this assumption and consider the geometry shown in Fig. 1-c, in which the finite height of the mountain is taken into account.

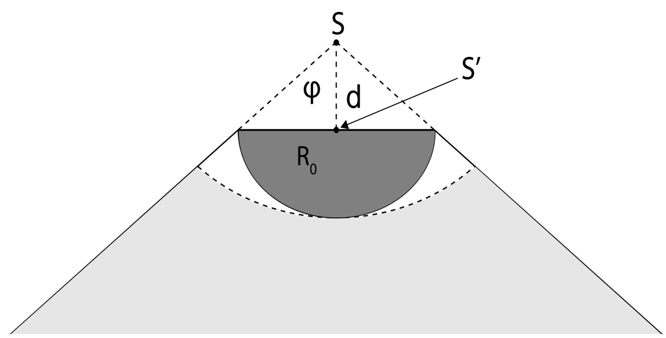

(a)

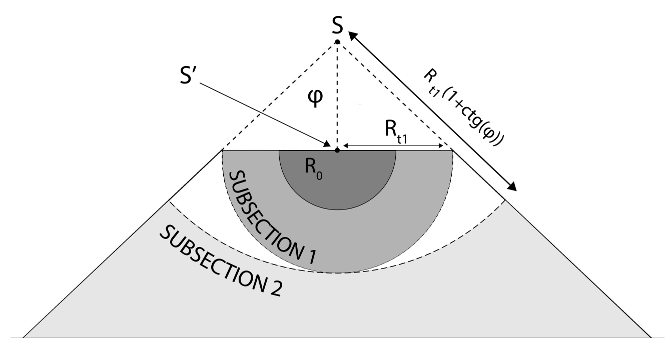

(b)

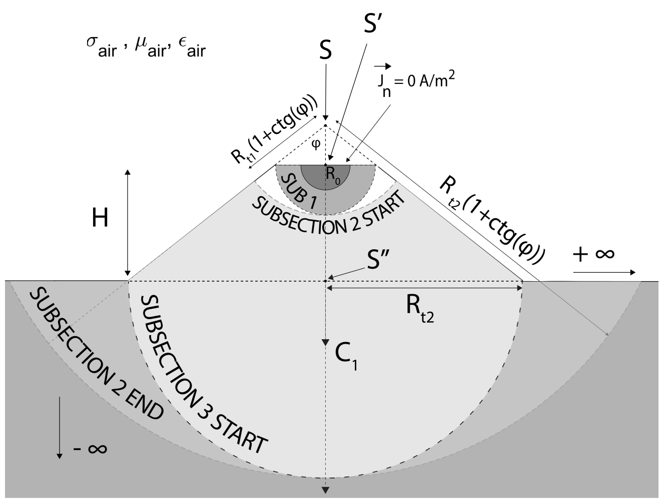

(c)

Fig. 1. Hemispheric grounding electrode in three different geometries of the soil. (a) Electrode buried on the top of a truncated cone-shaped ground. The top radius of the cone is assumed to be equal to the radius of the electrode (b) Same as in (a) but the top radius of the cone is bigger than the radius of hemispheric electrode (c) Same as in (b) but considering a cone-shaped mountain with a finite height.

The analytical solution for the grounding resistance for the simplified model shown on Fig. 1-a is given in [11]:

$$R_a = \frac{1}{2\pi\sigma R_0(1-\cos(\varphi))(1+ctg(\varphi))} \qquad (1)$$

where φ is the apex angle of the cone, σ is the soil conductivity, and R_0 is the radius of hemispheric electrode.

In [18], the solution for the model shown in Fig. 1-b was obtained, splitting the soil into two subsections and summing the respective potentials. The two subsections are illustrated in Fig. 1-b The potential of the first subsection is governed by equations related to a flat ground, while the potential for the second one is governed by the same set of equations corresponding to the geometry of Fig. 1-a [11]. The derived expression for the grounding resistance is [18]:

$$R_b = \left(\frac{1}{R_0} - \frac{1}{R_{t1}} + \frac{1}{R_{t1}(1-\cos(\varphi))(1+ctg(\varphi))}\right)\frac{1}{2\pi\sigma} \qquad (2)$$

in which R_{t1} is the distance from the center of the hemisphere S' to the edge of the cone (see Fig. 1-b).

Using a similar approach as the one used in [18], one can divide the geometry in Fig. 1-c into three subsections. Each subsection in the figure is an annulus sector formed by the space between two arcs of the same circle as follows: Subsection 1, labeled SUB1 in Fig. 1-c, is the annulus sector centered at S' and bounded by the arcs with radii R_0 and R_{t1} (the latter not labeled explicitly in the figure). Subsection 2 is the annulus sector centered at S and bounded by the circular arcs with radii $R_{t1}(1-\cos(\varphi))$ and $R_{t2}(1-\cos(\varphi))$. Finally, subsection 3 is the annulus sector centered at S'' and bounded by the arcs of radii R_{t2} and ∞.

As can be seen from Fig. 1-c, the first and third subsections are governed by the equations associated with a flat ground. The second subsection is governed by the equations associated with the geometry presented in Fig. 1-a and given in [11] with the origin of the coordinate system at the tip of the cone. Note that the region between subsections one and two shown in white in Fig. 1-c is not part of any of the considered subsections and it is the result of the adopted approximation. On the other hand, the region delimited by the start of subsection 3 and the end of subsection 2 belongs to both, subsections 2 and 3. In the following analysis, the potential will be calculated along the curve C_1 (shown in Fig. 1-c.) in order to avoid these undefined regions.

The electrode potential with respect to the remote earth can be obtained as:

$$V_\infty \approx \int_{r'=R_0}^{r'=\infty} \vec{E} \cdot \overrightarrow{dr'} \qquad (3)$$

This voltage can be obtained by integrating the electric field along the curve C_1 and splitting the domain into the three subsections as shown in Fig. 1-c.

First, the voltage drop along C_1 in the first subsection can be obtained using the flat ground voltage expression with the origin of the coordinate system being the center of the hemisphere electrode marked with S' (Fig 1-c):

$$V_1 \approx \int_{r'=R_0}^{r'=R_{t1}} \vec{E} \cdot \overrightarrow{dr'} = \left(\frac{1}{R_0} - \frac{1}{R_{t1}}\right)\frac{I}{2\pi\sigma} \qquad (4)$$

where I is the injected current.

The voltage drop along C_1 in the second subsection can be obtained using the expression derived in [11], considering the origin of the coordinate system at the tip of the cone marked with S (Fig 1-c):

$$V_2 \approx \int_{r=R_{t1}(1+ctg(\varphi))}^{r=R_{t2}(1+ctg(\varphi))} \vec{E} \cdot \overrightarrow{dr} = \left(\frac{1}{R_{t1}(1-\cos(\varphi))(1+ctg(\varphi))} - \frac{1}{R_{t2}(1-\cos(\varphi))(1+ctg(\varphi))}\right)\frac{I}{2\pi\sigma} \qquad (5)$$

Finally, the voltage drop along C_1 in the third subsection can be approximated using the flat earth expression considering the origin of the coordinate system shown with S'' (Fig 1-c):

$$V_3 \approx \int_{r''=R_{t2}}^{r''=\infty} \vec{E} \cdot \overrightarrow{dr''} = \frac{I}{2\pi\sigma R_{t2}} \qquad (6)$$

The total electrode potential is equal to the sum of these three terms:

$$V_\infty = V_1 + V_2 + V_3 = \left(\frac{1}{R_0} - \frac{1}{R_{t1}} + \frac{1}{R_{t1}(1-\cos(\varphi))(1+ctg(\varphi))} - \frac{1}{R_{t2}(1-\cos(\varphi))(1+ctg(\varphi))} + \frac{1}{R_{t2}}\right)\frac{I}{2\pi\sigma} \qquad (7)$$

in which R_{t2} is:

$$R_{t2} = tan(\varphi)H + R_{t1} \tag{8}$$

Dividing (7) by the current, one can obtain the expression for the grounding resistance as:

$$R_c = \left(\frac{1}{R_0} - \frac{1}{R_{t1}} + \frac{1}{R_{t1}(1-\cos(\varphi))(1+ctg(\varphi))} - \frac{1}{R_{t2}(1-\cos(\varphi))(1+ctg(\varphi))} + \frac{1}{R_{t2}}\right)\frac{1}{2\pi\sigma} \tag{9}$$

It can readily be shown that when the mountain height tends to infinity, (8) tends to infinity as well, so that (9) reduces to (2). Furthermore, it can easily be shown that imposing $R_{t1}=R_0$, (2) will be reduced to (1).

III. Validation With Numerical Simulations

In this section, we present a comparison between the derived analytical solution (9) and numerical simulations obtained using the commercial software COMSOL [19]. More details about simulations can be found in [11]. Table 1 presents the numerical results considering different values for the height and apex angle for the studied geometry (Fig. 1-c). It can be seen that the assumption of an infinite mountain height results in an overestimation of the grounding resistance. Note that we only considered a single conductivity of 0.001 S/m in our calculations. The grounding resistance has a linear dependency with the soil conductivity, as can be readily seen in the analytical equation (9) and confirmed by numerical evaluation.

As the apex angle increases toward the limit of 90° and the height to the limit of zero, the grounding resistance will tend to the value corresponding to a flat ground:

$$R_{flat} = \frac{1}{2\pi\sigma R_0} \tag{10}$$

which is equal to 31.8 Ω for the observed case.

The relative errors of equation (9) are presented in Table 2. We can observe that the results obtained using the analytical solutions agree reasonably well with the reference numerical results.

TABLE 1. Grounding resistance simulation for σ=0.001 S/m, R_0=5 m, R_{t1}=10 m, and R_{flat}=31.8 Ω

Apex angle (φ)	Resistance (Ω)				
	H = 10 m	H = 25 m	H = 100 m	H = 250 m	H = ∞
45	32	35.7	39.2	41.3	46.2
30	36.3	44.4	54	57.5	62.9
15	42.2	60.3	92.2	105.8	121
10	44.7	69.1	121.2	148.6	188.7

Fig. 2 presents a plot of the increase of the grounding resistance as a function of the cone height and apex angle compared to the case of a flat ground. The grounding resistance was obtained analytically using (5). As the value of the apex angle increases, the results converge to those corresponding to the case of a flat ground. In a similar way, decreasing the height, the results converge to those of a flat ground. For the case of an apex angle of 30° and a height of about 100 m, the increase of the grounding resistance is almost a factor of two.

TABLE 2. Grounding resistance relative error of eq. (9) for σ=0.001 S/m, R_0=5 m, R_{t1}=10 m, and R_{flat}=31.8 Ω

Apex angle (φ)	Resistance (Ω)				
	H = 10 m	H = 25 m	H = 100 m	H = 250 m	H = ∞
45	7.6%	1%	-3.6%	-1.8%	6.7%
30	11.5%	6.12%	1.9%	1.6%	5.6%
15	6%	5.8%	4.6%	3.8%	5.27%
10	-8.1%	0.3%	3.6%	3.1%	8.35%

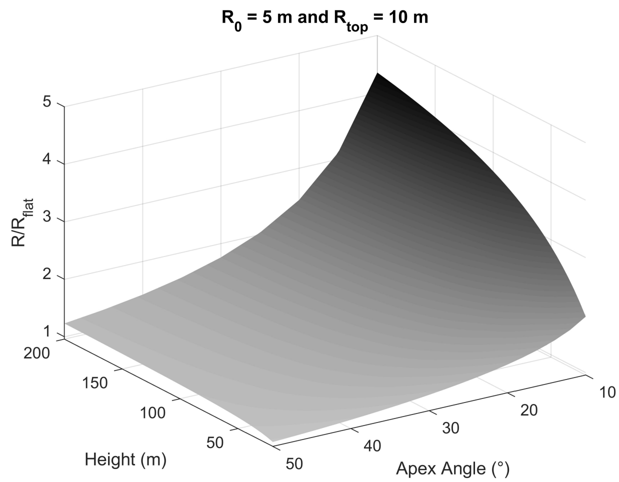

Fig. 2. Increase of the grounding resistance predicted by the derived analytical formula as a function of the height of the truncated cone and its apex angle, for a 5-m radius hemispheric electrode. The top radius of the truncated cone is 10 m.

IV. Conclusion

Recently, closed-form solutions for the grounding resistance have been derived first for a hemispheric electrode on top of a cone, and later for a more realistic case of a truncated cone with a flat region at its top. The height of the cone was considered infinite in those studies.

In this paper, we derived an analytical solution for the grounding resistance of a hemispheric electrode located on a mountaintop represented by a truncated cone, taking into account its finite height. The derived analytical solution was validated using as reference numerical simulations.

The effect of the cone height and apex angle on the resulting grounding resistance was discussed. The relative error incurred in when using the derived approximate analytical expression for the grounding resistance is much smaller than 10% for the cases studied in this paper with the exception of a single case for which the error was of the order of 10%.

Acknowledgments – This work was supported in part by the Swiss National Science Foundation (Project No. 200020_175594).

REFERENCES

[1] A. Smorgonskiy, F. Rachidi, M. Rubinstein, and G. Diendorfer, “On the relation between lightning flash density and terrain elevation,” in 2013 International Symposium on Lightning Protection (XII SIPDA), 2013.

[2] D. Poljak, D. Čavka, Properties and Characterization of Modern Materials, Chapter Electromagnetic Compatibility Aspects of Wind Turbine Analysis and Design July 2016.

[3] F. Rachidi, M. Rubinstein, J. Montanyà, J. Bermúdez, R.Sola, G. Solà, and N. Korovkin, “A Review of Current Issues in Lightning Protection of New-Generation Wind-Turbine Blades”, IEEE Transactions on Industrial Electronics, Vol. 55, No. 6, June 2008.

[4] F. Rachidi, M. Rubinstein and A. Smorgonskiy, Lightning Protection of Large Wind-Turbine Blades, in Wind Energy Conversion Systems, Springer, p. 227-242, 2012.

[5] "IEC International Standard. Lightning protection. IEC 61400e61424" in Wind turbine generation system, Geneva:International Electrotechnical Commission, vol. 24, 2010.

[6] Motorola R56, Standards and Guidelines for Communication Sites, 2005

[7] D. Cavka, D. Poljak, V. Doric, and R. Goic, “Transient analysis of grounding systems for wind turbines,” Renewable Energy, vol. 43, pp. 284–291, Jul. 2012.R.

[8] Alipio and S. Visacro, “Modeling the Frequency Dependence of Electrical Parameters of Soil,” IEEE Transactions on Electromagnetic Compatibility, vol. 56, no. 5, pp. 1163–1171, Oct. 201

[9] F. P. Dawalibi, J. Ma, and R. D. Southey, “Behaviour of grounding systems in multilayer soils: a parametric analysis,” IEEE Transactions on Power Delivery, vol. 9, no. 1, pp. 334–342, 1994.

[10] A. M. Mousa, “The soil ionization gradient associated with discharge of high currents into concentrated electrodes,” IEEE Transactions on Power Delivery, vol. 9, no. 3, pp. 1669–1677, Jul. 1994.

[11] A. Sunjerga, F. Rachidi, M. Rubinstein, and D. Poljak, “Calculation of the Grounding Resistance of Structures Located on Elevated Terrain,” IEEE Transactions on Electromagnetic Compatibility, pp. 1–5, 2018.

[12] A. Sunjerga, F. Rachidi, M. Rubinstein, and D. Poljak, “On the Influence of an Elevated Terrain on the Grounding Resistance of a Vertical Rod” presented at 19th International Conference on Environment and Electrical Engineering (EEEIC), 2019.

[13] A. Sunjerga, F. Rachidi, M. Rubinstein, and D. Poljak, “Reduction of the Cone Shaped Terrain Grounding Resistance by Remote Grounding” submitted to 27th International Conference on Software, Telecommunications and Computer Networks (SoftCOM), 2019.

[14] E. D. Sunde, Earth Conduction Effects in Transmission Systems. New York: Van Nostrand, 1949.

[15] L. Grcev and V. Arnautovski-Toseva, “Grounding systems modeling for high frequencies and transients: some fundamental considerations,” in 2003 IEEE Bologna Power Tech Conference Proceedings

[16] L. D. Grcev, A. Kuhar, V. Arnautovski-Toseva, and B. Markovski, “Evaluation of High-Frequency Circuit Models for Horizontal and Vertical Grounding Electrodes,” IEEE Transactions on Power Delivery, pp. 1–1, 2018.

[17] F. M. Tesche, M. Ianoz, T. Karlsson EMC Analysis Methods and Computational Models, N.J. Wiley, 1997.

[18] Tan, K. B., Lu, H. M., Zhang, Y., & Zuo, W. C. (2019). Analysis of the Grounding Resistance of a Hemispheric Electrode Located on a Truncated Cone. IEEE Transactions on Electromagnetic Compatibility, 1–3. https://doi.org/10.1109/temc.2019.2940902

[19] COMSOL Multiphysics® v.5.3. www.comsol.com. COMSOL AB, Stockholm, Sweden.